

X-ray observations of the
accreting Be/X-ray binary pulsar
A 0535+26 in outburst

Dissertation
zur Erlangung des Grades eines
Doktors der Naturwissenschaften
der Fakultät für Mathematik und Physik
der Eberhard Karls Universität Tübingen

vorgelegt von

ISABEL CABALLERO DOMÉNECH

aus Madrid
2009

Selbstverlegt von: I. Caballero Doménech, Neue Straße 16, 72070 Tübingen
Tag der mündlichen Prüfung: 20.04.2009
Dekan: Prof. Dr. W. Knapp
1. Berichterstatter: Prof. Dr. A. Santangelo
2. Berichterstatter: Prof. Dr. K. Werner

Abstract

Neutron stars are compact objects, characterized by $R \sim 10 - 14$ km radius, $M \sim 1.4 M_{\odot}$ mass and extremely high central densities $\rho \sim 10^{15} \text{g cm}^{-3}$. If they are part of a binary system, a flow of matter can take place from the companion star onto the neutron star. The accretion of matter onto neutron stars is one of the most powerful sources of energy in the universe. The accretion of matter takes place under extreme physical conditions, with magnetic fields in the range $B \sim 10^{8-15}$ G, which are impossible to reproduce on terrestrial laboratories. Therefore, accreting neutron stars are unique laboratories to study the matter under extreme conditions.

In this thesis, X-ray observations of the accreting Be/X-ray binary A 0535+26 during a normal (type I) outburst are presented. In this system, the neutron star orbits around the optical companion HDE 245770 in an eccentric orbit, and sometimes presents X-ray outbursts (giant or normal) associated with the passage of the neutron star through the periastron. After more than eleven years of quiescence, A 0535+26 showed outbursting activity in 2005. The normal outburst analyzed in this work took place in August/September 2005, and reached a maximum X-ray flux of $F_X \sim 400$ mCrab in the 5 – 100 keV range. The outburst, which lasted for ~ 30 days, was observed with the *RXTE* and *INTEGRAL* observatories.

We have measured the spectrum of the source. In particular, two absorption-like features, interpreted as fundamental and first harmonic cyclotron resonant scattering features, have been detected at $E \sim 46$ keV and $E \sim 102$ keV with *INTEGRAL* and *RXTE*. Cyclotron lines are the *only* direct way to measure the magnetic field of a neutron star. Our observations have allowed to confirm the magnetic field of A 0535+26 at the site of the X-ray emission to be $B \sim 5 \times 10^{12}$ G.

We studied the luminosity dependence of the cyclotron line in A 0535+26, and contrary to other sources, we found no significant variation of the cyclotron line energy with the luminosity. Changes of the cyclotron line energy with the X-ray luminosity are thought to be related to a change in the height of the accretion column as the mass accretion rate varies.

A detailed timing analysis has been performed, and we find for the first time the onset of a spin-up, at a phase close to the periastron passage, during a normal outburst, providing evidence for an accretion disk around the neutron star. Energy-dependent

pulse profiles of the source have been studied and compared to historical observations.

During the rising part of the outburst a series of flares were observed. *RXTE* observed one of these flares, and we found during the flare the energy of the fundamental cyclotron line shifted to a significantly higher position compared to the rest of the outburst. Also, the energy-dependent pulse profiles during the flare were found to vary significantly from the rest of the outburst. These differences have been interpreted in terms of a theoretical model, based on the presence of magnetospheric instabilities at the onset of the accretion.

We applied a decomposition method to A 0535+26 energy-dependent pulse profiles. Basic assumptions of the method are that the asymmetry observed in the pulse profiles is caused by non-antipodal magnetic poles, and that the emission regions have axisymmetric beam patterns. Using pulse profiles obtained from *RXTE* observations, the contribution of the two emission regions has been disentangled. Constraints on the geometry of the pulsar and a possible solution of the beam pattern are given. The reconstructed beam pattern is interpreted in terms of a geometrical model that includes relativistic light deflection.

To my father

Contents

1	Introduction	1
1.1	History of X-ray astronomy	1
1.2	Thesis outline	4
2	Accreting X-ray pulsars	6
2.1	Introduction	6
2.1.1	X-ray binaries	6
2.1.2	Neutron star basic properties	7
2.1.3	Accretion	12
2.1.4	Mass transfer mechanisms in X-ray binaries	15
2.2	Neutron star X-ray binaries	19
2.2.1	Accretion geometry	19
2.2.2	Disk accretion	21
2.2.3	Torque theory	22
2.2.4	Accretion into the polar caps	23
2.2.5	Spectral formation	24
2.2.6	Magnetic fields	26
2.3	Observations of neutron star X-ray binaries	28
2.3.1	Cyclotron lines	28
2.3.2	Pulse profiles	33
3	The Be/X-ray binary system A 0535+26	37
3.1	Overview	37
3.1.1	History of outbursts	38
3.1.2	The source in quiescence	38
3.2	Timing properties	40
3.2.1	Pulse period evolution	40
3.2.2	QPOs	41
3.2.3	Pulse profiles	42
3.3	Spectral properties	42
3.4	Optical observations	43

4	<i>RXTE</i> and <i>INTEGRAL</i> observatories	46
4.1	<i>RXTE</i>	46
4.1.1	The Proportional Counter Array <i>PCA</i>	46
4.1.2	The High Energy X-ray Timing Experiment <i>HEXTE</i>	48
4.1.3	The All Sky Monitor <i>ASM</i>	49
4.2	<i>INTEGRAL</i>	49
4.2.1	Imaging with <i>INTEGRAL</i>	50
4.2.2	<i>SPI</i>	52
4.2.3	<i>IBIS</i>	53
4.2.4	<i>JEM-X</i>	54
4.2.5	<i>OMC</i>	55
4.2.6	Dithering	55
5	A 0535+26 observations with <i>RXTE</i> and <i>INTEGRAL</i>	57
5.1	Overview of the August/September 2005 outburst	57
5.1.1	Optical light curve with <i>OMC</i>	60
5.2	<i>RXTE</i> and <i>INTEGRAL</i> data analysis	61
5.2.1	X-ray spectral analysis	61
5.2.2	<i>RXTE</i> data extraction	63
5.2.3	<i>INTEGRAL</i> data extraction	64
6	The main outburst	66
6.1	Overview: <i>RXTE</i> and <i>INTEGRAL</i> light curves	66
6.2	Pulse period determination	67
6.2.1	First estimate: epoch folding	67
6.2.2	Phase connection method	68
6.3	Pulse profiles	73
6.4	Spectral analysis	77
6.4.1	Cyclotron lines	79
6.4.2	Cyclotron line energy evolution with X-ray luminosity	81
6.4.3	Phase resolved spectroscopy	83
6.5	Discussion of results	85
6.5.1	Pulse period and pulse profiles	85
6.5.2	Cyclotron lines	89
6.5.3	Torque theory and spin-up.	91

7	Pre-outburst flaring activity	93
7.1	Observations during the <i>pre-outburst flare</i>	93
7.1.1	Change in the energy dependent pulse profiles	93
7.1.2	Change in the cyclotron line energy	94
7.2	Evidence for magnetospheric instability	96
7.2.1	Summary of results	96
7.2.2	Disk accretion and mass transport in the magnetosphere.	99
7.2.3	Low-mode magnetospheric instability in A 0535+26	102
8	Pulse profile decomposition	108
8.1	Description of the method	108
8.1.1	Assumptions	109
8.1.2	Steps of the method	111
8.2	Application to A 0535+26	118
8.2.1	Observations	118
8.2.2	Search for acceptable decompositions	118
8.2.3	From single-pole profiles to geometry and beam pattern	124
8.2.4	Interpretation of reconstructed beam pattern	127
9	Summary and Conclusions	134
9.1	Summary	134
9.2	Outlook	137
	Bibliography	141
A	Log of <i>RXTE</i> observations	149
B	Pulse period with <i>RXTE</i>	151
C	<i>RXTE</i> pulse profiles	153
D	Results of <i>RXTE</i> spectral analysis	165
E	Fundamental and astronomical physical constants	168
	Acknowledgments	171
	Curriculum vitae	173

List of Figures

1.1	Discovery of first extrasolar X-ray source Sco X-1	2
1.2	Attenuation of electromagnetic radiation in the atmosphere . . .	3
1.3	Discovery of X-ray pulsations from Cen X-3	4
2.1	Distribution of X-ray binaries in the Galaxy	7
2.2	Neutron star EOSs	8
2.3	Neutron star masses	9
2.4	Pulsar population in $P - \dot{P}$ diagram	13
2.5	Pulsar population in $P - B$ diagram	14
2.6	Roche potential	16
2.7	Roche Lobe overflow	17
2.8	Wind accretion	18
2.9	Schematic view of Be/X-ray binary system	19
2.10	Lighthouse effect	20
2.11	Magnetically threaded disk model	22
2.12	Accretion funnel	24
2.13	“Fan” and “pencil beam” emission patterns	25
2.14	Accretion column	26
2.15	Spectral continuum formation	27
2.16	CRSF in Her X-1	29
2.17	CRSFs sources in the Galaxy	30
2.18	CRSFs in 4U 0115+64	31
2.19	Simulated cyclotron line profiles	31
2.20	CRSF energy vs. luminosity for 4U 0115+64 and V 0332+53 . .	33
2.21	CRSF energy vs. luminosity for Her X-1	34
2.22	Vela X-1 energy dependent pulse profiles	35
2.23	Effect of relativistic light deflection in pulse profiles	36
3.1	A 0535+26 light curve and frequency evolution in 1994	40
3.2	Pulse period history of A 0535+26 before 2005	41
3.3	A 0535+26 pulse profiles during 1989 and 1994 outbursts	43
3.4	A 0535+26 cyclotron lines discovery spectrum	44
3.5	A 0535+26 optical activity	45

4.1	Schematic view of the <i>RXTE</i> spacecraft	47
4.2	Schematic views of the <i>PCA</i> and <i>HEXTE</i>	49
4.3	<i>INTEGRAL</i> spacecraft	50
4.4	Illustration of coded-mask imaging	51
4.5	PSF of coded-mask systems.	52
4.6	Fully and Partially Coded Field of View	53
4.7	<i>INTEGRAL</i> dithering patterns	56
5.1	2005 outbursts of A 0535+26 with <i>ASM</i> and <i>BAT</i>	58
5.2	August/September 2005 normal outburst with <i>ASM</i> and <i>BAT</i>	59
5.3	Sketch of the orbit of A 0535+26	60
5.4	<i>OMC</i> light curve	61
6.1	<i>IBIS</i> A 0535+26 mosaic image	67
6.2	<i>PCA</i> light curve during the August/September 2005 outburst	68
6.3	<i>OMC</i> , <i>JEM-X</i> and <i>IBIS</i> light curves of A 0535+26	69
6.4	Epoch folding χ^2 distributions	70
6.5	Example of phase reference	71
6.6	Pulse period history of A 0535+26	71
6.7	Spin-up of A 0535+26	72
6.8	<i>INTEGRAL</i> and <i>RXTE</i> energy dependent pulse profiles	74
6.9	<i>RXTE</i> pulse profiles during the <i>main outburst</i>	75
6.10	Pulse to pulse variation	76
6.11	A 0535+26 pulsed fraction	77
6.12	A 0535+26 power spectrum	78
6.13	<i>INTEGRAL</i> and <i>RXTE</i> phase averaged spectra	81
6.14	<i>INTEGRAL</i> and <i>RXTE</i> energy unfolded spectra	82
6.15	Cyclotron line evolution with the X-ray luminosity	83
6.16	Evolution of spectral parameters during the <i>main outburst</i>	84
6.17	Phase resolved spectroscopy	86
6.18	Phase resolved spectroscopy: CRSFs and line ratios	87
6.19	A 0535+26 spin-up vs. flux	92
7.1	<i>PCA</i> light curve with zoom on <i>pre-outburst flare</i>	94
7.2	Pulse profiles during the <i>flare</i> and <i>main outburst</i>	95
7.3	Contour plots showing cyclotron line energy change	97
7.4	Spectral parameters evolution including the <i>pre-outburst flare</i>	98
7.5	<i>RXTE</i> unfolded spectra during the <i>pre-outburst flare</i> and <i>main outburst</i>	99
7.6	Pre-outburst flares in GS 1843-024 and EXO 2030+375	100
7.7	Bounday layer in magnetically threaded disk model	101
7.8	Development of Kruskal-Schwarzschild instability	102
7.9	Example of unstable accretion	103

7.10	Stable and unstable accretion regimes	104
7.11	Approximate photon scattering cross-section	106
8.1	Illustration of beam pattern	109
8.2	Magnetic pole and its rotation	110
8.3	Sum of two symmetric functions	111
8.4	Schematic view of a rotating neutron star	112
8.5	Intrinsic neutron star geometry	113
8.6	Example of rejected decomposition	116
8.7	“Non-negative criterion” in $\Phi_1 - \Delta$ plane	119
8.8	Example of decompositions grouped in one type	120
8.9	Best decompositions in $\Phi_1 - \Delta$ plane	121
8.10	Best decompositions for region A (one observation)	122
8.11	Best decompositions for regions C and E	123
8.12	Best decompositions for regions B and D	124
8.13	Best decomposition for region A (merged observations)	125
8.14	Best decompositions for region A (seven energy bands)	126
8.15	Best decompositions for region A (low energy data)	127
8.16	Constraints on the geometry of A 0535+26	128
8.17	Schematic view of A 0535+26 using the obtained geometry	128
8.18	Reconstructed beam pattern of A 0535+26	129
8.19	Beam pattern for regions A and E	130
8.20	Hollow column model	131
8.21	Beam pattern models for A 0535+26	132
8.22	Computed beam pattern for different energies	132
9.1	BAT light curve of A 0535+26 in 2008–2009	138

List of Tables

2.1	List of cyclotron sources	32
3.1	A 0535+26 orbital ephemeris	37
3.2	History of giant outbursts of A 0535+26	39
4.1	<i>RXTE</i> performance parameters	48
4.2	<i>SPI</i> and <i>IBIS</i> performance parameters	54
4.3	<i>JEM-X</i> and <i>OMC</i> performance parameters	55
5.1	Log of <i>INTEGRAL</i> and <i>RXTE</i> observations	59
5.2	Critical $\Delta\chi^2$ to calculate confidence regions	62
6.1	Pulse period measured with <i>INTEGRAL</i>	70
6.2	Pulse period measured with <i>RXTE</i>	73
6.3	Best fit parameters	80
6.4	CRSF parameters using different models for the continuum	82
6.5	Neutron star magnetic field derived from cyclotron line	82
6.6	Best fit values from phase resolved analysis	85
7.1	Best-fit values for the <i>pre-outburst flare</i> observations	96
8.1	Symmetry points Φ_1 , Φ_2 and Δ for best decomposition	124
8.2	Geometrical parameters of A 0535+26 from the decomposition	126
8.3	Model parameters for beam pattern of A 0535+26	131
A.1	Log of <i>RXTE</i> observations	149
A.1	continued from previous page	150
B.1	Pulse period	151
B.1	continued from previous page	152
D.1	<i>RXTE</i> best fit parameters - Part I	166
D.2	<i>RXTE</i> best fit parameters - Part II	167
E.1	Fundamental and astronomical physical constants	169

CHAPTER 1

Introduction

1.1 History of X-ray astronomy

X-ray astronomy is a relatively young science. X-rays outside the Earth were measured for the first time in 1946, when using detectors mounted on V2 rockets Friedman et al. (1951) discovered X-rays from the Sun. The first extrasolar X-rays were discovered by Giacconi et al. (1962)¹ with Aerobee rockets. The experiment was intended to detect solar X-rays reflected from the surface of the Moon. Instead, an extrasolar source emitting in X-rays was discovered: Sco X-1, in the Scorpius constellation (see Fig. 1.1).

Due to the absorption of X-rays by the Earth's atmosphere, X-ray astronomical observations must be performed from balloons or satellites. This fact is a limiting factor in the weight and dimensions of the instruments used, compared to ground based experiments. The attenuation of the electromagnetic radiation in the atmosphere as a function of the energy is shown in Fig. 1.2.

Since the discovery of Sco X-1, several balloon flight experiments between 1963 and 1970 discovered up to 40 extra-solar X-ray sources. With the launch of the first X-ray satellite *Uhuru* (Giacconi et al. 1971b), operating between 1970–1973, the number of extra-solar X-ray sources increased to more than 400. Several other X-ray missions in the following years contributed to the discovery of X-ray sources, like *Ariel V*² (Smith & Courtier 1976), SAS-3 (Mayer 1975) or *HEAO-1* (Peterson 1975) among others. In 1978, the *Einstein* observatory (Giacconi et al. 1979) located up to 7000 X-ray sources in the sky, which increased to 125000 with the German *Roentgensatellite ROSAT* (Trümper 1984). With the modern X-ray satellites *XMM-*

¹Riccardo Giacconi was awarded the Nobel Prize in physics in 2002 for "for pioneering contributions to astrophysics, which have led to the discovery of cosmic X-ray sources". The Royal Swedish Academy of Sciences cited Herbert Friedman, Riccardo Giacconi and Bruno Rossi as pioneers in X-ray astronomy.

²The *Ariel V* catalog gave name to a large number of sources, including A 0535+26. Note that A 0535+26 is referred to as 1A 0535+262 in the Astronomical Database SIMBAD.

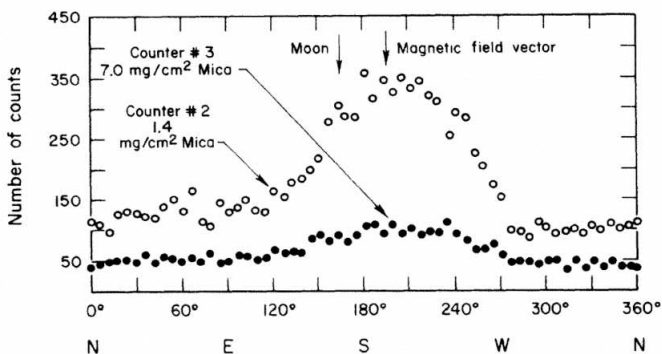


Figure 1.1: Discovery of first extrasolar X-ray emission from Sco X-1 (Giacconi et al. 1962). The azimuthal distributions of measured counts from two Geiger counters are shown.

Newton (Jansen et al. 2001) and *Chandra* (Weisskopf et al. 2002), the number of X-ray sources is, as of September 2007, of the order of 550000 (Fabbiano et al. 2007, Barcons et al. 2007), and about a million X-ray sources are expected to be discovered by 2010 (source: http://heasarc.gsfc.nasa.gov/docs/heasarc/headates/how_many_xray.html)

The X-ray observatories *RXTE* (1995–present, Bradt et al. 1993) and *BeppoSAX* (1996–2002, Boella et al. 1997) provided for the first time broad-band coverage from ~ 1 keV up to ~ 200 keV, with unprecedented timing resolution (*RXTE*) and spectral resolution (*BeppoSAX*). Both missions allowed (with *RXTE* still performing well today) the study of X-ray sources with unprecedented detail. In the following, the current X-ray and gamma-ray missions operating at the time of writing are briefly described. *Chandra* (Weisskopf et al. 2002) and *XMM-Newton* (Jansen et al. 2001), launched in July and December 1999 respectively, focus X-rays up to ~ 10 keV by using grazing incidence reflection. The *INTEGRAL* observatory (Winkler et al. 2003), launched in October 2002, makes use of coded-mask telescopes and allows to obtain images of the X-ray and gamma-ray sky, providing coverage in the broad band from ~ 3 keV up to ~ 10 MeV. *Suzaku* (Mitsuda et al. 2004), launched in July 2005, allows to perform broad-band (~ 0.4 –600 keV) high-resolution spectroscopy. *Swift* (Gehrels et al. 2005) is a gamma-ray burst dedicated mission, launched in November 2004. It contains three instruments that provide coverage in the optical, X-ray (0.3 – 10 keV) and gamma-ray (15 – 150 keV) regimes. More recently, in April 2007, *AGILE* (Tavani et al. 2008) was launched. It performs observations in the hard-X-ray and gamma-ray sky, covering the 18 – 60 keV and 30 MeV – 50 GeV energy ranges.

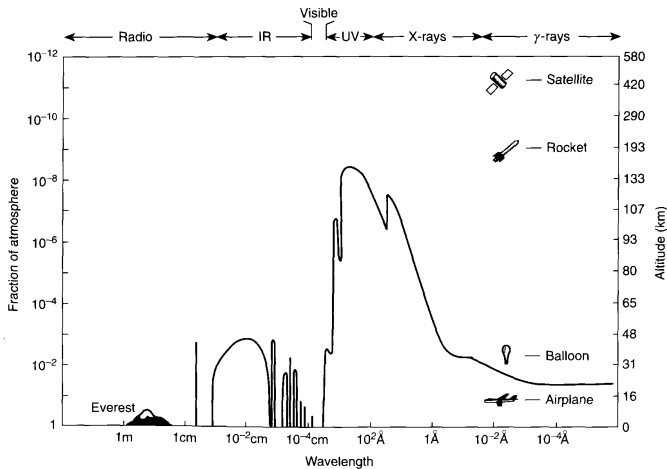


Figure 1.2: Attenuation of electromagnetic radiation in the Earth's atmosphere as a function of the wavelength and the energy. The solid line represents the altitude by which half of the radiation from space has been attenuated. (Figure from Seward & Charles 1995).

The most recent launch was that of Fermi (formerly *Glast*, Ritz et al. 2007), in June 2008. It is observing the 30 MeV – 300 GeV sky, and has a gamma-ray burst monitor sensitive in the 8 keV – 30 MeV energy range. The X-ray and gamma-ray missions in orbit cover almost entirely the wide energy range from a few keV up to ~ 300 GeV.

Monitoring instruments have played a major role in the development of X-ray astronomy. They allow to discover transient sources that otherwise could not be detected, and permit to study long-term behavior of sources. The first monitoring instrument, in orbit between 1977–1979, was *HEAO-1 A4* (Peterson 1975). After that, for more than ten years there were no monitoring instruments looking at the X-ray sky, until the *CGRO* was launched in 1991, carrying on board *BATSE* (Fishman et al. 1989). *BATSE* performed a very important mission for more than 9 years, monitoring the X-ray and gamma-ray sky in the 20 keV – 1 MeV band. Since the launch of *RXTE* in 1996, its monitoring instrument *ASM* (Levine et al. 1996) is scanning 80% of the (2 – 10) keV sky every 90 minutes. Another monitoring instrument currently operating is *BAT* (Barthelmy et al. 2005) on board the *Swift* satellite, which since 2005 monitors the (15 – 50) keV sky. Both missions provide almost real time light curves from the X-ray sources observed in the sky³. These light curves are of crucial importance to detect transient phenomena in the X-ray sky and to study long-term

³The *ASM* and *BAT* light curves are available at <http://xte.mit.edu/> and <http://swift.gsfc.nasa.gov/docs/swift/results/transients/> respectively

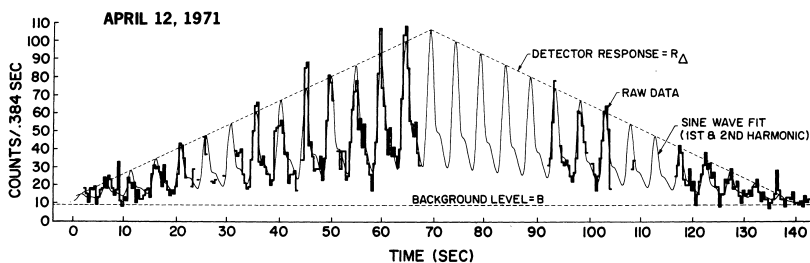


Figure 1.3: Discovery of pulsations from an X-ray source: the X-ray binary Cen X-3, identified as an X-ray pulsar (Giacconi et al. 1971a). A sinusoidal fit to the data is overlotted.

behavior of sources.

A very important finding in X-ray astronomy was the discovery of pulsations of Cen X-3 with *Uhuru* (see Fig. 1.3), leading to the identification of the source as an X-ray pulsar (Giacconi et al. 1971a). Pulsars are rotating neutron stars that emit beams of radiation, and are therefore observed in the Earth as pulsating sources. Neutron stars were theoretically predicted in 1934 by Baade & Zwicky (1934), only two years after the discovery of the neutron (Chadwick 1932). It took then more than 30 years until neutron stars were experimentally discovered, through the detection of radio pulsations from PSR 1919+21 by Jocelyn Bell (Hewish et al. 1968). With the discovery of X-ray pulsars, a new field of research rapidly developed, providing new insights into the physics of matter under extreme conditions.

1.2 Thesis outline

This thesis is based on *RXTE* and *INTEGRAL* observations of the accreting pulsar A 0535+26 in outburst. In Chapter 2 an introduction to X-ray binary systems is given, and basic properties of neutron stars are reviewed. The physics of accretion, which is the main source of energy of X-ray binaries, is introduced. Observations of X-ray binaries containing a neutron star are reviewed, with special emphasis on the cyclotron line features some of these sources present in their spectra. Chapter 3 gives a review the accreting pulsar A 0535+26. Historical observations and the physical picture that has emerged from them are presented.

Chapter 4 provides an overview of the *RXTE* and *INTEGRAL* observatories, with a brief description of the instruments on board both satellites. The observations subject of this thesis are presented in Chapter 5. Technical details on the data analysis are also given in this chapter.

In Chapter 6, results from spectral and timing analysis of the main part of the outburst are presented. We dedicate special attention to the cyclotron lines present in the A 0535+26 photon spectrum, as well as to the pulse period and pulse profile evolution. Chapter 7 focuses on *RXTE* observations of a flare that was observed on the rising part of the outburst. These observations reveal an unexpected behavior of the source, which we interpret in the context of magnetospheric instabilities.

In Chapter 8 a decomposition analysis is applied to the A 0535+26 energy dependent pulse profiles. Based on symmetry considerations, and assuming an offset-dipole magnetic field, the method allows to reconstruct the visible sections of the beam pattern and to extract information on the geometry of the system. A possible solution for the beam pattern of A 0535+26 and its geometry are given, and the reconstructed beam pattern is interpreted in terms of a model that includes relativistic light deflection.

Chapter 9 contains a summary and conclusions of the presented work and an outlook to the future work.

CHAPTER 2

Accreting X-ray pulsars

2.1 Introduction

2.1.1 X-ray binaries

Stars end their life as compact objects. Depending on the initial mass of the star, they will follow different evolutionary tracks. If the initial mass of the star is $0.8 M_{\odot} \lesssim M \lesssim 11 M_{\odot}$ it will end its life as a white dwarf. If the initial mass $11 M_{\odot} < M \lesssim 40 M_{\odot}$, it will end its life as a neutron star. And for an initial mass $M \gtrsim 50 M_{\odot}$, the star will collapse completely and form a black hole. (See Iben 1991, Iben & Tutukov 1997, Iben 1998).

X-ray binaries are binary systems consisting of a neutron star or a black hole and an optical companion (Liu et al. 2007). Roughly, the basic picture of X-ray binaries is the following: the compact object accretes matter from the companion, and as a result of the gravitational energy released X-rays are emitted.

According to the nature of the donor star, X-ray binaries can be classified as High-Mass X-ray Binaries (hereafter HMXBs) or Low-Mass X-Ray Binaries (hereafter LMXBs). HMXBs have a young optical companion of spectral type O or B and mass $M \gtrsim 5 M_{\odot}$. These systems have high magnetic fields $B \sim 10^{12}$ G. LMXB systems have older optical companions, with masses in general $M \leq 1 M_{\odot}$ and lower magnetic fields $B \sim 10^9\text{--}10^{10}$ G. X-ray binaries are numerous objects in the Galaxy. There are 114 HMXBs in the Galaxy (Liu et al. 2006) and 128 HMXBs in the Magellanic Clouds (Liu et al. 2005), and 187 LMXBs in the Galaxy and Magellanic Clouds (Liu et al. 2007). The distribution of X-ray binaries in our Galaxy as of 2002 is shown in Fig. 2.1. A detailed description of these systems can be found for instance in Frank et al. (1992), Longair (1994), Lewin et al. (1995) and in the recent review from Lewin & van der Klis (2006).

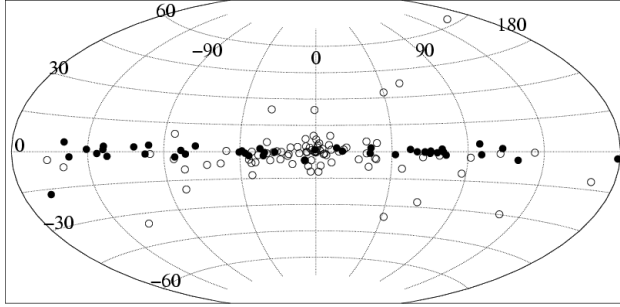


Figure 2.1: Distribution of X-ray binaries in the Galaxy. 86 LMXBs (hollow circles) and 51 HMXBs (solid circles) are shown. There is a higher concentration of LMXB in the Galactic Bulge and HMXB towards the Galactic plane. More recent values are 242 HMXBs and 187 LMXBs in the Galaxy and the Magellanic Clouds. (Figure from Grimm et al. 2002).

2.1.2 Neutron star basic properties

This thesis is based on observations of an X-ray binary system with a neutron star as compact object. Before entering into details of these systems, the basic properties of neutron stars are reviewed.

The canonical values for the mass and radius of a neutron star are $M = 1.4 M_{\odot}$, $R = 10$ km. The density in the surface is $\rho \sim 10^6$ g/cm³, and increases up to $\rho \sim 10^{15}$ g/cm³ in the center. The equation of state (EOS) of neutron stars interior (i.e., the relation between the pressure and the density) is unknown. There are different models for EOS. Each of them is parametrized in terms of the central density. Therefore, if the mass and the radius of a neutron star could be determined simultaneously, the EOS and therefore the internal composition could be constrained. Different EOSs yield to different mass-radius relations. A very common representation of the different EOSs is the radius-mass plane, as shown in Fig. 2.2. See Lattimer & Prakash (2007) for a recent review of neutron star properties.

Neutron star masses can be measured very accurately in eclipsing systems. From Kepler's third law,

$$\left(\frac{P_{\text{orb}}}{2\pi}\right)^2 = \frac{a_{\text{ns}} + a_{\text{star}}}{G(M_{\text{ns}} + M_{\text{star}})} \quad (2.1)$$

the mass function is

$$f_{\text{ns}}(M_{\text{ns}}, M_{\text{star}}) = \frac{M_{\text{ns}}^3 \sin^3 i}{(M_{\text{star}} + M_{\text{ns}})^2} = \frac{P_{\text{orb}} K_{\text{star}}^3}{2\pi G} \quad (2.2)$$

where P_{orb} is the orbital period of the binary system, a_{ns} and a_{star} are the distance from the neutron star and the companion to the center of mass of the system, G is

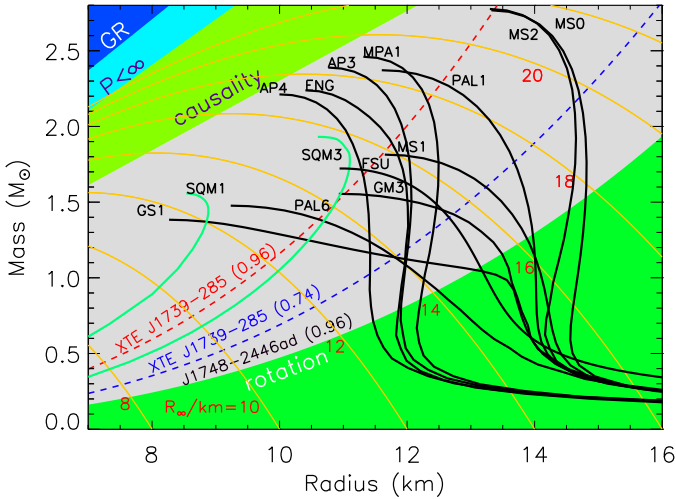


Figure 2.2: Different mass-radius relations for typical EOSs (black curves). The blue and green regions are excluded by causality and GR. The notation can be found in Lattimer & Prakash 2001 (a detailed discussion of the different neutron star EOS is out of the scope of this work). (Figure from Lattimer & Prakash 2007).

the gravitational constant, M_{ns} and M_{star} are the neutron star and companion star masses, i is the inclination of the binary plane to the plane of the sky, and K_{star} is the radial velocity amplitude of the companion star.

By measuring the radial velocity, determining the Doppler shift of the X-ray pulse period, and if the inclination of the system is known, it is possible to determine the neutron star mass with high accuracy. Figure 2.3 shows a recent compilation of measured neutron star masses. See also Thorsett & Chakrabarty (1999), van der Meer et al. (2007).

Contrary to the mass, the radius of the neutron star can be less well constrained. The only measurements of the radius have been performed in X-ray bursters, observed in LMXBs (see Strohmayer & Bildsten 2003 for a review). These systems host an old neutron star that accretes material from a companion in a close orbit, and builds layers of material on the surface. Once the mass of the surface layer has reached a critical value, it will undergo a thermonuclear flash. The basic concept of the method is the following: during the burst, the neutron star radiates like a spherical black body, and thus $L_{\text{burst}} = L_{\text{blackbody}}$. The standard black body radiation $L_{\text{blackbody}} = 4\pi R^2 \sigma T^4$, where R is the radius of the neutron star, σ is the

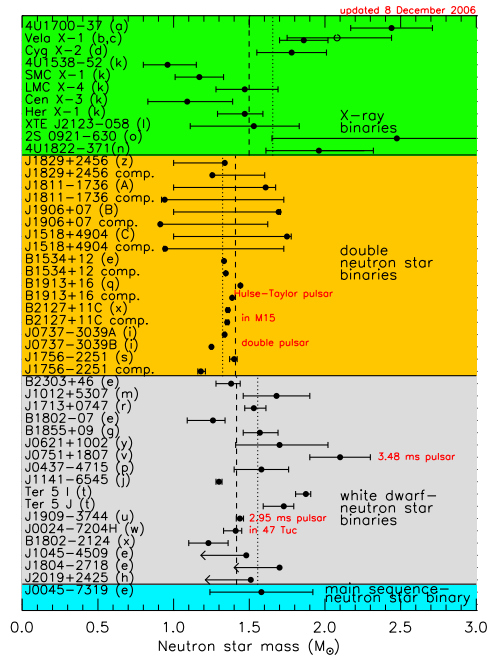


Figure 2.3: Measured masses of neutron stars. (Figure from Lattimer & Prakash 2007).

Stefan-Boltzmann constant¹, and T is the temperature. The luminosity of the burst $L_{\text{burst}} = 4\pi d^2 F$, where d is the distance to the source and F the measured flux. The distance of these systems is typically well known (they are normally located in globular clusters), the flux and temperature can be obtained from the burst spectrum, and it is therefore possible to obtain an estimate of the radius of the neutron star. For instance, Shaposhnikov et al. (2003) obtained a narrow constraint for the radius of the neutron star in the LMXB 4U 1728-34, in the range 8.7 – 9.7 km. The recently discovered relativistically broadened iron lines in neutron stars (Piraino et al. 2000, Bhattacharyya & Strohmayer 2007) can be a powerful tool to determine the neutron star radius. First estimates (using a “diskline” model from Fabian et al. (1989), which is not completely adequate since it does not include relativistic light bending) provide an upper limit for the neutron star radius of 14.5–16.5 km for a 1.4 M_{\odot} neutron star (Cackett et al. 2008). However, more appropriate models are necessary to deter-

¹ $\sigma = \frac{2\pi^5 k^4}{15h^3 c^2} = 5.670 \times 10^{-5} \text{ erg cm}^{-2} \text{ K}^{-4} \text{ s}^{-1}$ where k is the Boltzmann’s constant and h is the Planck’s constant

mine the radius with better accuracy. The next generation of X-ray observatories (like *Simbol-X*, Ferrando et al. 2006) will allow to measure simultaneously kHz QPOs and relativistically broadened Fe lines, allowing to constrain both the mass and the radius of the neutron star. In general today, observational evidence that points to harder EOS in neutron stars and therefore larger radius around 13–14 km is growing (Özel 2006, Lattimer & Prakash 2007).

Due to the strong gravitational field around a neutron star, its radiation will appear red-shifted to a distant observer. The gravitational redshift for a neutron star can be calculated assuming the Schwarzschild metric:

$$z = \frac{1}{\sqrt{1 - R_S/R}} - 1 \quad (2.3)$$

where r_S is the Schwarzschild radius, given by (see Misner et al. 1973):

$$R_S = \frac{2GM}{c^2} \quad (2.4)$$

A measurement of the gravitational redshift z for a neutron star provides a direct constraint to the mass-radius relation. Cottam et al. (2002) have measured the gravitational redshift for the LMXB EXO 0748-676, identifying absorption lines in the X-ray spectrum during X-ray bursts. They obtain a gravitational redshift of $z = 0.35$, and this result excludes several models of EOS for exotic matter (like quark stars). They derived a radius of $R = 9 - 12$ km for a neutron star mass in the range $M = 1.4 - 1.8M_\odot$. Rauch et al. (2008), using local thermodynamic equilibrium (LTE) and non-LTE neutron star atmosphere models, were not able to confirm the line identification made by Cottam et al. (2002). They arrive to a different value for the gravitational redshift of $z = 0.24$, which yields to a larger neutron star radius in the range $R = 12 - 15$ km for a mass range $M = 1.4 - 1.8M_\odot$.

Neutron stars are the result of a supernova II explosion. Assuming that the magnetic flux $\Phi = 4\pi R^2 B$ is a conserved quantity, before and after the supernova explosion:

$$R_{\text{ns}}^2 B_{\text{ns}} = R_{\text{star}}^2 B_{\text{star}} \quad (2.5)$$

Taking the canonical neutron star radius $R_{\text{ns}} = 10$ km, a stellar radius $R_\star \sim 700000$ km, and a stellar magnetic field $B_\star \sim 100$ G (typical pre-supernova magnetic field) gives a magnetic field for a young neutron star of the order of $B_{\text{ns}} \sim 10^{12}$ G. This is actually of the order of magnitude of the magnetic field observed directly from cyclotron lines or indirectly derived from accretion theory (see below).

Neutron stars can be isolated or in binary systems. The sources of energy that can power the emission from neutron stars are accretion (see Section 2.1.3), rotation or

magnetic field decay. In this work we will focus on neutron stars powered by accretion. Below the other two power mechanisms for neutron stars are briefly described.

The most famous example of a rotation powered pulsar is the Crab pulsar (Staelin & Reifenstein 1968), characterized by a rotation period of $P_{\text{spin}} \sim 33$ ms. Rotation powered pulsars have a rapidly changing magnetic moment (Goldreich & Julian 1969). The change in the rotational energy produces a change in the neutron star spin period. The loss of energy due to the rotation of the neutron star can be estimated by:

$$L_{\text{rot}} = \frac{dE_{\text{rot}}}{dt} = \frac{d(I\omega)}{dt} = 4\pi^2 I \frac{\dot{P}}{P^3} \quad (2.6)$$

where E_{rot} is the rotational energy, I is the moment of inertia, ω is the frequency and P is the pulse period $P = 2\pi/\omega$.

The magnetic radiation from the neutron star can be estimated assuming a rotating magnetic dipole (Gold 1968). The amount of magnetic dipole radiation is (Landau & Lifshitz 1977):

$$L_{\text{dipole}} = \frac{2}{3} \frac{\mu^2 \sin^2 \beta}{c^3} \omega^4 \quad (2.7)$$

where β is the angle between the rotational axis and the magnetic dipole axis and μ is the magnetic dipole moment of the neutron star:

$$\mu = \frac{BR^3}{2} \quad (2.8)$$

with R the neutron star radius and B the surface magnetic field.

Assuming that the loss of rotational energy from the neutron star equals the amount of magnetic dipole radiation, the following expression for the magnetic field as a function of the period and spin-down rate emerges (making $\beta = 90^\circ$):

$$B = \left(\frac{3c^3 I}{8\pi^2 R^6} P \dot{P} \right)^{1/2} \simeq 3.2 \times 10^{10} (P \dot{P})^{1/2} \text{G} \quad (2.9)$$

where the numerical coefficient is obtained using the canonical values of the neutron star mass and radius and a moment of inertia $I \simeq 10^{45} \text{g/cm}^3$, and P is given in seconds (Bhattacharya & van den Heuvel 1991). Making use of this expression, measurements of the rotational period and period derivative can be used to derive the magnetic field of the neutron star.

The population of pulsars, according to P and \dot{P} , is plotted in Fig. 2.4, in which constant magnetic field lines and constant pulsar characteristic age² $\tau = P/\dot{P}$ are shown. Young pulsars are located in the upper left area of the figure.

²The true age of the neutron star can be approximated by the characteristic age assuming that the initial spin-down is much smaller than the present period

It is believed that the magnetic fields of pulsars decay with the age (Ostriker & Gunn 1969, Bhattacharya & van den Heuvel 1991). The evolution of pulsars is typically visualized in the $P - B$ diagram (Fig. 2.5). The “graveyard” is the region for which old radio pulsars are expected to switch off their radio emission. Millisecond pulsars (with spin-periods of the order of milliseconds) have low magnetic fields, of the order of $B \sim 10^{8-10}$ G. They represent the oldest population of pulsars, and are often referred to as “recycled pulsars”. Such high spin-up rates can be reached when the neutron star is in a later stage of its evolution, and has been spun-up to the “graveyard”. The evolutionary expansion of the optical companion may cause mass transfer, causing the accretion of matter by the neutron star and X-ray emission. The system is then observed as an X-ray binary. In agreement with the theory, in 1998 an accreting millisecond pulsar was discovered with the *RXTE* observatory: SAX 1808.4-3658, a LMXB with ~ 2.5 ms pulsations (Wijnands & van der Klis 1998). Since then, up to ten other millisecond accreting pulsars have been discovered in LMXBs (Burderi et al. 2008). See Wijnands (2006), Galloway (2007), Falanga (2008) for recent reviews.

Another class of pulsar are the magnetars. They are young, slowly rotating neutron stars, observed in X-rays and gamma-rays, historically grouped in two categories, Anomalous X-ray Pulsars (AXPs) and Soft Gamma Repeaters (SGRs). Magnetars possess extremely high magnetic fields, $B \sim 10^{14-15}$ G, and show no radio emission. These isolated neutron stars are thought to be powered by the decay of their huge magnetic field (Duncan & Thompson 1992). They can produce bursts with luminosities as high as $L_{\sim(10-100)\text{ keV}} \sim 10^{39-42}$ erg s $^{-1}$. A review of magnetars is given in Woods & Thompson (2006).

Very recently, the Fermi Gamma-Ray Space Telescope (Ritz et al. 2006) has discovered a new class of pulsars, *gamma-ray-only pulsars* (Abdo et al. 2008, Saz Parkinson et al. 2009). Further investigation and observations of this new class of pulsars will lead to a better understanding of the physics of neutron stars.

2.1.3 Accretion

Accretion is the physical process responsible for the emission of X-rays from X-ray binaries. It consists of the conversion of gravitational energy into kinetic energy. It is a very powerful source of energy in binary systems. This can be easily seen estimating the energy released when a mass m falls from infinity into a body with mass M and radius R :

$$E_{\text{acc}} = GMm/R \quad (2.10)$$

where G is the gravitational constant. Assuming canonical values for a neutron star, $M = 1.4 M_{\odot}$ and $R = 10$ km, the energy released when a mass of $m = 1$ g falls onto the surface of the neutron star from infinity is

$$E_{\text{acc}} \sim 10^{20} \text{ erg} \quad (2.11)$$

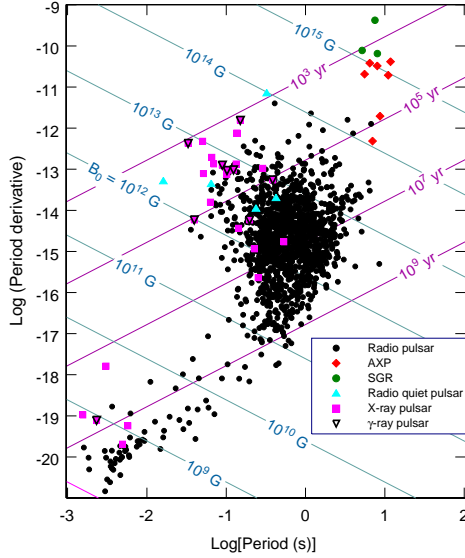


Figure 2.4: Pulsar population in $P - \dot{P}$ diagram. Constant magnetic field lines and constant pulsar characteristic age lines are drawn. (Figure from Harding & Lai 2006).

We can compare this value to the energy released in nuclear fusion, in the conversion of hydrogen to helium:



The energy released per gram of hydrogen converted to helium is

$$E_{\text{nucl}} \sim 6 \times 10^{18} \text{ erg} \quad (2.13)$$

From the estimates above it can be easily seen that accretion is almost ~ 20 times more efficient than nuclear fusion reactions. Accretion is the most effective way to produce energy for astrophysical sources. Therefore accreting sources are between the most luminous ones in the Universe.

The energy released by an accreting object is proportional to M/R (Eq. 2.10). Therefore the more compact the object is, the more effective the accretion will be.

The luminosity produced by an accreting object is given by

$$L = \frac{dE_{\text{acc}}}{dt} = G \frac{M}{R} \frac{dm}{dt} = G \frac{M}{R} \dot{m} \quad (2.14)$$

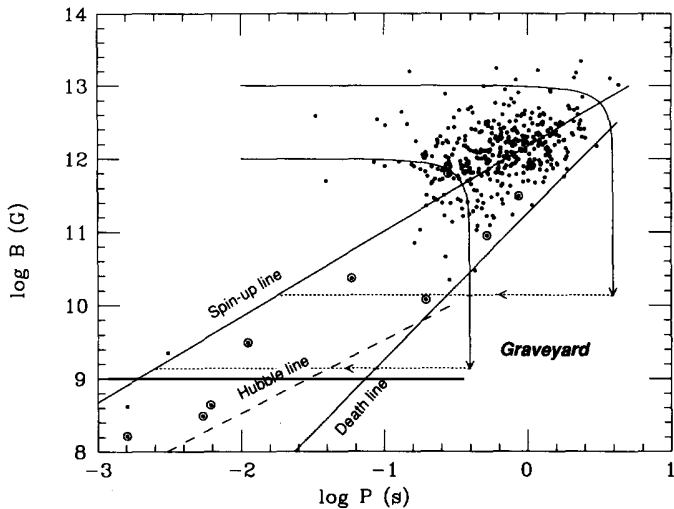


Figure 2.5: Pulsar population in $P - B$ diagram, with magnetic fields derived from radio pulsars measurements ($B \propto \sqrt{P\dot{P}}$, see text). The “Hubble line” represents a spin-down age τ of 10^{10} yr for a pulsar. The “spin-up line” represents the minimum spin-period to which such a spin-up may occur in an Eddington-limited accretion. The “death line” delimits the “graveyard” (region for which old radio pulsars are expected to switch off their radio emission). The arrowed lines show the evolutionary paths for “recycled” millisecond pulsars. (Figure from Bhattacharya & van den Heuvel 1991).

where \dot{m} is the mass accretion rate. For a given accreting object, its accretion luminosity will only depend on its accretion rate. The higher the accretion rate is, the higher the luminosity will be. But there is a limit on the luminosity that an accreting body can reach, referred to as Eddington luminosity. The Eddington luminosity can be obtained by balancing the gravitational force pulling the matter inwards and the pressure of the radiation outwards. The gravitational force acts on electron-proton pairs:

$$F_{\text{grav}} = G \frac{M}{r^2} (m_{\text{p}} + m_{\text{e}}) \approx G \frac{M m_{\text{p}}}{r^2} \quad (2.15)$$

The radiation force acts on electrons due to Thomson scattering:

$$F_{\text{rad}} = \frac{\sigma_{\text{T}} L}{4\pi r^2 c} \quad (2.16)$$

where σ_{T} is the Thomson scattering cross-section.

Equating these two terms (Eq. 2.15 and Eq. 2.16) leads to the Eddington luminosity:

$$L_{\text{Edd}} = \frac{4\pi GMm_{\text{p}}c}{\sigma_{\text{T}}} \approx 1.3 \times 10^{38} \frac{M}{M_{\odot}} \text{erg s}^{-1} \quad (2.17)$$

This is the maximum luminosity an accreting object can have, assuming spherically symmetric accretion and steady flow. However, this limit can be exceeded in non steady cases like supernova explosions, or assuming different geometries for the source (see below for more details on Eddington luminosity).

2.1.4 Mass transfer mechanisms in X-ray binaries

In order to understand how the transfer of matter occurs in binary systems, one has to study the gravitational potential of the binary system. We can calculate the orbit of a test particle under the gravitational field of two massive objects orbiting their common center of mass. Let M_1 and M_2 be the masses of the two bodies, \vec{r} the position vector of the test particle and \vec{r}_1, \vec{r}_2 the position vectors of the two stars. The equipotential surfaces of the system are given by:

$$\Phi_{\text{R}}(\vec{r}) = \frac{GM_1}{|\vec{r} - \vec{r}_1|} + \frac{GM_2}{|\vec{r} - \vec{r}_2|} - \frac{1}{2}(\vec{\omega} \wedge \vec{r})^2 = \text{constant} \quad (2.18)$$

known as the Roche potential (Roche 1873). The first two terms take into account the gravitational potential of each star, and the third term accounts for the centrifugal potential associated with the binary motion. $\vec{\omega} = \omega \vec{e}$, with ω the angular velocity of the binary system and \vec{e} a unity vector normal to the orbital plane. The motion of a particle at a large distance from the system (distance much larger than the binary separation) will be circular: the particle will see the system as a point mass. The same will happen to a particle close to the center of each of the two bodies, it will move in a circular orbit around the massive object. The equipotential surfaces of Φ_{R} are plotted in Fig. 2.6. There is a critical surface which connects both stars, called the *Roche lobe* of the system. The two lobes connect at the *inner Lagrangian point* L_1 . At this point matter can freely go from one lobe to the other.

The size of the lobes around each star are a limit to their size. If the star grows and exceeds its Roche lobe matter will be transferred to the companion through the inner Lagrange point (see Frank et al. 1992, Longair 1994 for more details).

Three different ways of accretion can take place in X-ray binaries, (or a combination of them): Roche lobe overflow, wind accretion and accretion in Be/X-ray binary systems.

2.1.4.1 Roche Lobe overflow

It takes place when the donor star fills its Roche lobe, which happens when the star evolves and expands (Iben 1991). When this happens, the matter exceeding the Roche

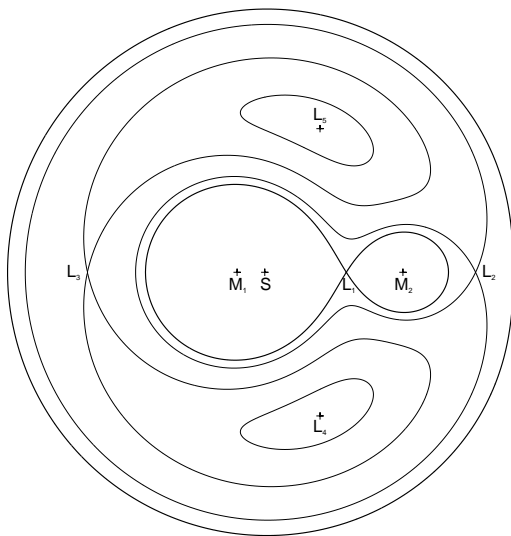


Figure 2.6: Equipotential surfaces of the Roche potential. M_1 and M_2 represent the masses of the two objects, with a mass ratio $M_1/M_2 = 0.2$. S represents the center of mass of the system. The Inner Lagrangian Point L_1 and the other turning points in the value of the potential L_2, L_3, L_4 and L_5 are labeled. (Figure from Kretschmar 1996).

lobe is no longer gravitationally bound to the star and can be captured by the compact object through the inner Lagrange point. Due to the rotation of the donor star, the accreted matter has a large amount of angular momentum, and instead of being accreted directly into the compact object, the matter will form an accretion disk. Details on disk accretion are given in Sec. 2.2.2. Roche Lobe overflow typically takes place in LMXBs. A binary system with accretion via Roche Lobe overflow is drawn in Fig. 2.7.

2.1.4.2 Wind Accretion

Normal stars have a weak stellar wind, but in the case of O and B stars it can be very intense. The mass loss rate can be as high as $\dot{M}_{\text{wind}} \sim 10^{-4} M_{\odot}/\text{yr}$. If these stars are in a binary system, the compact object typically orbits the optical star at a distance from the surface of the optical companion of less than one stellar radius. The compact object is thus deeply embedded in the stellar wind, and can accrete matter from the wind. Most of the material of the wind passing within a cylinder of radius r_{acc} from



Figure 2.7: Artist's impression of binary system with accretion via Roche Lobe overflow. (Source: NCSA-University of Illinois).

the compact object will be accreted:

$$r_{\text{acc}} = \frac{2GM_1}{v_{\text{rel}}^2} \quad (2.19)$$

with $v_{\text{rel}}^2 = v_{\text{wind}}^2 + v_{\text{ns}}^2 \approx v_{\text{wind}}^2$, where v_{wind} and v_{ns} are the wind and neutron star velocities (typically the velocity of the wind is much higher than that of the neutron star). Assuming that the wind is emitted over a solid angle Ω implies an accretion rate of:

$$\dot{M} \sim \frac{\pi r_{\text{acc}}^2}{\Omega a^2} \dot{M}_{\text{wind}} \quad (2.20)$$

where $a \sim 10^{12}$ cm is the binary separation. Typically, in X-ray binaries containing O or B stars the winds are isotropic ($\Omega \sim 4\pi$), having high velocities $v_{\text{wind}} \sim 1 - 2 \times 10^3$ m/s. Therefore, we obtain $r_{\text{acc}} \sim 10^{10}$ cm, much smaller than the binary separation, and only a fraction of the wind $\lesssim 10^{-4}$ will be accreted. But the very high accretion rates from the wind make \dot{M} high enough to power X-ray emission from the compact object. Details can be found in Davidson & Ostriker (1973) and Frank et al. (1992). An accretion wake is formed (Fig. 2.8), that focuses a significant fraction of the stellar wind (Davidson & Ostriker 1973). In some cases, an accretion disk will form. The archetypical wind accretor is Vela X-1 (Kreykenbohm et al. 2008).

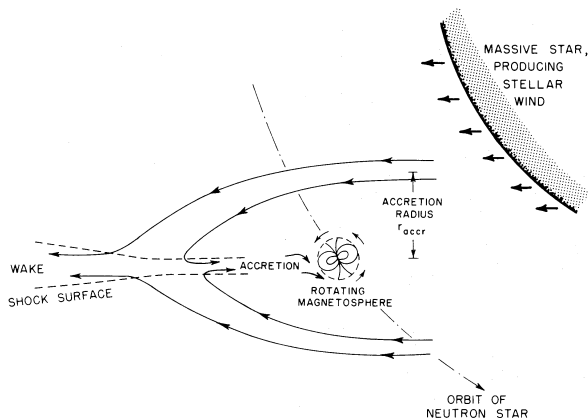


Figure 2.8: Schematic representation of wind accretion, showing streamlines of stellar-wind material. The relative dimensions are not to scale. (Figure from Davidson & Ostriker 1973).

2.1.4.3 Be/X-ray binary systems

A large fraction of X-ray binaries (about 60% of the HMXBs) falls in the category of the Be/X-ray binary systems. They consist of a neutron star and a Be star as optical companion, and present quite eccentric orbits. Recent reviews can be found in Coe (2000), Ziolkowski (2002) and Negueruela (2004a,b). Be stars are early type stars (mostly B-type and also late O-type) which present emission lines in their spectra. The emission lines are originated in a disk of material that surrounds the equator, formed due to the mass loss of the Be star. See Porter & Rivinius (2003) for a recent review of classical Be stars.

Be/X-ray binary systems are transient sources and present three different luminosity states:

- Giant or Type II outbursts (classification according to Stella et al. 1986): they present strong X-ray luminosities $L_X > 10^{37} \text{ erg s}^{-1}$, becoming one of the brightest X-ray objects in the sky for several weeks. Giant outbursts are not necessarily associated with the periastron, and are thought to be due to an increase of activity of the companion star, leading to an expansion of its envelope and making it possible for an accretion disk around the neutron star to form (Coe 2000, Ziolkowski 2002). Quasi-periodic oscillations (QPOs) have been observed during giant outbursts, confirming the formation of an accretion disk around the neutron star.
- Normal or Type I outbursts: they are weaker than type II outburst, with lu-

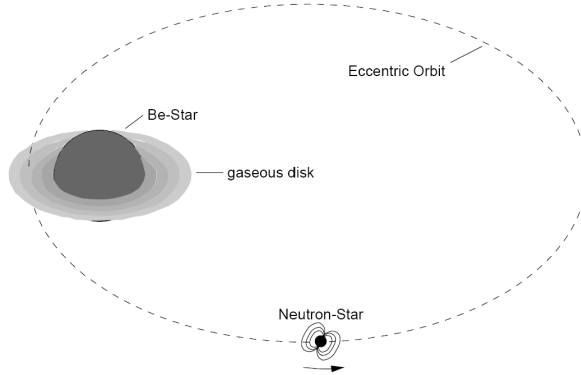


Figure 2.9: Schematic view of a Be/X-ray binary system. (Figure from Kretschmar 1996).

minisities $L_X \sim 10^{36-37} \text{ erg s}^{-1}$. They are connected to the passage of the neutron star through the periastron of the binary orbit. They are shorter than type II outbursts, lasting from days to weeks. Some sources present type I outburst at most periastron passages (e.g. EXO 2030+375, Wilson et al. 2002), and other sources present type I outbursts much less frequently, like A 0535+26.

- Quiescent states: some Be/X-ray binary systems present a persistent low X-ray luminosity $L_X \lesssim 10^{36} \text{ erg s}^{-1}$, and others are not visible at all in X-rays.

Fig. 2.9 shows a sketch of a Be/X-ray binary system. More details on these systems will be given in Chapter 3, dedicated to the Be/X-ray binary system A 0535+26.

2.2 Neutron star X-ray binaries

2.2.1 Accretion geometry

Independently of the accretion being by Roche lobe overflow, wind accretion or Be accretion, at a closer distance to the neutron star the accretion is dominated by the strong magnetic field ($B \sim 10^{12} \text{ G}$).

According to the theory of accretion, the strong magnetic field around the neutron star disrupts the accretion disk, and the plasma is forced to follow the field lines. The matter forms accretion funnels that go towards the magnetic poles of the neutron star. This model was first elaborated by Ghosh & Lamb (1978), and later revisited in Lovelace et al. (1995), Wang (1996) and Wang (1997). The magnetic field of a

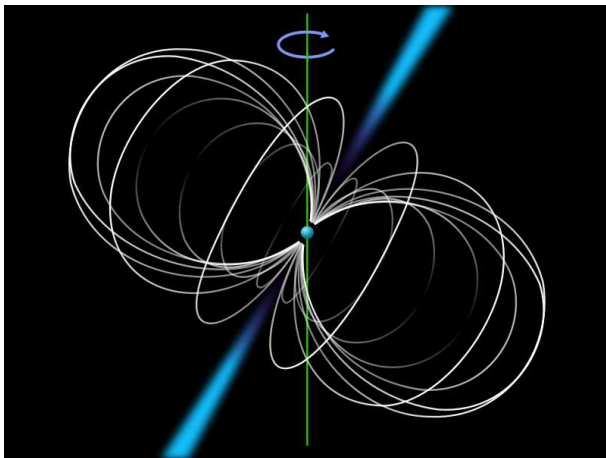


Figure 2.10: Illustration of the lighthouse effect: as the neutron star rotates, flashes of light are periodically directed towards the observer, producing a periodic signal. (Figure from Wikipedia).

neutron star can be approximated by a multipole of order 2^k ,

$$B_k \simeq B_0 (R_0/R)^{k+2}, \quad (2.21)$$

with B_0 the surface magnetic field strength, R_0 the neutron star radius and R the distance from the neutron star. In early models, the neutron star's magnetic field was assumed to be a pure dipole, with $k = 1$ (Inoue 1975, Ghosh & Lamb 1979a,b, Camenzind 1990). Magnetohydrodynamic (MHD) simulations of magnetospheric accretion confirmed many predictions, and also revealed new details of the accretion onto a compact object assuming a dipole magnetic field (see e.g. Romanova et al. 2002, 2003, 2004). Under the assumption of a pure dipole field, disk-magnetospheric interactions have been investigated numerically in Miller & Stone (1997), von Rekowski & Brandenburg (2004) and theoretically in Lovelace et al. (1995). Higher multipole terms in neutron stars have been considered in Lipunov 1978, Shakura et al. 1991 and Panchenko & Postnov 1994. MHD simulations of accretion to a star with non-dipolar magnetic field have been performed in Long et al. (2007, 2008).

If the rotation axis is inclined with respect to the magnetic axis, the observer will periodically see flashes of light (lighthouse effect, see Fig. 2.10).

Before entering in details of how the flow of matter takes place, in the following important geometrical considerations, under the assumption of a dipole field configuration, are described.

The Alfvén radius or magnetospheric radius is defined as the distance at which the magnetic pressure and the ram pressure are equal:

$$P_{\text{mag}} = \frac{\mu^2}{8\pi r^6} \quad (2.22)$$

$$P_{\text{ram}} = \frac{(2GM)^{1/2}\dot{M}}{4\pi r^{5/2}} \quad (2.23)$$

Equating these two terms gives:

$$r_{\text{m}} = 2.9 \times 10^8 M_1^{1/7} R_6^{-2/7} L_{37}^{-2/7} \mu^{4/7} \text{cm} \quad (2.24)$$

where M_1 is given in units of $1 M_{\odot}$, R_6 is given in units of 10^6 cm and L_{37} is the luminosity in units of 10^{37} erg s $^{-1}$. The co-rotation radius is the radius at which the angular velocity of the magnetosphere ωr and the Keplerian velocity of the disk $\sqrt{GM_X/r}$ are equal,

$$r_{\text{co}} = \left(\frac{GM_X}{\omega^2} \right)^{1/3} \quad (2.25)$$

This scenario is depicted in Fig. 2.11. Accretion will take place when the neutron star angular velocity is smaller than the disk Keplerian velocity, $\omega r < \sqrt{GM_X/r_{\text{co}}}$ or $r_{\text{m}} < r_{\text{co}}$. If the neutron star rotates faster than the disk, the material is not able to follow the magnetic field lines and a centrifugal barrier arises, preventing the accretion of matter onto the compact object. This is called the propeller effect, described in Illarionov & Sunyaev (1975).

2.2.2 Disk accretion

If the angular momentum of a particle is too high, it will not fall directly onto the compact object. The particle will tend to stay in the orbit of the lowest energy for its angular momentum: a circular orbit. Assuming the particle does not lose any angular momentum, it will stay in an orbit with the following circularization radius:

$$R_{\text{circ}} = \frac{J^2}{GM_X} \quad (2.26)$$

where J is the specific angular momentum of the accreted matter and M_X the mass of the compact object (Pringle 1981).

A particle in such an orbit will experience a dissipative processes (like viscosity, which is one of the major uncertainties in accretion disk theory, see Shakura & Sunyaev 1973, Pringle 1981), and it will lose angular momentum. It will then sink deeper into the gravitational potential of the compact object to an orbit with smaller radius.

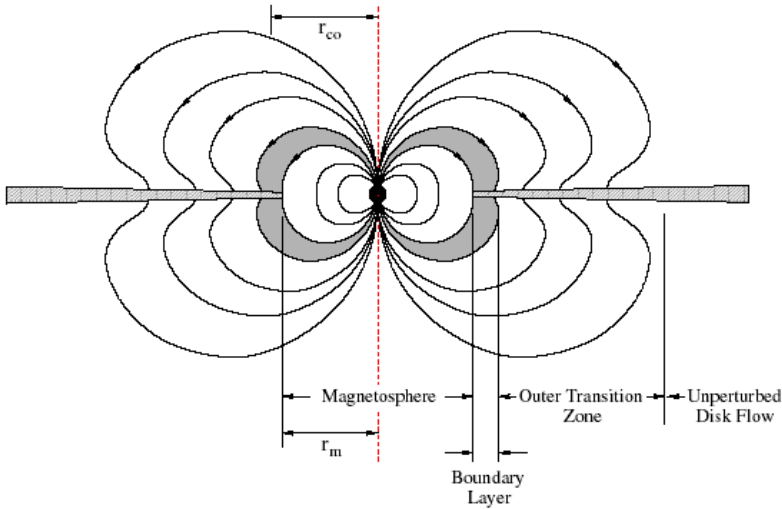


Figure 2.11: Sketch of the magnetically threaded disk model from Ghosh & Lamb (1978). The Alfvén radius and co-rotation radius are shown. Accretion is centrifugally permitted when the magnetosphere rotates slower than the disk, $r_m < r_{co}$. (Figure from Kuster 2004).

Accretion will take place along a series of circular orbits with gradually decreasing angular momentum forming an accretion disk.

For an accretion disk to form, the circularization radius should be larger than the effective size of the accreting object. This will always happen if accretion takes place via Roche lobe overflow, and not always if wind accretion takes place.

The main mechanism for the transport of matter across the magnetosphere is the Rayleigh-Taylor instability. This has been studied in Arons & Lea (1976), Elsner & Lamb (1977), Scharlemann (1978). Recently, Romanova et al. (2008), Kulkarni & Romanova (2008) have performed 3D MHD simulations that confirm the basic features of the disk-magnetospheric interaction, revealing two possible regimes for accreting neutron stars: stable or unstable. (These simulations have been performed for quite small magnetospheres, applicable to millisecond pulsars). In Chapter 7 further details on the accretion regimes and on how the transport of matter in the magnetosphere takes place are given.

2.2.3 Torque theory

According to the theory of accretion, fluctuations in the mass accretion rate produce fluctuations in the accretion luminosity and in the accretion torque. In the case of

accretion from a disk, it exerts a torque onto the neutron star that causes a spin-up in the neutron star. Therefore, the measurement of a spin-up in a neutron star provides evidence for an accretion disk.

In the case of a spin-up, the torque onto the neutron star is given by

$$\frac{d\mathcal{L}}{dt} = \frac{d(I\omega)}{dt} = \dot{M}R\Omega, \quad (2.27)$$

where \mathcal{L} is the angular momentum of the disk, I the moment of inertia, ω the angular velocity and R the neutron star radius. Combining Eq. 2.27 with Eq. 2.14 and after some algebra (the details can be found in Ghosh & Lamb 1979b) a relation between the spin-up \dot{P} and the X-ray flux F_X or X-ray luminosity ($L_X = 4\pi d^2 F_X$) emerges:

$$-\dot{P} = 5.0 \times 10^{-5} \mu_{30}^{2/7} n(\omega_s) S_1(M) (PL_{37}^{3/7})^2 (\text{s yr}^{-1}), \quad (2.28)$$

where μ_{30} is the magnetic moment in units of 10^{30} G cm^3 , ω_s is the fastness parameter or dimensionless stellar angular velocity defined as $\omega_s = \Omega_s/\Omega_K(r_0)$, with $\Omega_K(r_0)$ the Keplerian angular velocity at $r = r_0$ (see Fig. 7.7), $n(\omega_s)$ is a dimensionless torque defined in Ghosh & Lamb (1979b) that depends on the fastness parameter, $S_1(M)$ is a structure function that depends on the mass, equation of state and dynamical response of the neutron star, P is the pulse period in seconds and L_{37} is the X-ray luminosity in units of $10^{37} \text{ erg s}^{-1}$.

Fitting the observed values of the spin-up as a function of the X-ray flux to Eq. 2.28 allows to estimate the dipole magnetic moment μ and the distance d (related to the flux via $L_X = 4\pi d^2 F_X$). This method, based on Ghosh & Lamb (1979b), is described in Lipunov et al. (1992) and Popov (2000).

2.2.4 Accretion into the polar caps

We will study now the motion of the matter close to the neutron star surface, where it is completely dominated by the magnetic field. This will be independent of the accretion regime far from the magnetosphere. As seen in Sec. 2.2.1, matter is channeled onto the magnetic poles by the magnetic field lines creating funnels. Accretion columns are formed, and the X-ray emission is produced near the neutron star surface. This is sketched in Fig. 2.12. The radius of the accreting spot is small compared to the neutron star radius, $\sim 0.1 R$, giving an area of the accreting spot of the order of $\sim 1 \text{ km}^2$ (Davidson & Ostriker 1973).

The hydrodynamics of this process was studied in the pioneering work of Basko & Sunyaev (1976). The flow of matter will be different for low and high accretion rates. A critical luminosity is defined,

$$L^* = 2.72 \times 10^{37} \frac{\sigma_T}{\sqrt{\sigma_{\perp}\sigma_{\parallel}}} \frac{r_0}{R} \frac{M}{M_{\odot}} \text{ erg s}^{-1} \quad (2.29)$$

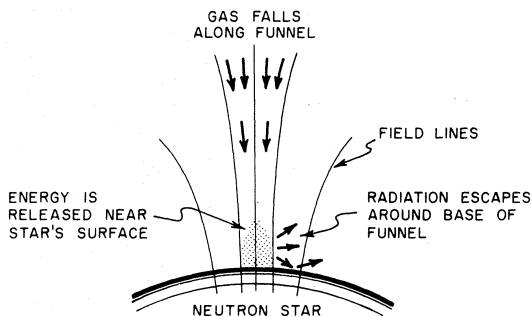


Figure 2.12: Schematic representation of an accretion funnel near the surface of the neutron star. (Figure from Davidson & Ostriker 1973).

where σ_T is the Thomson scattering cross section, σ_{\parallel} and σ_{\perp} the scattering cross-section of photons propagating either parallel or perpendicular to the magnetic field, r_0 is the polar cap radius, and M and R denote the stellar mass and radius (see also Becker & Wolff 2007).

For low accretion rates $L_X < L^*$, matter will fall freely almost until the neutron star surface, causing the breaking of the plasma by a hydrodynamical shock close to the neutron star surface. The X-ray emission will then be able to escape vertically along the accretion column (the so called “pencil beam” pattern, see Fig. 2.13 right panel). The flow of matter is in the sub-Eddington regime.

At high accretion rates, the radiation pressure is much larger than the gas pressure. The flow is in the super-Eddington regime. The infalling gas will lose almost all its kinetic energy in a radiation dominated shock (Riffert & Meszaros 1988). The shock rises above the surface of the neutron star as the accretion rate grows. Below the shock, the gas slowly sinks, and the emission of photons takes place sideways (the so called “fan beam” pattern, see Fig. 2.13 left panel).

2.2.5 Spectral formation

Numerous authors have made attempts to derive the shape of X-ray pulsar spectra analytically or numerically (Nagel 1981a, Nagel 1981b, Meszaros et al. 1983, Meszaros & Nagel 1985, Burnard et al. 1988, Burnard et al. 1991, Becker 1998, Becker & Wolff 2005). However no self-consistent, general model applicable to X-ray sources has been established, due to the complexity of the physical processes that take place in the accretion column and in the magnetosphere. The spectral shape of the radiation, or “standard” X-ray continuum (White et al. 1983), is a powerlaw in the $\sim (5 - 20)$ keV energy range with an exponential cutoff at energies $\sim (20 - 30)$ keV (Coburn et al.

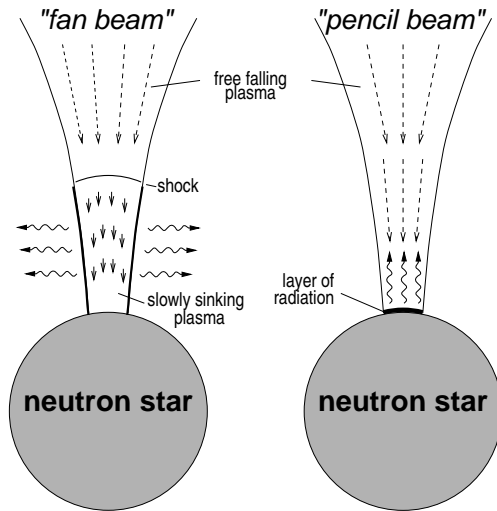


Figure 2.13: Simplified emission patterns in the polar caps of an accreting neutron star. Left panel: “fan beam” pattern. For high accretion rates, a radiation dominated shock is formed, with a slowly sinking plasma below the shock. The emitted radiation from the surface of the neutron star will escape sideways. Right panel: “pencil beam” pattern. For low accretion rates, matter falls directly almost onto the neutron star surface. Photons are then emitted vertically. (Figure from Kretschmar 1996).

2002). Additionally, fluorescence Fe $K\alpha$ lines are produced in the circumstellar material, and cyclotron absorption lines also modify the continuum emission (see below for more details). Observers use phenomenological models to describe the X-ray continuum. The most commonly used models are described in Chapter 6, Sec. 6.4. Only recently, Becker & Wolff (2007) have developed a model for the continuum formation (averaged over all rotational phases) that successfully reproduces the spectral shape of Her X-1, Cen X-3 and LMC X-4. In this model, scattering takes place via bulk and thermal Comptonization. A radiation dominated shock is formed in the column (see Fig. 2.14). This model applies to high luminosity sources. The seed photons are emitted at the base of the column (black body radiation), and in the column (bremsstrahlung and cyclotron emission). The transfer of energy from the gas to the photons is generally dominated by bulk Comptonization. Thermal Comptonization transfers energy from high energy to lower energy photons, contributing to the cutoff observed in the spectrum and to the flattening observed at lower energies. In Fig. 2.15, a theoretical spectrum computed for Her X-1 compared to a *BeppoSAX* observation

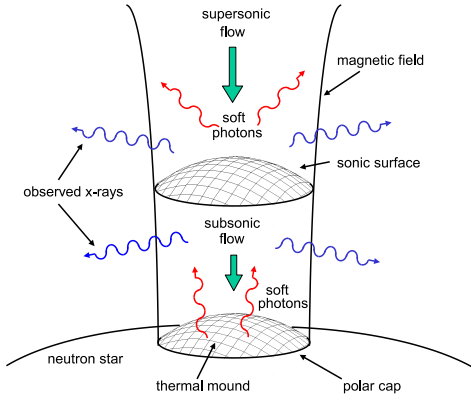


Figure 2.14: Schematic view of accretion column in a neutron star according to Becker & Wolff (2007). A radiation dominated shock is formed. The seed photons are emitted from the base of the column and via bremsstrahlung and cyclotron emission throughout the column.

is shown. Ferrigno et al. (2009) have implemented the model in the standard X-ray fitting package *XSPEC* (Arnaud 1996), making the model available for direct comparison with observational data. In their work, the model is applied to the accreting X-ray pulsar 4U 0115+64.

2.2.6 Magnetic fields

As matter falls onto the neutron star surface along the magnetic field lines, the electrons are subject to the Lorentz force. The radius of gyration of the electrons $R = mc\nu/eB$ (in classical physics) is close to the de Broglie wavelength of the electron $\lambda_{\text{de Broglie}} = \hbar/m\nu$, and therefore quantum mechanics becomes important (Landau & Lifshitz 1977).

The basic energy quantum for an electron is the cyclotron energy:

$$E_{\text{cyc}} = \hbar\omega = \hbar \frac{eB}{m_e c} = 11.6 \text{ keV} B_{12} \quad (2.30)$$

where B_{12} is the magnetic field in units of 10^{12} G. The energy of the electrons perpendicular to the magnetic field is quantized into the Landau levels:

$$E_n = m_e c^2 \sqrt{1 + \left(\frac{p}{m_e c}\right)^2} + 2n \frac{B}{B_{\text{crit}}} \quad (2.31)$$

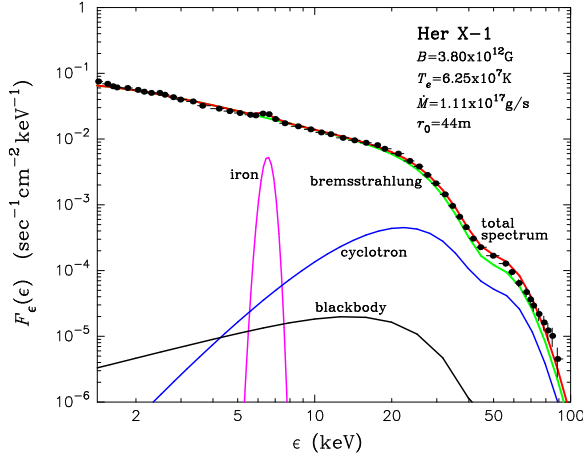


Figure 2.15: Theoretical spectrum of Her X-1 compared to *BeppoSAX* observation of the source (Becker & Wolff 2007).

where n is the principal quantum number ($n = 0, 1, 2, \dots$), p is the momentum of the electron parallel to the magnetic field and B_{crit} is the magnetic field strength where the energy of the electron equals $m_e c^2$ (see Harding & Lai (2006) and references therein):

$$B_{\text{crit}} = \frac{m_e^2 c^3}{e \hbar} = 4.414 \times 10^{13} \text{ G} \quad (2.32)$$

When a photon with energy $E = E_{\text{cyc}}$ interacts with an electron in the plasma, the electron will be raised to an excited state, “absorbing” the photon. For plasma temperatures $kT \ll E_{\text{cyc}}$, the life time of the Landau levels is short compared to the time for collisional de-excitation. Thus, the electrons in an excited state $n > 1$ almost instantaneously return to the ground state by emitting a resonant photon. This excitation-de-excitation process is similar to a resonant scattering process rather than absorption. The only possibility for photons with energies $E = E_{\text{cyc}}$ to leave the plasma is that inelastic scattering processes slightly change their energy. Consequently, this process produces absorption-like features in the photon spectrum at energies $E = nE_{\text{cyc}}$ (in the non-relativistic approximation), designated as Cyclotron Resonance Scattering Features (CRSFs, or simply cyclotron lines).

Since the cyclotron energy is directly related to the magnetic field (Eq. 2.30), measurements of cyclotron lines in the spectra of highly magnetized accreting X-ray pulsars are a very powerful tool to determine magnetic fields of neutron stars. It is the *only* direct way to determine the magnetic field of a neutron star.

For $B \approx B_{\text{crit}}$, relativistic corrections become important and the cyclotron energy further depends on the angle θ between the primary photon and the magnetic field axis:

$$E_n = \frac{m_e c^2}{\sin^2 \theta} \left(\sqrt{1 + 2n \frac{B}{B_{\text{crit}}} \sin^2 \theta} - 1 \right) \quad (2.33)$$

The cyclotron line energy is extremely sensitive to the angle between the line of sight and the magnetic field axis.

Since in X-ray binaries the strong gravitational energy plays an important role, the apparent cyclotron energy will be gravitationally red-shifted (see Eq. 2.3):

$$E_{\text{cyc,obs}} = \frac{E_{\text{cyc}}}{1+z} = E_{\text{cyc}} \sqrt{1 - \frac{2GM}{Rc^2}} \quad (2.34)$$

Assuming canonical values of the neutron star, $R = 10 \text{ km}$ and $M = 1.4 M_{\odot}$, the gravitational redshift is $z = 0.3$. For a higher value of the radius, $R = 14 \text{ km}$, and $M = 1.4 M_{\odot}$, $z = 0.19$.

2.3 Observations of neutron star X-ray binaries

2.3.1 Cyclotron lines

The first cyclotron line in an X-ray spectrum was discovered in Her X-1 with a balloon flight experiment from a MPE/AIT collaboration (Truemper et al. 1978). The spectrum of the discovery is shown in Fig. 2.16. Since then, cyclotron absorption features have been discovered in more than a dozen accreting X-ray pulsars (HMXBs, LMXBs, transient or persistent sources), most of them with the X-ray observatories *Ginga* (Turner et al. 1989), *RXTE* (Bradt et al. 1993) and *BeppoSAX* (Boella et al. 1997). These sources are listed in Table 2.1, with the energy of the cyclotron line and the discovery instrument given. Sources for which the presence of a cyclotron line is not clear are also listed. The galactic distribution of these sources is shown in Fig. 2.17. Except Her X-1, they all more or less lie in the galactic plane. The cyclotron lines imply for the accreting sources a magnetic field of the order of $B \sim 10^{12} \text{ G}$. Several sources exhibit a fundamental line plus harmonics, like V 0332+53 (Pottschmidt et al. 2005). The record holder is 4U 0115+64, showing up to five cyclotron lines in its spectrum (Santangelo et al. 1999b, Heindl et al. 1999) (see Fig. 2.18).

All the values of the cyclotron energy given in Table 2.1 have been obtained using phenomenological models (Gaussian or Lorentzian profiles) for the cyclotron absorption features (see Coburn et al. (2002) and Chapter 6 Sec. 6.4.1). Monte Carlo simulations of the propagation of photons through a low density plasma assumed to be threaded by an uniform magnetic field, have revealed that the CRSFs are expected to

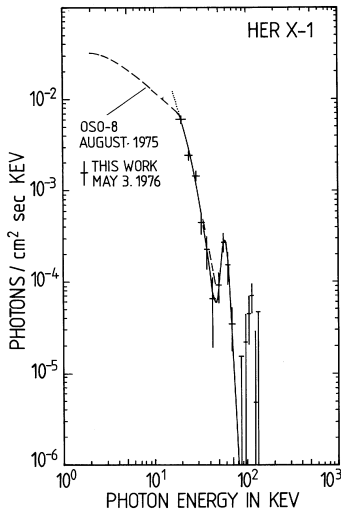


Figure 2.16: Discovery of a cyclotron line in Her X-1. (Truemper et al. 1978).

vary in shape, depth and width over the pulse phase (Araya & Harding 1999, Araya-Góchez & Harding 2000, Schönherr et al. 2007). This is shown in Fig. 2.19. A complex line profile has also emerged from observations, for instance in V 0332+53 (Pottschmidt et al. 2005). Recently, a code based on the model of Araya-Góchez & Harding (2000) called `cyclomc` has been implemented in `XSPEC` (Schönherr et al. 2007). First fits to real data have been performed to Cen X-3 (Suchy et al. 2008). `cyclomc` is a self-consistent model, which can fit up to four lines simultaneously, reprocessing the continuum flux with a special convolution and interpolation model. This model allows to extract physical information from the cyclotron lines, like the electron temperature in the plasma and the magnetic field.

2.3.1.1 Evolution of the cyclotron line energy with the luminosity

As shown in Sec. 2.2.4, for high luminosity sources it is generally believed that an increase in the mass accretion rate (or increase in luminosity) causes an increase in the height of the accretion column (Basko & Sunyaev 1976).

Burnard et al. (1991), based on Basko & Sunyaev (1976), predicted theoretically an increase of the height of the accretion column with increasing luminosity:

$$\frac{h_{\text{top}}}{R_{\text{ns}}} \approx \frac{L_X}{L_{\text{Edd}}^{\text{eff}} H_{\perp}} \quad (2.35)$$

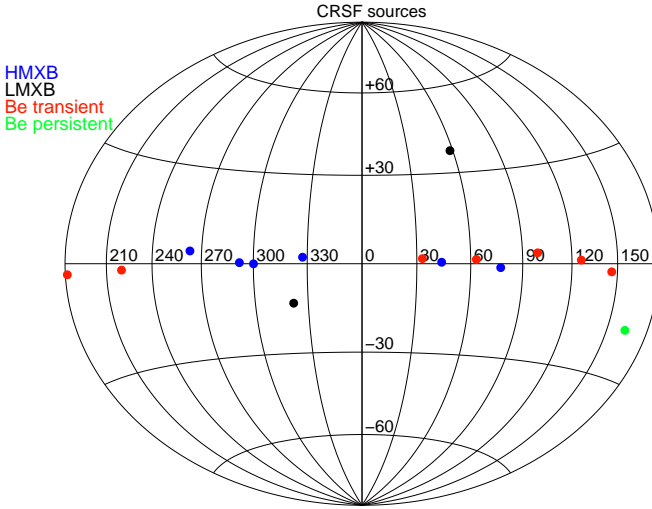


Figure 2.17: Galactic distribution of sources that exhibit cyclotron lines in their spectrum. They are divided into HMXBs, LMXBs, transients and persistents. Most of them lie in the galactic plane.

This relation was experimentally confirmed with *Ginga* observations of 4U 0115+64 (Mihara 1995, Mihara et al. 2004, Nakajima et al. 2006).

Assuming a dipole magnetic field ($B \propto 1/r^3$), and assuming the cyclotron line to be formed at a height h_r above the neutron star surface, we can write:

$$E_{cyc} \propto \frac{1}{(R_{ns} + h_r)^3} \frac{1}{1 + z} \quad (2.36)$$

Taking $z = 0$, we obtain the following relation between the relative resonance height h_r/R and the cyclotron energy:

$$\frac{h_r}{R_{ns}} \approx \left(\frac{E_{cyc}}{E_{cyc,0}} \right)^{-1/3} - 1 \quad (2.37)$$

with $E_{cyc,0}$ the cyclotron energy at the neutron star surface.

Cyclotron line observations allow to calculate h/R_{NS} as a function of the X-ray luminosity and to compare with the theoretical prediction from Burnard et al. 1991 (Eq. 2.35). This has been done with *Ginga* and *RXTE* observations of 4U 0115+64

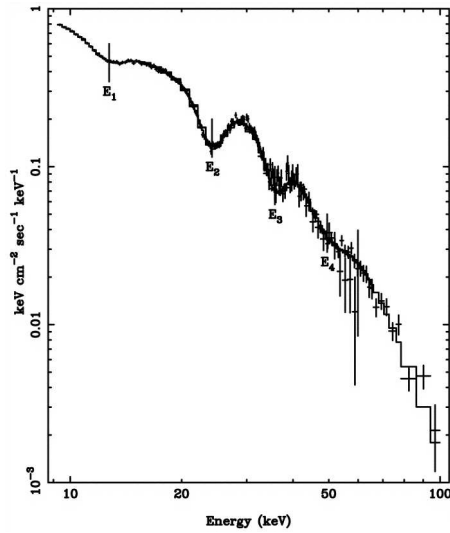


Figure 2.18: *BeppoSAX* spectrum of 4U 0115+64, showing up to four cyclotron lines (Santangelo et al. 1999b).

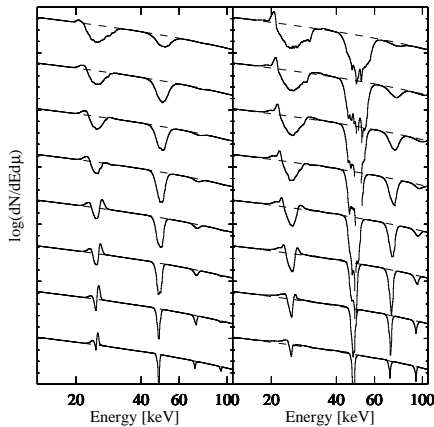


Figure 2.19: Simulated cyclotron line profiles as a function of the angle (left panel) and optical depth (right panel). The variation of the line profiles is evident. The line profiles have been calculated using a cylinder geometry, for a “fan beam” pattern. (Figure from Schönherr et al. 2007).

Table 2.1: List of sources with cyclotron line(s) significantly detected in their spectrum, updated from Makishima et al. (1999) and Heindl et al. (2004). The cyclotron line energy, the discovery instrument and reference are given. For the last four sources listed there is weak evidence for a cyclotron line but this has not been firmly confirmed.

Source	$E_{n,cyc}$ (keV)	Discovery	Reference
Her X-1	41	Balloon	Trümper et al. (1977)
4U 0115+64	14,24,36,48,62	<i>HEAO-1</i>	Wheaton et al. (1979)
V 0332+53	26,49,74	<i>Ginga</i>	Makishima et al. (1990)
Cen X-3	28.5	<i>RXTE</i>	Heindl & Chakrabarty (1999)
		<i>BeppoSAX</i>	Santangelo et al. (1998)
4U 1626-67	37	<i>RXTE</i>	Heindl & Chakrabarty (1999)
		<i>BeppoSAX</i>	Orlandini et al. (1998)
XTE J1646+274	36	<i>RXTE</i>	Heindl et al. (2001)
Cep X-4	28	<i>Ginga</i>	Mihara et al. (1991)
A 0535+26	46,100	<i>HEXE</i>	Kendziorra et al. (1992)
MXB 0656-072	36	<i>RXTE</i>	Heindl et al. (2003)
Vela X-1	24,52	<i>HEXE</i>	Kendziorra et al. (1992)
4U 1907+09	18,38	<i>Ginga</i>	Makishima & Mihara (1992)
4U 1538-52	20	<i>Ginga</i>	Clark et al. (1990)
GX 301-2	37	<i>Ginga</i>	Makishima & Mihara (1992)
X Per	29	<i>RXTE</i>	Coburn et al. (2001)
EXO 2030+375	11?	<i>RXTE</i>	Wilson et al. (2008)
	63?	<i>INTEGRAL</i>	Klochkov et al. (2008a)
OA0 1657-415	36?	<i>BeppoSAX</i>	Orlandini et al. (1999)
LMC X-4	100?	<i>BeppoSAX</i>	La Barbera et al. (2001)
GS 1843+00	20?	<i>Ginga</i>	Mihara (1995)

(Mihara 1995, Mihara et al. 2004) and *RXTE* observations of 4U 0115+64 (Nakajima et al. 2006, Tsygankov et al. 2006) and V 0332+53 (Tsygankov et al. 2007).

A negative correlation between the cyclotron line energy and the X-ray luminosity has been found for 4U 0115+64 and V 0332+53. Under the assumption of a change in the height of the line forming region with the luminosity, and assuming a dipole magnetic field configuration³, for a relative change in the fundamental cyclotron line of 60%, Tsygankov et al. (2007) find a relative change in the formation height of 20%, corresponding to a change of 2 km for 4U 0115+64. For V 0332+53, the relative change in the cyclotron line energy is 17%, that gives about 6% variation in the stellar radius, about 500 m.

³ $B \propto r^{-3}$ and $B \propto E$ gives $\frac{\Delta E}{E} \propto -3 \frac{\Delta R}{R}$

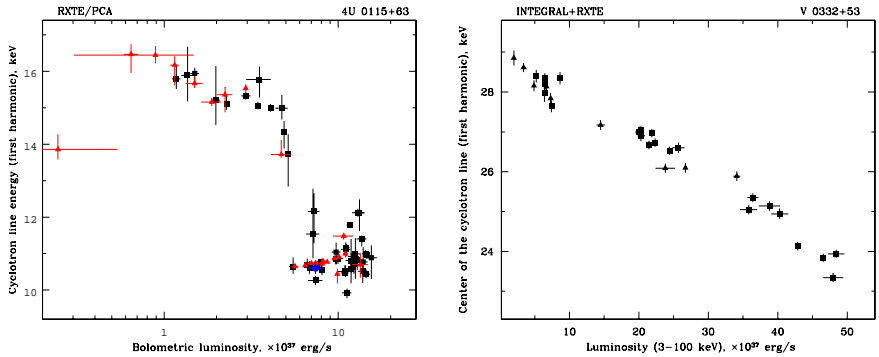


Figure 2.20: Negative correlation between the cyclotron line energy and the X-ray luminosity. Left panel: 4U0115+64 (Tsygankov et al. 2006). Right panel: V 0332+53 (Tsygankov et al. 2007).

For low luminosity sources in the sub-Eddington regime, a different behavior is expected. Staubert et al. (2007) found for Her X-1 a positive correlation between the cyclotron line energy and the luminosity (see Fig. 2.21). They find a change in the cyclotron line of 5% for a luminosity variation of $\Delta L/L \sim 1$.

For low luminosity sources, no radiation dominated shock is expected to form in the accretion column. Based on Basko & Sunyaev (1976) and Nelson et al. (1993), where the physics of accretion in low-luminosity sources is studied, Staubert et al. (2007) find the following relation between the cyclotron line energy and the luminosity:

$$\frac{\Delta E_{cyc}}{E_{cyc}} = 3 \frac{l_*}{R} \frac{\Delta L}{L} \quad (2.38)$$

where l_* is the height of the scattering region above the neutron star surface and R is the neutron star radius. For $\Delta L/L \sim 1$, this implies a change of $\sim 3\%$, very close to the 5% obtained from the Her X-1 observations.

Another evidence for a positive correlation between the cyclotron line energy and the luminosity was found for GX 301-2 by La Barbera et al. (2005) (however this was based just on two observations and at low significance).

2.3.2 Pulse profiles

Accreting X-ray pulsars exhibit very different pulse profiles typically showing more complex shapes at low energies and simpler shapes at high energies. Pulse profile modeling is very complex, far from being completely understood. Many processes contribute to the complex shapes we observe. Pulse profiles present variations with

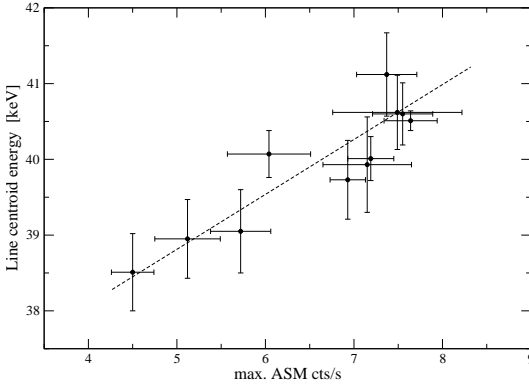


Figure 2.21: Positive correlation between the cyclotron line energy and the X-ray luminosity for Her X-1 (Staubert et al. 2007).

the source luminosity (e.g. EXO 2030+375, Klochkov et al. 2007) and variations with the energy (e.g., Vela X-1, see Fig. 2.22). Individual pulses usually show significant pulse to pulse variations, while average pulse profiles are more stable (Staubert et al. 1980).

Several authors have worked in modeling pulse profiles. This includes modeling the emission regions, specifying the local emission pattern. Both emission regions (when considering a dipole field) contribute to the formation of the pulse profile that a distant observer would see. A proper model calculation should include relativistic light deflection, which can have a significant effect in the pulse shape (Riffert & Meszaros 1988). In Fig. 2.23 the importance of relativistic light deflection in pulse profile model calculations is shown. Comparison of model calculations with observations has been performed for instance in Wang & Welter (1981), Meszaros & Nagel (1985), Leahy (1991).

The ray tracing method of computer graphics (Foley et al. 1990) has been generalized including relativistic light deflection in order to calculate beam patterns and pulse profiles (Nollert et al. 1989), and can be applied to arbitrary geometric shapes of the emission region. This method has been applied to different geometries, like filled columns or hollow columns (Kraus 2001). Due to the strong gravitational field around the neutron star, X-rays are observed at red-shifted energies. For slowly-rotating neutron stars, the metric around a neutron star can be approximated by the Schwarzschild metric (Kraus 1998).

An alternative method to analyze pulse profiles is to start from the observed pulse profiles, and based on symmetry considerations obtain a decomposition of the pulse profile into single-pole contributions. This is then transformed into the visible section

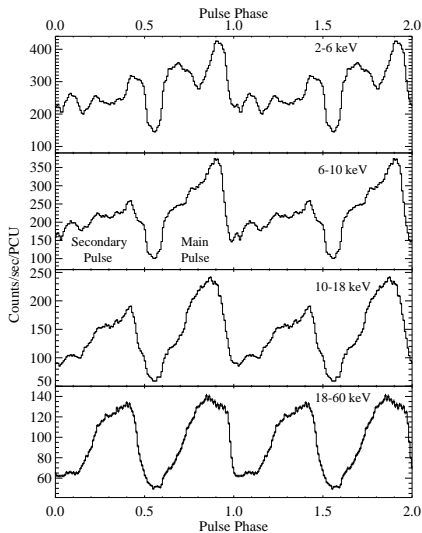


Figure 2.22: Example of energy dependent pulse profiles of Vela X-1 from Kreykenbohm et al. (2002). The low energy profile show a complex pattern, which becomes simpler at higher energies.

of the beam pattern. This method has been successfully applied to Cen X-3 and Her X-1 (Kraus et al. 1996, Blum & Kraus 2000) and is applied in this work to A 0535+26. More details are given in Chapter 8.

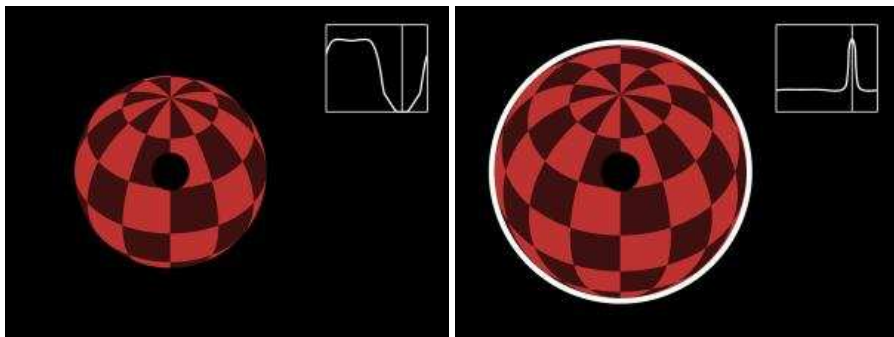


Figure 2.23: Pulse profile formation. In both figures, the small inset (top right) shows the computed pulse profile. The vertical line indicates the rotational phase of the neutron star shown in the figure. Left panel: pulse profile formation without taking into account relativistic light deflection. The neutron star is in a rotational phase in which one pole points away from the observer, and therefore no emission from that pole is seen. Right panel: pulse profile formation including relativistic light deflection. The same rotational phase is shown, with one pole pointing away from the observer, illustrating the effect of light bending. Figures from Ute Kraus, available with animation at http://www.spacetime travel.org/xpulsar06/xpulsar06_5.html.

CHAPTER 3

The Be/X-ray binary system A 0535+26

3.1 Overview

The Be/X-ray binary A 0535+26 was discovered by Ariel V (Smith & Courtier 1976) during a giant outburst in 1975 (Rosenberg et al. 1975). The binary system consists of the pulsating neutron star A 0535+26 and the optical companion HDE 245770 (Hudec 1975). It lies in an eccentric orbit of $e = 0.47$ with an orbital period of $P_{\text{orb}} \sim 111$ days. The estimated distance of the system is $d = 2$ kpc (Steele et al. 1998), and its equatorial and galactic coordinates are $\alpha = 05^{\text{h}} 38^{\text{m}} 54.5720^{\text{s}}$, $\delta = +26^{\circ} 18' 56''.822$ (J2000.0) and $l = 181.4450^{\circ}$, $b = -02.6435^{\circ}$ respectively (Perryman et al. 1997). Table 3.1 contains the orbital ephemeris of the binary system. An extensive review of the system is given in Giovannelli & Graziati (1992).

The optical companion HDE 245770 has been classified as O9.7IIIe (Giangrande et al. 1980) or B0 IIIe star (Steele et al. 1998). It has a luminosity of $L \sim 0.7 \times 10^5 L_{\odot}$, and the effective temperature lies in the range $T_{\text{eff}} = 26000 - 28000$ K (Giovannelli & Graziati 1992). The mass, radius and mass-loss rate are estimated to be $M \sim 14 M_{\odot}$, $R \sim 14 R_{\odot}$, $\dot{M} \sim 10^{-8} M_{\odot} \text{ yr}^{-1}$ (de Loore et al. 1984).

The neutron star pulsates with a spin period of $P \sim 103$ s. Its surface magnetic field, derived from cyclotron line measurements, is $B \sim 4 \times 10^{12}$ G. A 0535+26

P_{orbit} (days)	111.1 ± 0.3
$\tau_{\text{periastron}}$	MJD 53613.0 \pm 1.3
$a \sin i$ (lt-sec)	267 ± 13
ω_x ($^{\circ}$)	130 ± 5
e	0.47 ± 0.02

Table 3.1: A 0535+26 orbital ephemeris from Finger et al. (1996); P_{orbit} and $\tau_{\text{periastron}}$ were updated with new observations from 2005 (Finger et al. 2006).

presents quiescence states with luminosities $L_X \lesssim 10 \times 10^{36} \text{ erg s}^{-1}$, interrupted by normal (type I) outbursts, generally associated with the periastron passage, where a luminosity $L_X \sim 10^{36-37} \text{ erg s}^{-1}$ is reached, and giant (type II) outbursts, where the luminosity $L_X > 10^{37} \text{ erg s}^{-1}$. In Fig. 2.9 a schematic view of such systems was shown.

3.1.1 History of outbursts

Since its discovery in 1975 during a giant outburst (Rosenberg et al. 1975), five giant outbursts have been detected in October 1980 (Nagase et al. 1982), June 1983 (Semba et al. 1990), March/April 1989 (Makino et al. 1989), February 1994 (Finger et al. 1994b) and May/June 2005 (Tueller et al. 2005). Unfortunately, due to Sun constraints the 2005 giant outburst could not be observed by most instruments. An overview of the history of giant outbursts of A 0535+26 is given in Table 3.2. The time of periastron, calculated with the updated ephemeris from Finger et al. (2006), is also given. As can be seen from the table, almost all of the giant outbursts are associated with the periastron time. This is not always the case in Be/X-ray binary systems.

Associated with the periastron, the source shows sometimes normal outbursts. Between March 1993 and September 1994 a sequence of six outbursts were detected, spaced by the $P_{\text{orb}} \sim 111 \text{ days}$ orbital period. One of these was the giant outburst in February 1994, and the rest of them were normal outbursts (Finger et al. 1996). Fig. 3.1 (top panel) shows the light curve of the giant and normal outbursts in 1993–1994.

3.1.2 The source in quiescence

A 0535+26 shows a persistent low X-ray emission outside outbursts. In most of the observations performed during those quiescent states, X-ray pulsations have been detected, indicating that the source still accretes matter during quiescence.

A 0535+26 was observed by *EXOSAT* between 1985 and 1986 at a luminosity level of $L_{(1-20) \text{ keV}} = 2.5 \times 10^{35} \text{ erg s}^{-1}$. Pulsations were detected during two observations, with pulse periods of $P = 103.36 \pm 0.06 \text{ s}$ at MJD 46331 and $P = 103.290 \pm 0.07 \text{ s}$ at MJD 46479 (Motch et al. 1991).

Two observations during quiescence were performed with *RXTE* between 1998 August and 1998 November (Negueruela et al. 2000), where the source was detected at a luminosity level of $L_{(2-20) \text{ keV}} = 0.029 \times 10^{35} \text{ erg s}^{-1}$ and $L_{(2-20) \text{ keV}} = 0.043 \times 10^{35} \text{ erg s}^{-1}$ respectively. The observations were systematically limited by the contribution of the diffuse emission from the Galactic disk. Pulsations at $\sim 103.5 \text{ s}$ ($> 5 \sigma$ significant) were detected during the November 1998 observation, while in August a weak indication ($< 3 \sigma$) was found for periodicity at $P \sim 103.0 \text{ s}$. During

MJD	Periastron	Flux (Crab)	E(keV)	Experiment	Reference
April 1975					
42515–42531	42503.0	~ 2	3–7	<i>Ariel V</i>	Rosenberg et al. (1975)
October 1980					
44521–42522	44502.8	~ 1.5	1-22	<i>Hakucho</i>	Nagase et al. (1982)
June 1983					
45503–45505	45502.7	~ 2	32–91	<i>SMM</i>	Sembay et al. (1990)
March/April 1989					
47616	47613.6	0.45	1–20	<i>Ginga</i>	Makino et al. (1989)
47617		0.49	1–20	“	“
47620		0.6	1–20	“	“
47620		2.4 ± 0.5	23–52	balloon	“
47624–47625		4.3 ± 1	16-26	<i>Mir-Kvant</i>	“
February 1994					
49386	49391.2	0.4	20–40	<i>CGRO-BATSE</i>	Finger et al. (1994b)
49387		0.9	“	“	“
49388		1.4	“	“	“
49389		1.9	“	“	“
49390		2.2	“	“	“
49391		2.7	“	“	“
49392		3.1 ± 0.2	“	“	Finger et al. (1994c)
49395		5.6 ± 0.2	“	“	“
49397		6.2 ± 0.2	“	“	“
49401		8	“	“	Wilson et al. (1994)
49409		4	“	“	“
May/June 2005					
53506	53501.9	> 3	15–195	<i>Swift-BAT</i>	Tueller et al. (2005)
53533		4.5	30	<i>RHESSI</i>	Smith et al. (2005)
53544		2.4	30	“	“

Table 3.2: History of giant outbursts of the Be/X-ray binary A 0535+26. The flux is given in Crab units (see Footnote 1 on Chap. 5). The time of the passage through the periastron has been calculated using the same ephemeris from Finger et al. (2006).

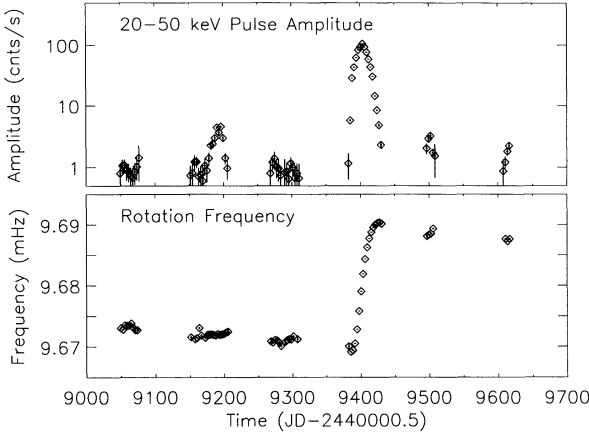


Figure 3.1: Top panel: light curve of A 0535+26 during the giant and normal outbursts in 1994. Bottom panel: pulse frequency evolution during the outbursts (Finger et al. 1996).

those observations the optical companion of A 0535+26, HDE 245770, showed no evidence of a circumstellar disk.

Observations during quiescence were also performed with *BeppoSAX* in September/October 2000 and March 2001 at luminosities $L_{(2-20)\text{ keV}} = 0.015 \times 10^{35} \text{ erg s}^{-1}$ and $L_{(2-20)\text{ keV}} = 0.044 \times 10^{35} \text{ erg s}^{-1}$ respectively (Orlandini et al. 2004). During these observations, a circumstellar disk around the optical companion was detected. Pulsations of $P = 103.40 \pm 0.02 \text{ s}$ at MJD 51973 were measured. The pulse profiles are noisy but rather indicate a broad single peaked structure. A soft excess was clearly detected in the LECS data. The same observations have also been analyzed by Mukherjee & Paul (2005) with very similar results. They note that a soft component is required for the third observation, the only in which pulsations are clearly detected.

Between 1994 and 2005, during a long quiescence state, *INTEGRAL* observed the source in October 2003 during an “unexpected” brief brightening of $\sim 6 \text{ ks}$ (Hill et al. 2007). The luminosity level reached was $L_{(18-100)\text{ keV}} = 3.8 \times 10^{35} \text{ erg s}^{-1}$, and a pulse period of $P \sim 103.7 \pm 0.1 \text{ s}$ (MJD 53615.5137) was determined.

3.2 Timing properties

3.2.1 Pulse period evolution

Figure 3.2 shows the pulse period history of A 0535+26 since its discovery in 1975 until 2003, and the period measurements that have been obtained from observations in

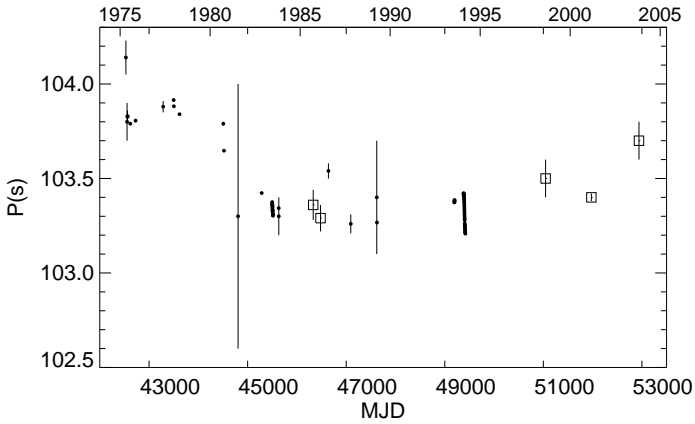


Figure 3.2: Pulse period history of A 0535+26 since its discovery in 1975 until 2003. The hollow squares indicate the observations performed during quiescence. A spin-up is observed during outbursts, and a spin-down trend is observed during quiescence.

quiescence are indicated. In 1975 the pulse period was $P = 104.14$ s (Rosenberg et al. 1975). During quiescence periods, the pulsar behavior appears to be consistent with a spin-down trend (Finger et al. 1994a, Hill et al. 2007), while during giant outbursts a spin-up trend has been observed. In the June 1983 giant outburst, a spin-up of $\dot{\nu} \sim 0.6 \times 10^{-11}$ Hz s $^{-1}$ was measured (Sembay et al. 1990), and in the February 1994 giant outburst a spin-up of $\dot{\nu} \sim 1.2 \times 10^{-11}$ Hz s $^{-1}$ was also measured. From 1994 to 2005 no X-ray outbursts have been detected.

In quiescence, the system is expected to be in the centrifugally inhibited regime (Illarionov & Sunyaev 1975). An estimate of the co-rotation radius and magnetospheric radius using the *BeppoSAX* observations (Mukherjee & Paul 2005) gives $r_m \approx 10^{10}$ cm and $r_{co} \approx 3 \times 10^9$ cm. With $r_{co} > r_m$, a centrifugal barrier, preventing the accretion of matter onto the neutron star, should arise.

Nevertheless, all historic observation campaigns have found pulsations in at least part of their data, indicating that matter is still being accreted along the magnetic field lines.

3.2.2 QPOs

QPOs were discovered in the 1994 giant outburst (Finger et al. 1996), confirming the presence of an accretion disk. The QPO was observed for 33 days. It was initially detected at 27 mHz, reaching 72 mHz at the peak of the outburst and falling to

25 mHz during the decay of the outburst. The QPO frequency was highly correlated both with the X-ray flux and the spin-up rate, revealing that the QPO was mostly controlled by the mass accretion rate. Two models are usually used to explain the QPOs observed, the beat frequency and the Keplerian frequency models. In the beat frequency model, the QPO center frequency $\nu_{\text{QPO}} = \nu_{\text{K}} - \nu_{\text{ns}}$, where ν_{K} is the Keplerian orbital frequency of the material at the inner edge of the accretion disk and ν_{ns} the spin frequency of the neutron star. In the Keplerian frequency model, the QPO center frequency is the the Keplerian frequency at the inner edge of the accretion disk, $\nu_{\text{QPO}} = \nu_{\text{K}}$. The A 0535+26 observations were compared with the predictions of the beat frequency and the Keplerian frequency QPO models in Finger et al. (1996), and it was found that both models agree with the data.

3.2.3 Pulse profiles

Energy dependent pulse profiles of A 0535+26 were obtained with a balloon experiment during the 1980 giant outburst (Frontera et al. 1985), with *HEXE* during the 1989 giant outburst (Kendziorra et al. 1994) and with *BATSE* during the 1989 giant outburst (Bildsten et al. 1997). These profiles are shown in Fig. 3.3. Excluding the *BATSE* profiles at low luminosity ($L_{(20-100)\text{ keV}} = 4 \times 10^{36} \text{ erg s}^{-1}$), the pulse profiles obtained in the different outbursts show similar general features. Above $E \approx 20 \text{ keV}$ they show a relatively simple double peak profile up to $E \sim 45 \text{ keV}$. At higher energies the second peak is significantly reduced. With the balloon experiment pulsations were measured up to $E \sim 130 \text{ keV}$, and *HEXE* measured pulsations up to $E \sim 110 \text{ keV}$.

3.3 Spectral properties

The X-ray spectrum of A 0535+26 can be phenomenologically modeled by an absorbed power law with a high-energy cutoff. In the March/April 1989 giant outburst, two cyclotron resonance scattering features were detected at $E_{\text{cyc},1} \sim 45 \text{ keV}$ and $E_{\text{cyc},2} \sim 100 \text{ keV}$ (Kendziorra et al. 1994). The spectrum of the discovery is shown in Fig. 3.4. In the February 1994 outburst the presence of the fundamental line at $E \sim 45 \text{ keV}$ could not be confirmed because of *OSSE*'s low-energy threshold at $E \sim 40 - 50 \text{ keV}$ (Grove et al. 1995). The presence of the fundamental line at $E_{\text{cyc},1} \sim 45 \text{ keV}$ has been confirmed during the August/September 2005 outburst with *INTEGRAL* (Kretschmar et al. 2005), *RXTE* (Wilson & Finger 2005) and *Suzaku* (Inoue et al. 2005) observations.

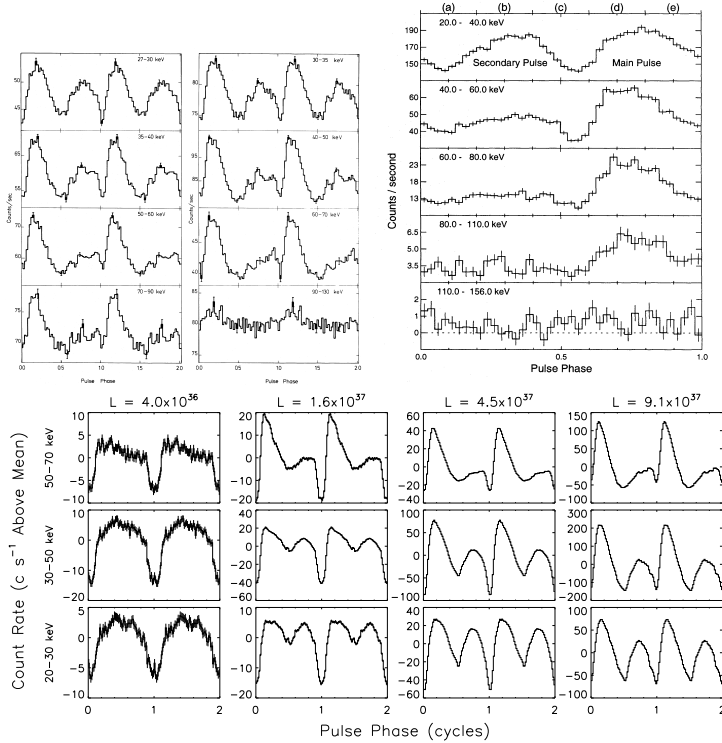


Figure 3.3: Top left panels: energy dependent pulse profiles of A 0535+26 during its October 1980 giant outburst (Frontera et al. 1985). Top right panels: *HEXE* energy dependent pulse profiles obtained during the 1989 giant outburst (Kendziorra et al. 1994). Bottom panels: energy dependent pulse profiles obtained at different luminosity levels during the 1994 giant outburst (Finger et al. 1996).

3.4 Optical observations

The binary system A 0535+26 does not show X-ray outbursts at every periastron passage. This is due to the fact that the optical companion HDE 245770 does not always present a disk around it which provides the fuel for the neutron star.

In Coe et al. (2006), ten years of optical monitoring of A 0535+26 were presented. Their results clearly show that the optical star HDE 245770 went through a period in which the circumstellar disk reached a minimum in 1998, and then a dramatic recovery of the disk took place. This was most probably the cause of the X-ray outbursts observed in 2005.

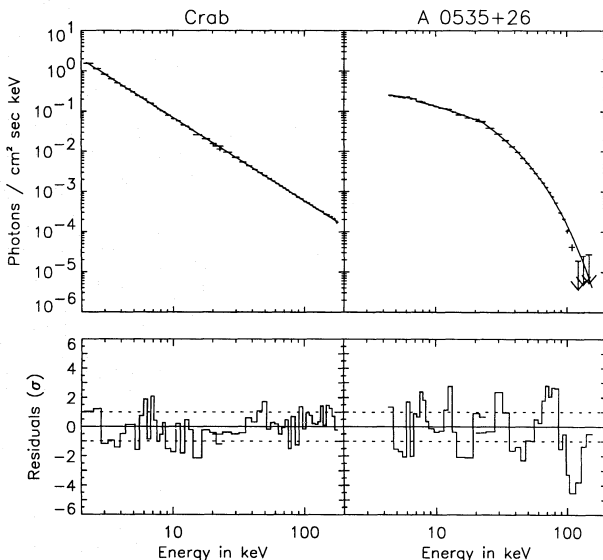


Figure 3.4: Right panel: *HEXE* spectrum of A 0535+26 from the discovery of the cyclotron lines at $E_{\text{cyc},1} \sim 45$ keV and $E_{\text{cyc},2} \sim 100$ keV. The upper panel shows the spectrum and best fit model, and the lower panel shows the residuals of a fit without including in the model absorption features, in which the two lines can be appreciated (Kendziorra et al. 1994). Left panel: spectrum and residuals of the Crab, which was observed simultaneously.

In the circumstellar disk around the optical companion, $H\alpha$ line forms in emission. The total flux is closely related to the size of the disk. The monitoring of this line during more than 10 years for A 0535+26 is shown in Fig. 3.5. A clear evolution of the $H\alpha$ line can be seen. It went from emission, through an almost complete loss of the disk in 1998, and then evolved progressively to stronger emission until 2005, coincident with the strong X-ray outburst observed. The He 6678 Å line shows a similar pattern, also shown in the figure, with a complete loss of the emission in 1998 and a recovery of the emission in 2005. Grundstrom et al. (2007) obtained similar results from an independent monitoring of the $H\alpha$ line of HDE 245770.

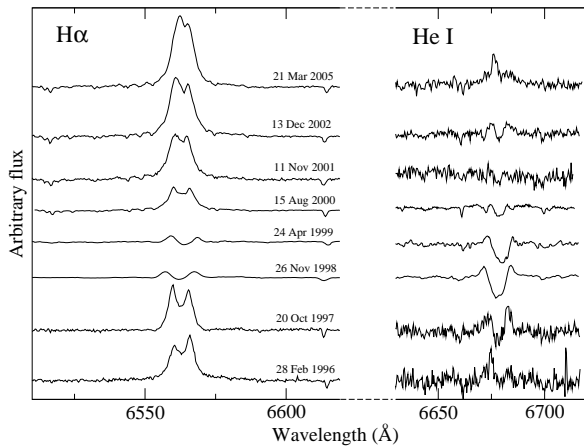


Figure 3.5: Evolution of the H α and He I lines profiles of A 0535+26 from 1996 until 2005. The emission lines are related to a circumstellar disk around the optical companion, which almost disappeared in 1998 and progressively reappeared, showing a maximum emission in 2005 coincident with the X-ray outburst. (Figure from Coe et al. 2006).

CHAPTER 4

***RXTE* and *INTEGRAL* observatories**

4.1 RXTE

The *Rossi X-ray Timing Explorer RXTE*¹ (Bradt et al. 1993) was launched on December 30 1995, and is still operational today. It provides an unprecedented time resolution together with moderate spectral resolution, allowing to study the variability of X-ray sources in timescales from milliseconds to months. *RXTE* covers the $\sim 2 - 250$ keV range with two co-aligned instruments, the Proportional Counter Array *PCA* (2 – 60 keV) and the High Energy X-ray Timing Experiment *HEXTE* (20 – 250 keV). It also has an independent instrument, the All-Sky Monitor *ASM* (2–10 keV), which scans about 80 % of the X-ray sky in every orbit. *RXTE* was launched into a low-earth circular orbit at an altitude of 580 km, with an orbital period of 90 minutes and 23° inclination. See Fig. 4.1 for a schematic view of the satellite.

4.1.1 The Proportional Counter Array PCA

Proportional counters are based on photoelectric effect. A proportional counter consists of a cell filled with gas (typically noble) with a wire connected to a high voltage. The wire is coupled via a capacitor to a charge sensitive preamplifier. X-rays entering the cell interact with the gas via photoelectric effect, and an ion-electron pair is produced, which will go to its corresponding cathode-anode. The detector enters the proportional counter mode when a sufficiently large electric field is applied, so that the electrons ionize the atoms in the gas by collisions and generate a charge multiplication, which is proportional to the original charge. The measured pulse is proportional to the original X-ray photon energy.

The *PCA* on board *RXTE* consists of five proportional counter units (*PCU*) filled with xenon gas. Each detector has an effective area of ~ 1300 cm², giving a total

¹Named in honor of the cosmic ray and astrophysicist Bruno B. Rossi

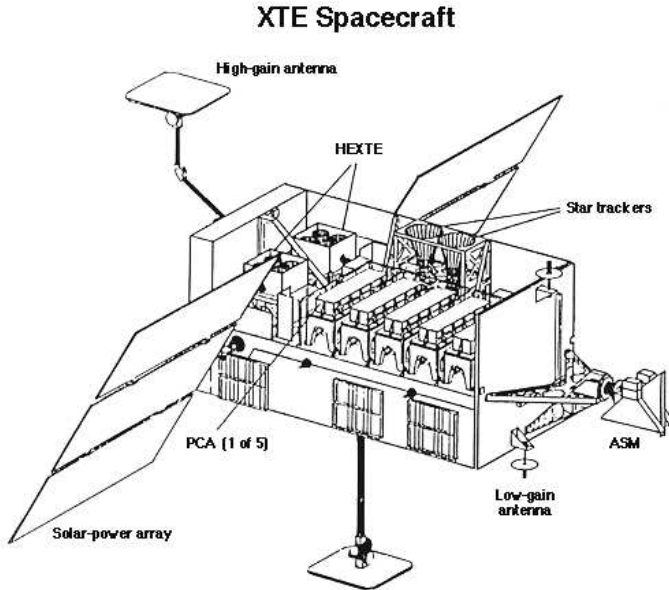


Figure 4.1: Schematic view of the *RXTE* spacecraft. The three instruments *PCA*, *HEXTE* and *ASM* are labeled. (Credit: NASA).

effective area of $\sim 6250 \text{ cm}^2$. In order to limit the field of view and to reduce the background² that such a large collective area has, a collimator of beryllium copper is used. It blocks the X-ray radiation that comes from a different direction than that of the source of interest. The background signal is further reduced with an efficient anti-coincidence system. The primary detector, which is oriented to the target and shielded from other directions, is surrounded by a secondary detector. A signal measured from the primary detector is only accepted when it is not accompanied by a coincident detection in the secondary detector.

The Experiment Data System (EDS) pre-analyzes and compresses the *PCA* data before its transmission to the ground. *PCA* basic performance characteristics are

²The sensitivity of an X-ray detector is the minimum flux that can be distinguished from the background. The background is made of two components: a diffuse cosmic X-ray background, of astrophysical origin, (discovered by Giacconi et al. 1962), and an internal background associated with the detector

The area of the detector plays an important role in the sensitivity. Non-focusing instruments in X-rays have larger detection areas, and therefore the internal background associated with the detector is larger. This results in a lower sensitivity. See e.g. Peterson (1975), Fraser (1989) or Longair (1992) for more details. A comparison of sensitivities for different X-ray missions can be found in Tenzer (2008).

Table 4.1: *RXTE* performance parameters, from Jahoda et al. (1996), Rothschild et al. (1998) and Levine et al. (1996).

	<i>PCA</i>	<i>HEXTE</i>	<i>ASM</i>
Energy Range	2 – 60 keV	15 – 250 keV	2 – 10 keV
Detector	Xe proportional counter array	NaI(Tl), CsI(Na) scintillator counters	Xe-CO ₂ PSPC
Sensitive Area	6250 cm ²	1600 cm ²	90 cm ²
Energy resolution	<18% @ 6 keV	<17% @ 60 keV	–
Time resolution	1 μ s	7.6 μ s	1.5 h
Sensitivity	0.1mCrab (10 min)	1mCrab (105 s)	30mCrab (1.5 h)
Field of View	1° × 1°	1° × 1°	6° × 90°

summarized in Table 4.1. See Fig. 4.2 (left) for a schematic view of the *PCA* assembly. A detailed description of the instrument can be found in Jahoda et al. (1996).

4.1.2 *The High Energy X-ray Timing Experiment HEXTE*

In X-ray astronomy, for energies above ~ 15 keV inorganic scintillator counters can be used. They consist of a scintillating crystal, coupled to a photodetector. An incident X-ray interacting with the detector generates scintillation light in the optical range. This optical light is converted into charge by a photomultiplier. Common scintillation detectors used in X-ray astronomy are thallium activated sodium iodide NaI(Tl) or caesium iodide activated with sodium, CsI(Na) or thallium CsI(Tl). Scintillator detectors are used in the phoswich (or phosphor sandwich) configuration in order to reduce the internal background of the detector. It consists of the combination of two different scintillators, a main one and a shielding one, optically coupled to a single photomultiplier tube. The two scintillators have different fluorescence decay times allowing to distinguish events generated in only one crystal from events generated in both. A common combination used is NaI(Tl) as main detector (decay time $\tau = 0.23\mu$ s) and CsI(Tl) ($\tau = 0.68\mu$ s) or CsI(Na) ($\tau = 0.46\mu$ s) as shielding detectors.

The *HEXTE* on board *RXTE* consists of two independent clusters, each with 4 detectors. Each detector consists of a scintillator counter (NaI(Tl) crystals), coupled to a photomultiplier through a CsI(Na) crystal. Each detector has a collimator, and they are all co-aligned on source, providing an angular resolution of 1°. See Fig. 4.2 (right) for a schematic view of the *HEXTE*.

The two clusters can rotate either $\pm 1.5^\circ$ or $\pm 3.0^\circ$ around the pointing position, and their rocking axis are orthogonal. This allows to obtain four different background measurements around the source-pointing direction. Table 4.1 summarizes the basic performance characteristics of *HEXTE*. A detailed description of the instrument is

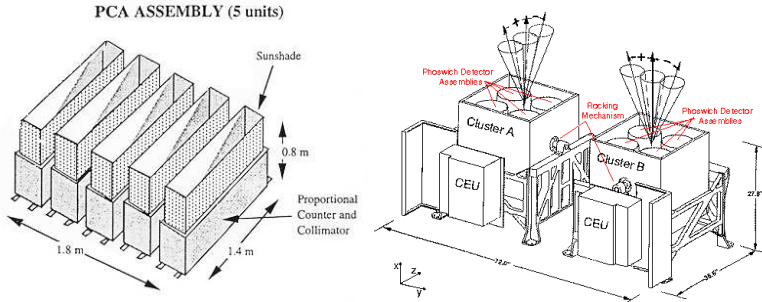


Figure 4.2: Left: schematic view of the *PCA* assembly. (Credit: NASA). Right: schematic view of the *HEXTE* clusters. The phoswich detector assemblies are labeled. (Figure from UCSD).

given in Rothschild et al. (1998).

4.1.3 The All Sky Monitor ASM

The *ASM* consists of three rotating cameras (Scanning Shadow Cameras, *SSC*), which scan 80% the X-ray sky in the (2 – 12) keV band in every *RXTE* revolution. Each of the *SSC* cameras has a one-dimensional mask 50% open (see Sect. 4.2 for details on coded masks) and a position-sensitive proportional counter *PSPC* containing a 95% Xe–5%CO₂ mixture. Basic performance characteristics of the *ASM* are given in Table 4.1. A detailed description of the cameras and the detectors can be found in Levine et al. (1996).

The *ASM* allows to detect transient sources and other time-variable phenomena, and provides long term light curves of bright X-ray sources. The *ASM/RXTE* team³ provides *ASM* light curves at http://xte.mit.edu/ASM_lc.html, updated on a near-weekly basis. The data is processed on board by the *EDS*, which also controls the rotation of the *SSC* cameras.

4.2 INTEGRAL

The *International Gamma-Ray Astrophysics Laboratory INTEGRAL* (Winkler et al. 2003) was launched on October 17, 2002. Its main scientific goals are to perform high-resolution spectroscopy with fine imaging and accurate positioning of gamma-ray emitting sources. *INTEGRAL*'s fine imaging capability as well as large field of view provide an ideal instrument to discover soft-gamma-ray sources. Its instruments

³at MIT and the Goddard Space Flight Center SOF and GOF

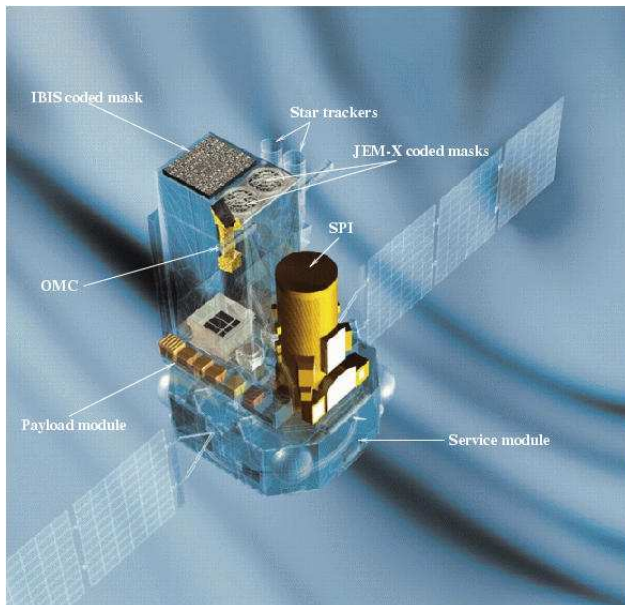


Figure 4.3: Schematic view of the *INTEGRAL* spacecraft. The *IBIS* and *JEM-X* coded masks are labeled (located 3.2 m above the detection plane), as well as the spectrometer *SPI*, the optical monitor *OMC* and the star trackers. Overall dimensions of the spacecraft are $4\text{ m} \times 6\text{ m}$, excluding the solar arrays. (Image source: ESA).

cover a broad energy range from $\sim 3\text{ keV}$ up to $\sim 10\text{ MeV}$. It carries two main gamma-ray instruments, the spectrometer *SPI* ($20\text{ keV} - 8\text{ MeV}$) and the imager *IBIS* ($20\text{ keV} - 8\text{ MeV}$), as well as two monitoring instruments in the X-ray and optical ranges, *JEM-X* ($3 - 35\text{ keV}$) and *OMC* (V-band). See Fig. 4.3 for a schematic view of the payload and service modules.

INTEGRAL has been launched into a high eccentric orbit, taking three days for one revolution around the Earth. The orbit was chosen in a way that minimizes the background noise due to protons trapped in the radiation belt, and has the advantage that it allows to perform long uninterrupted observations.

4.2.1 Imaging with *INTEGRAL*

The X-ray and gamma-ray instruments on board *INTEGRAL* make use of the coded mask technique to obtain images of the sky. Below $E \sim 10\text{ keV}$ it is possible to focus X-rays using grazing incidence. However, above $E \sim 10\text{ keV}$ nowadays the only pos-

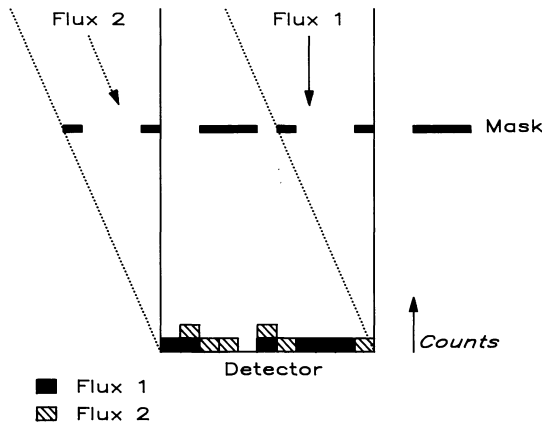


Figure 4.4: Basic illustration of coded-mask imaging. The flux from two sources is recorded in the detector coded by the mask. A deconvolution has to be applied to the shadowgram recorded in the detector to reconstruct the image from the sky. (Figure from Caroli et al. 1987).

sibility to obtain images is to use the coded mask technique. A coded mask consists of a plaque with opaque and transparent elements placed above the detector plane. The basic concept behind a coded mask is the pinhole camera, an opaque plaque with one transparent element or hole, placed between the source and the detector plane, which produces an image on the detector plane. In a coded-mask telescope, X-rays coming from the sources in the field of view are coded through the mask, and a shadowgram is recorded on a position sensitive detector. Imaging with coded-masks is a two-step process, since after obtaining the shadowgram, a deconvolution process has to be applied in order to obtain the image of the sky. Details on this process are given in Chapter 5, Sec. 5.2.3. Fig. 4.4 illustrates the basic concept of coded-mask imaging. Fig. 4.5 shows the Point Spread Function (PSF) in coded-mask telescopes, which is, in contrast to classical imaging systems, spread all over the detector. Two different fields of view are defined in coded-mask telescopes: Fully Coded Field of View (FCFOV), for which all the source flux is modulated by the mask, and Partially Coded Field of View (PCFOV), for which only a fraction of the source flux is coded by the mask (see Fig. 4.6). Details on the design of optimum coded-mask telescopes can be found in Proctor et al. (1979). Further details on coded-mask telescopes can be found for example in Caroli et al. (1987) or Skinner & Ponman (1994), and at <http://www.sron.nl/~jeanz//cai/>.

Coded mask telescopes have an advantage compared to focusing X-ray telescopes,

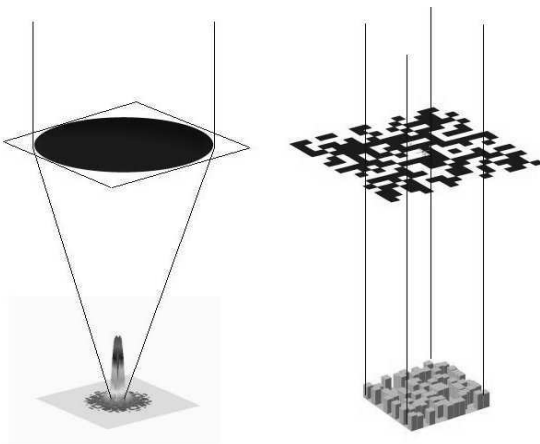


Figure 4.5: Left panel: Classical focusing system and its PSF. Right panel: coded-mask system and its PSF spread all over the detector. (Fig. from Skinner 2004).

and that is their large field of view. Even if the angular resolution of coded mask telescopes is worse than that of focusing X-ray telescopes (e.g. \sim arcsecond for *XMM-Newton* or *Chandra* compared to \sim arcminutes for *INTEGRAL IBIS*, see below), the field of view is much larger (for instance 16° for *INTEGRAL SPI* compared to 30° for *Chandra* or *XMM-Newton*), allowing to discover new X-ray sources or transients which otherwise would not have been detected.

An advantage of imaging X-ray telescopes is that the background is measured simultaneously with the source. In non-imaging instruments, the background can be modeled (e.g. in *PCA*) or measured with rocking instruments (e.g. in *HEXTE*).

In the following sections, brief descriptions of the four instruments on board *INTEGRAL* are given.

4.2.2 *SPI*

The *SPI* telescope operates in the 20 keV – 8 MeV range. It provides medium angular resolution together with high energy resolution, allowing to resolve astrophysical lines and to perform spectroscopy.

The coded mask has a HURA pattern (Hexagonal Uniform Redundant Array, see Cook et al. 1984), and the opaque cells are made of tungsten. It has a 75 % transparency at $E = 35$ keV, and reaches 85 % transparency at $E = 300$ keV.

The position sensitive detector in *SPI* is made of the semi-conductor germanium (Ge). During many years the workhorse in gamma-ray astronomy have been NaI

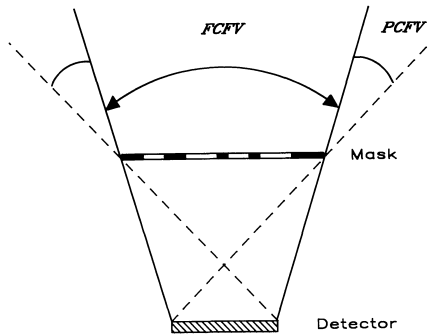


Figure 4.6: Illustration of Fully Coded Field of View and Partially Coded Field of View in a coded mask telescope. (Figure from Caroli et al. 1987).

scintillator detectors. However, Ge detectors have the advantage to offer a very high-energy resolution, but have the inconvenient that they require cooling down to $T \sim 90$ K. Details on Ge and other detectors used in gamma-ray astronomy can be found in Gehrels et al. (1988).

The detector in *SPI* is an array made of 19 germanium detectors, with an hexagonal shape in an area of 508 cm^2 . The detector is cooled down at $T \sim (85 - 90)$ K with a cryogenic system.

The mask is much larger than the detector, with only 1.7 m separation, which gives the wide field of view of 16° (see Fig. 4.7). Basic instrument characteristics are summarized in Table 4.2. A detailed description of *SPI* can be found in Vedrenne et al. (2003).

4.2.3 *IBIS*

The *IBIS* telescope operates in the $15 \text{ keV} - 10 \text{ MeV}$ range, and is optimized for high angular resolution. The detection system is formed by two independent detectors, *IS-GRI* and *PICsIT*. *ISGRI* is optimized for low energies, $15 \text{ keV} - 1 \text{ MeV}$, and *PICsIT*⁴ is optimized for higher energies, $200 \text{ keV} - 10 \text{ MeV}$.

The coded mask is based on a cyclic replication of a MURA (Modified Uniformly Redundant Array, see Gottesman & Fenimore 1989) of order 53. It is an array $1064 \times 1064 \times 16 \text{ mm}^3$ made of 95×95 individuals cells. Approximately 50% of the cells are opaque to photons.

⁴Due to limitations of the public software available to analyze *INTEGRAL* data (Off-line Science Analysis OSA, available in the Integral Science Data Center ISDC, Geneva), at the moment *PICsIT* is limited to very strong sources and will not be used in this thesis

Table 4.2: *SPI* and *IBIS* performance parameters, from Vedrenne et al. (2003) and Ubertini et al. (2003). Continuum sensitivity in units of $\text{ph cm}^{-2} \text{s}^{-1} \text{keV}^{-1}$, line sensitivity in units of $\text{ph cm}^{-2} \text{s}^{-1}$, for a 3σ detection and 10^6 s observation.

	<i>SPI</i>	<i>IBIS</i>
Energy Range	18 keV – 8 MeV	15 keV – 10 MeV
Sensitive Area	508 cm ² Ge	2600 cm ² CdTe 2890 cm ² CsI
Energy resolution (FWHM)	3 keV @ 1.7 MeV	8 keV @ 100 keV
Continuum Sensitivity @100 keV	5.5×10^{-6}	6×10^{-7}
Line Sensitivity @100 keV	3.3×10^{-5}	1.9×10^{-5}
Fully Coded Field of View	16° (diameter)	9° × 9°
Angular Resolution (FWHM)	2.5°	12'
Point Source Location Accuracy	10'	30''
Absolute timing accuracy	≤ 200 μs	≤ 200 μs

ISGRI is made of CdTe semiconductor detectors. The small size of the detectors (2 mm thick, 4 × 4 mm) allows to obtain a pixelated image with high spatial resolution. Each CdTe detector is read out by its own dedicated electronics. There are in total 16384 detectors (128 × 128), in a total area of 2600 cm². Basic instrument characteristics are summarized in Table 4.2. A detailed description of the instrument can be found in Lebrun et al. (2003).

4.2.4 *JEM-X*

The Joint European Monitor for X-rays operates in the 3 – 35 keV range. Operating simultaneously with *IBIS* and *SPI*, *JEM-X* provides low energy data complementary to the gamma-ray data. Its spacial resolution is higher than in the gamma-ray instruments, which helps in the identification of sources. *JEM-X* consists of two identical telescopes, *JEM-X1* and *JEM-X2*, each with its own mask, detector and associated electronics.

The coded mask is a hexagonal array (HURA pattern, Hexagonal Uniform Redundant Array, see Cook et al. 1984) made of 22 501 elements, with 25 % open area.

The *JEM-X* position sensitive detector is a microstrip gas chamber. Microstrip detectors were developed to replace the wires on proportional counters, and contain narrowly spaced conductor strips. See Oed (1988) for details on microstrip detectors. Multiwires proportional counters consist of a large grid of thin anode wires on a flat plate placed between two large flat plates with cathode wire grids. This is placed inside the gas detector, and allows to localize the events that hit the detector in two dimensions. The gas is a mixture of 90% xenon and 10% methane (at 1.5 bar pressure),

Table 4.3: *JEM-X* and *OMC* performance parameters, from Lund et al. (2003) and Mas-Hesse et al. (2003). Continuum sensitivity in units of $\text{ph cm}^{-2} \text{s}^{-1} \text{keV}^{-1}$, line sensitivity in units of $\text{ph cm}^{-2} \text{s}^{-1}$, for a 3σ detection and 10^6 s observation.

	<i>JEM-X</i>	<i>OMC</i>
Energy Range	4 keV–35 keV	500 nm–600 nm
Sensitive Area	500 cm ² (each <i>JEM-X</i> unit)	CCD 2061 × 1056 pixels
Energy resolution (FWHM)	2.0 keV @ 22 keV	-
Continuum Sensitivity @6 keV	1.2×10^{-5}	-
Line Sensitivity @100 keV	1.9×10^{-5}	-
Fully coded field of view	4.8° (diameter)	5° × 5°
Angular Resolution (FWHM)	3'	25''
Point Source Location Accuracy	15''	6''
Absolute timing accuracy (3σ)	≤ 200 μs	>1 s

with 500 cm² sensitive area. A detailed description of *JEM-X* can be found in Lund et al. (2003). The basic instrument characteristics are summarized in Table 4.3.

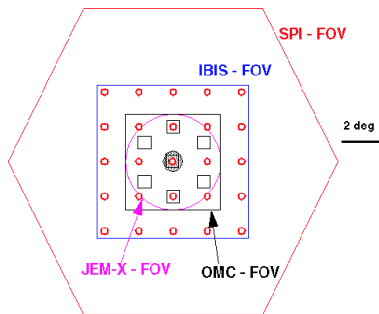
Currently only *JEM-X1* is operated, because at the beginning of the mission a gradual loss in sensitivity in both *JEM-X* units took place due to the erosion of the microstrip anodes. *JEM-X* is operated at a lower voltage and therefore at a lower gain, to reduce the anode damage rate.

4.2.5 *OMC*

The Optical Monitoring Camera on board *INTEGRAL* provides simultaneous V-band photometry (centered at 550 nm) of the gamma-ray sources observed with *SPI* and *IBIS*. It allows to identify optical counterparts of high-energy sources discovered with the gamma-ray instruments. The *OMC* has refractive optics, focused onto a CCD detector. The basic performance parameters are summarized in Table 4.3. More details can be found in Mas-Hesse et al. (2003).

4.2.6 *Dithering*

The four instruments on board *INTEGRAL* have very different fields of view, as shown in Fig. 4.7. In order to reduce the systematic effects on spatial and background variations, dithering observation modes are used. The dithering consists of several off-pointings with respect to the target in steps of 2°. There are two dithering patterns in *INTEGRAL*: rectangular and hexagonal. The hexagonal pattern is well suited for single known gamma-ray point sources. The rectangular pattern is more appropriate for crowded fields of view, for sources with unknown positions and for diffuse sources.



- Target position
- 7 point hexagonal pattern
- 25 point rectangular pattern

Figure 4.7: Fully coded field of view and dithering pattern for all instruments on board *INTEGRAL*. (Figure from Jensen et al. 2003).

These patterns are shown in Fig. 4.7.

A 0535+26 observations with *RXTE* and *INTEGRAL*

5.1 Overview of the August/September 2005 outburst.

A 0535+26 remained in quiescence for more than 11 years, since the 1994 giant outburst until 2005 (see Chapter 3). In May/June 2005 (MJD 53490–53550) a giant (type II) outburst took place, associated with the periastron passage of the source. The outburst unfortunately could not be observed by most astronomical satellites due to Sun constraints (Tueller et al. 2005). Two subsequent normal (type I) outbursts took place in August/September (MJD 53605–53625) and December 2005 (MJD 53720–53740), in the successive periastron passages. The *RXTE ASM* and *Swift BAT* light curves of A 0535+26 (MJD 53480–53750) showing the three outbursts are plotted in Fig. 5.1. During the giant outburst, the highest value of the flux measured with *ASM* was $F_{(2-10)\text{ keV}} \sim 1.58$ Crab and $F_{(15-50)\text{ keV}} \sim 5.7$ Crab measured with *Swift BAT*¹. During the August/September normal outburst, *ASM* registered a maximum flux of $F_{(2-10)\text{ keV}} \sim 173$ mCrab and *Swift BAT* $F_{(15-50)\text{ keV}} \sim 0.88$ Crab. The weaker normal outburst in December 2005 reached $F_{(2-10)\text{ keV}} \sim 110$ mCrab in the *ASM* and $F_{(15-50)\text{ keV}} \sim 0.44$ Crab in *Swift BAT*.

The normal outburst in August/September 2005 was observed with *INTEGRAL* and *RXTE* through the activation of a *Target of Opportunity* program. The timetable of the observations is summarized in Table 5.1, and all the individual *RXTE* pointings are listed in Appendix A. The *ASM* and *BAT* light curves relative to the type I outburst of August/September (MJD 53600–53640) are shown in Fig. 5.2. In the same figure the times of the *RXTE* and *INTEGRAL* pointings are indicated. A sketch of the 111.1 day orbit of the neutron star around the optical companion is shown in Fig. 5.3, with the section of the orbit in which the *INTEGRAL* and *RXTE* observa-

¹The Crab is typically used in X-ray astronomy as calibration source and as a unit of measure for the flux. 1 Crab in the (2-10) keV energy range corresponds to a flux of approximately $F_{(2-20)\text{ keV}} \sim 2.3 \times 10^{-8}$ erg cm⁻² s⁻¹. The Crab nebula flux is about 75 *ASM* counts s⁻¹ (2 – 10 keV) and 0.2263 *Swift BAT* counts cm⁻²s⁻¹ (15 – 50 keV).

tions were performed highlighted. The ~ 200 ks *INTEGRAL* observation is divided in 56 *science windows* (see Sec. 5.2.3), and the ~ 140 ks *RXTE* observation consists of 44 pointings.

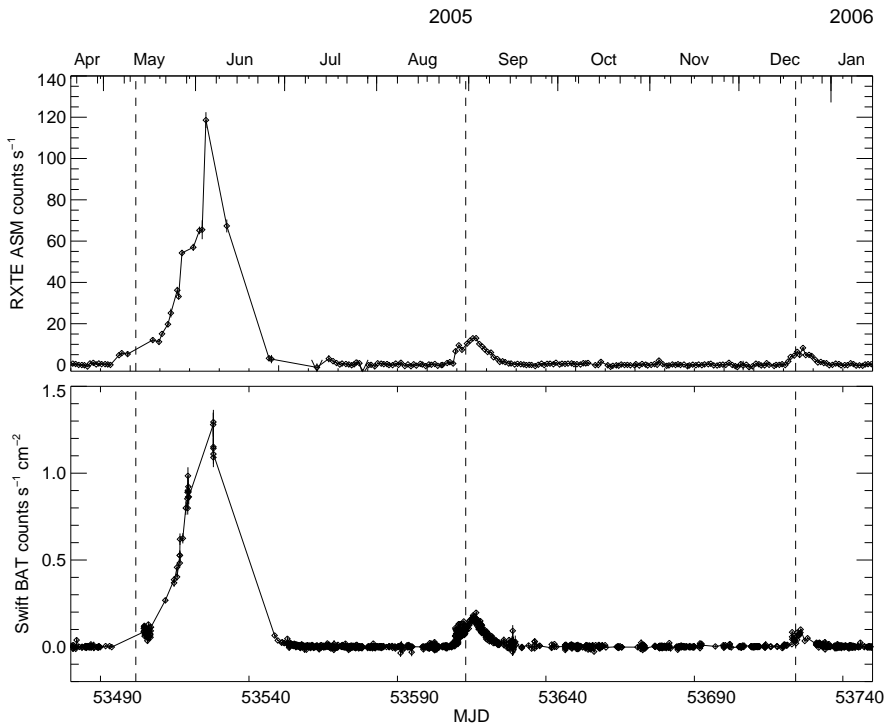


Figure 5.1: Top panel: *RXTE ASM* light curve (2 – 10 keV) of A 0535+26 showing the giant outburst and subsequent normal outbursts in 2005. Bottom panel: *Swift BAT* light curve (15 – 50 keV) during the same time interval. The vertical dotted lines indicate the periastron passages (ephemeris from Finger et al. 2006).

From the analysis of the *ASM* light curve of the August/September 2005 outburst the presence of a flare is detected in the rise to the peak, with a duration of $\tau_{flare} \sim 1$ day. The *Swift BAT* light curve reveals that the flare seen with *ASM* is just one of a collection of flares occurred before the periastron passage. After that, the outburst presents a smoother evolution. A detailed analysis of the observations during the *main outburst* is presented in Chapter 6 while the analysis of the observations of the *pre-outburst flare* is described in Chapter 7.

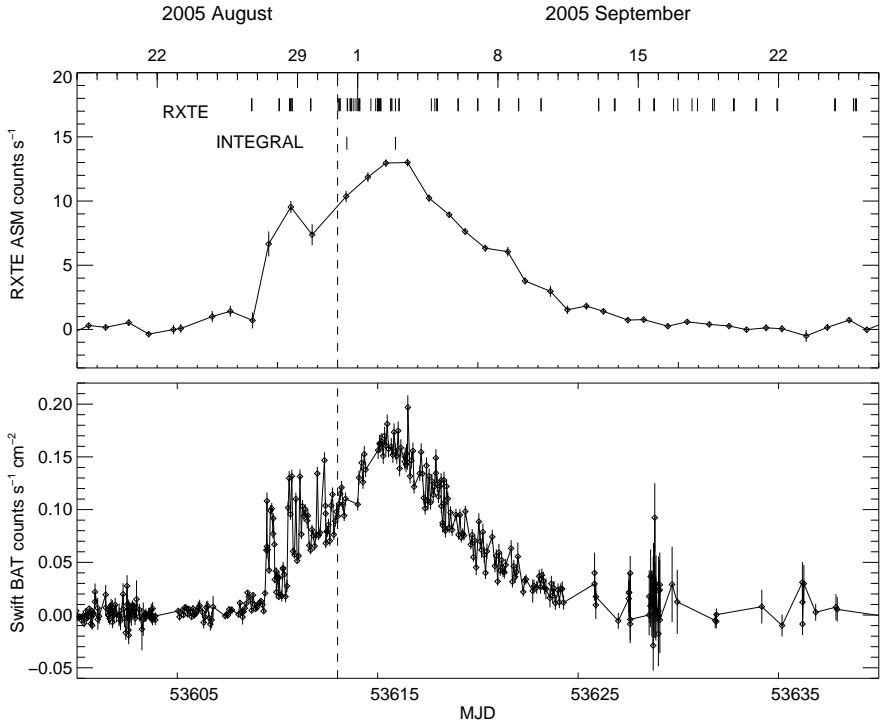


Figure 5.2: Top panel: *RXTE* ASM light curve of A 0535+26 during the normal outburst in August/September 2005. The start and stop times of our *INTEGRAL* observation are indicated, as well as each of the individual *RXTE* observations and the periastron passage. Bottom panel: *Swift* BAT light curve during the same outburst. The flare during the rise to the peak of the outburst seen in the ASM light curve is one of a collection of flares seen in the BAT light curve (ephemeris from Finger et al. 2006).

Table 5.1: Log of the observations used in this work. The observation ID, start and stop time and total observation time are given. Appendix A contains all the *RXTE* pointings.

	Obs.ID	start-stop time (MJD)	duration
<i>INTEGRAL</i>	03200490001 (56 scws)	53613.46–53615.89	~ 200 ks
<i>RXTE</i>	P91085, P91086 (44 pointed obs.)	53608.7–53638.8	~ 140 ks

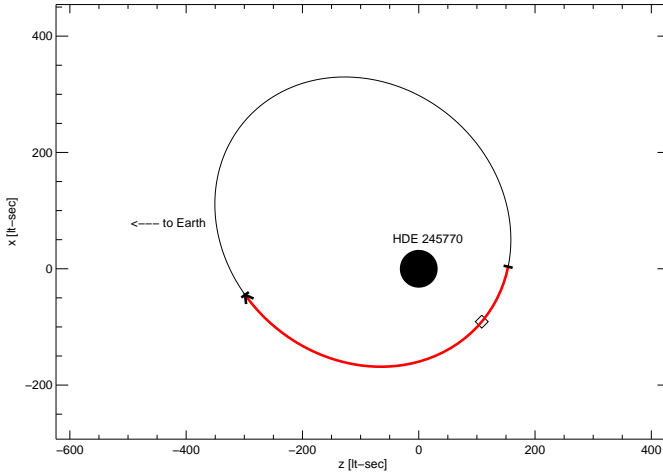


Figure 5.3: Sketch of the 111.1 days orbit of A 0535+26 around the optical companion HDE 245770. The red line indicates the fraction of the orbit during which the *INTEGRAL* and *RXTE* observations were performed, with an arrow indicating the direction of motion of the neutron star. The periastron time is represented with a square (ephemeris from Finger et al. 2006).

5.1.1 Optical light curve with *OMC*

The binary system A 0535+26 happens to be in the *INTEGRAL* FOV of the routine observations of the Crab source performed for calibration purposes. No X-ray emission from A 0535+26 was observed (except during a flare in 2003, Hill et al. 2007), while the optical companion HDE 245770 has been periodically monitored with the *OMC*. The evolution of the visual magnitude for the available observations of A 0535+26 with *OMC*² is shown in Fig. 5.4 (in Chapter 6, Fig. 6.3, the *OMC* light curve corresponding to the *INTEGRAL* observation in 2005 is shown). A decline in the optical brightness of the star is observed in the August/September 2005 outburst, reaching a minimum of $m_v = 9.570 \pm 0.012$. After that, the optical magnitude has increased again, reaching $m_v = 8.881 \pm 0.012$.

As observed by Lyutyi et al. (1989) and Lyuty & Zaitseva (2000) in past giant outbursts of A 0535+26, the optical magnitude of HDE 245770 decreased prior to the observed giant outbursts, and increased during the outburst. This was also seen in

²Based on data from the *OMC* Archive at LAEFF (<http://sdc.laeff.inta.es/omc/index.jsp>), pre-processed by ISDC

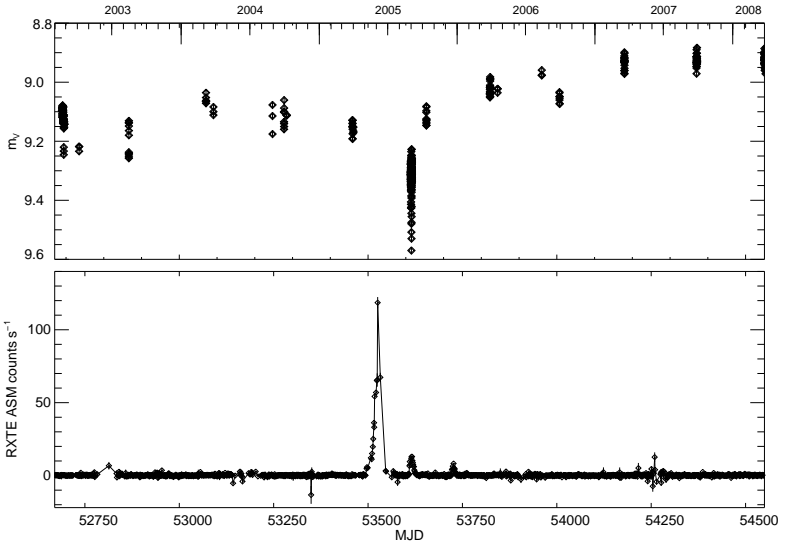


Figure 5.4: Top panel: *OMC* light curve of A 0535+26 using all available *INTEGRAL* observations. Bottom: *ASM* ($2 - 10$ keV) X-ray light curve for the same period of time.

V 0332+53: X-ray outbursts were preceded by optical brightening in 1983, 1989 and 2004 (Kiziloglu et al. 2008). The same behavior is seen in the *OMC* light curve, with an increase of the optical flux before 2005 reaching a minimum of $m_v = 9.036 \pm 0.012$ in March 2004.

5.2 *RXTE* and *INTEGRAL* data analysis

5.2.1 X-ray spectral analysis

The spectral analysis of *RXTE* and *INTEGRAL* data was performed with the X-ray Spectral Fitting Package *XSPEC* v11.3³ (Arnaud 1996), provided by the HEASARC⁴.

The count rate observed with an X-ray detector, $C(I)$ (photon counts per instrument channel) is not the actual spectrum of the source $f(E)$. The actual spectrum of

³<http://heasarc.gsfc.nasa.gov/docs/xanadu/xspec/xspec11/index.html>

⁴NASA's High Energy Astrophysics Science Archive Research Center http://heasarc.gsfc.nasa.gov/docs/software/ftools/ftools_menu.html

Table 5.2: Critical $\Delta\chi^2$ to calculate confidence regions for the cases used in this work (values from Avni 1976).

Confidence level (%)	$\Delta\chi^2$	
	No. of interesting parameters 1	2
68 % (1σ)	1.00	2.30
90 %	2.71	4.61
99 % (3σ)	6.63	9.21

the source relates to the observed spectrum in the following way:

$$C(I) = \int_0^\infty f(E)R(I, E)dE \quad (5.1)$$

where $R(I, E)$ is the *detector instrumental response*, proportional to the probability that a photon of energy E is detected in the channel I . Inverting this equation will give the spectrum of the source. But this inversion is not unique. The usual approach to solve this problem is to define a model $f'(E)$, and calculate an observed spectrum $C_p(I)$ by convolving $f'(E)$ with the response $R(I, E)$. We then fit this calculated spectrum with the observed one until we obtain a “good match” between the convolved model and the measured data. Typically χ^2 statistic is used, which assumes a Gaussian distribution for the spectral channels. The χ^2 is defined as:

$$\chi^2 = \sum \frac{(C(I) - C_p(I))^2}{\sigma(I)^2} \quad (5.2)$$

where $\sigma(I)$ is the error for channel I . If χ^2 exceeds a critical tabulated value, the model used is not appropriate. The reduced χ^2 is defined as $\chi_{\text{red}}^2 = \chi^2/\text{dof}$, where dof is the number of degrees of freedom. Generally, $\chi_{\text{red}}^2 \approx 1$ indicates a good fit (see Bevington & Robinson 1992), but does not imply that the model is the *only* possible one. In general a model will be acceptable if $\chi_{\text{red}}^2 \approx 1$ is obtained together with an acceptable physical explanation for the model.

Once a best fit model is obtained, confidence limits for the model parameters can be obtained. The method used here is described in Avni (1976) and implemented in XSPEC. This is done varying the parameter value until the χ^2 increases by a particular amount above the best fit value. The critical $\Delta\chi^2$, or amount that χ^2 is allowed to vary, depends on the confidence level required and on the number of parameters that are being varied. Typical values for the critical $\Delta\chi^2$ for one and two parameters of interest are given in Table 5.2.

In order to perform spectral fitting, the instrumental response ($R(I, E)$ in Eq. 5.1) has to be known. The response, as described above, is a continuous function of E ,

proportional to the probability that a photon of energy E is detected in a channel I . The continuous function is converted into a discrete function, the response matrix $R_D(I, J)$, such as:

$$R_D(I, J) = \int_{E_{J-1}}^{E_J} R(I, E) dE / (E_J - E_{J-1}) \quad (5.3)$$

The response matrix includes non-linearities of the detector, like escape peaks⁵ or Compton scattered photons. The effective area and the quantum efficiency as a function of the energy are usually taken into account via an auxiliary response file, ARF, that must be multiplied by $R_D(I, J)$.

5.2.2 *RXTE data extraction*

RXTE data were extracted using the *FTOOLS v6.3.1*⁶ package provided by the HEASARC. Information on the *RXTE* data extraction is available at *The ABC of XTE* and *The RXTE Cook Book*, both available at the *RXTE GOF*⁷. Specific scripts mainly developed at AIT and at the University of Erlangen-Nuremberg were used for the data reduction. A description of these tools is available at <http://pulsar.sternwarte.uni-erlangen.de/wilms/research/analysis/rxte/>.

The selection of the data, and creation of good time intervals (GTIs), were performed according to the following criteria, following the *RXTE GOF* recommendations: observations performed within 30 min of the South Atlantic Anomaly⁸ passage were rejected. The minimum source elevation above the horizon allowed was 10° to avoid X-ray contamination from the Earth's limb. And for *PCA* we excluded data for which the electron ratio was higher than 0.1 in at least one of the detectors. This is a measure of the electron contamination, given by a certain ratio of veto rates in the detector (Wilms et al. 1999). With those GTIs, using the appropriate *FTOOLS v6.3.1* for each task, we extracted high resolution spectra and light curves, performed the modeling of the *PCA* background and generated the response matrices.

Pulse phase resolved analysis has been performed with the *ikfasebin* tool based on *fasebin* from *FTOOLS v6.3.1*, which takes the *HEXTE* dead time correction

⁵The detection of photons is mainly due to photoabsorption by the detector gas. As a consequence of the photoabsorption, a characteristic fluorescence photon (or an Auger electron) is emitted. In most of the cases, this fluorescence photon is reabsorbed near the interaction site. However, in some cases (for instance if the photoelectric absorption takes place near the surface of the detector) the X-ray can escape the detector. In this case, the energy deposited in the detector is smaller by an amount of energy equals to the original X-ray photon energy minus the characteristic X-ray energy. This produces a peak in the response function or "escape peak" (Knoll 2000).

⁶http://heasarc.gsfc.nasa.gov/docs/software/ftools/ftools_menu.html

⁷Guest Observer Facility http://heasarc.gsfc.nasa.gov/docs/xte/xte_1st.html

⁸South Atlantic Anomaly (SAA): dip in the Earth's magnetosphere that produces a higher particle flux in that region, that can contaminate the observations

into account (Kreykenbohm 2004). Dead time correction in *HEXTE* data is necessary, because the movement of the cluster while rocking is treated as dead time in the off-source data, and without this correction the background subtraction would be wrong.

We included 0.5% systematic errors for *PCA* data. For most of our observations the *PCA* count rate is large and the uncertainty is dominated by systematic uncertainties and not Poisson errors. In the case of *HEXTE*, the uncertainty is dominated by the Poisson error of the data, because the count rate at higher energies and the effective area of the detector are smaller. We therefore included no systematic errors in the *HEXTE* data.

5.2.3 INTEGRAL data extraction

The *INTEGRAL* data analysis was performed with *OSA*, the *INTEGRAL* Off-line Scientific Analysis software (available at ISDC⁹) following the instructions from the *JEM-X*, *IBIS* and *SPI* cookbooks. For all the *INTEGRAL* instruments, the analysis is made of several steps, in which corrections are applied to the data, the image reconstruction is performed and the spectra and light curves are extracted. A detailed explanation of these steps is given in the *Introduction to the INTEGRAL Data Analysis* available at ISDC.

Due to the dithering pattern (see Chapter 3), *INTEGRAL* observations are made of many pointings of ~ 30 minutes separated by slews. Each of these pointings is called *science window*, that are grouped in *observation groups*.

As was mentioned in Sec.4.2.1, *INTEGRAL* makes use of the coded mask technique. In the following the basic concept in deconvolving coded mask data, relevant to *INTEGRAL* analysis, is summarized.

Let S be the sky image, M the mask array and B the background. The mask is made of 1 (transparent) and 0 (opaque) elements. The shadowgram recorded on the detector will be given by the convolution of the sky image with the mask array plus the background,

$$D = S \otimes M + B \quad (5.4)$$

By building an array G such as $M \otimes G = \delta$ (where δ is the Dirac's delta function), the deconvolved image S' on the sky can be obtained:

$$S' = D \otimes G = S + B \otimes G \quad (5.5)$$

One problem of coded mask instruments, compared to focusing telescopes, is that the source of interest can be contaminated by bright sources in the field of view. Contamination can occur using the *JEM-X* standard spectral extraction tool (see *known issues* of the *OSA* software at <http://isdc.unige.ch/?Soft+download>).

⁹*INTEGRAL* Science Data Centre <http://isdc.unige.ch/index.cgi?>

Therefore we checked that the *JEM-X* A 0535+26 spectrum is not contaminated by the Crab, that was observed simultaneously. We extracted A 0535+26 *JEM-X* spectra for all the science windows, and also excluding the science windows which were pointing closer to the Crab (dithering pointings 2 and 7). The flux of both spectra is the same, so we are sure that the Crab is not contaminating our *JEM-X* A 0535+26 spectra. The Crab is a very well known source typically used for calibration (Toor & Seward 1974, Kirsch et al. 2005). Systematics of 3 % for *JEM-X* were evaluated from the Crab spectrum in the same observation.

We have made use of alternative calibration files provided by INAF-IASFPa to extract *IBIS (ISGRI)* data. Instead of the standard LUT2 (look up table) file provided with *OSA*, we used a LUT2 which corrects the Charge Loss effect that provides a better energy correction of the *IBIS (ISGRI)* events. We used ARF files provided by the IASF-Pa group calibrated with the simultaneous Crab observations. Details are given in Mineo et al. (2006) and the alternative calibration files can be downloaded from <http://www.ifc.inaf.it/~ferrigno/integral/>.

High resolution light curves were extracted using the alternative `ii_light` tool, because this is not possible with the standard *OSA* tool. The ISDC cookbook recommends the use of `ii_light` to analyze temporal behavior only within one science window. *OSA* builds shadowgrams for each requested energy and time bin to produce the light curves, while `ii_light` makes use of the PIF¹⁰ to create the light curves. This alternative method has been successfully used in Fritz et al. (2006) and Kreykenbohm et al. (2008). The last author performed tests on all public available data of the Crab pulsar up to revolution 464 and checked that `ii_light` produces count rates consistent with those obtained with the standard *OSA* software for sources with an off-axis angle up to 14°. Since A 0535+26 lies in the fully coded field of view in our observations, the use of `ii_light` is justified.

¹⁰PIF: Pixel Illuminated Fraction, number between 0 and 1 that represents the theoretical degree of illumination of each detector pixel for a given source in the sky

CHAPTER 6

The main outburst

In this chapter we present results from the timing and spectral analysis of the observations of A 0535+26 during the August/September 2005 outburst performed with *RXTE* and *INTEGRAL*. These results will be then compared to those obtained during the *pre-outburst flare* in Chapter 7. As we will see, there is observational evidence of a change during the flare compared to the rest of the outburst.

During the data extraction process, an image has been produced for each science window. An *IBIS* mosaic image adding all the science windows is shown in Fig. 6.1, in which A 0535+26 and the Crab can be seen.

6.1 Overview: *RXTE* and *INTEGRAL* light curves

We extracted *INTEGRAL* and *RXTE* light curves of all the A 0535+26 observations. An overview of the outburst is given in Fig. 6.2, which shows the $\sim 3 - 30$ keV *PCA* light curves of the 44 *RXTE* pointed observations, extracted with 128 s resolution [MJD 53608.7–53638.8]. In this chapter we focus on the observations of the source during the *main outburst*. With *main outburst* we refer to all observations except the ones performed during the *pre-outburst flare* [MJD 53610.595–53610.755], as indicated in the figure. *JEM-X* and *IBIS* light curves of the *INTEGRAL* observation [MJD 53613.46–5361989], near the peak of the outburst, are shown in Fig. 6.3. Those light curves have also been extracted with 128 s resolution. The *OMC* light curve of the same *INTEGRAL* observation is also plotted in the figure. A variability in the optical flux is seen during the observation, with short flares with a time scale of the order of 10 ks, and a change in the optical magnitude up to $\Delta V \sim 0.7$. Trunkovsky (1995), from more than ten years of monitoring the optical companion, reported of rapid changes in the optical variability with similar time scales, sometimes correlated with the X-ray pulsar outbursts. The author proposed that such optical variability may be caused by irregular activity of the unstable gaseous envelope around the Be star (see also Lyuty & Zaitseva 2000).

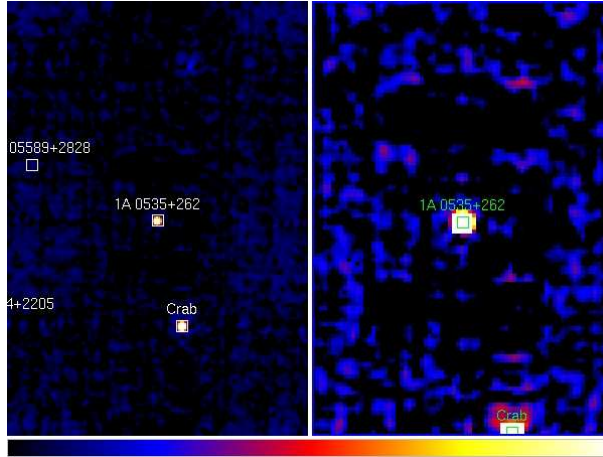


Figure 6.1: 20 – 40 keV *IBIS* mosaic image. Left panel: intensity mosaic image of A 0535+26. The white boxes show the catalog sources. Right panel: significance mosaic image. The green boxes show the detected sources (A 0535+26 and the Crab).

6.2 Pulse period determination

The first step of the analysis is the determination of the pulse period of the neutron star. In the 1975 giant outburst, Rosenberg et al. (1975) discovered pulsations of the neutron star with a period of a $P \sim 104$ s. As seen in Chapter 3, the source shows an overall spin-down trend during quiescence, while during giant outbursts a spin-up has been observed. We determined the pulse period using *INTEGRAL* and *RXTE* data and studied its evolution during the outburst. In Sec. 6.2.1 a first estimate of the pulse period from *INTEGRAL* data using the *epoch folding* technique is given. A more accurate determination of the pulse period using both *INTEGRAL* and *RXTE* data follows in Sec. 6.2.2.

6.2.1 First estimate: epoch folding

The pulse period can be obtained using the *epoch folding* technique, described in Leahy et al. (1983). The basic steps of this method are the following: photon arrival times are barycentric corrected to eliminate the effect of the movement of the satellite around the Earth and the Earth around the Sun. These arrival times are then corrected for the movement of the neutron star on the binary orbit. The light curve is folded with a range of trial periods, and a χ^2 maximization method is applied, calculating the deviation of each profile from a flat distribution. The highest value of χ^2 will give

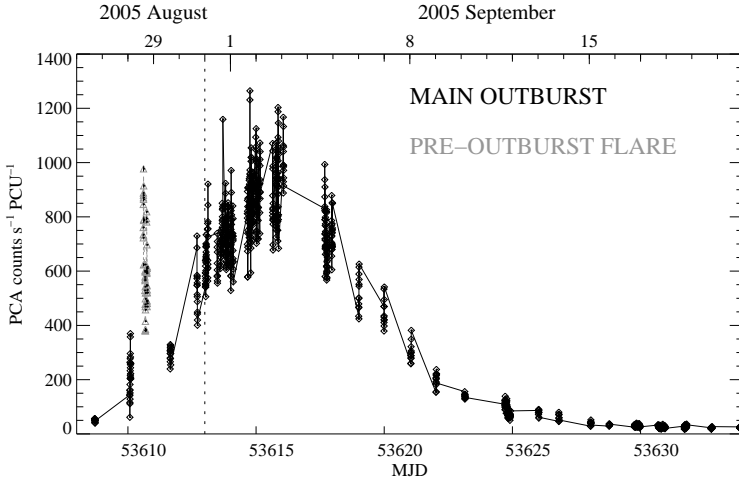


Figure 6.2: *PCA* light curves of all available observations during the August/September 2005 outburst. This chapter is dedicated to the analysis of the *main outburst* (shown in black), while in Chapter 7 a dedicated analysis of the *pre-outburst flare* (gray in the figure) will be presented.

the best estimate for the period.

We applied the epoch folding technique to *IBIS* and *JEM-X* light curves, extracted with $\Delta t = 1$ s time resolution. We performed barycentric correction to the photon arrival times, as well as the binary correction using the updated ephemeris from Finger et al. 2006 (given in Table 3.1). To produce the trial pulse profiles we used 100 different trial periods in the range $P_{\text{trial}} \in [103 - 103.45]$ s and 80 phase bins for the profile. The energy range used for *IBIS* is 25 – 35 keV and 5 – 35 keV for *JEM-X*. The result is shown in Fig. 6.4. As best value for the pulse period we take the maximum of the χ^2 fitted to a Gaussian. The FWHM of the distribution gives an upper limit for the uncertainty, and can be calculated as P^2/t_e approximating the distribution by an isosceles triangle (where P is the best period and t_e the elapsed time). We obtained the following value for the pulse period both with *JEM-X* and *IBIS*: $P = (103.39 \pm 0.05)$ s.

6.2.2 Phase connection method

A more accurate value for the pulse period has been obtained using the *phase connection* method (Fritz et al. 2006, Ferrigno et al. 2007). The first step of the method is to divide the barycentric and binary corrected light curve into intervals, each of them with good enough statistics to reproduce the pulse profile. For each light curve, a

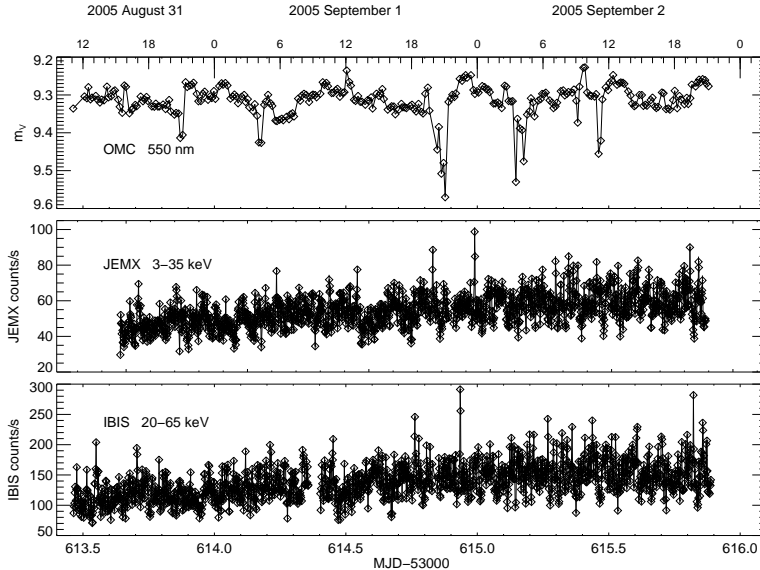


Figure 6.3: *OMC* (top panel), *JEM-X* (middle panel) and *IBIS* (bottom panel) A 0535+26 light curves of the ~ 200 ks *INTEGRAL* observation. The observation was performed shortly before the peak of the outburst.

pulse profile is produced using as first estimate for the period the one obtained from epoch folding. A stable feature of the pulse profile is selected as reference, and this reference phase is converted to absolute pulse arrival time. From the differences of those times for the different pulse profiles, the number of cycles between the different profiles (very close to an integer) can be determined.

The absolute pulse arrival times can be calculated using the following expansion (Lyne & Graham-Smith 1990):

$$T = T_0 + nP + \frac{1}{2}n^2P\dot{P} + \dots \quad (6.1)$$

where n is the number of cycles, P the pulse period, \dot{P} the period derivative and T_0 a reference time. Excluding higher order terms, the values of P and \dot{P} are modified in an iterative process, until the difference between the observed and calculated pulse arrival times is minimized.

The final values of P and \dot{P} are determined by fitting the values of $T - T_0$ vs n to a second order polynomial. The coefficients of the polynomial allow to obtain P and

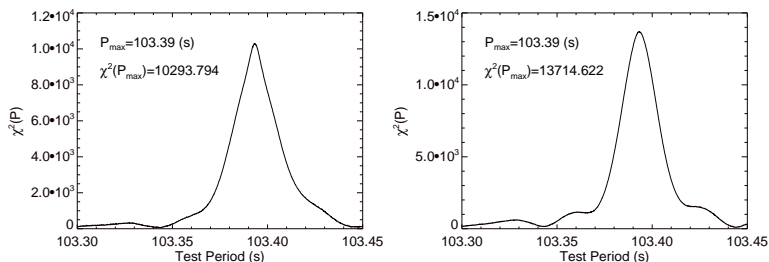


Figure 6.4: χ^2 distributions obtained from epoch folding for *JEM-X* (left panel) and *IBIS* (right panel). The best values for the period and the maximum χ^2 obtained are indicated in the figures.

\dot{P} (comparing with Eq. 6.1) and their correspondent uncertainties.

6.2.2.1 Phase connection with INTEGRAL IBIS

We first applied the *phase connection* method to the *IBIS* data. We extracted the *IBIS* (*ISGRI*) 15 – 60 keV light curve with $\Delta t = 1$ s resolution and divided it into 27 light curves of $t \sim 6$ ks each (grouping every 2 science windows). For each of these light curves we produced a pulse profile, using the period obtained from epoch folding. We then selected a reference phase, and calculated the absolute pulse arrival time of that reference phase. The reference phase used from the pulse profiles is shown in Fig. 6.5 (left panel). We used the mid point of the sharp edge in the pulse profile. We performed a linear fit using the pulse profile data points corresponding to the edge, and determined the mid point. The number of cycles between those reference phases is then counted.

Eq. 6.1 allows to calculate the absolute pulse arrival times using the number of cycles. An iterative process is applied to determine the pulse period. The result is given in Table 6.1. The pulse period evolution of A 0535+26 since its discovery in 1975 until 2005 is shown in Fig. 6.6.

Table 6.1: Pulse period measured with *INTEGRAL IBIS* (*ISGRI*), and formal (non-significant) value for the spin-up.

$P = (103.39315 \pm 0.00005) \text{ s for MJD } 53614.5137$ $\dot{P} = (-3.7 \pm 2.0) \times 10^{-9} \text{ s s}^{-1}$
--

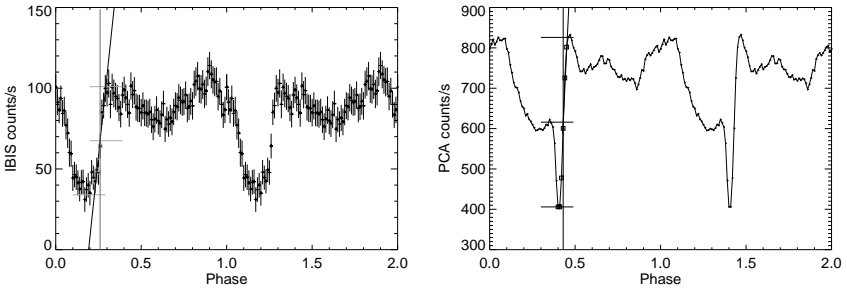


Figure 6.5: Left panel: *IBIS* example pulse profile used in the *phase connection* method. The vertical line crossing the mid-point of the sharp edge indicates the phase used as reference. Right panel: *PCA* example pulse profile. The phase used as reference is also indicated, calculated in the same way as for *IBIS* data.

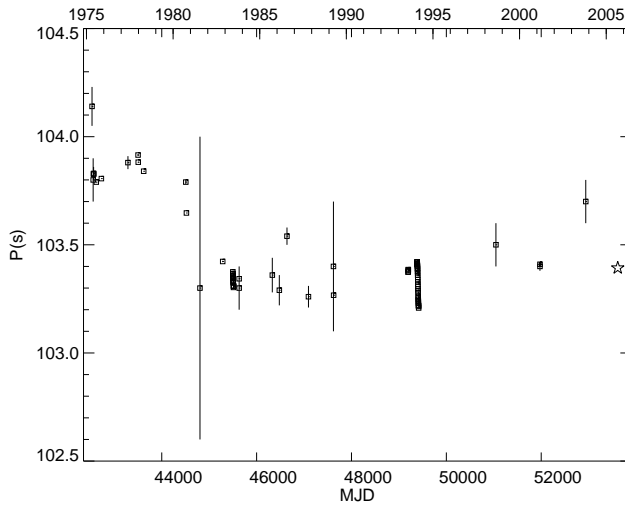


Figure 6.6: Pulse period history of A 0535+26 since its discovery in 1975 until 2005. The last point (star) is our *INTEGRAL IBIS* measurement.

6.2.2.2 Phase connection with *RXTE*

We applied the same method to determine the pulse period using *RXTE* data. For each available observation, we extracted barycentric-corrected *PCA* and *HEXTE*

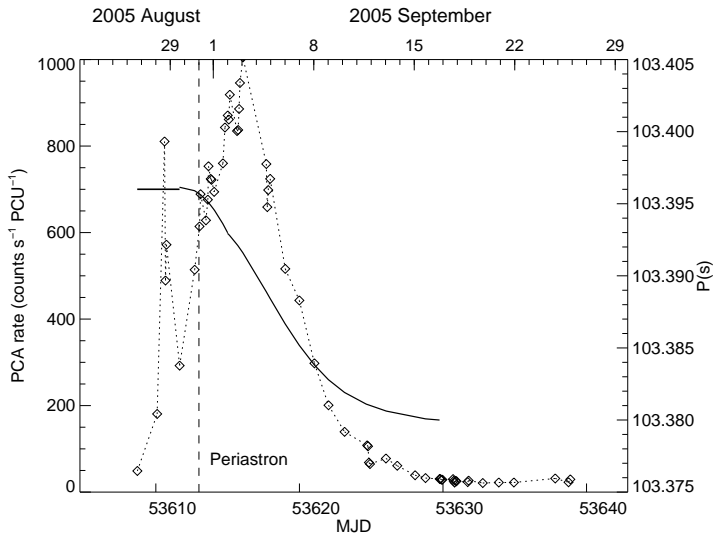


Figure 6.7: The solid line represents the pulse period evolution of A 0535+26 during the outburst (right axis). The diamonds represent the $\sim 3 - 30$ keV PCA mean count rate for each available observation during the August/September 2005 outburst (left axis), and the dotted line connects these points. The mean was obtained averaging each individual light curve. The error bars represent the standard deviation of the distribution for each observation. The vertical dashed line indicates the time of periastron.

light curves and corrected the photon arrival times for the orbital motion. We then produced pulse profiles using as a trial period the one obtained with the *INTEGRAL* observations. For both PCA and *HEXTE* we determined a reference phase in the pulse profiles. As phase reference we selected the midpoint of a sharp edge present in the pulse profiles, an apparently stable feature (see Fig. 6.5 right panel).

The pulse period is approximately constant during the initial pre-outburst flare, and a significant spin-up is measured after periastron. The period evolution after the periastron can be described by a third-order polynomial. The results of the fit are provided in Table 6.2. The period at any time during the outburst is well-described using those functions, and ± 5 ms is a conservative estimate of the uncertainty. It is consistent with the period measured using *INTEGRAL* data within uncertainties. The function describing the period evolution is plotted in Fig. 6.7. It should be noted that the sharp change of the pulse period at periastron is an artificial feature of the model used, the real transition is smoother. The best values obtained for the pulse period are given in Appendix B.

Table 6.2: Formal function describing the pulse period evolution during the outburst. The reference for the third order polynomial fit is MJD 53618. From MJD 53629 on the period is essentially constant.

MJD	53608.70 – 53613	53613 – 53629
$P(\text{s})$	103.3960(5)	103.3883(5)
$\dot{P}(10^{-8}\text{s/s})$	-	-1.69(4)
$\ddot{P}(10^{-14}\text{s/s}^2)$	-	0.9(3)
$d^3P/dt^3(10^{-20}\text{s/s}^3)$	-	2.5(9)

6.3 Pulse profiles

Applying the measured pulse period and its derivatives to fold light curves, we studied the energy dependent pulse profiles both with *INTEGRAL* and *RXTE*. Fig. 6.8 shows the pulse profiles obtained with *JEM-X* and *IBIS* (left panel) and *PCA* and *HEXTE* (right panel), from ~ 3 keV to up to 200 keV. Two pulse cycles are shown for clarity. The *RXTE* observation was performed relatively near to the *INTEGRAL* observation, at a similar luminosity level, and the energy dependent pulse profiles with *INTEGRAL* and *RXTE* as expected do not show significant differences. Similar to other accreting pulsars, the source shows a complex profile in the low energy range ($\sim 2 - 20$ keV). A simpler double-peak profile is observed from $E \sim 20$ keV to $E \sim 45$ keV. At higher energies the second peak is significantly reduced. The source is observed to pulsate up to $E \sim 120$ keV, while above $E \sim 120$ keV no modulation is detected.

We also studied the *RXTE* pulse profile evolution during the outburst. A selection of pulse profiles at different luminosity levels during the outburst has been made, and several similar observations have been grouped to increase the statistics. An overview of the evolution of the energy dependent pulse profiles during the outburst is given in Fig. 6.9. The pulse profiles during the main part of the outburst do not show dramatic differences. They do show some differences (e.g. between phases 0.8–1 between groups 2 and 3 in Fig. 6.9), but they evolve slowly remaining very similar for days. The individual pulse profiles of the 44 *RXTE* pointed observations are shown in Appendix C.

We wish however to mention that the light curve presents a strong pulse to pulse variation, which disappears when averaging over several pulses. This can be seen in Fig. 6.10, where the *PCA* light curve is shown overplotted with the pulse profile for several cycles.

The pulsed fraction from a pulse profile in a given energy range is defined as:

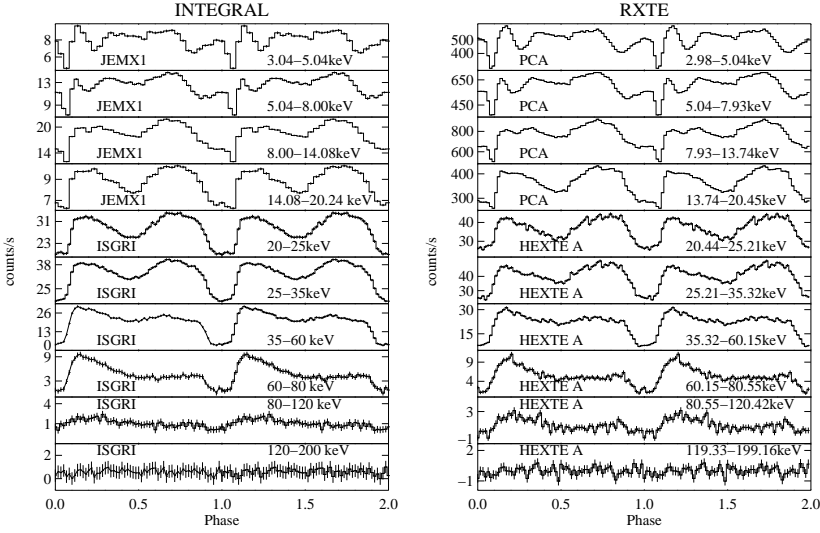


Figure 6.8: Left panel: *JEM-X1* and *IBIS (ISGRI)* energy dependent pulse profiles. The reference time for the folding is MJD 53613.461. Right panel: *PCA* and *HEXTE* energy dependent pulse profiles (corresponding to observation 16 in Appendix A). The reference time is MJD 53614.663.

$$PF = \frac{F_{\max} - F_{\min}}{F_{\max} + F_{\min}}, \quad (6.2)$$

where F_{\max} and F_{\min} are the maximum and minimum values of the flux in the pulse profile.

The pulsed fraction of A0535+26 as a function of the energy using *PCA* and *HEXTE* data has been calculated. As an example, the pulsed fraction for one *RXTE* observation using all phases is shown in Fig. 6.11 (left panel). Above $E \sim 20$ keV the pulsed fraction increases with the energy. However, a decrease of the pulsed fraction with increasing energy below $E \sim 20$ keV is observed. At low energies, the photospheric absorption plays an important role. We have recalculated the pulsed fraction removing the phases corresponding to the sharp dip present in the low energy pulse profiles (phases 0.05–0.15 in the right panel of Fig. 6.8). As can be seen in Fig. 6.11 (left panel), the decrease of the pulsed fraction with increasing energy is caused by this sharp dip. The dip, which is an extremely stable feature along the whole outburst, can be due to a strong absorption, and is responsible for the change

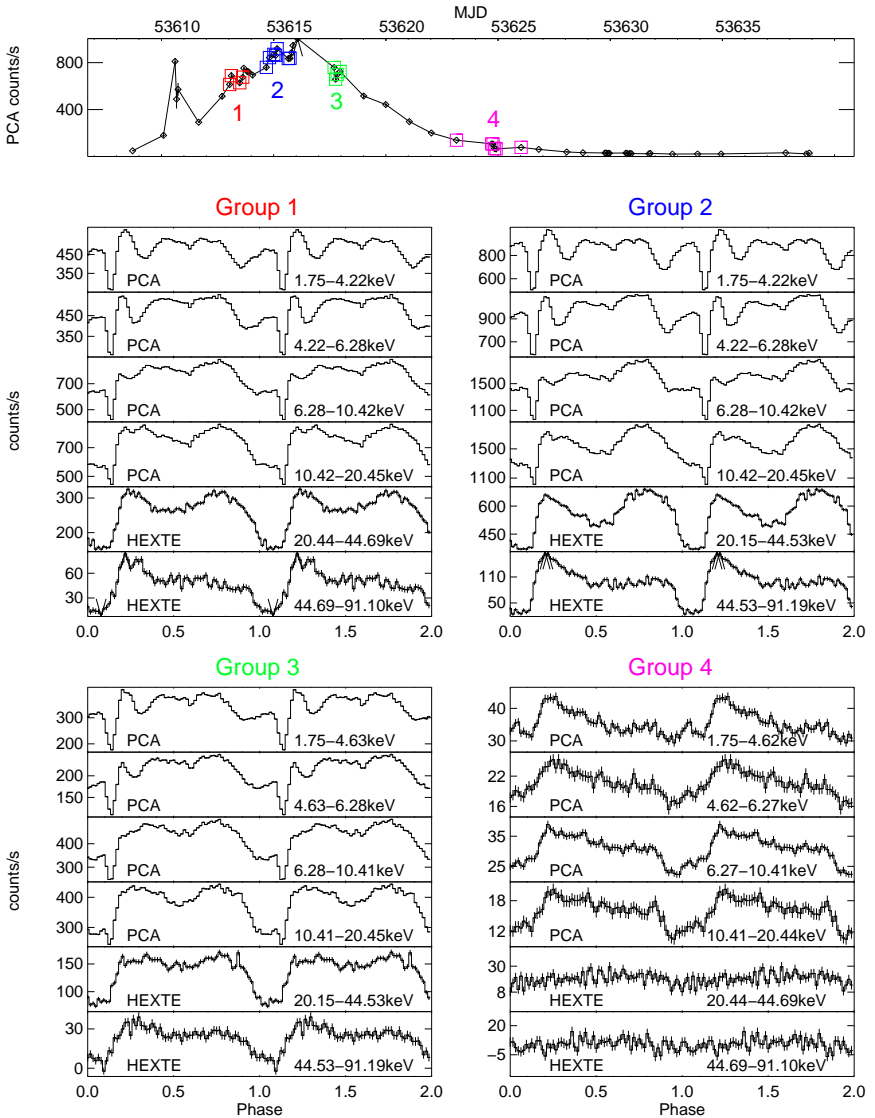


Figure 6.9: *PCA* and *HEXTE* energy dependent pulse profiles at four different luminosity levels during the August/September 2005 normal outburst. The upper panel contains the *PCA* light curve, and the different observations that have been grouped are labeled. The four panels below the light curve show the pulse profiles for the different groups. (Groups 1,2,3,4 correspond to observations 7–10, 16–21, 26–29 and 34–39 from Appendix A respectively).

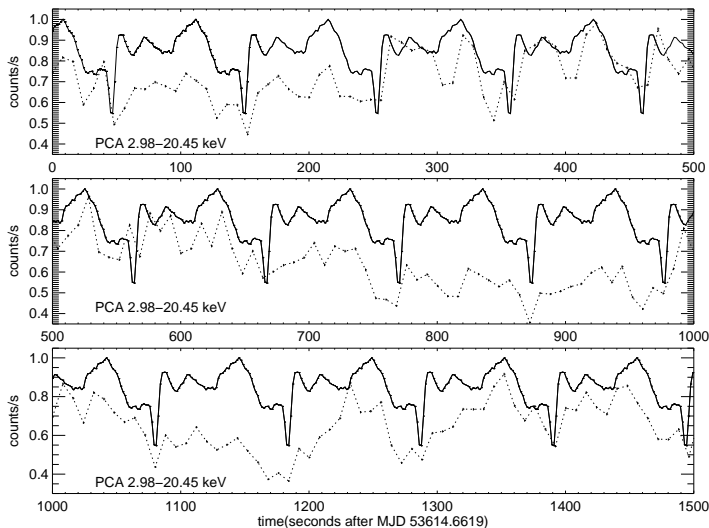


Figure 6.10: Pulse to pulse variation of A 0535+26. The dashed line represents the *PCA* light curve, and the solid line represents the pulse profile obtained in the same energy range.

in the pulsed fraction evolution. However, even with the exclusion of this dip there is still a slight decrease of the pulsed fraction with increasing energies for energies below $E \approx 5$ keV. We explored this behavior in the phase resolved spectra (see Section 6.4.3).

The evolution of the pulsed fraction during the outburst, and therefore its evolution with the luminosity, has also been studied. For this purpose two energy bands have been selected: 5 – 20 keV (*PCA* data) and 20 – 40.8 keV (*HEXTE* data). The pulsed fraction evolution during the outburst is plotted in the right panel of Fig. 6.11. During the rise to the peak of the outburst, the pulsed fraction presents a scatter in both energy ranges, and no correlation between the pulsed fraction and the luminosity is seen. On the other hand, during the decay of the outburst the 5 – 20 keV pulsed fraction increases with decreasing luminosity. This correlation can not be assessed with the *HEXTE* data because at lower luminosities and higher energies the uncertainties become too large.

During the giant outburst in 1994, quasi periodic oscillations were found, confirming the presence of an accretion disk. Apart from the pulse period and its harmonics,

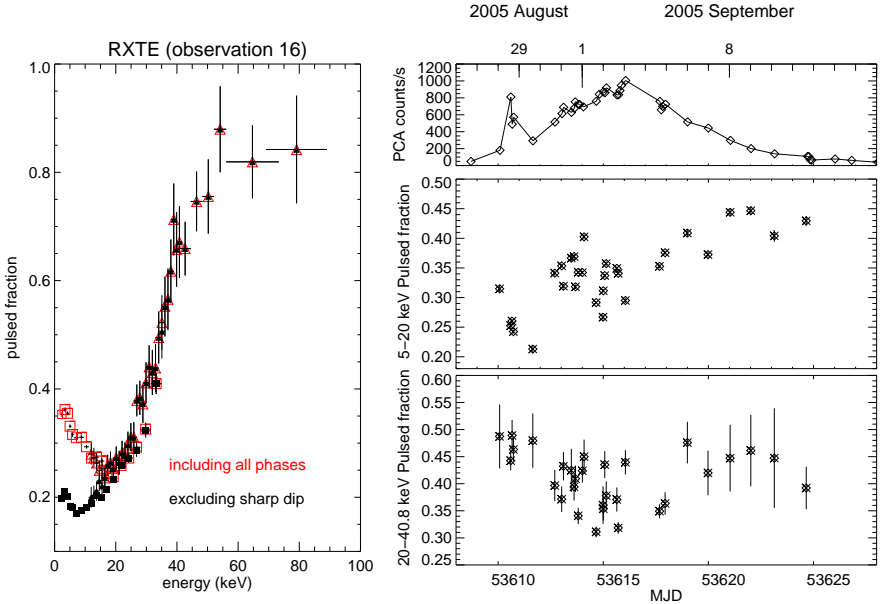


Figure 6.11: Left panel: A 0535+26 pulsed fraction as a function of the energy for *RXTE* (observation 16 from Appendix A). Squares represent *PCA* data and triangles *HEXTE* data. The red hollow data points represent the pulsed fraction calculated using all phases. The solid black data points represent the pulsed fraction calculated excluding the phases of the sharp *dip* in the pulse profile (see text). Right panel: pulsed fraction evolution during the outburst. The upper panel shows the *PCA* light curve. The middle panel shows the 5–20 keV *PCA* pulsed fraction, and the lower panel shows the 20–40.8 keV *HEXTE* pulsed fraction.

we found no QPO-like features in the power spectrum of the August/September 2005 normal outburst (see Fig. 6.12).

6.4 Spectral analysis

X-ray spectra of A 0535+26 have been extracted for *RXTE* and *INTEGRAL*. Both instruments allow to perform broad band spectroscopy, for energies from a few keV up to ~ 200 keV.

In accreting X-ray pulsars, the continuum spectrum is typically modeled with a

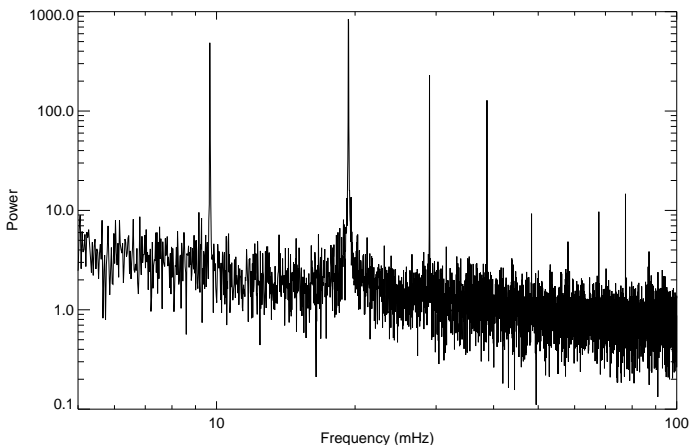


Figure 6.12: A0535+26 power spectrum from *IBIS* light curve. A strong peak at the pulsar spin-frequency $\nu = 1/P \sim 9.6$ mHz (and harmonics of the frequency) is seen. We find no evidence for QPOs.

power law with a cutoff at higher energies. The cutoff for most accreting pulsars lies in the 5 – 25 keV range, and the power law index is in most of the cases $\alpha \lesssim 1.5$ (Coburn et al. 2002, see also Sec. 2.2.4 in Chap. 2). The continuum can be modified by a Fe fluorescence line at 6.4 keV, and as seen in Chapter 2 (Sect. 2.2.6) cyclotron absorption lines modify the continuum of some accreting X-ray pulsars.

The most common functions to phenomenologically model the continuum of accreting X-ray pulsars are the following: (the names of the models and parameters as are those used in *XSPEC*).

Powerlaw with an exponential cutoff, `cutoffpl`:

$$F(E) = KE^{-\alpha}e^{-E/E_{\text{fold}}} \quad (6.3)$$

where K is the powerlaw normalization, α the photon index and E_{fold} the folding energy.

Powerlaw with a high energy cutoff, `highcut`:

$$F(E) = \begin{cases} KE^{-\alpha} & E < E_{\text{cut}} \\ KE^{-\alpha}e^{(E_{\text{cut}}-E)/\beta} & E > E_{\text{cut}} \end{cases}$$

where K is the normalization, α the photon index, β the folding energy and E_{cut} the cutoff energy. This function has a discontinuity in the first derivative at $E = E_{\text{cut}}$ that can produce a line-like feature in the residuals at $E \sim E_{\text{cut}}$. This is usually solved adding a Gaussian line in absorption at $E = E_{\text{cut}}$ (e.g. `mplcut` in Coburn et al. 2002) or adding a smoothing function around the cutoff energy (Burderi et al. 2000).

Negative positive exponential `npex` (Mihara 1995):

$$F(E) = (A_1 E^{-\alpha_1} + A_2 E^{+\alpha_2}) e^{-E/kT} \quad (6.4)$$

Powerlaw with Fermi-Dirac cutoff `fdcut` (Tanaka 1986):

$$F(E) = A E^{-\alpha} \frac{1}{1 + e^{(E - E_{\text{cut}})/E_{\text{fold}}}} \quad (6.5)$$

We tried the above models to fit the X-ray continuum of A 0535+26, and we selected the `cutoffpl`, because it is the simplest model that reproduces the data well. We included in the model a fluorescence Fe line at 6.4 keV modeled with a Gaussian line. The line results do not depend strongly on the model for the continuum chosen.

6.4.1 Cyclotron lines

Both in *INTEGRAL* and *RXTE* two strong absorption features are present in the residuals at energies around $E \sim 46$ keV and $E \sim 102$ keV, interpreted as cyclotron resonance scattering features (fundamental and first harmonic). To model the absorption features, we used a Gaussian optical depth profile, which modifies the continuum in the following way:

$$F(\text{transmitted flux}) = F(\text{intrinsic}) \times e^{-\tau(E)}, \quad (6.6)$$

with

$$\tau(E) = \tau_c e^{-(E - E_c)^2 / (2\sigma_c^2)} \quad (6.7)$$

where E_{cyc} is the energy of the cyclotron resonance, τ_c is the optical depth at the resonance energy and σ_c is the width (Coburn et al. 2002).

The fit of *INTEGRAL* data without including absorption lines in the model gives a $\chi_{\text{red}}^2 = 26.7/255$ dof. After the inclusion of a line at $E \sim 46$ keV, χ_{red}^2 improves to 1.98/222 dof. The improvement of the fit when including a second line at $E \sim 102$ keV is less dramatic, but the χ_{red}^2 is further reduced to 1.39/219 dof. The best fit parameters including two absorption lines are given in Table 6.3.

We performed a spectral analysis of all the available *RXTE* observations, for energies above 5 keV. Using data below 5 keV, the *RXTE* data is compatible with a black body component at $k_B T \sim 1.2$ keV. However, due to a feature in the residuals around ~ 4.7 keV (instrumental xenon L edge, see Rothschild et al. 2006), we

Table 6.3: Best fit parameters for *INTEGRAL* and *RXTE* data. *RXTE* observation is observation 16 from Appendix A. Errors are 90% confidence for one parameter of interest.

	<i>INTEGRAL</i>	<i>RXTE</i>
α	$0.66^{+0.03}_{-0.02}$	$0.55^{+0.02}_{-0.02}$
$E_{\text{fold}}(\text{keV})$	$17.5^{+0.2}_{-0.2}$	$17.7^{+0.3}_{-0.3}$
$E_{\text{cyc},1}(\text{keV})$	$45.9^{+0.3}_{-0.3}$	$46.1^{+0.4}_{-0.5}$
$\sigma_{\text{cyc},1}(\text{keV})$	$9.0^{+0.3}_{-0.3}$	$10.3^{+0.5}_{-0.5}$
$\tau_{\text{cyc},1}$	$0.40^{+0.01}_{-0.01}$	$0.48^{+0.02}_{-0.02}$
$E_{\text{cyc},2}(\text{keV})$	102^{+4}_{-3}	102^{+4}_{-3}
$\sigma_2(\text{keV})$	8^{+2}_{-2}	8^{+3}_{-3}
τ_2	$1.1^{+0.4}_{-0.3}$	$1.0^{+0.4}_{-0.3}$
$\chi^2_{\text{red}}/\text{dof}$	1.40/219	1.10/211
$\text{Flux}_{(20-50)\text{keV}}(\text{erg cm}^{-2}\text{ s}^{-1})$	$(5.848^{+0.007}_{-0.016}) \times 10^{-9}$	$(6.042^{+0.017}_{-0.003}) \times 10^{-9}$

excluded data for energies below 5 keV in our analysis. For the observations with higher flux and good statistics, two Gaussian absorption lines at $E_1 \sim 46$ keV and $E_2 \sim 102$ keV were necessary in the model. In some of the observations only one line at $E_1 \sim 46$ keV was included in the model. For the low luminosity observations during the decay of the outburst no absorption lines were added to the model. As an example, for *RXTE* observation 16 from Appendix A, the fit to the data with no absorption lines in the model gives a $\chi^2_{\text{red}} = 13.8/217$ dof. Including one absorption line at ~ 46 keV improves the fit to $\chi^2_{\text{red}} = 1.14/214$ dof, and including a second line at ~ 102 keV further reduces the χ^2_{red} to 1.10/211 dof. In Table 6.3 the best fit parameters of this *RXTE* observation, performed at a similar luminosity level than the *INTEGRAL* observation, are given. The best fit parameters for all the other *RXTE* observations are given in the Appendix D.

In Fig. 6.13 *INTEGRAL* and *RXTE* spectra are shown. The upper panel includes the data plus model, and the lower panels show the residuals from a fit without including absorption lines, including one line and including two lines.

In order to evaluate if the absorption features detected in the residuals are real or an artifact of the model used, we calculated the energy of the resonance adopting the different models for the continuum defined above. The best fit parameters for the cyclotron line using the different models are given in Table 6.4, and allow to confirm that the cyclotron line energy is model independent.

The ratio between the pulse phase averaged centroid energies $E_{\text{cyc},2} : E_{\text{cyc},1}$, calculated using the *INTEGRAL* values, is $2.23 \pm 0.04 : 1$ (at 68% confidence level).

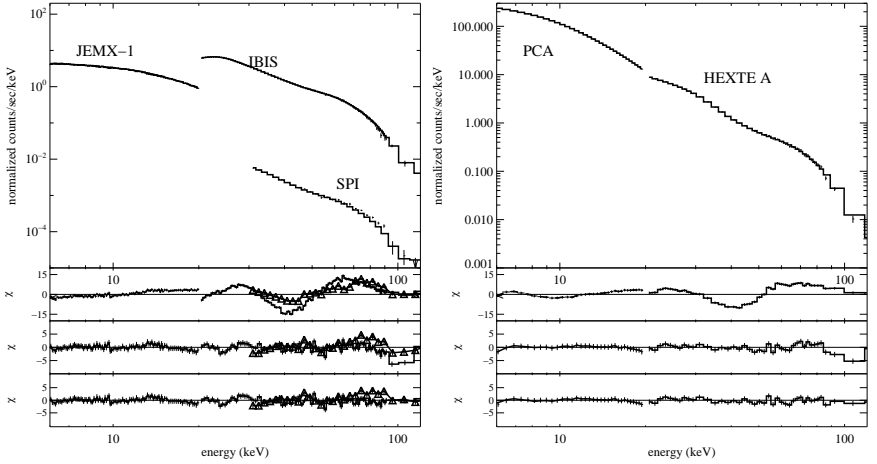


Figure 6.13: *INTEGRAL* (left panel) and *RXTE* (right panel) phase average spectra. In both figures the upper panel shows the data plus model. The three lower panels show, from top to bottom, the residuals of a fit without absorption lines, including one absorption line at $E \sim 46$ keV and including two absorption lines at $E \sim 46$ keV and $E \sim 102$ keV.

From the values obtained of the cyclotron energy, it is possible to estimate the magnetic field (see Chapter 2, Sec. 2.2.6). Taking into account the gravitational redshift, the cyclotron energy (and magnetic field) will be shifted to a higher position. In Table 6.5 the magnetic field derived from the cyclotron energy measured with *INTEGRAL* for different values of the gravitational redshift $z=0$, $z=0.19$ (assuming $R = 14$ km, $M = 1.4 M_{\odot}$) and $z=0.3$ (assuming $R = 10$ km, $M = 1.4 M_{\odot}$) is given.

The deconvolved spectrum and the best fit model for *INTEGRAL* and *RXTE* data are plotted in Fig. 6.14.

6.4.2 Cyclotron line energy evolution with X-ray luminosity

RXTE monitoring observations have allowed to study the evolution of the spectral parameters during the outburst. Of special interest is the evolution of the cyclotron line energy with the luminosity, since it can reflect variations of the line forming region (see Chapter 2, Section 2.3.1.1).

The centroid energy of the fundamental CRSF versus the X-ray luminosity during the main outburst is shown in Fig. 6.15. The luminosity was calculated assuming a

Table 6.4: Cyclotron line parameters of A 0535+26 using different models for the continuum for *RXTE* observation 16 from Appendix A. The errors are 90 % confidence for one parameter of interest. In this work we adopted the `cutoffpl` model.

	<code>cutoffpl</code>	<code>mplcut</code>	<code>fdcut</code>	<code>npex</code>
$E_{\text{cyc},1}$ (keV)	$46.1^{+0.5}_{-0.5}$	$46.0^{+0.6}_{-0.5}$	$45.9^{+0.5}_{-0.6}$	$46.0^{+0.6}_{-0.6}$
σ_1 (keV)	$10.1^{+0.5}_{-0.5}$	$10.1^{+0.6}_{-0.6}$	$11^{+0.8}_{-0.8}$	$10.0^{+0.5}_{-0.5}$
τ_1	$0.45^{+0.02}_{-0.02}$	$0.46^{+0.03}_{-0.03}$	$0.58^{+0.06}_{-0.07}$	$0.47^{0.02}_{-0.2}$
$E_{\text{cyc},2}$ (keV)	103^{+5}_{-3}	103^{+4}_{-3}	101^{+5}_{-3}	102 (fixed)
σ_2 (keV)	8^{+3}_{-3}	8^{+3}_{-3}	7^{+4}_{-3}	8 (fixed)
τ_2	$1.0^{+0.4}_{-0.3}$	$1.0^{+0.4}_{-0.3}$	$0.9^{+0.5}_{-0.3}$	$1.0^{+0.3}_{-0.2}$
$\chi^2_{\text{red}}/\text{dof}$	1.08/364	1.05/360	1.00/362	1.08/364

Table 6.5: Magnetic field of A 0535+26 derived from the cyclotron line energy measured with *INTEGRAL* using $E_{\text{cyc}}^{\text{obs}} [\text{keV}](1+z) = 11.6B_{12}$ for different values of the gravitational redshift.

	$z = 0$	$z = 0.19$	$z = 0.3$
B (10^{12} G)	~ 3.96	~ 4.71	~ 5.14

distance to the system of $d = 2$ kpc (Steele et al. 1998). Values of the cyclotron line measured from *Suzaku* observations of the declining phase of the outburst (Terada et al. 2006), as well as from a *TTM* & *HEXE* observation of the April 1989 giant outburst (Kendziorra et al. 1994) are included in the figure.

The evolution of the cyclotron line energy and of the continuum parameters (pho-

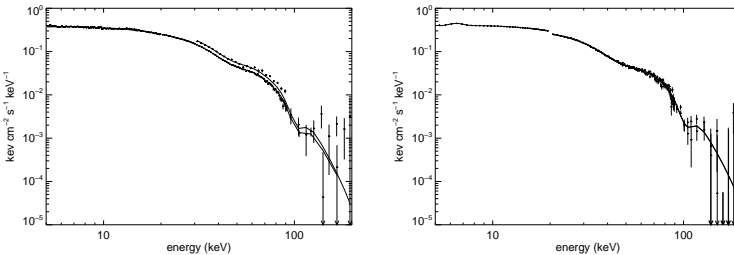


Figure 6.14: Energy unfolded spectrum and model of A 0535+26. Left panel: *INTEGRAL* observation. Right panel: *RXTE* observation 16 from Appendix A.

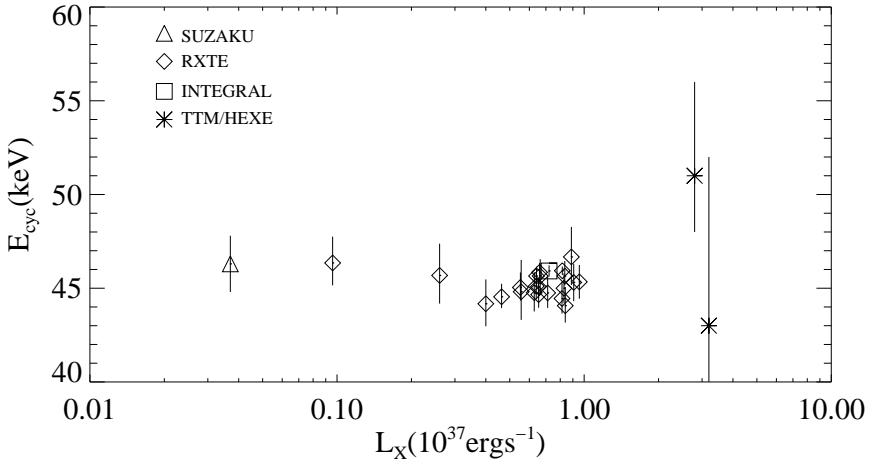


Figure 6.15: Evolution of the energy of the fundamental line in different luminosity states in the 3–50 keV range for our *INTEGRAL* and *RXTE* values. We included data points from *Suzaku* (Terada et al. 2006) from the declining phase of the August/September 2005 outburst and values from *TTM/HEXE* (Kendziorra et al. 1994) from the March/April 1989 giant outburst.

ton index and folding energy) for the observations in which the cyclotron line was detected are plotted in Fig. 6.16. As seen in Fig. 6.15, there is no significant correlation between the cyclotron line energy and the luminosity, with the cyclotron line energy remaining constant within uncertainties during the main outburst. The rise to the peak of the outburst presents a hard, relatively constant spectrum, with $\alpha \sim 0.6$. The decay of the outburst shows a smooth softening of the spectrum, reaching a photon index of $\alpha = 1.00 \pm 0.03$.

6.4.3 Phase resolved spectroscopy

Depending on the rotational phase of a neutron star, the observer looks at the emission region from different angles. Therefore, one would expect the spectral parameters obtained at different rotational phases to differ. We have performed pulse phase resolved spectroscopy for A 0535+26 to study this possible effect. We have extracted *RXTE* spectra for ten phase intervals. The evolution of the spectral parameters as a function of the phase is plotted in Fig. 6.17. In Fig. 6.18, the pulse phase evolution of the centroid energy of the fundamental and first harmonic cyclotron lines is plotted, as well as the ratio between the first harmonic and fundamental cyclotron energies. Table 6.6 contains the best fit values from the phase resolved analysis. The cyclotron

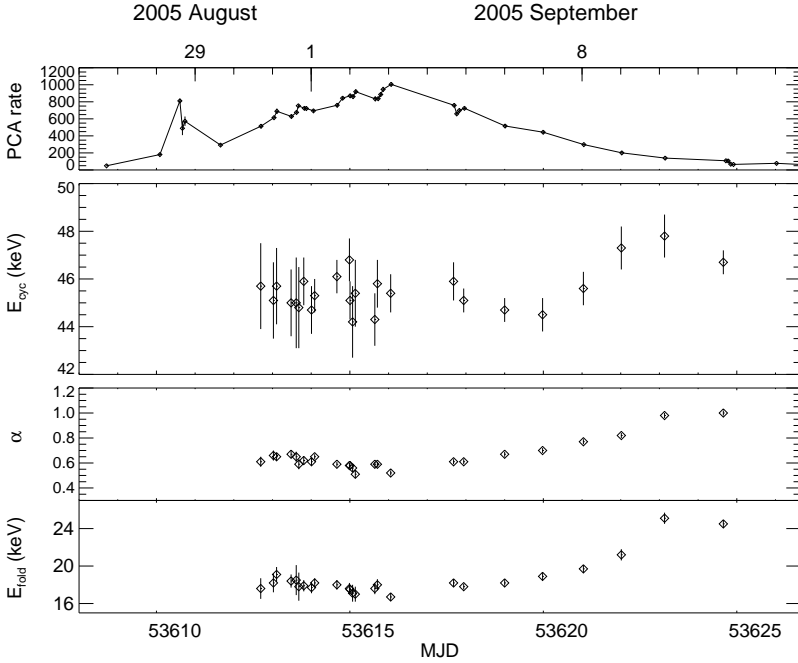


Figure 6.16: Evolution of the cyclotron line energy, photon index and folding energy during the *main outburst*.

line slightly varies with the pulse phase. The centroid energy is smaller during the main peak of the pulse profile (phase interval 0.1 – 0.2) and increases with the phase reaching a maximum in the phase interval 0.5 – 0.6. The separation of the maximum and minimum is ~ 5 keV ($\sim 11\%$). We can conclude that the variation in the cyclotron line energy between the maximum and minimum values is significant at a 5σ level. The ratio between the two cyclotron lines $E_{cyc,2} : E_{cyc,1}$, rather than being constant, presents a variation with the pulse phase, reaching $2.38 \pm 0.05 : 1$ for phase 0.1 – 0.2 compared to $1.95 \pm 0.07 : 1$ (at 68% confidence level) in the phase interval 0.6 – 0.7. The continuum parameters of A 0535+26 show a significant variation within the pulse phase. The photon index reaches a minimum during the main pulse, revealing a harder spectrum.

Table 6.6: Best fit values of phase resolved analysis. The first column (PI) gives the phase interval. The first harmonic width and depth have been fixed to $\sigma_{\text{cyc},2} = 8$ keV and $\tau_{\text{cyc},2} = 1$ respectively. In phase intervals 0.8–0.9 and 0.9–1.0, the first harmonic energy has also been fixed to $E_{\text{cyc},2} = 103$ keV. The uncertainties are 90% confidence for one parameter of interest.

PI	α	E_{fold}	$E_{\text{cyc}(1,2)}$	$\sigma_{\text{cyc}(1,2)}$	$\tau_{\text{cyc}(1,2)}$	$\chi_{\text{red}}^2/\text{dof}$
0.0–0.1	$0.29^{+0.06}_{-0.06}$	$15.2^{+0.5}_{-0.6}$	$44.8^{+1.0}_{-0.9}$ 106^{+7}_{-6}	$11.1^{+1.5}_{-1.1}$ 10	$0.65^{+0.07}_{-0.03}$ 1	1.76/180
0.1–0.2	$0.24^{+0.14}_{-0.02}$	$17.2^{+0.8}_{-1.3}$	$43.3^{+0.9}_{-0.9}$ 103^{+3}_{-3}	$14.5^{+1.0}_{-0.9}$ 10	$0.68^{+0.13}_{-0.04}$ 1	1.29/94
0.2–0.3	$0.60^{+0.03}_{-0.04}$	$19.8^{+0.6}_{-0.6}$	$44.2^{+0.9}_{-0.9}$ 105^{+4}_{-3}	$11.5^{+1.4}_{-1.2}$ 10	$0.50^{+0.05}_{-0.05}$ 1	1.10/197
0.3–0.4	$0.85^{+0.03}_{-0.03}$	$22.5^{+0.7}_{-0.7}$	$45.4^{+1.1}_{-1.0}$ 103^{+3}_{-3}	$10.7^{+1.4}_{-1.2}$ 10	$0.38^{+0.04}_{-0.03}$ 1	1.36/198
0.4–0.5	$0.86^{+0.03}_{-0.03}$	$21.5^{+0.7}_{-0.7}$	$45.9^{+1.3}_{-1.2}$ 103^{+4}_{-4}	$8.5^{+1.5}_{-1.3}$ 10	$0.31^{+0.04}_{-0.04}$ 1	1.42/190
0.5–0.6	$0.70^{+0.03}_{-0.03}$	$18.7^{+0.8}_{-0.7}$	$48.4^{+1.4}_{-1.3}$ 99^{+6}_{-5}	$8.8^{+1.5}_{-1.3}$ 10	$0.35^{+0.05}_{-0.05}$ 1	1.41/175
0.6–0.7	$0.59^{+0.04}_{-0.04}$	$17.3^{+0.8}_{-0.7}$	$48.2^{+1.4}_{-1.3}$ 94^{+6}_{-4}	$8.7^{+1.4}_{-1.3}$ 10	$0.37^{+0.05}_{-0.05}$ 1	1.46/182
0.7–0.8	$0.44^{+0.03}_{-0.03}$	$15.9^{+0.6}_{-0.5}$	$46.5^{+1.2}_{-1.0}$ 102^{+7}_{-5}	$8.6^{+1.2}_{-1.1}$ 10	$0.45^{+0.05}_{-0.05}$ 1	1.25/182
0.8–0.9	$0.37^{+0.03}_{-0.03}$	$15.1^{+0.5}_{-0.5}$	$45.5^{+1.0}_{-0.9}$ 103	$9.1^{+0.9}_{-0.8}$ 10	$0.69^{+0.06}_{-0.06}$ 1	1.36/97
0.9–1.0	$0.27^{+0.12}_{-0.12}$	$11.4^{+1.4}_{-1.1}$	$44.1^{+2.1}_{-1.7}$ 103	$7.2^{+1.8}_{-1.5}$ 10	$0.89^{+0.17}_{-0.15}$ 1	0.98/97

6.5 Discussion of results

6.5.1 Pulse period and pulse profiles

The pulse period of the neutron star appears to be constant during the beginning of the outburst, $P = 103.3960(5)$ s, and a spin-up starts around the periastron, $\dot{P} = (-1.69 \pm 0.04) \times 10^{-8}$ s/s measured at MJD 53618. The pulse period falls exponentially at the end of the outburst. As seen in Chap. 3 (Sec. 3.2.1), a spin-up of $\dot{\nu} \sim 0.6 \times 10^{-11}$ Hz s $^{-1}$ was measured during the June 1983 giant outburst (Sembay

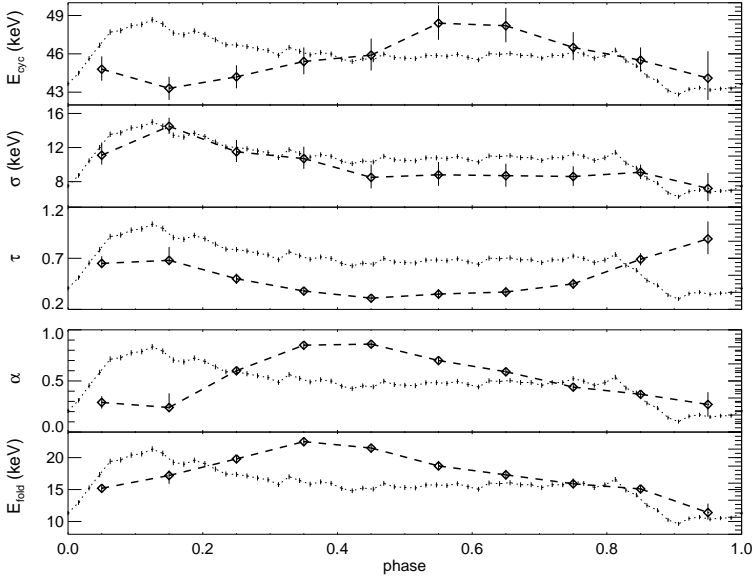


Figure 6.17: Best fit parameters of A 0535+26 as a function of the pulse phase for *RXTE* observation 16 (Appendix A). The diamonds in the first three panels show the evolution of the fundamental cyclotron line parameters energy E_{cyc} , width σ and depth τ as a function of the pulse phase. The diamonds in the two lower panels show the evolution of the continuum parameters as a function of the pulse phase. The dashed line connecting the diamonds is shown to guide the eye. In all panels the dotted line represents the (44.5–80.6) keV *HEXTE* pulse profile. Uncertainties are 90% confidence for one parameter of interest.

et al. 1990), and a spin-up of $\dot{\nu} \sim 1.2 \times 10^{-11} \text{ Hz s}^{-1}$ was measured during the 1994 giant outburst (Finger et al. 1996). In this work, a spin-up has been measured for the first time during a normal outburst of A 0535+26, giving evidence for the presence of an accretion disk.

Energy dependent pulse profiles of A 0535+26 during the *main outburst* were analyzed. We find very complex shape of the pulse profiles for energies below $E \sim 20$ keV. A simpler double peak profile is observed from $E \sim 20$ keV to $E \sim 45$ keV, while at higher energies one of the peaks is significantly reduced. The source is observed to pulsate up to $E \sim 120$ keV, while above $E \sim 120$ keV no modulation is

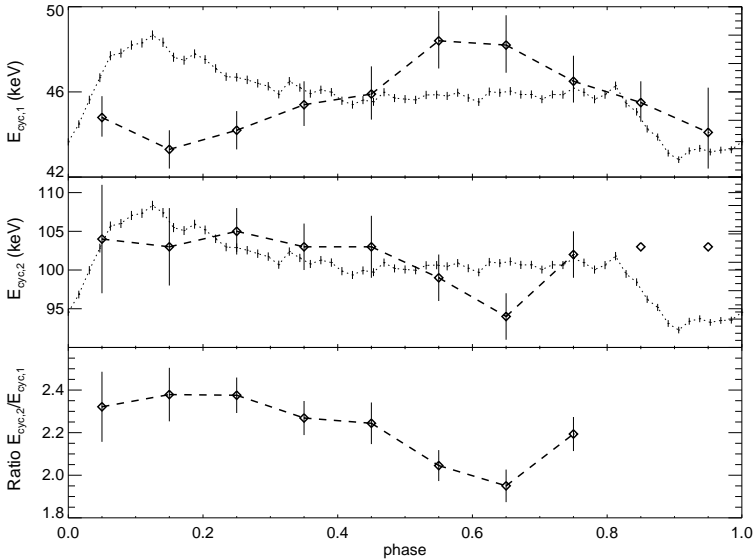


Figure 6.18: Best fit values of the cyclotron line energy as a function of the pulse phase: fundamental (top panel) and first harmonic (middle panel), represented with diamonds. Values for *RXTE* observation 16 (same as in Fig. 6.17). The bottom panel represents the ratio between the first harmonic and fundamental cyclotron energies, $E_{\text{cyc},2}/E_{\text{cyc},1}$. The dashed line connecting the diamonds is shown to guide the eye. The dotted line represents the (44.5 – 80.6) keV *HEXTE* pulse profile. The uncertainties are 90% confidence for one parameter of interest.

detected. A dedicated analysis of the energy dependent pulse profiles will be presented in Chap. 8. On average, the energy dependent pulse profiles obtained during the August/September 2005 normal outburst show basic features very similar to those observed in past giant outbursts in 1980 (Frontera et al. 1985), 1989 (Kendziorra et al. 1994) and 1994 (Bildsten et al. 1997), as can be seen comparing Fig. 3.3 with Fig. 6.8. This suggests that the basic mechanisms and geometry of the accretion remains stable for the source.

A strong pulse to pulse variability is however seen in A 0535+26 (see Fig. 6.10). Strong pulse to pulse variation, giving on average stable pulse profiles, was already observed for A 0535+26 in past outbursts (Frontera et al. 1985, Kretschmar 1996),

as well as for other accreting X-ray pulsars, like Vela X-1 (Staubert et al. 1980), and GX 1+4 (Elsner et al. 1985). For GX 1+4, the authors suggest that the variability might be caused by time-variable processes occurring in the neutron star magnetosphere, away from the region of the pulse formation. Plasma sheets, filaments and blobs of matter may penetrate deep into the magnetosphere away from the polar regions (Elsner & Lamb 1976), causing the variations seen from pulse to pulse. But this could also be explained with changes in the physical conditions at the base of the accretion column, resulting from variations in the accretion flow. The mechanism causing the variability in the single pulses, in contrast to the stable pulse profile shapes, is up to date highly unknown.

As seen in Fig. 6.11 (left panel), for energies above $E \sim 20$ keV the pulsed fraction is found to increase with the energy. The increase of the pulsed fraction with the energy is a known feature in accreting pulsars (see e.g. White et al. 1983). It was already reported for A 0535+26 in Frontera et al. (1985), as well as for 4U 0115+64 in Tsygankov et al. (2007), GX 1+4 (Ferrigno et al. 2007), OAO 1657-415 (Barnstedt et al. 2008), EXO 2030+375 (Klochkov et al. 2008a), and for a selection of other accreting pulsars in Lutovinov & Tsygankov (2008). These last authors propose that the increase of the pulsed fraction with the energy is caused by the fact the harder photons are emitted closer to the neutron star surface, and this region can be obscured during certain rotational phases.

For A 0535+26, we have found a decrease of the pulsed fraction with increasing energies in the $\sim (3 - 20)$ keV range. To our knowledge, this is the first time that a decrease of the pulsed fraction with the energy for an accreting X-ray pulsar is reported. The pulsed fraction of 4U 0115+64 was calculated down to $E \sim 3$ keV in Tsygankov et al. (2007), and it was found to increase with the energy at all energies. As seen in Sec. 6.3, the decrease is mainly caused by the sharp dip present in the pulse profiles at low energies (see left panel of Fig. 6.11). This was explored with phase resolved spectroscopy (Sec. 6.4.3). We would have expected a stronger absorption in the phases around the sharp dip. However, no absorption was present in the low energy spectra. It should be noted however that due to the instrumental xenon L edge, it is difficult to model the spectrum below 5 keV, and we have excluded data below 5 keV in the analysis.

During the rise to the peak of the outburst a scatter of the pulsed fraction, showing no correlation with the X-ray luminosity, is observed. A possible interpretation will be given in Chapter 7, motivated by the findings related to the *pre-outburst flare*.

During the decay of the outburst, however, there is a correlation between the pulsed fraction and the X-ray luminosity. As the luminosity decreases, the pulsed fraction increases. The evolution of the pulsed fraction of 4U 0115+64 with the luminosity was presented in Tsygankov et al. (2007), where a decrease of the pulsed fraction with increasing luminosity was reported. The authors explain it with the fact that the geo-

metrical size of the emission region increases with the luminosity (or accretion rate), and therefore the pulsations are smeared out at higher luminosities. This trend is seen in A 0535+26 during the decay of the outburst. As the accretion rate decreases, the size of the emitting region becomes smaller, causing the pulsed fraction to increase, since the emission region can be obscured during a larger fraction of the rotational phase.

6.5.2 Cyclotron lines

Our observations have allowed to confirm the presence of the fundamental cyclotron line at $E_{\text{cyc},1} \sim 46$ keV, with the first harmonic at $E_{\text{cyc},2} \sim 102$ keV. As seen in Chap. 2, cyclotron lines are the *only* direct way to measure the neutron star magnetic field. We find a magnetic field of the order of $B \sim 5 \times 10^{12}$ G for A 0535+26. We find a ratio between the measured pulse phase averaged centroids $E_{\text{cyc},2}$, $E_{\text{cyc},1}$ of $2.23 \pm 0.04 : 1$, that deviates from the harmonic relation. A non-harmonic ratio has been found between the fundamental and the harmonics in other sources (in 4U 0115+64, Santangelo et al. 1999b, and marginally in Vela X-1, Kreykenbohm et al. 2002). A non-harmonic ratio is actually expected when introducing relativistic corrections (Eq. 2.33), but this effect is very small, and in any case the expected spacing is smaller than the harmonic one. The effect of higher ratios in cyclotron lines was studied by Nishimura (2005), who proposed that the deviations from the harmonic ratio originate in a magnetic field that varies significantly in the line forming region. This is still a debated topic under investigation (see e.g. Schönherr et al. 2007).

The evolution of the cyclotron line energy with the X-ray luminosity has been studied, in the context of the recent findings by Tsygankov et al. (2007) and Staubert et al. (2007). A review of these results, in agreement with the theory developed by Basko & Sunyaev (1976), was given in Sec. 2.3.1.1. To briefly summarize, for some sources (for instance V 0332+53) a negative correlation between the cyclotron line energy and the X-ray luminosity has been found. On the other hand, for Her X-1 a positive correlation between the cyclotron line energy and the X-ray luminosity exists (Staubert et al. 2007). This has been interpreted with a change of the height of the line forming region with the X-ray luminosity, with a different behavior for sub- and super-Eddington regimes. In the case of A 0535+26, considering all our values from *RXTE* and *INTEGRAL*, as well as *Suzaku* (Terada et al. 2006) and *TTM & HEXE* (Kendziorra et al. 1994), no correlation is detected, suggesting that the line forming region does not vary with the luminosity of the system. The absence of a negative correlation between the cyclotron line energy and the luminosity, together with the fact that all the measurements have been performed at low luminosities $L_{(3-50)\text{ keV}} \lesssim 10^{37} \text{ erg s}^{-1}$ (except the *HEXE* data, for which the too large uncertainties do not allow to distinguish any positive or negative correlation) suggests that A 0535+26 is in the sub-Eddington regime. It will be interesting to observe A 0535+26 during a giant

outburst with the present generation of X-ray satellites, to study the behavior of the cyclotron line energy at higher luminosities.

We have studied the behavior of the cyclotron line energy as a function of the pulse phase. Due to the rotation of the neutron star, the observer sees the emission region under different angles. Therefore, a variation of the cyclotron line parameters is expected to emerge with the pulse phase, as seen in line profile simulations (Araya & Harding 1999, Araya-Góchez & Harding 2000, Schönherr et al. 2007). This is actually what has been observed for a number of sources, like Her X-1, Vela X-1, 4U 0115+64 or GX 301-2 (see for instance Klochkov et al. 2008b, La Barbera et al. 2003, Mihara et al. 2004, Kreykenbohm et al. 2004 and reviews from Santangelo et al. 1999a and Heindl et al. 2004). On the other hand, for V 0332+53 no significant variation of the cyclotron line energy with the pulse phase was found, and a relatively simple accretion geometry was suggested to explain this effect (Pottschmidt et al. 2005).

Compared to most of the above reported sources, for A 0535+26 we have found a less dramatic variation of the cyclotron line energy with the pulse phase. The cyclotron line energy is lower during the main peak of the pulse profile, $E = 43_{-0.9}^{+0.9}$ keV and about half a pulse phase later reaches $E = 48.2_{-1.3}^{+1.4}$ keV (at 90% confidence), implying a lower magnetic field during the main peak of the pulse profile. This can be qualitatively explained with the following picture. We consider the formation of a “fan beam” pattern in the source during the main part of the outburst, and assume that the main peak of the profile corresponds to the instant when the observer looks directly along the accretion column (evidence for this will be discussed in Chapter 7). Assuming that a radiative shock has formed in the column at a certain height from the neutron star surface, the magnetic field is expected to be lower during the main peak of the profile, since due to the higher optical depth in the shock, we can’t look deep into the accretion column. However, about half a pulse phase later, we look at the column from one side, and therefore we can observe closer to the neutron star surface, explaining the higher cyclotron line measured.

Due to the angle dependence of the scattering cross-sections (Harding & Lai 2006, discussed in more detail in Chapter 7, see Eqs. 7.7, 7.8 and Fig. 7.11), harder photons, originated closer to the polar cap, escape more effectively in the direction parallel to the magnetic field. This can explain the hardening we observe in the main peak of the pulse profile. A hardening of the spectrum during the main peak of the pulse profile has also been observed for Her X-1. In this case however the evolution of the cyclotron line with the pulse phase is different, probably due to the “pencil beam” pattern believed to exist for this source (Klochkov et al. 2008b).

However we would like to mention that one has to be careful when interpreting the results from phase resolved spectroscopy. As seen in Sec. 2.3.2 (in Chap. 3), relativistic light deflection plays an important role in the emission a distant observer

sees from a neutron star (see Fig. 2.23). Therefore, in every rotational phase we can be seeing emission from both magnetic poles. This mixing of the components of both magnetic poles makes the interpretation of phase resolved spectroscopy not a straightforward task.

6.5.3 Torque theory and spin-up.

We have obtained a value for the magnetic field of A 0535+26 of $B \sim 5 \times 10^{12}$ G, using the fundamental cyclotron line measured in the X-ray spectrum. It is possible to test the theory of accretion by estimating the magnetic field derived from it. According to the theory of accretion, (see Sec. 2.2.1), fluctuations in the mass accretion rate produce fluctuations in the accretion luminosity and in the accretion torque. The theory of accretion (Ghosh & Lamb 1978, revisited in Lovelace et al. 1995, Wang 1996 or Wang 1997), predicts the following relation between the X-ray flux F_X (or X-ray luminosity $L_X = 4\pi d^2 F_X$) and the spin-up, already discussed in Chapter 2 (Eq. 2.28):

$$-\dot{P} = 5.0 \times 10^{-5} \mu_{30}^{2/7} n(\omega_s) S_1(M) (PL_{37}^{3/7})^2 (\text{s yr}^{-1}), \quad (6.8)$$

(see Sec. 2.2.1 for the meaning of the different terms in the above expression).

Fitting observed values of spin-up as a function of the X-ray flux to Eq. 6.8 allows to estimate the dipole magnetic moment μ and the distance d to the source (method described in Popov 2000, based on Lipunov et al. 1992).

We have applied this method to A 0535+26, using the values obtained for the spin-up (Sec. 6.2.2.2). For A 0535+26, a relation between the spin-up and the X-ray flux during a giant outburst was already reported in Finger et al. (1996). However, our 2005 *RXTE* observations provide the first evidence for a spin-up during a normal outburst.

The spin-up at different times during the outburst has been calculated approximating every four successive values of P with a straight line, and we have derived the flux from the spectra for these different times. We have fitted our data to Eq. 6.8, leaving as free parameters the distance and the magnetic moment. We have assumed the following neutron star parameters: $R = 14$ km, $M = 1.4 M_\odot$ and $I = \frac{2}{5} MR^2$, as well as $R = 10$ km for comparison. The data and the model, for $R = 14$ km, are plotted in Fig. 6.19. As can be seen, there is a good agreement between the measurements and the model. From the fit, the following values for the magnetic moment and the distance are obtained: $\mu_{30} \sim 9$, $d \sim 1.2$ kpc. Using Eq. 2.8, the obtained magnetic moment implies a surface magnetic field of $B \sim 6.5 \times 10^{12}$ G. Using the canonical radius of the neutron star $R = 10$ km and leaving both the distance and the magnetic moment free gives $\mu_{30} \sim 6.43$ and $d \sim 1.045$ kpc. The magnetic moment implies a magnetic field of $B \sim 4.7 \times 10^{12}$ G. Due to all the model parameters that

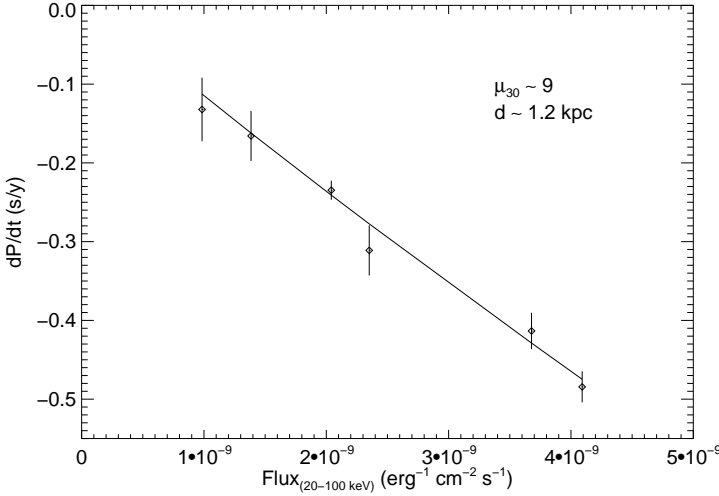


Figure 6.19: A 0535+26 values for the spin-up vs. the flux, fitted to the Ghosh & Lamb (1979b) model.

are unknown, these values should only be taken as approximations. These values are however consistent with the magnetic field derived from the cyclotron energy. We can conclude that the theory of accretion is valid for A 0535+26, reproducing a magnetic field value consistent with the magnetic field measured from the cyclotron lines.

If we fix the distance to $d = 2 \text{ kpc}$ (reported value in Steele et al. 1998), for $R = 14 \text{ km}$ we obtain a magnetic moment of $\mu_{30} \sim 0.23$, that implies a surface magnetic field of $B \sim 0.17 \times 10^{12} \text{ G}$. This too low value for the magnetic field lies probably on the fact that the model depends on several assumptions like disk accretion, assumptions for the mass, radius, moment of inertia . . . For $R = 10 \text{ km}$, fixing the distance to $d = 2 \text{ kpc}$ gives $\mu_{30} \sim 0.06$, that implies an even lower surface magnetic field of $B \sim 0.04 \times 10^{12} \text{ G}$.

Using $R = 14 \text{ km}$ and assuming a dipole field configuration, with the values of the magnetic field derived from the cyclotron line and from the torque theory, one can estimate the height of the line forming region above the neutron star surface to be $\sim 1.3 \text{ km}$. But considering the uncertainties of the model, this value should be taken with a grain of salt.

Pre-outburst flaring activity

The observational results and physical interpretation presented in this chapter have been published in Caballero et al. (2008b) and Postnov et al. (2008) respectively. This chapter is based on these two publications.

7.1 Observations during the pre-outburst flare

RXTE performed three observations during a flare that took place before the periastron, during the rise to the peak of the outburst, in the interval MJD [53610.595–53610.755]. The flux during the flare reached $F_{(3-50)\text{ keV}} = 479\text{ mCrab}$ (luminosity $L_{(3-50)\text{ keV}} = 0.91 \times 10^{37}\text{ erg s}^{-1}$), comparable to the flux reached at the peak of the outburst, $F_{(3-50)\text{ keV}} = 493\text{ mCrab}$ (luminosity $L_{(3-50)\text{ keV}} = 0.93 \times 10^{37}\text{ erg s}^{-1}$). The *PCA* light curve of the outburst and a zoom on the *pre-outburst flare* are plotted in Fig. 7.1. The timing and spectral analysis of the source has revealed different properties during the flare compared to the rest of the outburst. As already mentioned in Chapter 5.1, the inspection of the *Swift-BAT* light curve reveals that the flare observed with *RXTE* is just one of a collection of flares (Fig. 5.2).

7.1.1 Change in the energy dependent pulse profiles

We studied the energy dependent pulse profiles during the *pre-outburst flare*. Strong changes in the pulse-profile shape with photon energy are observed for both the main outburst and pre-outburst flare but in quite different ways. Fig. 7.2 shows pulse profiles from observation number 4, performed during the pre-outburst flare, and for observation 16, performed close to the maximum of the main outburst (Appendix A). Observation 16 was chosen because of its high data quality and the pulse profiles are representative of data acquired during the outburst peak. The low-energy ($E \lesssim 20\text{ keV}$) pulse profiles in both cases show a complex pattern, but different structures and evolution. At higher energies ($E \gtrsim 20\text{ keV}$) both pulse profiles show a simpler double-peak shape. During the main outburst, one of the peaks is strongly

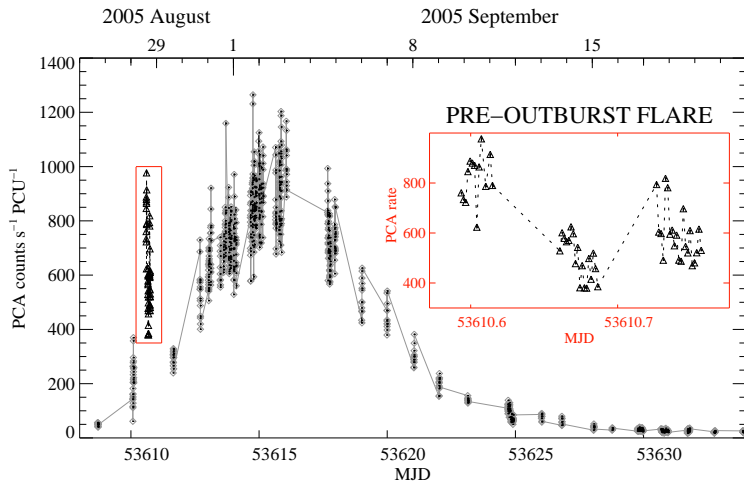


Figure 7.1: PCA light curves for the available observations of the August/September 2005 outburst. The inset shows a zoom of the three *RXTE* observations during the *pre-outburst flare*.

reduced above the cyclotron energy, while during the pre-outburst flare there is a smooth evolution towards higher energies without a noticeable change crossing the cyclotron energy.

7.1.2 Change in the cyclotron line energy

We have studied the phase-averaged spectra of the observations during the *pre-outburst flare*. The model selected for the X-ray continuum is the same as the model used for the observations during the *main outburst* (see Sec. 6.4), a power law times an exponential cutoff `cutofpl` plus a Gaussian emission line to account for the Fe $K\alpha$ fluorescence line. The cyclotron-centroid energy is measured at a higher value than during the main part of the outburst, reaching $E_{cyc} = 52.0^{+1.6}_{-1.4}$ keV, compared to $E_{cyc} = 46.1^{+0.5}_{-0.5}$ keV during the main outburst (at 90% confidence). Table 7.1 contains the best-fit values for the three observations during the pre-outburst flare and for the sum of these observations, as well as the best-fit values for the main outburst (observation 16) for comparison.

To study the significance of the change, we have produced χ^2 contour plots for the observations during the flare and during the main outburst. As an example, in Fig. 7.3 contour plots are shown for observation 16 and for the sum of three avail-

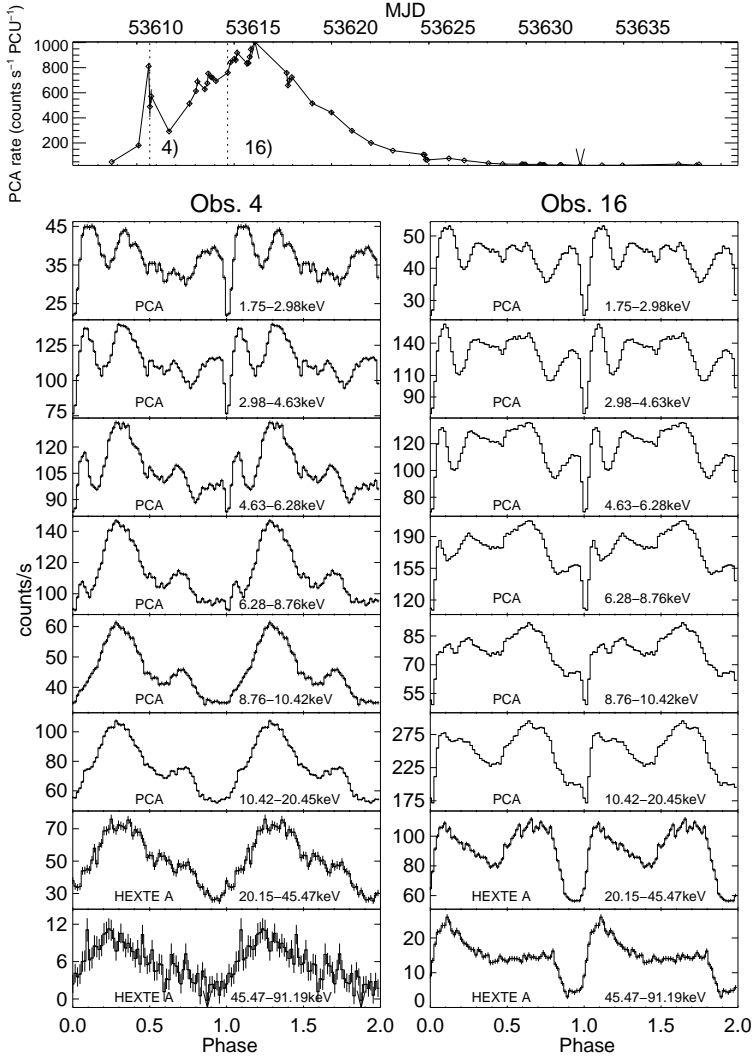


Figure 7.2: *PCA* and *HEXTE* background subtracted pulse profiles from one observation during the pre-periastron flare (obs. 4), with $L_{(3-50)\text{ keV}} \sim 0.91 \times 10^{37} \text{ erg s}^{-1}$, and from one observation near the maximum of the outburst (obs. 16), with $L_{(3-50)\text{ keV}} \sim 0.93 \times 10^{37} \text{ erg s}^{-1}$. Two pulse cycles are shown for clarity. In the upper panel the *PCA* light curve is shown. The dashed vertical lines indicate the times of the corresponding observations.

Table 7.1: Best-fit values for the available observations during the pre-outburst flare, where the CRSF energy is measured at a higher position, for the sum of the observations during the flare, and for one observation close to the maximum of the main outburst. $E_{\text{cyc},1}$, $\sigma_{\text{cyc},1}$ and E_{fold} are given in keV. The given flux is in the (5 – 50) keV energy range, in units of $10^{-8} \text{ erg cm}^{-2} \text{ s}^{-1}$. Errors are 90 % confidence for one parameter of interest ($\chi^2_{\text{min}} + 2.7$).

	Pre-outburst flare				Main out.
	Obs. 3	Obs. 4	Obs. 5	sum 3-5	Obs. 16
$E_{\text{cyc},1}$	$48.3^{+1.1}_{-1.0}$	$50.2^{+1.8}_{-1.6}$	$52.0^{+1.6}_{-1.4}$	$49.9^{+0.8}_{-0.8}$	$46.1^{+0.5}_{-0.5}$
$\sigma_{\text{cyc},1}$	$6.4^{+1.0}_{-1.0}$	$8.7^{+1.4}_{-1.3}$	$10.8^{+1.3}_{-1.1}$	$8.6^{+0.7}_{-0.7}$	$10.1^{+0.5}_{-0.5}$
$\tau_{\text{cyc},1}$	$0.27^{+0.03}_{-0.03}$	$0.57^{+0.08}_{-0.08}$	$0.53^{+0.06}_{-0.06}$	$0.40^{+0.03}_{-0.03}$	$0.47^{+0.03}_{-0.02}$
E_{fold}	$18.2^{+0.4}_{-0.4}$	$18.8^{+1.0}_{-1.0}$	$19.2^{+0.8}_{-0.7}$	$18.3^{+0.4}_{-0.4}$	$18.0^{+0.4}_{-0.3}$
α	$0.73^{+0.02}_{-0.02}$	$0.91^{+0.04}_{-0.04}$	$0.83^{+0.03}_{-0.03}$	$0.77^{+0.02}_{-0.02}$	$0.59^{+0.02}_{-0.02}$
Flux	$1.780^{+0.007}_{-0.013}$	$0.944^{+0.004}_{-0.018}$	$1.189^{+0.005}_{-0.014}$	$1.369^{+0.007}_{-0.008}$	$1.569^{+0.006}_{-0.007}$
$\chi^2_{\text{red}}/\text{dof}$	1.19/170	0.88/170	0.90/17	1.18/220	1.19/214

able observations during the pre-outburst flare. In observation 16 we included a harmonic cyclotron line with the energy fixed at $E_{\text{cyc}} = 102.5 \text{ keV}$ (it is measured at $E_{\text{cyc}} = 102.5^{+4.5}_{-3.3} \text{ keV}$ at 90 % confidence). We conclude from the contour plots that the change in energy is statistically significant.

Fig. 7.4 shows the evolution of the CRSF energy during the outburst, as well as the evolution of the continuum parameters (photon index α and folding energy E_{fold}) for the observations in which the cyclotron line was significantly detected. The continuum parameters are quite variable at the beginning of the outburst. The spectrum at the beginning of the outburst appears to be softer, with photon index $\alpha \sim 1.2$, and then becomes harder in the flare. The rising part of the main outburst presents a harder spectrum, with $\alpha \sim 0.6$. To compare the spectral shape of A 0535+26 during the *pre-outburst flare* to the rest of the outburst, energy unfolded spectra are shown in Fig. 7.5. The harder spectrum during the main outburst can be appreciated in the figure.

7.2 Evidence for magnetospheric instability

7.2.1 Summary of results

During the rise to the peak of the outburst of A 0535+26 there are significant changes in the timing and spectral behaviour with respect to the main outburst that point to a different physical scenario. They can be summarized as follows:

Feature 1. During the rise to the peak of the outburst, an X-ray *pre-outburst flare*

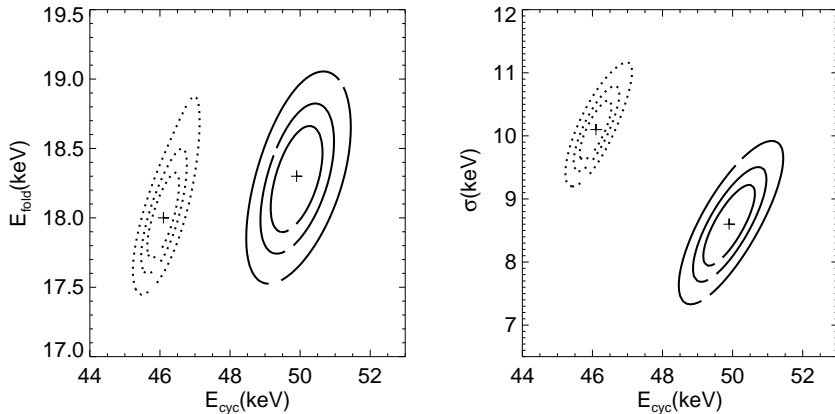


Figure 7.3: E_{fold} vs E_{cyc} (left) and σ vs E_{cyc} (right) contour plots for one observation near the maximum (observation 16 in Fig. 7.2) and for the sum of the three available observations during the pre-outburst flare (solid lines). The contours indicate $\chi^2_{\text{min}} + 2.30$ (68%), 4.61 (90%), 9.21 (99%) levels.

of $\tau_{\text{flare}} \sim 1$ day takes place. The luminosity of the flare is comparable to the one reached during the peak of the outburst.

Feature 2. The pulse period of the neutron star appears to be constant during the *pre-outburst flare*, $P = 103.3960(5)$ s, and a spin-up starts at periastron, $\dot{P} = (-1.69 \pm 0.04) \times 10^{-8}$ s/s measured at MJD 53618. The pulse period falls exponentially at the end of the outburst.

Feature 3. During the *pre-outburst flare*, the fundamental cyclotron-line energy centroid reaches $E_{\text{cyc}} = 52.0^{+1.6}_{-1.4}$ keV, significantly higher than for the main outburst, $E_{\text{cyc}} = 46.1^{+0.5}_{-0.5}$ keV.

Feature 4. The fundamental cyclotron line energy energy is independent of the X-ray luminosity (within uncertainties) during the *main outburst*.

Feature 5. The energy-dependent pulse profiles during the *pre-outburst flare* are significantly different from those measured for the *main outburst*. During the *main outburst*, the pulse profiles show an abrupt change above the cyclotron energy. This change is not observed in the pulse profiles obtained during the *pre-outburst flare*.

Feature 6. The flare detected with *RXTE* is one of a collection of flares with a characteristic time up to a few times 10^4 s that appear during the rise to the peak of the outburst. The flux evolution during the spin-up of the neutron star is smoother (see Fig. 5.2).

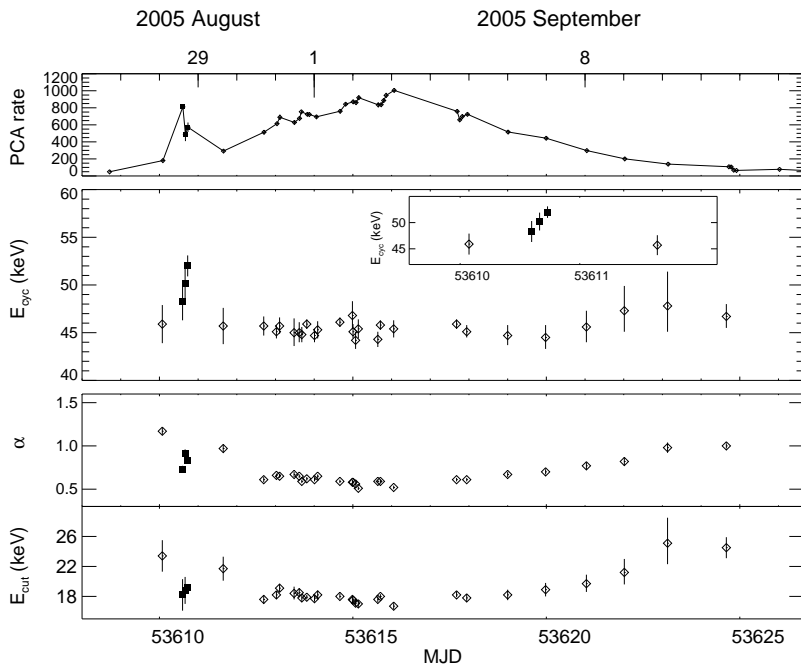


Figure 7.4: First panel: *PCA* light curve. Second panel: fundamental CRSF energy during the outburst. Inset shows a zoom on the pre-outburst flare. Third and fourth panels: photon index and folding energy evolution. The solid squares represent values from the *pre-outburst flare*, and the diamonds represent the values from the *main outburst*. Errors are 90% confidence for one parameter of interest ($\chi_{\min}^2+2.7$).

We show in the following that the observed flaring activity during the rise to the peak of the outburst can be due to magnetospheric instability in the unstable regime that takes place at the onset of the accretion. The instability can cause the plasma accumulated in the boundary layer between the accretion disk and the magnetosphere to fall directly onto the neutron star surface, explaining the observational differences during the *pre-outburst flare* compared to the main outburst. In Sec. 7.2.2 a review of accretion theory is given, followed by the application to A 0535+26 in Sec. 7.2.3.

The flaring activity observed is not exclusive of this outburst of A 0535+26. In other normal outbursts in 1994 there are hints of flares in the *BATSE* light curve (Finger et al. 1996), as can be seen in Fig. 3.1. Similar *pre-outburst flares* have been observed in other Be/X-ray binaries, e.g. GS 1843-024 (Finger et al. 1999) and EXO 2030+375

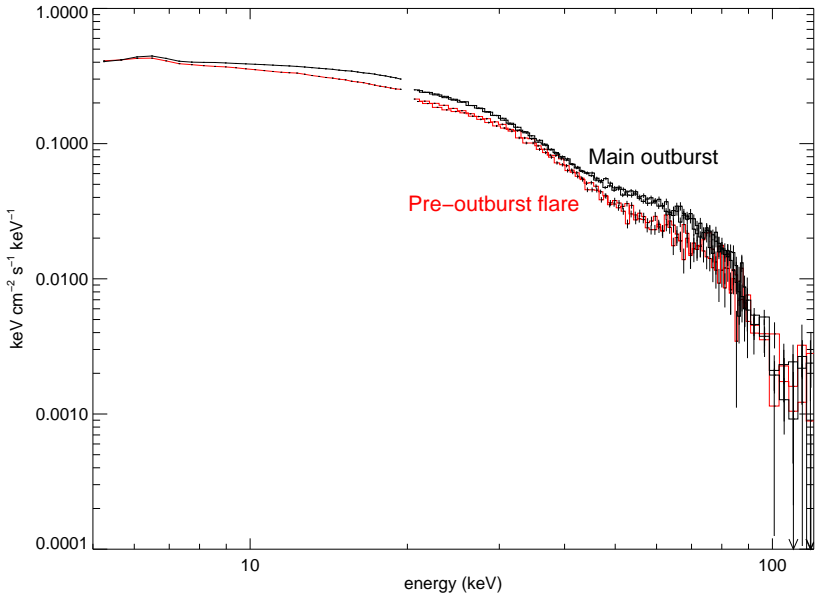


Figure 7.5: *RXTE* energy unfolded spectra of A 0535+26 during the *pre-outburst flare* (red), corresponding to the sum of the three observations during the flare, and during the *main outburst* (black, observation 16 from Appendix A.)

(Camero Arranz et al. 2005). The light curves for these two sources showing the flares are shown in Fig. 7.6. The physical interpretation we propose could also apply to these sources.

7.2.2 Disk accretion and mass transport in the magnetosphere.

As seen in Chap. 2 (Sec. 2.2.2), the strong magnetic field around the neutron star disrupts the accretion disk, forcing the plasma to follow the magnetic field lines. A boundary layer between the disk and the neutron star magnetosphere should exist from which the matter is gradually captured by the magnetic field lines (see Fig. 7.7). The matter forms accretion funnels that go towards the magnetic poles of the neutron star.

Rayleigh-Taylor instability takes place in the interface between two fluids, when the density of the fluid on the top is higher. The name of these instabilities in the

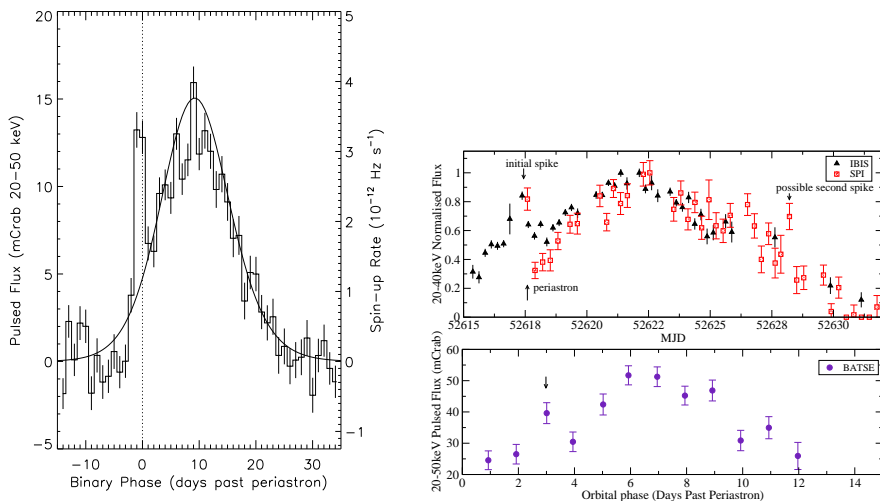


Figure 7.6: Pre-outburst flares observed in GS 1843-024 (left panel, Finger et al. 1999) and EXO 2030+375 (right panel, Camero Arranz et al. 2005).

case of a plasma in a magnetic field is Kruskal-Schwarzschild (Kruskal et al. 1977). This process is the main mechanism for the transport of matter across the magnetosphere. An increase in the accretion rate, causing a density build up in the magnetosphere, triggers the instabilities. Kruskal-Schwarzschild instabilities develop at the inner edge of the disk and allow the matter to drip through the magnetopause and into the magnetosphere (Scharlemann 1978).

Kelvin-Helmholtz instability can then break-up blobs of matter into smaller pieces that can be entrained by the magnetic field lines and channeled to the magnetic poles of the neutron star (Arons & Lea 1976, Arons & Lea 1980). Kelvin-Helmholtz instability takes place in the plasma-magnetic field interface, caused by the motion of the plasma with respect to the magnetic field. (More generally, Kelvin-Helmholtz instability takes place when two fluids move relative to each other. Irrespective of their densities, the interface is unstable). The effect of these instabilities is the turbulent mixing of the plasma and the magnetic field, allowing the plasma to be channeled by the field. The schematic evolution of the Kruskal-Schwarzschild instability is shown in Fig. 7.8.

There are two regimes for the instability. For low accretion rates, non steady accretion causing flaring events is expected. At higher accretion rates, a more steady accretion is expected. Recently, using more realistic assumptions, Romanova et al.

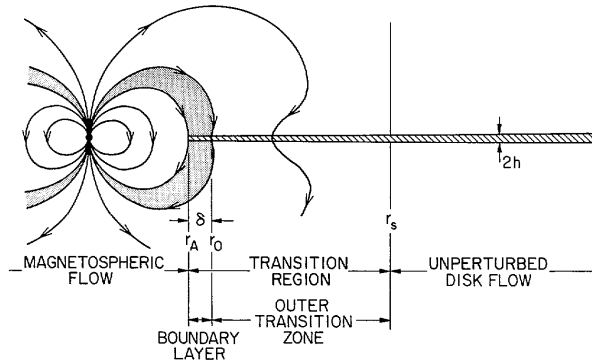


Figure 7.7: Schematic picture of magnetically threaded disk model from Ghosh & Lamb (1978). The boundary layer between the magnetosphere and the disk is indicated.

(2008) and Kulkarni & Romanova (2008) have performed 3D MHD simulations that confirm the basic features of the disk-magnetospheric interaction, revealing the two possible regimes for accreting neutron stars: stable or unstable. Fig. 7.9 shows the effect of Kruskal-Schwarzschild instability in the case of unstable regime, and the displacement of the magnetic field lines, allowing *tongues* of matter to penetrate in the magnetosphere and to fall directly into the neutron star surface (Romanova et al. 2008¹).

The Kruskal-Schwarzschild instability grows initially with time as $e^{\Gamma t}$, with

$$\Gamma^2 = k g_{\text{eff}} \tanh(k z_s) \quad (7.1)$$

where k is the angular wavenumber, z_s is a characteristic scale height above the interface and g_{eff} is the effective gravitational constant near the equatorial plane. g_{eff} includes several terms apart from the gravitational attraction ($\propto 1/R_m^2$), like centrifugal force ($\propto \omega^2 R_m$), bending of field lines by the instability, curvature of the magnetic field at the magnetopause ($\propto 1/\rho_m R_m^6$) or possible velocity gradients in the plasma flow (details can be found in Baan 1979).

For values of $g_{\text{eff}} < 0$ there is stability. The condition for the instability to occur is that $g_{\text{eff}} > 0$ in the magnetopause (directed towards the neutron star). $g_{\text{eff}} = 0$ defines a *zero-surface* at a certain distance from the neutron star. Inside this surface, the magnetopause is unstable, and outside the surface it is stable. As the accretion rate increases, the magnetopause moves inwards ($r_m \propto \dot{M}^{-2/7}$), until a Kruskal-Schwarzschild instability occurs.

¹animation available at <http://astrosun2.astro.cornell.edu/~romanova/instab.htm>

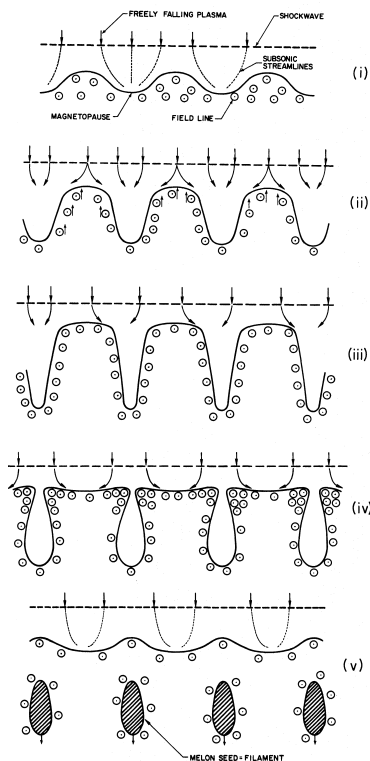


Figure 7.8: Development of Kruskal-Schwarzschild instability. Time increases from (i) to (v). Bubbles and spikes develop (ii). Kelvin-Helmholtz instability causes the formation of the filaments (iv) that fall almost freely in the magnetosphere. (Figure from Arons & Lea 1976).

7.2.3 Low-mode magnetospheric instability in A 0535+26

From the analysis of Baan (1979) it can be inferred that A 0535+26 at low accretion rates ($\dot{M} \sim 10^{16}$ g/s) may be on the verge of a Kruskal-Schwarzschild instability, becoming stable when the mass accretion rate increases. The author shows that the lowest harmonics are the first to become unstable. The same conclusion arises from the 3D MHD simulations of the disk magnetospheric interaction via Kruskal-Schwarzschild instability from Romanova et al. (2008). These 3D simulations show that for small accretion rates matter is accreted through funnel streams, and at large accretion rates matter accretes through Kruskal-Schwarzschild instabilities. The simulations have been performed for quite small magnetospheres, more applicable for

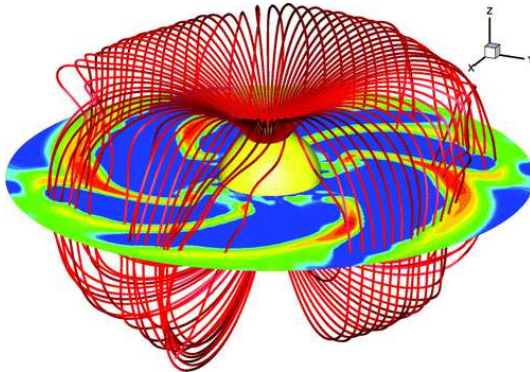


Figure 7.9: Example of unstable accretion onto a magnetized neutron star, with filaments penetrating the magnetosphere via Kruskal–Schwarzschild instability. The filaments are represented by density contours, with red indicating the highest density and dark blue the lowest. (Figure from Romanova et al. 2008).

millisecond pulsars. But we can assume that for A 0535+26, with a large magnetosphere, low-mode magnetospheric instability can develop.

We assume the existence of a disk. This assumption is supported by the spin-up measured during the main outburst. This was the case in past giant outbursts, confirmed by the presence of QPOs and spin-up (Sembay et al. 1990, Finger et al. 1996).

Assuming the standard α -theory (Shakura & Syunyaev 1973), the amount of mass accumulated in the boundary layer can be roughly estimated by the following expression:

$$\Delta M = \rho 2\pi R_a 2h \Delta l \simeq (4 \times 10^{19} \text{ g}) R_{a,9}^{7/5} \alpha^{-4/5} \dot{M}_{-10}^{3/5} (1 - \xi)^{3/5} \quad (7.2)$$

where Δl is the width of the boundary layer, $R_{a,9}$ is the stopping radius in units of 10^9 cm, \dot{M}_{10} is the mass accretion rate in units of $10^{-10} M_\odot / \text{yr}$ and

$$\xi = \dot{J} / (\dot{M} \sqrt{GM R_a}) \quad (7.3)$$

is the angular momentum flux through the disk normalized to the flux from the stopping radius. The width of the boundary layer is of the order of the thickness of the disk. We assume $\Delta l \sim h \simeq R_m$. We also assume the gas pressure to dominate over the radiation pressure in the boundary layer, the main opacity due to Thomson scattering and the disk to be Keplerian. At the onset of the accretion, $\xi \simeq 0$ and $\alpha \lesssim 0.01$.

Using Eq. 7.2, we obtain the following estimate for the amount of matter accumulated in the boundary layer:

$$\Delta M \sim 10^{21} \text{ g}$$

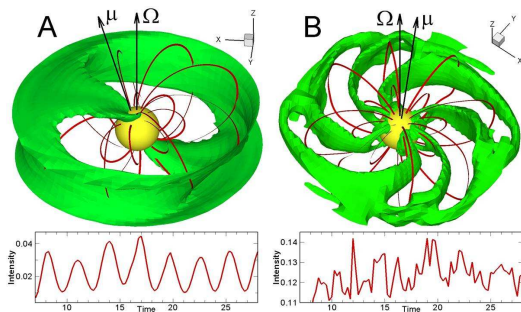


Figure 7.10: Top left: example of stable accretion onto a magnetized neutron star. Top right: example of unstable accretion. The surface represents a constant-density surface. The black lines represent magnetic field lines. The figure in the bottom show the light curves from the hot spots in the two cases. The light curve in the unstable regime is highly irregular. (Figure from Romanova et al. 2008).

As we saw above, in the case of A 0535+26 low-mode magnetospheric instability can develop, and break-up the boundary layer in the disk. This means that the 10^{21} g of matter accumulated in the boundary layer can fall directly onto the neutron star surface. On a free-fall time scale ($t_{\text{ff}} = (R^3/GM)^{1/2} \sim 20$ s) the 10^{21} g reaching the neutron star surface can produce a short spike with a luminosity of $\sim 10^{37}$ erg s $^{-1}$. This explains **feature 1** from Sec. 7.2.1.

The amount of matter that falls onto the neutron star surface during the spike ($t \sim 10^4$ s), estimated from the light curve, is

$$\Delta M \simeq \int \dot{M} dt \lesssim 10^{21} \text{ g} \quad (7.4)$$

The characteristic timescale of the spike agrees with the time required to replenish the boundary layer, $\Delta M/\dot{M} \sim 10^4$ s.

To explain the lack of noticeable spin-up during the flare, we can estimate how much the spin-up will change during the flare due to the angular momentum supply from the disk. Assuming a Keplerian disk,

$$\frac{d(I\omega)}{dt} = \dot{M} \sqrt{GM R_a} \quad (7.5)$$

Using this expression, we can estimate how much the angular momentum supply from the disk changes the spin-up during the flares:

$$\left| \frac{\Delta P}{P} \right| = \Delta M \frac{P}{2\pi I} \sqrt{GM R_a} \quad (7.6)$$

Assuming the moment of inertia of the neutron star to be $I = 10^{45} \text{g cm}^2$ and $R_a = R_c = 10^9 \text{cm}$ gives

$$\left| \frac{\Delta P}{P} \right| \lesssim 7 \times 10^{-6}$$

This lies within the uncertainty of the measured period $\Delta P/P \sim 5 \times 10^{-6}$ (see Chapter 6, Sec. 6.2.2.2) and explains why during the flare no spin-up was measured (**feature 2** from Sec. 7.2.1).

The plasma that enters the magnetosphere via low-mode Kruskal-Schwarzschild instability may become frozen to the magnetic field lines closer to the neutron star surface, and therefore can follow different field lines than those by which the quasi-stationary accretion takes places. This explains the difference measured in the cyclotron line energy during the flare (**feature 3** from Sec. 7.2.1). The absence of a change of the cyclotron line energy with the luminosity suggests the absence of a radiation-dominated accretion column (**feature 4** from Sec. 7.2.1). Therefore, the emission takes place closer to the neutron star surface, above several hundred meters. Assuming a dipole magnetic field, the observed change in the cyclotron energy $\Delta E_{\text{cyc}}/E_{\text{cyc}} \sim 10\%$ requires a change in the emission region towards the neutron star surface of $\Delta R/R_{\text{NS}} \sim 3\%$, by about 300 m. The emission is therefore more likely to originate closer to the neutron star surface. This explains the different pulse profiles during the flare (**feature 5** from Sec. 7.2.1)

The smooth evolution of the pulse profiles at energies $E \approx E_{\text{cyc}}$ during the *pre-outburst flare* in contrast to the absorption of one of the peaks above $E \approx E_{\text{cyc}}$ in the *main outburst* can be explained with the energy and angle dependence of the photon scattering cross-section.

Linear polarization of incident photons has two modes: ordinary and extraordinary, with the electric vector parallel or perpendicular to the plane containing the wave vector and the magnetic field. For photon energies above the cyclotron energy, $E \gg E_{\text{cyc}}$, the scattering cross-section for both modes:

$$\sigma_{\perp} \simeq \sigma_{\parallel} \simeq \sigma_{\text{T}} \quad (7.7)$$

where σ_{T} is the Thomson scattering cross-section², σ_{\parallel} is the cross-section for ordinary photons and σ_{\perp} is the cross-section for extraordinary photons.

For photon energies below the resonance, $E \ll E_{\text{cyc}}$:

$$\begin{aligned} \sigma_{\parallel} &\simeq \sigma_{\text{T}} \left[\sin^2 \theta + \cos^2 \theta \left(\frac{E}{E_{\text{cyc}}} \right)^2 \right] \\ \sigma_{\perp} &\simeq \sigma_{\text{T}} \left(\frac{E}{E_{\text{cyc}}} \right)^2 \end{aligned} \quad (7.8)$$

² $\sigma_{\text{T}} = \frac{8\pi}{3} \left(\frac{e^2}{m_e c^2} \right)^2 = 6.65 \times 10^{-25} \text{cm}^2$

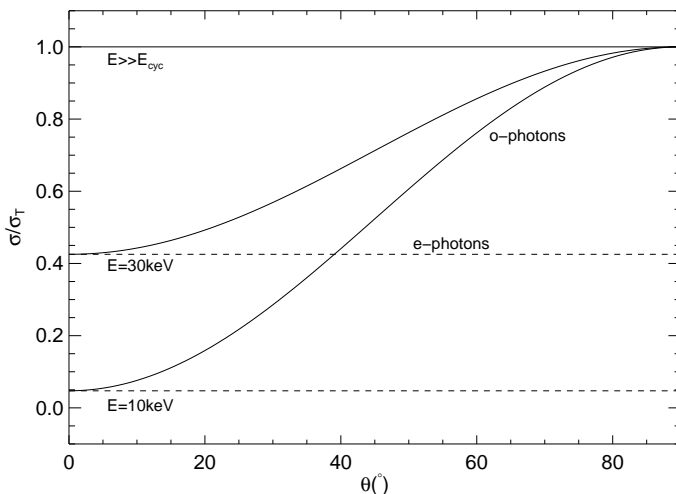


Figure 7.11: Approximate photon scattering cross-section (units of σ_T) as a function of θ for different photon energies and $E_{\text{cyc}} = 46 \text{ keV}$. The cross-section for ordinary photons σ_{\parallel} is represented with a solid line and the cross-section for extraordinary photons σ_{\perp} with a dashed line.

where θ and E are the angle and energy of the incident photon with respect to the magnetic field (scattering cross-sections from Harding & Lai 2006). The energy and angle dependence of the cross-sections for A 0535+26 is represented in Fig. 7.11.

The smooth evolution of the pulse profile above the cyclotron energy during the flare suggests a “pencil beam” diagram. The photon cross-section for $\theta \approx 0^\circ$ changes smoothly across the cyclotron resonance.

However, during the main outburst, one of the peaks is strongly reduced. During the main outburst, the accretion column is higher than during the flare, the density increases and the column becomes optically thick. A “fan beam” pattern can be additionally formed by extraordinary photons (perpendicular to the magnetic field). The cross-section of e-photons is smaller than that of ordinary photons, (see Fig. 7.11), and they can escape effectively from much higher optical depths. Above the cyclotron energy, however, both cross-sections are equal (Eq. 7.7), and the photons can only escape from small optical depths. The strong absorption of one of the peaks can be explained with the weakening of the “fan beam” component above the cyclotron energy.

As the accretion rate increases, the neutron star starts spinning-up, and the param-

eter ξ in Eq. 7.2 increases from zero to almost one. Therefore the amount of mass accumulated in the boundary layer, available for unstable accretion, is strongly reduced. The amplitude of the spikes rapidly decreases, and during the spin-up of the neutron star we do not see strong flaring activity (**feature 6** from Sec. 7.2.1). This suggests that once the neutron star stops spinning-up, flaring activity could appear again. This is indeed observed in the *Swift-BAT* light curve (Fig. 5.2).

The scenario described above can also explain evolution of the pulsed fraction during the outburst (Fig. 6.11). The pulsed fraction shows a scatter coincident with the flaring activity and unstable regime. It shows a smoother evolution during the spin-up of the neutron star, when the accretion is believed to be in the stable regime.

Hayasaki & Okazaki (2006) have modeled accretion disks around neutron stars in Be/X-ray binaries. Their Smoothed Particle Hydrodynamics (SPH) simulations reproduce a series of normal outbursts from the accretion disk formed about the neutron star at periastron. In some cases, single flares are found preceding the outburst maximum. We note first of all that the timescale of the flare in their simulations appears to be too long (10% of the orbital period) compared to the flare duration observed. The collection of flares seen in the *Swift-BAT* light-curve of A 0535+26 during the outburst (Fig. 5.2) are not reproduced by the above simulations. Moreover, this model does not take into account the disk-magnetospheric interaction.

CHAPTER 8

Pulse profile decomposition

In this chapter pulse profiles of A 0535+26 from a few keV up to ~ 100 keV are analyzed with a decomposition method. The decomposition of the pulse profiles allows to extract information on the geometry of the system and on the beam pattern. This method is described in detail in Kraus et al. (1995), and it has been applied to the accreting X-ray pulsars Cen X-3 and Her X-1 in Kraus et al. (1996) and Blum & Kraus (2000) respectively.

The chapter is organized as follows: in Sec. 8.1 a description of the method is given, and the assumptions that are made are discussed. In Sec. 8.2, the decomposition method is applied to the *RXTE* energy dependent pulse profiles of A 0535+26. Geometrical parameters of the neutron star are inferred from the decomposition, and the observable part of the beam pattern is reconstructed. In Sec. 8.2.4 a possible interpretation of the reconstructed beam pattern in terms of a relativistic model is discussed.

8.1 *Description of the method*

In Chapter 2 we introduced X-ray pulsars in binary systems. A basic property of these systems is the pulsed emission we observe. Models of the emission from a small column or mound on the magnetic poles of a neutron star can be found for instance in Kraus (2001) and Kraus et al. (2003). These models predict the beam pattern or direction dependence of the flux of one emission region as seen by a distant observer (see Fig. 8.1), including relativistic light deflection. Introducing the rotation of the pulsar and its geometry, i.e., the orientation of the rotation axis with respect to the magnetic axis and the location of the magnetic poles, the single-pole pulse profiles can be modeled. This is the pulsed emission that a distant observer would see from each emission region. The sum of the single-pole contributions gives the total pulse profile.

In this work a decomposition analysis is applied which inverts the process described above. From the observed pulse profile the single-pole pulse profiles are

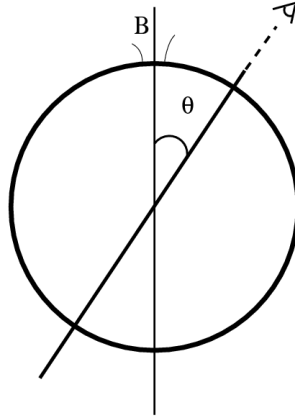


Figure 8.1: Illustration of beam pattern or emission from one magnetic pole as seen by a distant observer as a function of the angle between the direction of observation and the magnetic axis θ .

obtained, and from the single-pole contributions information on the geometry of the neutron star and the beam pattern can be extracted. Of course the backwards process is not straightforward and involves ambiguities which will be discussed.

To reconstruct the observable part of the beam pattern is as far as one can go from the observations with a minimum of assumptions and without involving any model. Once the visible part of the beam pattern is obtained, it can be used as input to the construction of an emission region model.

8.1.1 Assumptions

In this work a **dipole structure of the magnetic** field near the surface of the neutron star is assumed. We must note that this is a simplification, since the neutron star magnetic field might be more complex and present higher order terms. This has been theoretically investigated in Lipunov (1978), Shakura et al. (1991) or Panchenko & Postnov (1994). The decomposition of the observed pulse profile in two components is based on symmetry considerations. The basic assumption, which is often adopted in model calculations, is that the **emission regions at the magnetic poles are axisymmetric** (see for instance Kraus et al. 2003). Therefore the magnetic dipole axis is a symmetry axis of the emission from the neutron star, and the beam pattern is only a function of the angle θ between the direction of observation and the magnetic axis. This makes the single-pole pulse profile necessarily symmetric. One of the symmetry points will be the instant when the dipole axis is closest to the line of sight, and the

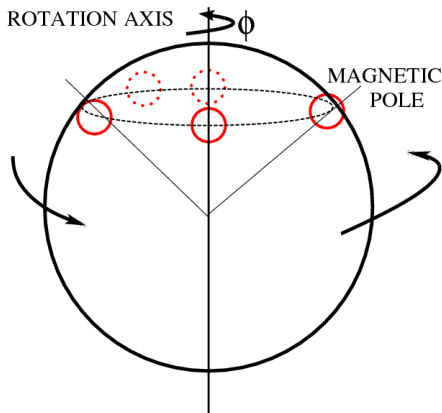


Figure 8.2: Illustration of one magnetic pole of a neutron star and its movement around the rotation axis. Under the assumption that the emission region at the magnetic poles is axisymmetric, the single-pole pulse profiles are necessarily symmetric.

other symmetry point will be half a period later, with the dipole axis pointing away from the observer (see Fig. 8.2).

The above assumptions necessarily imply a symmetric pulse profile. However, in most of the cases observations of accreting pulsars reveal an asymmetric pulse profile. The assumption of an ideal dipole magnetic field is slightly modified by introducing a **small displacement of one of the two poles with respect to the antipodal position**. This has not been proved for neutron stars, but seems to be a general feature of other systems. In white dwarfs, Zeeman spectroscopy and polarimetry, and cyclotron spectroscopy, have allowed to make constraints on the magnetic field structure. To a first order approximation, the white dwarf magnetic fields can be modeled with offset dipoles, that have an offset from the center of $\sim 10\%–30\%$ of the stellar radius along the dipole axis. An extensive review on white dwarfs magnetism can be found in Wickramasinghe & Ferrario (2000). The Earth's magnetic field has also two magnetic poles which are not exactly antipodal. They have an offset from the antipodal position of $\delta_{\text{Earth}} \approx 24.7^\circ$ (source: Canadian Geologic Survey and Australian Antarctic Division). A distorted dipole field can explain the observed asymmetry in the pulse profiles: if the two magnetic poles are exactly opposite to each other, the single-pole pulse profiles have the same symmetry points, and their sum will give a symmetric pulse profile. A small deviation from the antipodal position will make the symmetry points of the two single-pole pulse profiles different, causing the asymmetry in the total pulse profile. Fig. 8.3 illustrates this effect with the sum of two symmetric func-

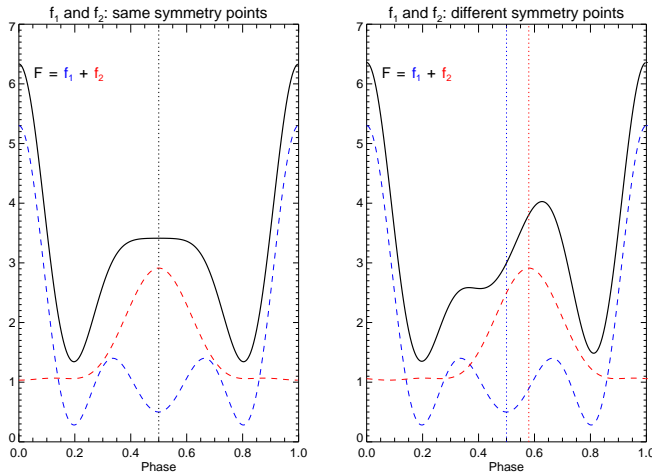


Figure 8.3: Left panel: symmetric functions f_1 (blue dashed curve) and f_2 (red dashed curve) with same symmetry points (vertical line) and sum $F = f_1 + f_2$ (black solid line), also symmetric. Right panel: same two functions f_1 and f_2 with symmetry points shifted by 28.6° , or ~ 0.08 in phase (indicated by vertical lines). The sum $F = f_1 + f_2$ (black solid line) is asymmetric.

tions in two different cases: two symmetric functions with the same symmetry points, and the same functions with a small shift between their symmetry points.

Another assumption is that **the two emission regions have the same beam pattern**. This implies that each of the two poles will make visible one section of the same beam pattern. Depending on the geometry of the neutron star and the angle of observation, these two regions will in some cases have coincident parts (see below, Sec. 8.1.2.2). This assumption has been tested with the accreting pulsars Cen X-3 (Kraus et al. 1996) and Her X-1 (Blum & Kraus 2000). In those cases an overlapping region was found, that indicates that both emission regions have the same beam pattern.

8.1.2 Steps of the method

In Fig. 8.4 a schematic view of a rotating neutron star is given. A spherical coordinate system is used with the rotation axis as polar axis. As explained above, the beam pattern is assumed to be axisymmetric, and therefore to depend only on the angle θ between the direction of observation and the magnetic axis. The value of θ changes

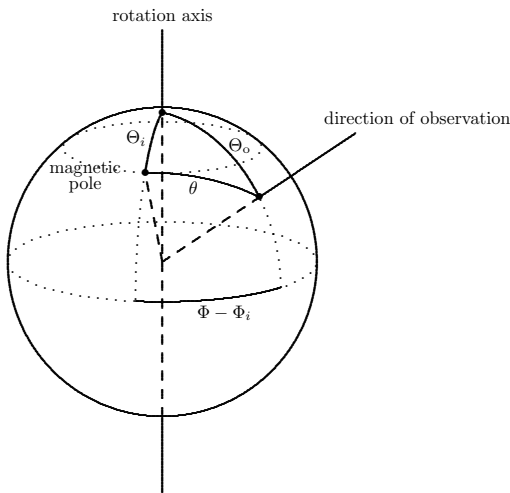


Figure 8.4: Schematic view of a rotating neutron star. The spherical coordinate system we used has the rotation axis aligned with the polar axis. Θ_i is the polar angle of the i th pole. Θ_0 is the polar angle of the direction of observation. The angle θ between the magnetic pole and the direction of observation changes with the azimuthal angle Φ , which coincides with the phase rotational angle. (Figure from Kraus et al. 1995).

with the rotation angle Φ . Depending on the position of the poles with respect to the rotation axis and on the direction of observation with respect to the rotation axis, we will observe a certain section of the beam pattern for each pole.

Applying the cosine formula to the spherical triangle in Fig. 8.4, we obtain θ as a function of the phase Φ :

$$\cos \theta = \cos \Theta_0 \cos \Theta_i + \sin \Theta_0 \sin \Theta_i \cos(\Phi - \Phi_i) \quad (8.1)$$

where Θ_0 is the polar angle of the direction of observation, Θ_i the polar angle of the i th pole and Φ_i one symmetry point for the i th pole. Since $\theta(\phi)$ is symmetric around the maximum and minimum values of θ , the contribution of the emission region to the single pole pulse profile has symmetry points at $\Phi = \Phi_i$ and $\Phi = \Phi_i + \pi$. Eq. 8.1 provides the relation between the pulse profile and the geometric parameters of the pulsar for a given beam pattern. The decomposition analysis of the pulse profiles allows to extract information on the geometric parameters and therefore on the beam pattern.

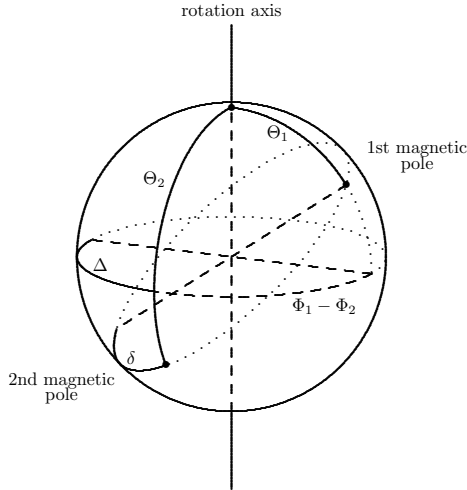


Figure 8.5: Intrinsic geometry of the neutron star. With the rotation axis as polar axis, the magnetic poles are located at polar angles Θ_1 and Θ_2 . The angular distance δ between the second magnetic pole and the point that is antipodal to the first magnetic pole gives the deviation from an ideal dipole field. A complete description of the pulsar geometry is given in terms of Θ_1 , Θ_2 and the difference in the azimuthal angles $\Phi_1 - \Phi_2 = \pi - \Delta$. (Figure from Kraus et al. 1995).

The first step of the analysis is to determine the symmetry points Φ_1 and Φ_2 . By decomposing the original pulse profile in two symmetric single-pole contributions, the values of Φ_1 and Φ_2 can be obtained. Mathematically, the decomposition of the original pulse profile into two symmetric functions will be not unique. Physical criteria must be applied to reject all the solutions that do not match the astrophysical requirements. This process and the criteria applied are explained in detail in Sec. 8.1.2.1.

It can be shown that an appropriate transformation of the single-pole pulse profiles turns them into scaled undistorted sections of the beam pattern. The relation between the beam pattern and the single-pole pulse profiles can be seen by looking at Eq. 8.1. Considering the beam pattern as a function of $\cos \theta$ and the single pole pulse profiles as a function of $\cos(\Phi - \Phi_i)$, as the relation between $\cos \theta$ and $\cos(\Phi - \Phi_i)$ is linear, there is no distortion between the two functions. Therefore, once we have obtained the single-pole pulse profiles, plotting them as a function of $\cos(\Phi - \Phi_i)$ we obtain two sections of the beam pattern (see Sec. 8.1.2.2. for details).

The intrinsic pulsar geometry is shown in Fig. 8.5. A complete description of the pulsar can be given in terms of the polar angles Θ_1 and Θ_2 , and the difference in their azimuthal angles $\Phi_1 - \Phi_2$. Since we are assuming a distorted magnetic dipole field, the two poles are not exactly opposite to each other and $\Phi_1 - \Phi_2$ differs from π by some amount Δ :

$$\Delta = \pi - (\Phi_1 - \Phi_2) \quad (8.2)$$

The angular distance δ between the location of the second magnetic pole and the point that is antipodal to the first magnetic pole can be used as a measure for the deviation from an ideal dipole field. From Fig. 8.5, applying the cosine formula to the spherical triangle of sides Θ_1 , Θ_2 , $(180 - \delta)$:

$$\cos \delta = -\cos \Theta_2 \cos \Theta_1 + \sin \Theta_2 \sin \Theta_1 \cos \Delta \quad (8.3)$$

In Sec. 8.1.2.2, details on how to obtain information on the position of the two poles after having obtained a possible decomposition and the symmetry points Φ_1 , Φ_2 and Δ are given.

8.1.2.1 Decomposition into single-pole pulse profiles

The first step of the analysis is to find an acceptable decomposition of the original pulse profile into two symmetric functions. This is done via Fourier analysis. The original pulse profile and the single-pole pulse profiles are written as a Fourier series. The total pulse profile F is written as:

$$F(\Phi) = \frac{1}{2}u_0 + \sum_{k=1}^{n/2-1} [u_k \cos(k\Phi) + v_k \sin(k\Phi)] + u_{n/2} \cos\left(\frac{n}{2}\Phi\right) \quad (8.4)$$

where n is the number of sampled points or bins of the original pulse profile and Φ is the phase. Eq. 8.4 gives a valid representation of the original pulse profile at all phases if the Fourier transform of F approaches to zero as the frequency approaches $n/2$. If this is not the case (phenomenon called *aliasing*), less Fourier coefficients are taken into account to describe the original pulse profile. See for instance Press et al. (1992) for details on Fourier analysis.

The single-pole pulse profiles are two symmetric functions f_1 and f_2 such that $F = f_1 + f_2$. We write them as Fourier series, with cosine terms only:

$$f_1(\Phi) = \frac{1}{2}c_0 + \sum_{k=1}^{n/2} c_k \cos[k(\Phi - \Phi_1)] \quad (8.5)$$

$$f_2(\Phi) = \frac{1}{2}d_0 + \sum_{k=1}^{n/2} d_k \cos\{k[\Phi - (\Phi_2 + \pi)]\} \quad (8.6)$$

Φ_1 and Φ_2 are the symmetry points of f_1 and f_2 respectively. Formally, a decomposition of $F(\Phi)$ in two symmetric functions $f_1(\Phi)$ and $f_2(\Phi)$ exists for every choice of their symmetry points Φ_1 and Φ_2 . For convenience, we use the parameter Δ (see Eq. 8.2). All formal decompositions will be contained in the parameter space $\Phi_1 - \Delta$, with $0 \leq \Phi_1 \leq \pi$ and $0 \leq \Delta \leq \pi/2$. Once all the formal decompositions are found, physical criteria are applied to decrease the number of decompositions to physically meaningful ones. Those criteria are the following:

- “non-negative” criterion: the functions $f_1(\Phi)$ and $f_2(\Phi)$ must be both positive. Since they represent photon fluxes, all the solutions for which $f_1(\Phi)$ or $f_2(\Phi)$ are negative are rejected.
- “no-ripples” criterion: the two functions $f_1(\Phi)$ and $f_2(\Phi)$ should not have “ripples” or features that cancel out in the sum. In terms of X-ray pulsar modeling, one would not expect the single-pole contributions to be much more complicated than their sum, or that complicated features exactly match each other and cancel out in the sum. Fig.8.6 shows an example of rejected decomposition applying this criterion.
- pulse profiles are typically energy dependent. The decomposition must be done in all energy ranges independently, and the same symmetry points must give valid decompositions in all energy bands.

The “non-negative” criterion is very restrictive if the pulse profiles have a large pulsed fraction. This is typically the case in accreting pulsars at high energies (this was discussed in sec. 6.3). If the pulsed fraction is low at all energy ranges, almost all the $\Phi_1 - \Delta$ parameter space will contain positive decompositions, making the task of selecting physically acceptable decompositions a very difficult task.

Once a possible decomposition is found, the symmetry points of the single-pole pulse profiles Φ_1 and Φ_2 and the parameter Δ , related to the position of the emission regions on the neutron star, are obtained.

8.1.2.2 From single-pole profiles to geometry and beam pattern

As was explained above, the single-pole pulse profiles provide undistorted copies of the beam pattern. Assuming that both emission regions are equal, and have therefore the same beam pattern (see 8.1.1) each of the single-pole pulse profiles shows a different section of the same beam pattern. These two sections are combined to reconstruct the total observable section of the beam pattern.

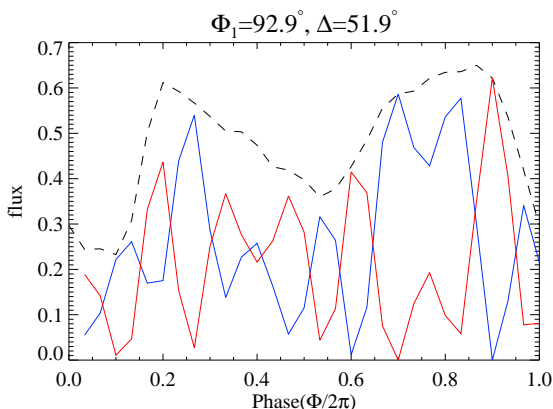


Figure 8.6: Example of rejected decomposition applying the non-ripples criterion. Black dashed line: original pulse profile $F(\Phi)$. Red and blue solid lines: single-pole contributions $f_1(\Phi)$ and $f_2(\Phi)$, such as $F(\Phi) = f_1(\Phi) + f_2(\Phi)$. This particular choice of symmetry points Φ_1, Δ (shown on the top of the panel) is rejected.

Taking Eq. 8.1, as the neutron star rotates, the value of θ for the i th pole will reach its minimum at $\Phi = \Phi_i$:

$$\theta_{\min} = |\Theta_i - \Theta_0| \quad (8.7)$$

and it will reach its maximum at $\Phi = \Phi_i + \pi$:

$$\theta_{\max,i} = \Theta_i + \Theta_0 \quad \text{if } \Theta_i + \Theta_0 \leq \pi \quad (8.8)$$

$$\theta_{\max,i} = 2\pi - (\Theta_i + \Theta_0) \quad \text{if } \Theta_i + \Theta_0 > \pi \quad (8.9)$$

Each single-pole pulse profile will show a section of the beam pattern, with $\theta_{\min,i} \leq \theta \leq \theta_{\max,i}$. Depending on the geometry of the system, these two ranges can show an overlapping region in the beam pattern. At an instant Φ , the first pole will be seen at an angle θ . At another instant $\tilde{\Phi}$, the second pole will be seen at the same angle θ . We can use Eq. 8.1 to express the relation between Φ and $\tilde{\Phi}$ in terms of the geometric parameters:

$$\cos(\Phi - \Phi_1) = \frac{\cot \Theta_0 (\cos \Theta_2 - \cos(\Theta_1))}{\sin \Theta_1} + \frac{\sin \Theta_2}{\sin \Theta_1} \cos(\tilde{\Phi} - \Phi_2) \quad (8.10)$$

that we write as:

$$\cos(\Phi - \Phi_1) = a + b \cos(\tilde{\Phi} - \Phi_2), \quad b > 0 \quad (8.11)$$

Plotting the single-pole pulse profiles as a function of $\cos(\Phi - \Phi_i)$, the sections they have in common can be found, and therefore the values of a and b can be determined. Once this is done, both sections of the beam pattern can be plotted as a function of the same variable q , defined as:

$$q := \frac{\cos \theta - \cos \Theta_0 \cos \Theta_1}{\sin \Theta_0 \sin \Theta_1} \quad (8.12)$$

Using Eq. 8.1 and Eq. 8.11:

$$\cos(\Phi - \Phi_1) = q, \quad (8.13)$$

$$\cos(\tilde{\Phi} - \Phi_2) = (q - a)/b \quad (8.14)$$

Since the relation between q and $\cos \theta$ is linear, by plotting the two single-pole pulse profiles as a function of q we obtain the total visible part of the beam pattern without distortion.

Eq. 8.10 and Eq. 8.11 provide two equations relating the three geometric parameters Θ_0 , Θ_1 and Θ_2 . They can be solved for Θ_1 and Θ_2 as a function of Θ_0 :

$$\tan \Theta_1 = \frac{-2a \tan \Theta_0}{(a \tan \Theta_0)^2 + b^2 - 1}, \quad (8.15)$$

$$\tan \Theta_2 = \frac{b \tan \Theta_1}{a \tan \Theta_0 \tan \Theta_1 + 1} \quad (8.16)$$

In order to obtain the location of the magnetic poles Θ_1 and Θ_2 , an independent determination of Θ_0 is necessary. Θ_0 is identical to the inclination of the system if the rotation axis of the neutron star is perpendicular to the orbital plane. If the inclination of the system is known (for instance, from eclipse observations), then using Eq. 8.15 and Eq. 8.16 the position of the two magnetic poles can be obtained.

The pulsar geometry is then completely determined: the location of the poles Θ_1 and Θ_2 , their displacement from the antipodal position Δ and the direction of observation Θ_0 .

Knowing the geometric parameters of the system allows to express the single-pole pulse profiles as a function of θ (Eq. 8.1), and therefore the observable part of the beam pattern is completely reconstructed.

8.2 Application to A 0535+26

8.2.1 Observations

Using the decomposition method described above we have analyzed the energy dependent pulse profiles of A 0535+26 obtained with *RXTE* during its August/September 2005 normal outburst. For the analysis, pulse profiles obtained during the main part of the outburst have been selected, as those profiles appear to be very stable, not only during the outburst but also compared to historical observations.

The analysis was performed using observation 16 from Appendix A, as well as six merged observations performed at a similar luminosity level (observations 16–21), resulting in a total observation time of ~ 20.4 ks. The pulse profiles have been accumulated using 30 phase bins.

8.2.2 Search for acceptable decompositions

We start the analysis using *HEXTE* pulse profiles from observation 16, extracted in four different energy ranges 18.3 – 30.9 keV, 30.9 – 44.5 keV, 44.5 – 59.1 keV and 59.1 – 99.8 keV. Each original pulse profile is written as a Fourier series $F(\Phi)$. 20 Fourier coefficients out of the 30 sampled points were enough to properly describe the original profiles. The highest frequency terms were not considered in order to avoid aliasing (see Sec. 8.1.2.1).

The next step is to decompose the original pulse profiles into two symmetric functions $f_1(\Phi)$ and $f_2(\Phi)$, with symmetry points Φ_1 and Φ_2 . The parameter space $\Phi_1 - \Delta$ is divided in $1^\circ \times 1^\circ$ boxes, and one decomposition per $1^\circ \times 1^\circ$ box is computed. The possible decompositions are represented in this parameter space, with $0 \leq \Phi_1 \leq \pi$ and $0 \leq \Delta \leq \pi/2$.

The “non-negative” criterion is applied. Only decompositions for which $f_1(\Phi)$ and $f_2(\Phi)$ are always positive are accepted. This criterion is specially restrictive in the 59.1–99.8 keV range, for which the pulsed fraction is very high, $\sim 80\%$. The knowledge of the background level is of special importance in this step. A small amount of negative flux is allowed in order to account for the $\sim 1\%$ uncertainty of the *HEXTE* background (Rothschild et al. 1998). The “non-negative” criterion reduces considerably the number of acceptable decompositions. The result of applying this criterion, requiring each decomposition to be valid at all energy ranges, is shown in Fig. 8.7. The black regions indicate where positive decompositions have been found. We limit the search of physically acceptable decompositions to those regions.

For every decomposition, there is a certain region in the $\Phi_1 - \Delta$ plane which contains other qualitatively similar decompositions. In order to handle the large amount of possible decompositions that have to be studied, similar ones are grouped together into types. We group decompositions in a same group when their square deviation is smaller than a certain $\chi^2 = 10^{-3}$. By grouping them into types the number of

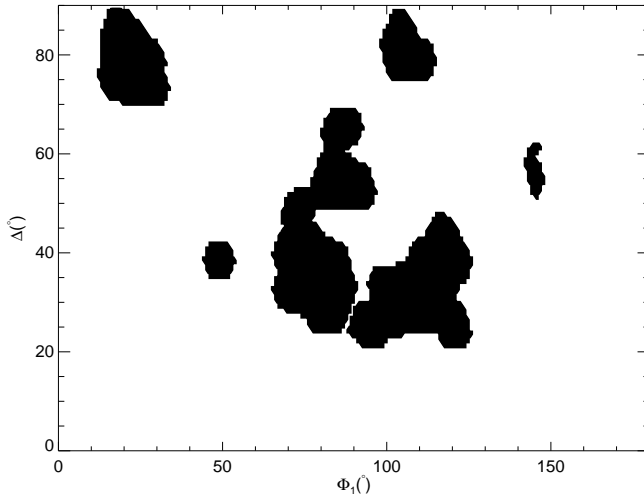


Figure 8.7: $\Phi_1 - \Delta$ parameter space after applying the “non-negative” criterion. All decompositions with positive flux are inside the black areas. All the decompositions outside the black areas have been discarded.

decompositions that are left to study is considerably reduced, since we only consider one representative of each type. For instance, in the 18 – 30 keV range, 1863 decompositions are grouped into 286 types. An example of decompositions that are grouped into one type is given in Fig. 8.8.

The “non-ripples” criterion is then applied. The original pulse profiles in the considered energy ranges have two main peaks. We therefore require the single-pole contributions not to have many more peaks than the original one. A quality function related to the number of peaks in each single-pole pulse profile is defined. The number of peaks of the single-pole pulse profiles are counted. The quality function is defined as the inverse of the total number of peaks. With this method we obtain the decompositions sorted according to their quality function. Higher values of the quality function correspond to decompositions that are simpler, not much more complicated than the original pulse profile. Fig. 8.9 shows the highest ranked profile representatives in the Φ_1 - Δ parameter space. In order to study them we group them into five regions: *A* with $\Phi_1 \in [50^\circ, 105^\circ]$, $\Delta \in [20^\circ, 45^\circ]$, *B* with $\Phi_1 \in [105, 130]$, $\Delta \in [20, 50]$, *C* with $\Phi_1 \in [10, 40]$, $\Delta \in [60, 90]$, *D* with $\Phi_1 \in [130, 180]$, $\Delta \in [50, 65]$, and *E* with $\Phi_1 \in [55, 100]$, $\Delta \in [45, 70]$.

The different decompositions in regions *A*, *B*, *C*, *D* and *E* are studied individually.

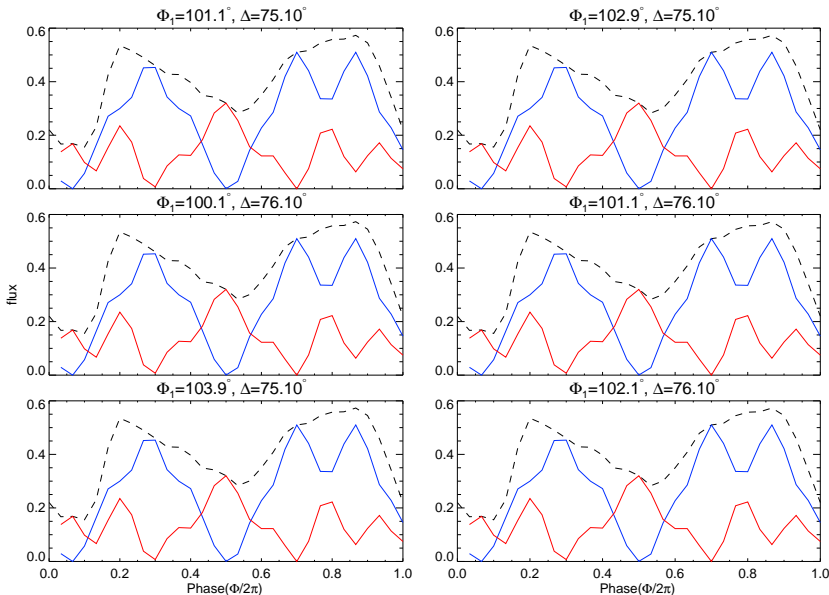


Figure 8.8: Example of similar decompositions grouped in one type. The values of Φ_1 and Δ for each decomposition are shown on the top of each panel.

We require the energy evolution of the single-pole pulse profiles to be as gradual as that of the original pulse profile, and also the single-pole pulse profiles not to be much more complicated than the original profile.

Region A: acceptable decompositions of the original pulse profile into two symmetric functions are plotted in Fig. 8.10. The symmetry points for this decomposition are $\Phi_1 \sim 72^\circ$ and $\Delta \sim 32^\circ$. The two components are not much more complicated than the sum, and do not show strong anti-correlation. This decomposition is the best one of all the decompositions in the $\Phi_1 - \Delta$ plane of Fig. 8.9.

The dotted horizontal line in Fig. 8.10 (and following figures of decompositions) corresponds to the remaining unmodulated flux available to distribute between the two symmetric functions, since the distribution of remaining flux can not be determined from the decomposition. The minima of the two symmetric functions have been shifted to zero, so that the sum of the two symmetric functions plus the unmodulated flux reproduces the original pulse profile.

Regions C and E: the best decompositions for these two regions are shown in

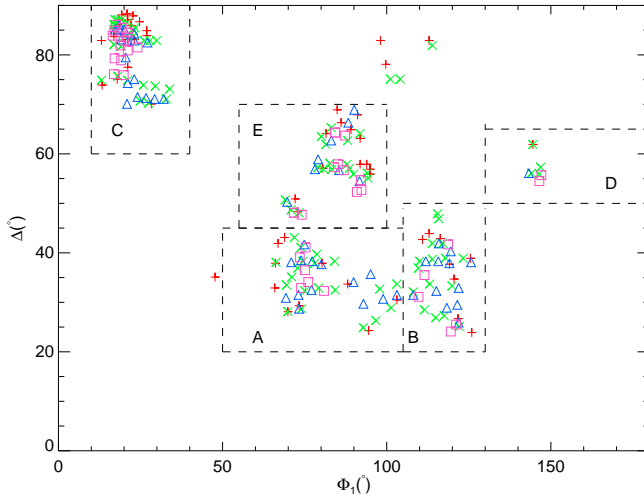


Figure 8.9: Highest ranked decompositions grouped in five regions *A*, *B*, *C*, *D* and *E*. The different symbols represent different energy ranges: $+$: (18.3 – 30.9) keV, \times : (30.9 – 44.5) keV, \triangle : (44.5 – 59.1) keV, \square : (59.1 – 99.8) keV.

Fig. 8.11. They are not “much more” complicated than the sum. However, they have been discarded because they present a very strong anti-correlation in the large features which seems artificial, not expected from two independent emission regions. In region *E*, the best decompositions have $\Phi_1 \sim 82^\circ$ and $\Delta \sim 63^\circ$. For region *C*, $\Phi_1 \sim 25^\circ$ and $\Delta \sim 84^\circ$.

Regions *B* and *D*: the best decompositions for regions *B* and *D* are shown in Fig. 8.12. Those decompositions have also been discarded. The single-pole pulse profiles are more complicated than the sum, and present an anti-correlation in many small features that cancel out in the sum, not likely to be real. In region *B*, $\Phi_1 \sim 121^\circ$, $\Delta \sim 30^\circ$. In region *D*, $\Phi_1 \sim 145^\circ$ and $\Delta \sim 56^\circ$.

Another argument to reject decompositions in regions *C*, *D* and *E* is that they all present high values of Δ . Under the assumption of slightly displaced magnetic poles, smaller values of Δ are expected. This was the case in the analysis of the accreting pulsars Cen X-3 (Kraus et al. 1996) and Her X-1 (Blum & Kraus 2000): the best decompositions were found for small values of Δ .

A further argument to discard regions *B*, *C* and *D* will emerge in the reconstruction of the beam pattern from the single-pole contributions, and will be discussed in Sec. 8.2.3.

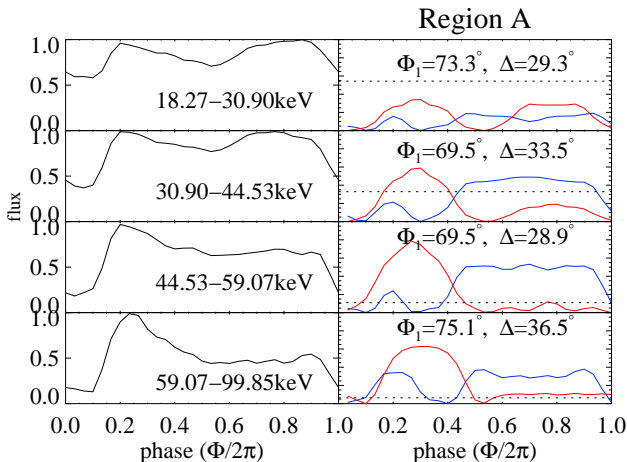


Figure 8.10: Left panel: *HEXTE* pulse profiles in different energy ranges. Right panel: best decomposition for region *A* for one observation. The two symmetric functions are represented in red and blue. The horizontal dashed line represents the unmodulated flux left available to distribute between the two functions. The values of Φ_1 and Δ for each decomposition are given.

The decomposition analysis has also been applied to the merged observations described in Sec. 8.2.1. Adding observations provides better statistics and allows to use more Fourier coefficients, and therefore a more accurate description of the original pulse profiles is obtained. We have made use of 24 Fourier coefficients, and did not consider the highest frequency terms to avoid aliasing. The same regions from Fig. 8.9 are allowed, and similar results as for the analysis using one single observation are obtained. The accepted decomposition of the original pulse profile into two symmetric functions corresponds again to region *A* and is shown in Fig. 8.13. We find $\Phi_1 \sim 73^\circ$ and $\Delta \sim 34^\circ$, consistent with the results from the analysis of one observation.

The decomposition analysis has been performed using a finer energy binning, in seven energy bands 18.6 – 25.2 keV, 25.2 – 34.3 keV, 34.3 – 43.8 keV, 43.8 – 48.3 keV, 48.3 – 60.1 keV, 60.1 – 80.6 keV, 80.1 – 99.8 keV. This has allowed to study the evolution of the different decompositions as a function of the energy, and to confirm that the energy evolution of the accepted decomposition is as smooth as that of the original pulse profile. The decompositions for region *A* are shown in Fig. 8.14, for which $\Phi_1 \sim 64^\circ$, $\Delta \sim 36^\circ$.

Low energy pulse profiles have also been analyzed, using *PCA* data. The energy

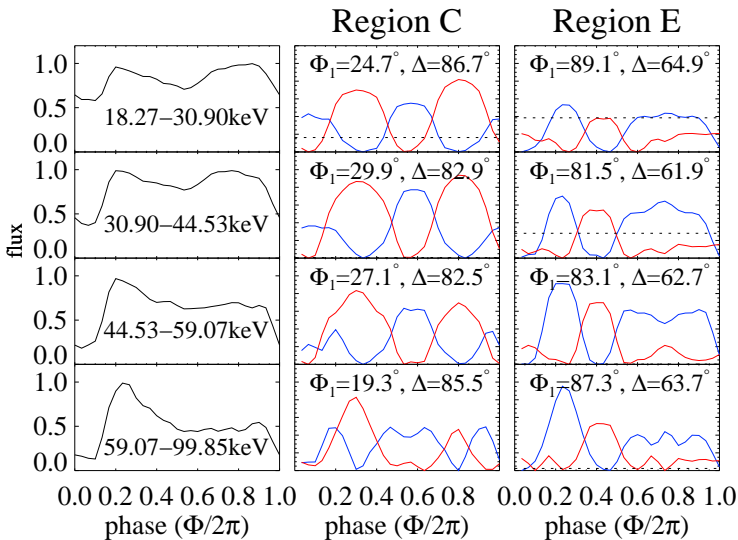


Figure 8.11: Left panel: *HEXTE* pulse profiles. Middle and right panels: best decomposition for regions *C* and *E* in two symmetric functions. The values of Φ_1 and Δ for each energy range are indicated.

ranges 3 – 7 keV, 7 – 11.25 keV, 11.25 – 15.41 keV and 15.41 – 19.19 keV have been used. The pulsed fraction is smaller than at higher energies, e.g. $\sim 24\%$ in the 15 – 20 keV range. The “non-negative” criterion is therefore not very restrictive: almost all the $\Phi_1 - \Delta$ parameter space is allowed. Since the decompositions have to be valid in all energy ranges, we restricted our search to the allowed regions obtained for the *HEXTE* profiles (Fig. 8.7).

As shown in Chapter 6, A 0535+26 pulse profiles are considerably more complicated at lower energies. From the decomposition analysis at lower energies, regions *B*, *C* and *D* can be discarded. The decompositions present many “ripples”, being considerably more complicated than the sum, and also present strong anti-correlations that do not seem real. The only two regions where we find acceptable decompositions, in which a gradual energy evolution is found, are regions *A* and *E*. We will however not make use of *PCA* data during the rest of the analysis, due to the very complex shape of the pulse profiles. However, the fact that we only find acceptable decompositions in region *A* and *E* provides a further argument to discard the decompositions in regions *B*, *C* and *D*. Just as an example, in Fig. 8.15 are shown the best decomposition found for region *A*, with values of $\Phi_1 \sim 77^\circ$ and $\Delta \sim 30^\circ$.

Combining the results of the analysis in different energy ranges and for different

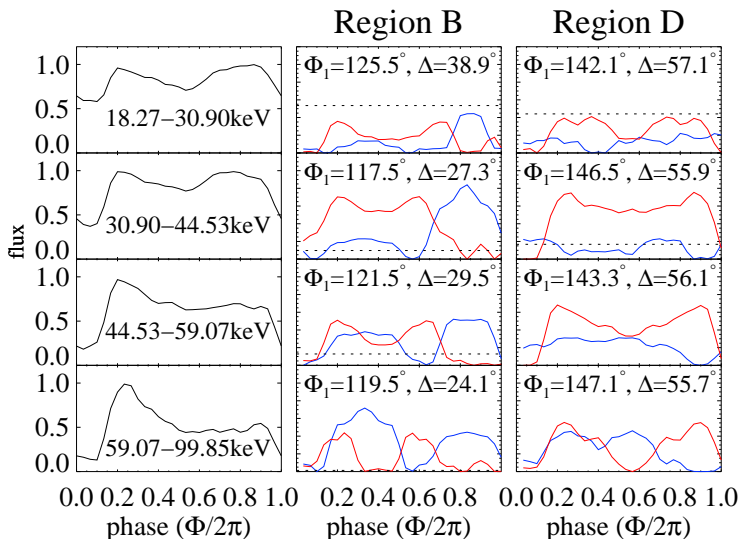


Figure 8.12: Left panel: original pulse profile. Middle and right panels: best decompositions for regions *B* and *D*. The values of Φ_1 and Δ for each energy range are indicated.

observations, we find a best decomposition of the original pulse profile in region *A*. To calculate an average value of the symmetry point Φ_1 and Δ , we use only the results from the analysis in four energy ranges and *HEXTE* data, as in seven energy ranges the statistics for each energy band is worse, and less Fourier coefficients are used. As estimate for the uncertainty of Φ_1 and Δ we take 5° , which is the approximate range in region *A* for which the decompositions are similar. The average values for Φ_1 , Δ and Φ_2 (using Eq. 8.2) are given in Table 8.1.

Table 8.1: Symmetry points and azimuthal displacement of one pole with respect to the antipodal position for the best decomposition of A 0535+26 pulse profiles.

Pole 1	Pole 2	$\Delta = \pi - (\Phi_1 - \Phi_2)$
$\Phi_1 = 72^\circ \pm 5^\circ$	$\Phi_2 = 285^\circ \pm 5^\circ$	$\Delta = 33^\circ \pm 5^\circ$
$\Phi_1 + \pi = 252^\circ \pm 5^\circ$	$\Phi_2 + \pi = 105^\circ \pm 5^\circ$	

8.2.3 From single-pole profiles to geometry and beam pattern

In the previous section, a possible decomposition of the A 0535+26 energy dependent pulse profiles has been found.

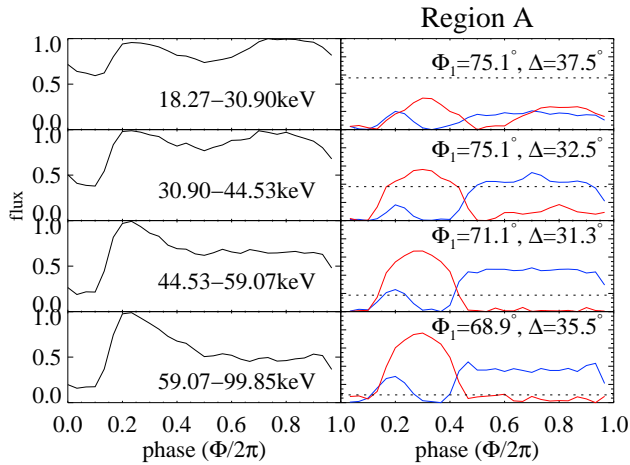


Figure 8.13: Left: original pulse profile from merged observations. Right: best decomposition for region A.

Once a possible decomposition of the energy dependent pulse profiles is found, it is possible to plot the pulse profiles as a function of the auxiliary variable q (Eqs. 8.13, 8.14) to obtain undistorted copies of the beam pattern. An overlapping region between the two sections, as in the case of Cen X-3 (Kraus et al. 1996) or Her X-1 (Blum & Kraus 2000), does not emerge for A 0535+26. However, the two single-pole pulse profiles can almost be connected to each other, with a small gap in between in the beam pattern that remains unobservable to us. This agrees with the assumption of two equal emission regions that show different sections of the same beam pattern. However, contrary to the case of an overlapping region, we can not determine the parameters a and b from a fit. But we can make estimates for the values of a and b . a represents the shift between the two profiles in units of the auxiliary variable q . The best estimate of a using the sections of the beam pattern in all energy ranges is $a = -2.2$. In the case of antipodal poles, $b = 1$ (Eqs. 8.10, 8.11). Since we are assuming small distortion, b should close to 1, and therefore we can make the assumption $b = 1$.

With these estimates for a and b , it is possible to obtain the location of the poles Θ_1 and Θ_2 , from Eqs. 8.15 and 8.16. These equations also involve the direction of observation Θ_0 . Giovannelli et al. (2007) report a value for the inclination of the system of $i = (37 \pm 2)^\circ$. Assuming that the rotation axis of the neutron star is perpendicular to the orbital plane, $i = \Theta_0$. This is often assumed in neutron stars in binary systems (e.g. Ghosh et al. 1977). We can therefore obtain the location of

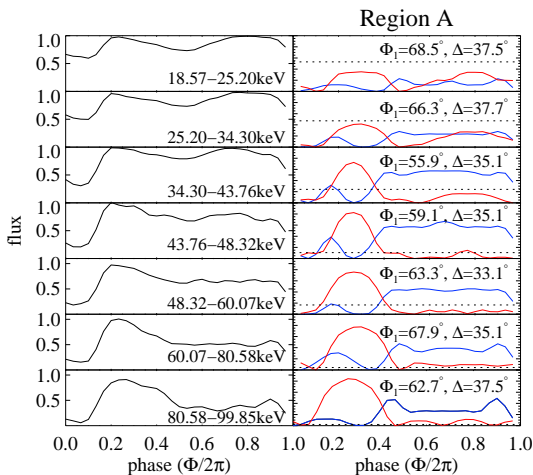


Figure 8.14: Left panel: original pulse profile using one observation in seven energy ranges. Right panel: decomposition for region *A*.

the poles Θ_1 and Θ_2 . The angular distance between the location of the second pole and the point that is antipodal to the first pole δ can be estimated using Eq. 8.3. In Fig. 8.16 the constraints on the geometry of the pulsar are shown. The values of Θ_1 , Θ_2 and δ are represented for all possible values of the direction of observation Θ_0 . The range of possible values of the geometrical parameters are indicated. The obtained values of the geometrical parameters for $i=37^\circ$ are shown in Table 8.2, and sketched in Fig. 8.17.

It is now possible to plot the reconstructed sections of the beam pattern as a function of θ . The two sections of the beam pattern are reconstructed for $\theta \in (13.34^\circ - 87.34^\circ)$ and $\theta \in (92.6^\circ - 166.6^\circ)$. The reconstructed beam pattern is plotted in 8.18 in linear and polar representations.

The decompositions in region *B*, *C*, *D* and *E* were discarded. A further argument against the decompositions in regions *B*, *C* and *D* emerges when trying to reconstruct

Table 8.2: Geometrical parameters of A 0535+26 from the decomposition analysis: polar angles of the two magnetic poles and offset from ideal dipole field.

Pole 1	Pole 2	offset from ideal dipole
$\Theta_1 \approx 50^\circ$	$\Theta_2 \approx 130^\circ$	$\delta \approx 25^\circ$

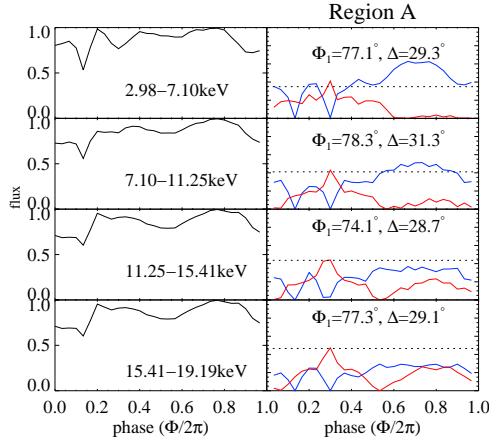


Figure 8.15: Left panel: *PCA* original pulse profiles for one observation. Right panel: best decomposition for region *A* as a function of the energy.

the beam pattern for those regions. It was not possible to find any way to connect the two sections of the beam pattern, so under the assumption of two equal emission regions this provides another argument to discard these decompositions. Region *E*, for which we find the “second best” decomposition, however suggests that the two emission regions are the same, in a similar way as for region *A*. We can connect them with the same values of a and b as in region *A*. This implies the same values for the polar angles of the magnetic poles Θ_1 and Θ_2 . The value of Δ is higher than in region *A*, and therefore also the offset from an ideal dipole field is higher, $\delta \approx 48^\circ$. In Fig. 8.19 the beam patterns for the best decompositions in regions *A* and *E* are represented for comparison. They differ slightly, but the main features of the two functions are similar (the single-pole pulse profiles had also very similar shapes, just different symmetry points).

8.2.4 Interpretation of reconstructed beam pattern

A characteristic feature of the reconstructed beam pattern is a minimum observed in the flux between $\theta \approx 30^\circ - 40^\circ$. This feature is present at all energies and we therefore believe that it could be related to the geometry of the accretion. Filled column models reproduce a beam pattern in which the flux decreases for low values of θ , corresponding to the instant when the observer looks along the accretion stream (Kraus et al. 2003). Introducing a hollow column plus a halo created on the neutron star surface from scattered radiation emitted from the column walls would explain

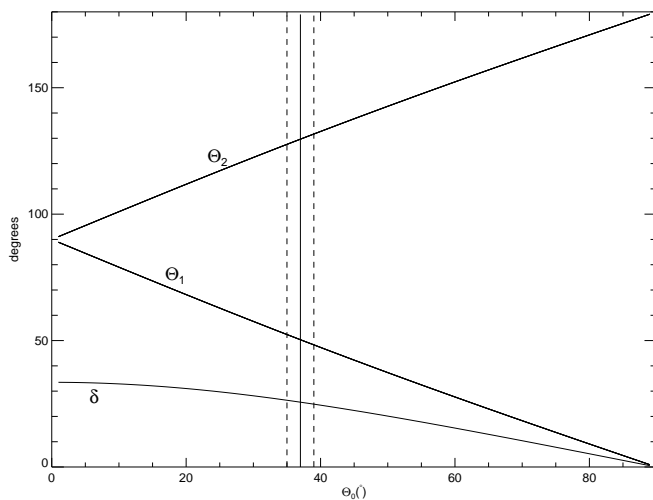


Figure 8.16: Constraints on the pulsar geometry. The vertical lines indicate the orbital inclination (solid line) and its error range (dashed lines).

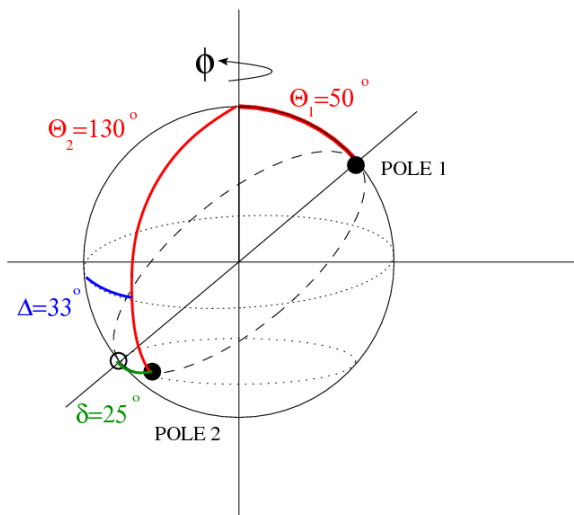


Figure 8.17: Schematic view of A 0535+26 using the values of the pulsar geometry obtained from the decomposition analysis.

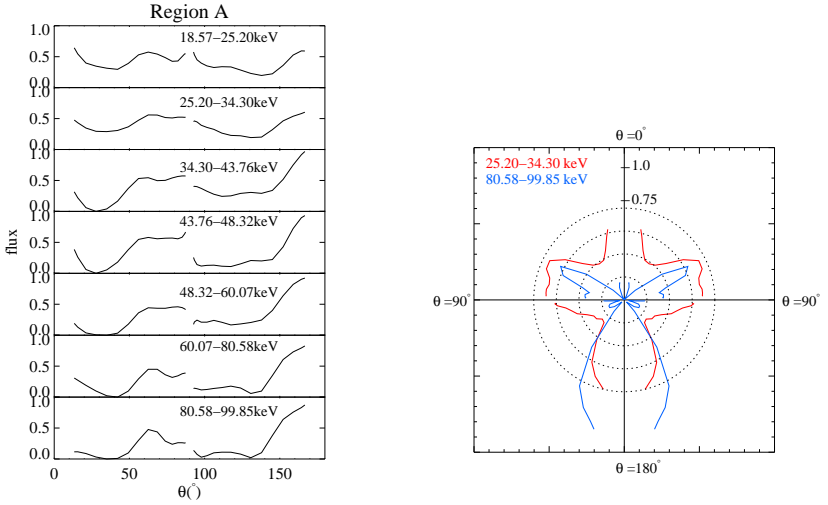


Figure 8.18: Reconstructed beam pattern of A 0535+26. Left panel: beam pattern as a function of the energy in a linear representation. Right panel: beam pattern in polar diagram in the 25.20 – 34.30 keV (red) and 80.58 – 99.85 keV (blue) energy ranges.

the increase in the flux seen for $\theta \lesssim 30 - 40^\circ$, and the minimum at $\theta \approx 30^\circ - 40^\circ$ corresponding to the instant when the observer looks directly into the column.

The steep increase in flux at high values of theta ($\theta > 120^\circ$) could be due to gravitational light bending, which produces a similar feature in model calculations.

To obtain estimates on the size of the accretion column, a model for a hollow column plus a halo has been calculated for $\theta \in [0^\circ, 40^\circ]$. Geometrical models of filled columns, including the formation of a halo around the accretion column, were presented in Kraus et al. (2003), where the relative importance of the different components (halo-column) to the observed flux was studied. In the work presented here, the modeling is performed as in Kraus et al. (2003), but introducing a hollow column. A detailed study of this model will be presented elsewhere. Beam patterns are computed using ray-tracing (Foley et al. 1990) and include relativistic light deflection (Nollert et al. 1989).

The emission of the column wall is assumed to be a black body of temperature T_{eff} , assumed to be isotropic. Part of the radiation that leaves the column hits the neutron star surface, creating a luminous halo around the column walls. This emission is assumed to be thermal. Photon paths are calculated using the Schwarzschild metric.

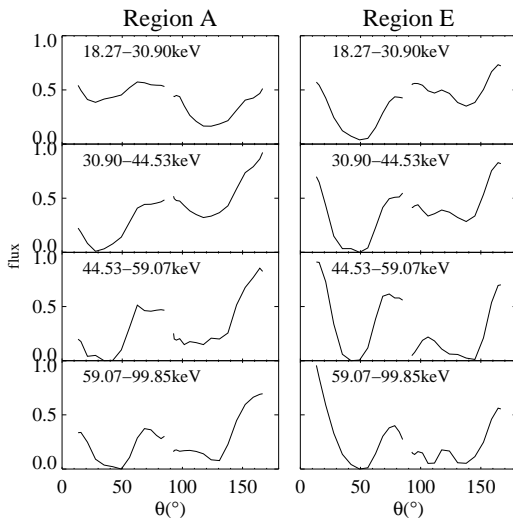


Figure 8.19: Reconstructed beam patterns for regions *A* (left panel) and *E* (right panel).

This is appropriate for A 0535+26 because it is a slowly rotating neutron star ($P_{\text{spin}} \sim 103.4$ s). The Schwarzschild radius is $r_S = 2GM/c^2$. The accretion funnel has an inner half-opening angle α_i and outer half-opening angle α_0 . A radiative shock is assumed to form close to the neutron star surface at radial coordinate r_t . See Fig. 8.20 for a sketch of the geometry of the hollow column. Below the shock, the column is optically thick and radiation is emitted from the inner and outer walls. Above the shock, the accretion is assumed to be in free-fall.

We use the canonical values for the mass and radius of the neutron star, $M_{\text{ns}} = 1.4 M_\odot$ and $r_n = 10$ km. Since we are calculating beam patterns for values of $\theta < 40^\circ$, our results will not change significantly assuming larger values for the neutron star radius, since light deflection is important at large viewing angles. The radiative shock is assumed to be formed at $r_t = 10.5$ km. According to observations of A 0535+26, we take an asymptotic luminosity per pole of $L_\infty = 0.8 \times 10^{37}$ erg s $^{-1}$, and a cyclotron energy (used to calculate the magnetic scattering cross-section) of $E_{\text{cyc}} = 45$ keV at the magnetic pole.

Different models have been computed for different values of the inner and outer half-opening angles, for $E = 7.6$ keV photons for a distant observer ($E = 10$ keV at the neutron star). For each model, the temperature of the Planck spectrum emitted by the column wall and the density that the accreting material has at the base of the free-

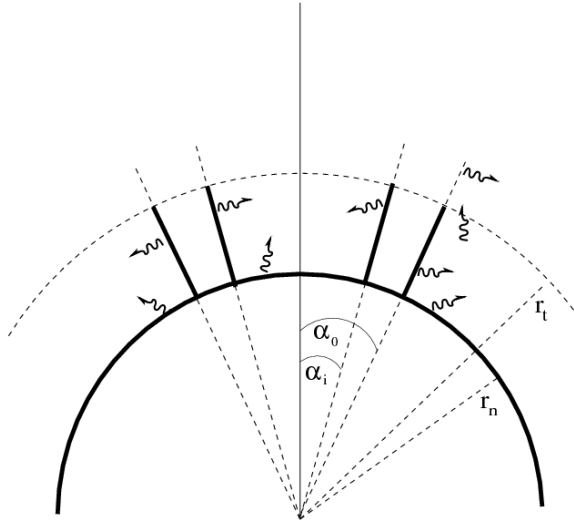


Figure 8.20: Geometrical model of hollow column. Figure adapted from Kraus (2001).

fall section follow from the assumed geometry and the value of L_∞ . The parameters used for each model are listed in Table 8.3. Results from the model calculations are shown in Fig. 8.21.

By comparing the A 0535+26 reconstructed beam pattern (Fig. 8.18 left) with the models in Fig. 8.21, it can be seen that the shape of the models reproduce well the shape of the reconstructed beam pattern. We can estimate the half-opening angle and column thickness to be $\alpha_o = 0.2 \text{ rad} \sim 11.5^\circ$ and $\alpha_o - \alpha_i = 0.06 \text{ rad} \sim 3.4^\circ$.

Using these values for the outer half-opening angle $\alpha_o = 0.2 \text{ rad}$ and thickness of the wall $\alpha_o - \alpha_i = 0.06 \text{ rad}$, (model 5 from Table 8.3), we investigated the energy

Table 8.3: Model parameters used in the computation of beam patterns for A 0535+26, for $\theta \in [0^\circ, 40^\circ]$.

model	α_i (rad)	α_o (rad)	kT (keV)	ρ ($10^{-5} \text{ g/cm}^{-3}$)
1	0.08	0.1	4.1	16
2	0.06	0.1	4.1	9
3	0.04	0.1	4.1	6.8
4	0.09	0.15	3.7	4
5	0.14	0.2	3.5	2.8

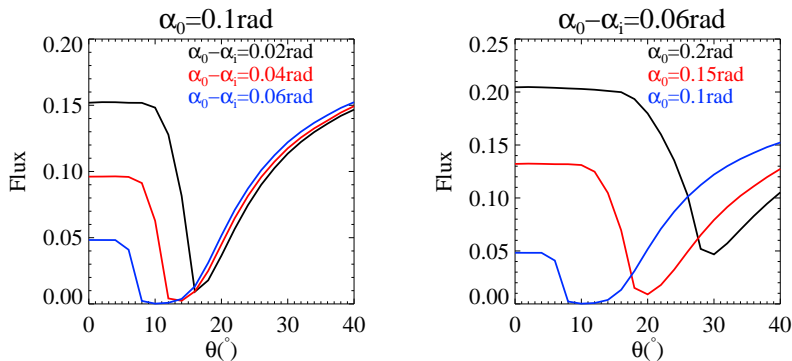


Figure 8.21: Beam pattern models for hollow column with halo for different column thickness and the same outer opening angle α_o (left panel) and different opening angles with same column thickness $\alpha_o - \alpha_i$ (right panel), calculated for $\theta \in [0^\circ, 40^\circ]$.

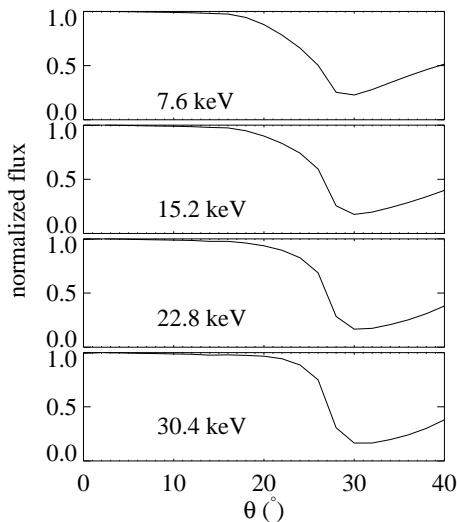


Figure 8.22: Computed beam patterns for different photon energies, taking the outer opening angle $\alpha_o = 0.6$ rad and a column thickness $\alpha_o - \alpha_i = 0.06$ rad.

dependence of the computed beam patterns. We calculated beam patterns for photon energies $E = 10$ keV, $E = 20$ keV, $E = 30$ keV and $E = 40$ keV at the neutron

star (or $E = 7.6$ keV, $E = 15.2$ keV, $E = 22.8$ keV and $E = 30.4$ keV for a distant observer). The computed beam patterns for different photon energies are shown in Fig. 8.22. It can be seen that the position and the depth of the minimum in the curves are very weakly energy dependent. This supports our statement that the minimum can be regarded mainly as a geometric effect.

We have found that a geometrical model of a hollow column which includes scattered radiation on the surface of the neutron star can be applied to A 0535+26. We would like to stress however that the model used is a simplified model, which we not claim to be true in detail, but however reproduces well the basic shape of the energy dependent reconstructed beam pattern of A 0535+26 for values of $\theta < 40^\circ$.

Summary and Conclusions

9.1 Summary

In this work, the timing and spectral properties of the accreting Be/X-ray binary A 0535+26 during a normal (type I) outburst have been investigated. The analysis is based on observations performed with the *RXTE* and *INTEGRAL* observatories, which cover the $\sim 3 - 200$ keV energy band.

One of the most important results of this work has been the measurement of the fundamental cyclotron line at $E \sim 46$ keV and the first harmonic at $E \sim 102$ keV. This measurement firmly establishes the magnetic field of the neutron star at the site of the X-ray emission to be $B \sim 5 \times 10^{12}$ G, putting end to a long debate. In fact, the fundamental line at $E \sim 46$ keV was discovered during a giant outburst in 1989 with *HEXE* (Kendziorra et al. 1994). However, later observations with *OSSE* during the 1994 giant outburst could not confirm this result (Grove et al. 1995), and measured the fundamental line at $E \sim 110$ keV, probably due to the $\sim 40-50$ keV energy threshold of the *OSSE* instrument. Our observations put end to this debate, confirming the earlier results from Kendziorra et al. (1994).

The *RXTE* observations have allowed to study, for the first time, the evolution of the cyclotron line energy with the X-ray luminosity for A 0535+26. Recently, for the accreting pulsars 4U 0115+64 and V 0332+53, a negative correlation between the cyclotron line energy with the X-ray luminosity has been discovered. This correlation agrees with the theory developed by Basko & Sunyaev (1976), that assumes the formation of a radiative shock in the accretion column for high luminosity sources in the super-Eddington regime. An increase in the accretion rate moves the radiative shock upwards, further away from the neutron star surface. Therefore, an increase in the accretion rate is correlated with an increase in the height of the shock, and therefore with a decrease in the magnetic field and cyclotron energy. On the other hand, in the case of Her X-1 a positive correlation between the cyclotron line energy and the luminosity has been discovered (Staubert et al. 2007). For sources in the sub-Eddington

regime an increase in the accretion rate is expected to “push” the matter closer to the neutron star surface, and therefore a positive correlation between the accretion rate and the magnetic field (or cyclotron line) should emerge. The evolution of the cyclotron line energy of A 0535+26 with the X-ray luminosity has been studied in this context. We found, contrary to the sources mentioned before, no changes of the cyclotron line energy with the luminosity, suggesting that the line forming region does not change with the mass accretion rate of the system.

We have studied the evolution of the pulse period along the outburst. During the beginning of the outburst the pulse period remains constant within uncertainties. Starting around the periastron, we measure a spin-up rate of $\dot{P} = -1.69 \times 10^{-8} \pm 0.04$ s/s (at MJD 53618). This is the first time that a spin-up rate is measured for A 0535+26 during a normal outburst, and therefore the first time there is evidence for an accretion disk around the neutron star during a normal outburst.

We have also studied the energy dependent pulse profiles of A 0535+26 during the *main outburst* (excluding a *pre-outburst flare* that we studied independently). Similar to other accreting X-ray pulsars, the pulse profiles exhibit a complex shape at lower energies ($\sim 3 - 20$ keV), while at higher energies the pulse profile evolves towards a simpler double-peak shape. Above the fundamental cyclotron energy one of the peaks is strongly reduced. This has been interpreted as due to the presence of a “fan beam” emission component during the main outburst. The scattering cross section for extraordinary photons (propagating perpendicular to the magnetic field) is smaller than that of ordinary photons (propagating parallel to the field) for energies below the cyclotron energy. Therefore, extraordinary photons escape effectively perpendicular to the magnetic field, across the column walls. However, for energies above the cyclotron energy both cross-sections are approximately equal, and photons can only escape from smaller optical depths. The “fan-beam” component weakens, explaining the disappearance of one of the peaks in the pulse profiles above $E \sim 46$ keV.

We have studied the evolution of the cyclotron line energy with the pulse phase. We find a change of the cyclotron line with the pulse phase (smaller than in other sources), with a lower cyclotron line energy during the main peak of the pulse profile $E_{\text{cyc},1} = 43_{-0.9}^{+0.9}$ keV, and a higher cyclotron line energy $E_{\text{cyc},2} = 48.4_{-1.3}^{+1.4}$ keV during the pulse phase in which a secondary peak disappears when crossing the cyclotron energy. This agrees with the “fan-beam” pattern proposed above. The presence of a shock explains the lower magnetic field we measure when looking directly into the polar cap. The higher magnetic field is observed about half a pulse phase later, corresponding to the instant when we look perpendicular to the accretion column, where we can observe closer to the neutron star surface. We find also a harder spectrum during the main peak of the outburst, which agrees with the proposed “fan beam” scenario. Harder photons, originated closer to the polar cap, escape more effectively in the direction parallel to the magnetic field, explaining the hardening of the spectrum in

the phase corresponding to the main peak and the softening in the other rotational phases.

We have compared the energy dependent pulse profiles obtained during the *main outburst* with historical observations from the 1980, 1989 and 1994 giant outbursts. The basic features of the pulse profiles remain constant over time, suggesting that the main accretion geometry of the neutron star did not change significantly in more than 20 years.

The *Swift-BAT* light curve of the outburst has revealed flaring activity during the rise to the peak of the outburst. The flux evolution becomes smoother after the periastron passage, coincident with the beginning of the spin-up of the neutron star. *RXTE* performed three observations during one of these flares. The pulse profiles exhibit significant differences during the flare compared to the rest of the outburst, and the cyclotron line energy is measured at a position more than 10% higher during the flare compared to the rest of the outburst, pointing to a higher magnetic field. The observed flaring activity and associated changes in the pulse profiles and cyclotron line energy have been explained in terms of a theoretical model. A 0535+26 is on the verge of low-mode magnetospheric instabilities, causing the matter accumulated in the thin boundary layer between the neutron star accretion disk and the magnetosphere to rapidly fall onto the neutron star surface. The matter is channeled by different field lines than those along which quasi-stationary accretion takes place, explaining the different pulse profiles observed. The matter falls closer to the neutron star surface, which explains the higher magnetic field measured during the flares. Once the neutron star starts spinning up, the amount of mass accumulated in the boundary layer is strongly reduced. Therefore, the amount of matter available for unstable accretion is reduced. This explains the lack of flaring activity during the spin-up phase of the neutron star. Once the neutron star stops spinning-up, flaring activity would be expected in this model, and there are actually hints for that in the *BAT* light curve of the outburst.

During the *pre-outburst flare*, contrary to the observations during the *main outburst*, no strong change of the energy dependent pulse profiles takes place across the cyclotron energy. This suggests that the emission forms a “pencil beam” pattern, with no radiative shock formed in the accretion column. The scattering cross-section of the ordinary photons evolves smoothly across the cyclotron resonance, explaining the smooth evolution of the pulse profiles.

Our observations provide therefore the first observational evidence for low-mode magnetospheric instabilities in A 0535+26. The model proposed in this work is generic and can be applied to other transients. To apply this model, the source must be on the verge of low-mode instability. This depends on several parameters, like the neutron star magnetic field, the spin-period or the accretion rate. It is possible then that for many sources the transition from propeller to accretion regime takes place without

flaring activity and instabilities being observed.

In the second part of the work, a decomposition analysis has been applied to A 0535+26 energy-dependent pulse profiles. The decomposition method is a backwards process: starting from the observed pulse profiles, a decomposition of the pulse profiles in two single-pole components is obtained. Then, from the single-pole pulse profiles, information on the geometry of the system and on the beam pattern is extracted. The method is based on symmetry considerations, and several assumptions are made. The first assumption is that the magnetic field has a dipole structure, with axisymmetric emission regions. This makes necessarily the single pole profiles symmetric. The asymmetry in the total pulse profile is introduced by a small offset of one of the magnetic poles with respect to the antipodal position.

We find a physically acceptable decomposition of the pulse profiles of A 0535+26 that allows us to extract information on the geometry of the pulsar. We obtain $\Theta_1 \approx 50^\circ$ and $\Theta_2 \approx 130^\circ$ for the position of the magnetic poles with respect to the rotation axis, and an offset of $\delta \approx 25^\circ$ from one of the poles with respect to its antipodal position.

The visible section of the beam pattern has been reconstructed. A characteristic feature of the reconstructed beam pattern at all energies is a minimum observed in the flux between $\theta \approx 30^\circ - 40^\circ$, where θ is the angle between the direction of observation and the magnetic axis. This has been interpreted in terms of a simple geometrical model that includes relativistic light deflection. The model includes a hollow column emitting isotropically black body radiation, plus a thermal halo created on the neutron star surface around the column from scattered radiation emitted from the column walls. Another characteristic feature of the reconstructed beam pattern is a steep increase in flux at high values of θ ($\theta > 120^\circ$). This could be due to gravitational light bending, which produces a similar feature in model calculations.

The results presented in this work have been published in Caballero et al. (2007), Caballero et al. (2008b), Postnov et al. (2008), as well as in conference proceedings (Caballero et al. 2008a, Caballero et al. 2009).

9.2 Outlook

The evolution of the cyclotron energy with the X-ray luminosity of A 0535+26 has been studied for observations at luminosities $L_X \lesssim 10^{37} \text{ erg s}^{-1}$ during a normal (type I) outburst. The only observations of the fundamental cyclotron line during a giant outburst were performed with *HEXE* in 1989 (Kendziorra et al. 1994), but the large uncertainties do not allow to determine any correlation. Therefore, new observations of A 0535+26 with a modern X-ray satellite during a giant outburst might reveal a positive or negative correlation of the cyclotron line with the luminosity.

Target of Opportunity proposals have been approved with *INTEGRAL*, *RXTE* (PI. Caballero) and *Suzaku* (PI. Pottschmidt) to observe A 0535+26 during a giant or normal outburst.

Since the December 2005 weak outburst until the end of 2008, A 0535+26 has been mainly in quiescence. However, new activity during the periastron passages in September 2008 and January 2009 is seen in the *Swift-BAT* light curve (see Fig. 9.1). Flaring activity, predicted by the low-mode magnetospheric instability proposed in this work for A 0535+26, is seen after both outbursts. *RXTE* performed one observation during the decay of the second outburst, starting at MJD 54844. However, the low flux level ($F_{(3-50)\text{ keV}} \sim 6\text{ mCrab}$) and short observation time ($\sim 2\text{ ks}$) do not allow to significantly detect cyclotron lines in the spectrum.

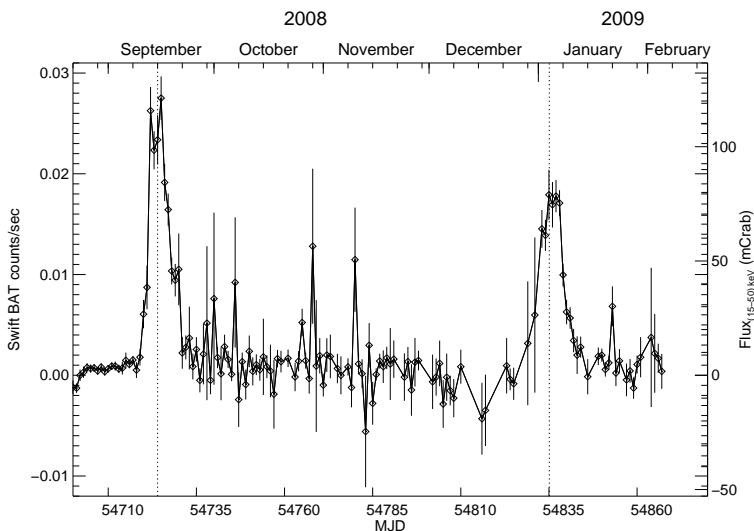


Figure 9.1: *Swift-BAT* light curve of A 0535+26 between August 2008 and February 2009. The dotted lines indicated the time of the periastron passage. Two weak outbursts are seen at each periastron passage. Flaring activity after both outbursts is also apparent.

The energy dependent pulse profiles of accreting neutron stars are still today, after more than three decades of observations, not understood. A systematic analysis of pulse profiles of a large sample of sources, applying the decomposition method used in this thesis, would be a step forward in understanding the general picture of pulse profile formation. It would allow to check if for a larger sample of sources the assumptions made in this work are supported by the data, and to study and compare the

inferred geometry and beam patterns of the different systems.

Theoretical models for cyclotron lines and the X-ray continuum will help to reach a better understanding of the physical properties of magnetized plasmas and the physics of accretion onto neutron stars. Both `cyclomc` (Schönherr et al. 2007) and the Becker & Wolff (2007) models will be applied to A 0535+26. An in-depth analysis of the application of these two models to A 0535+26 observations, and a careful interpretation of the results, requires a dedicated analysis that will be performed in the future. The existence of theoretical models, together with high quality data provided by X-ray observatories like *RXTE*, *INTEGRAL* or *Suzaku*, and the future X-ray missions like *Simbol-X* (Ferrando et al. 2006), *NuSTAR* (Harrison et al. 2005), *ASTRO-H* (Takahashi et al. 2008) or *IXO* (White & Hornschemeier 2009), will certainly bring new light into the understanding of these fascinating objects, unique laboratories of physics under extreme conditions.

Bibliography

- Abdo, A. A. et al. 2008, *Science*, 322, 1218
- Araya, R. A. & Harding, A. K. 1999, *ApJ*, 517, 334
- Araya-Góchez, R. A. & Harding, A. K. 2000, *ApJ*, 544, 1067
- Arnaud, K. A. 1996, in *Astronomical Society of the Pacific Conference Series*, Vol. 101, *Astronomical Data Analysis Software and Systems V*, ed. G. H. Jacoby & J. Barnes, 17
- Arons, J. & Lea, S. M. 1976, *ApJ*, 207, 914
- Arons, J. & Lea, S. M. 1980, *ApJ*, 235, 1016
- Avni, Y. 1976, *ApJ*, 210, 642
- Baade, W. & Zwicky, F. 1934, *Phys. Rev.*, 46, 76
- Baan, W. A. 1979, *ApJ*, 227, 987
- Barcons, X., Carrera, F. J., Ceballos, M. T., et al. 2007, *A&A*, 476, 1191
- Barnstedt, J., Staubert, R., Santangelo, A., et al. 2008, *A&A*, 486, 293
- Barthelmy, S. D., Barbier, L. M., Cummings, J. R., et al. 2005, *Space Science Reviews*, 120, 143
- Basko, M. M. & Sunyaev, R. A. 1976, *MNRAS*, 175, 395
- Becker, P. A. 1998, *ApJ*, 498, 790
- Becker, P. A. & Wolff, M. T. 2005, *ApJ*, 630, 465
- Becker, P. A. & Wolff, M. T. 2007, *ApJ*, 654, 435
- Bevington, P. & Robinson, D. 1992, *Data Reduction and Error Analysis for the Physical Sciences* (Boston:McGraw-Hill)
- Bhattacharya, D. & van den Heuvel, E. P. J. 1991, *Physics Report*, 203, 1
- Bhattacharyya, S. & Strohmayer, T. E. 2007, *ApJ*, 664, L103
- Bildsten, L., Chakrabarty, D., Chiu, J., et al. 1997, *ApJ*, 113, 367
- Blum, S. & Kraus, U. 2000, *ApJ*, 529, 968
- Boella, G., Butler, R. C., Perola, G. C., et al. 1997, *A&AS*, 122, 299
- Bradt, H. V., Rothschild, R. E., & Swank, J. H. 1993, *A&AS*, 97, 355
- Burderi, L., di Salvo, T., Riggio, A., Papitto, A., & Menna, M. T. 2008, in *American Institute of Physics Conference Series*, Vol. 1068, *American Institute of Physics Conference Series*, 17–24
- Burderi, L., Di Salvo, T., Robba, N. R., La Barbera, A., & Guainazzi, M. 2000, *ApJ*, 530, 429
- Burnard, D. J., Arons, J., & Klein, R. I. 1991, *ApJ*, 367, 575
- Burnard, D. J., Klein, R. I., & Arons, J. 1988, *ApJ*, 324, 1001
- Caballero, I., Kraus, U., Postnov, K., et al. 2009, 7th INTEGRAL workshop "An INTEGRAL View of Compact Objects" - Submitted to *Proceedings of Science*
- Caballero, I., Kretschmar, P., Santangelo, A., et al. 2008a, arXiv:0801.3897, proceedings of the 6th INTEGRAL Workshop "The Obscured Universe", Published by ESA, 2007, SP-622, P.471-474.
- Caballero, I., Kretschmar, P., Santangelo, A.,

- et al. 2007, *A&A*, 465, L21
- Caballero, I., Santangelo, A., Kretschmar, P., et al. 2008b, *A&A*, 480, L17
- Cackett, E. M., Miller, J. M., Bhattacharyya, S., et al. 2008, *ApJ*, 674, 415
- Camenzind, M. 1990, in *Reviews in Modern Astronomy*, Vol. 3, *Reviews in Modern Astronomy*, ed. G. Klare, 234–265
- Camero Arranz, A., Wilson, C. A., Connell, P., et al. 2005, *A&A*, 441, 261
- Caroli, E., Stephen, J. B., di Cocco, G., Natalucci, L., & Spizzichino, A. 1987, *Space Science Reviews*, 45, 349
- Chadwick, J. 1932, *Nat*, 129, 312
- Clark, G. W., Woo, J. W., Nagase, F., Makishima, K., & Sakao, T. 1990, *ApJ*, 353, 274
- Coburn, W., Heindl, W. A., Gruber, D. E., et al. 2001, *ApJ*, 552, 738
- Coburn, W., Heindl, W. A., Rothschild, R. E., et al. 2002, *ApJ*, 580, 394
- Coe, M. J. 2000, in *Astronomical Society of the Pacific Conference Series*, Vol. 214, *IAU Colloq. 175: The Be Phenomenon in Early-Type Stars*, ed. M. A. Smith, H. F. Henrichs, & J. Fabregat, 656
- Coe, M. J., Reig, P., McBride, V. A., Galache, J. L., & Fabregat, J. 2006, *MNRAS*, 368, 447
- Cook, W. R., Finger, M., Prince, T. A., & Stone, E. C. 1984, *IEEE Transactions on Nuclear Science*, 31, 771
- Cottam, J., Paerels, F., & Mendez, M. 2002, *Nat*, 420, 51
- Davidson, K. & Ostriker, J. P. 1973, *ApJ*, 179, 585
- de Loore, C., Giovannelli, F., van Dessel, E. L., et al. 1984, *A&A*, 141, 279
- Duncan, R. C. & Thompson, C. 1992, *ApJ*, 392, L9
- Elsner, R. F. & Lamb, F. K. 1976, *Nat*, 262, 356
- Elsner, R. F. & Lamb, F. K. 1977, *ApJ*, 215, 897
- Elsner, R. F., Weisskopf, M. C., Apparao, K. M. V., et al. 1985, *ApJ*, 297, 288
- Fabbiano, G., Evans, I., Evans, J., et al. 2007, in *Astronomical Society of the Pacific Conference Series*, Vol. 376, *Astronomical Data Analysis Software and Systems XVI*, ed. R. A. Shaw, F. Hill, & D. J. Bell, 172
- Fabian, A. C., Rees, M. J., Stella, L., & White, N. E. 1989, *MNRAS*, 238, 729
- Falanga, M. 2008, in *American Institute of Physics Conference Series*, Vol. 1054, *American Institute of Physics Conference Series*, 157–171
- Ferrando, P., Arnaud, M., Briel, U., et al. 2006, in *Presented at the Society of Photo-Optical Instrumentation Engineers (SPIE) Conference*, Vol. 6266, *Space Telescopes and Instrumentation II: Ultraviolet to Gamma Ray*. Edited by Turner, Martin J. L.; Hasinger, Günther. *Proceedings of the SPIE*, Volume 6266, pp. 62660F (2006).
- Ferrigno, C., Segreto, A., Santangelo, A., et al. 2007, *A&A*, 462, 995
- Ferrigno, C. et al. 2009, *A&A*, submitted
- Finger, M. H., Bildsten, L., Chakrabarty, D., et al. 1999, *ApJ*, 517, 449
- Finger, M. H., Camero-Arranz, A., Kretschmar, P., Wilson, C., & Patel, S. 2006, in *Bulletin of the American Astronomical Society*, Vol. 38, *Bulletin of the American Astronomical Society*, 359
- Finger, M. H., Cominsky, L. R., Wilson, R. B., Harmon, B. A., & Fishman, G. J. 1994a, in *AIP Conf. Proc. 308: The Evolution of X-ray Binaries*, ed. S. Holt & C. S. Day, 459
- Finger, M. H., Wilson, R. B., & Hagedorn, K. S. 1994b, *IAU Circ.*, 5931
- Finger, M. H., Wilson, R. B., & Harmon, B. A. 1994c, *IAU Circ.*, 5934, 1
- Finger, M. H., Wilson, R. B., & Harmon, B. A. 1996, *ApJ*, 459, 288

- Fishman, G. J., Meegan, C. A., Wilson, R. B., et al. 1989, in *Bulletin of the American Astronomical Society*, Vol. 21, *Bulletin of the American Astronomical Society*, 860
- Foley, J., van Dam, A., Feiner, S., & J., H. 1990, *Computer Graphics: Principles and Practice* (Addison-Wesley)
- Frank, J., King, A., & Raine, D. 1992, *Accretion Power in Astrophysics* (ISBN 0521408636, Cambridge University Press, 1992.)
- Fraser, G. W. 1989, *X-ray detectors in astronomy* (Cambridge and New York, Cambridge University Press, 1989, 312 p.)
- Friedman, H., Lichtman, S. W., & Byram, E. T. 1951, *Phys. Rev.*, 83, 1025
- Fritz, S., Kreykenbohm, I., Wilms, J., et al. 2006, *A&A*, 458, 885
- Frontera, F., dal Fiume, D., Morelli, E., & Spada, G. 1985, *ApJ*, 298, 585
- Galloway, D. 2007, in *Astronomical Society of the Pacific Conference Series*, Vol. 362, *The Seventh Pacific Rim Conference on Stellar Astrophysics*, ed. Y. W. Kang, H.-W. Lee, K.-C. Leung, & K.-S. Cheng, 105
- Gehrels, N., Chincarini, G., Giommi, P., et al. 2005, *ApJ*, 621, 558
- Gehrels, N., Crannell, C. J., Orwig, L. E., et al. 1988, *Sol. Phys.*, 118, 233
- Ghosh, P. & Lamb, F. K. 1978, *ApJ*, 223, L83
- Ghosh, P. & Lamb, F. K. 1979a, *ApJ*, 232, 259
- Ghosh, P. & Lamb, F. K. 1979b, *ApJ*, 234, 296
- Ghosh, P., Pethick, C. J., & Lamb, F. K. 1977, *ApJ*, 217, 578
- Giacconi, R., Branduardi, G., Briel, U., et al. 1979, *ApJ*, 230, 540
- Giacconi, R., Gursky, H., Kellogg, E., Schreier, E., & Tananbaum, H. 1971a, *ApJ*, 167, L67+
- Giacconi, R., Gursky, H., Paolini, F. R., & Rossi, B. B. 1962, *Physical Review Letters*, 9, 439
- Giacconi, R., Kellogg, E., Gorenstein, P., Gursky, H., & Tananbaum, H. 1971b, *ApJ*, 165, L27
- Giangrande, A., Giovannelli, F., Bartolini, C., Guarnieri, A., & Piccioni, A. 1980, *ApJ*, 40, 289
- Giovannelli, F., Bernabei, S., Rossi, C., & Sabau-Graziati, L. 2007, *A&A*, 475, 651
- Giovannelli, F. & Graziati, L. S. 1992, *Space Science Reviews*, 59, 1
- Gold, T. 1968, *Nat*, 218, 731
- Goldreich, P. & Julian, W. H. 1969, *ApJ*, 157, 869
- Gottesman, S. R. & Fenimore, E. E. 1989, *Appl. Opt.*, 28, 4344
- Grimm, H.-J., Gilfanov, M., & Sunyaev, R. 2002, *A&A*, 391, 923
- Grove, J. E., Strickman, M. S., Johnson, W. N., et al. 1995, *ApJ*, 438, L25
- Grundstrom, E. D., Boyajian, T. S., Finch, C., et al. 2007, *ApJ*, 660, 1398
- Harding, A. K. & Lai, D. 2006, *Reports on Progress in Physics*, 69, 2631
- Harrison, F. A., Christensen, F. E., Craig, W., et al. 2005, *Experimental Astronomy*, 20, 131
- Hayasaki, K. & Okazaki, A. T. 2006, *MNRAS*, 372, 1140
- Heindl, W., Coburn, W., Kreykenbohm, I., & Wilms, J. 2003, *The Astronomer's Telegram*, 200, 1
- Heindl, W. A. & Chakrabarty, D. 1999, in *Highlights in X-ray Astronomy*, ed. B. Aschenbach & M. J. Freyberg, 25
- Heindl, W. A., Coburn, W., Gruber, D. E., et al. 1999, *ApJ*, 521, L49
- Heindl, W. A., Coburn, W., Gruber, D. E., et al. 2001, *ApJ*, 563, L35
- Heindl, W. A., Rothschild, R. E., Coburn, W., et al. 2004, in *American Institute of Physics Conference Series*, Vol. 714, *X-ray Timing 2003: Rossi and Beyond*, ed. P. Kaaret, F. K. Lamb, & J. H. Swank, 323–330
- Hewish, A., Bell, S. J., Pilkington, J. D., Scott,

- P. F., & Collins, R. A. 1968, *Nat*, 217, 709
- Hill, A. B., Bird, A. J., Dean, A. J., et al. 2007, *MNRAS*, 381, 1275
- Hudec, R. 1975, Zentralinstitut fuer Astrophysik Sternwarte Sonneberg Mitteilungen ueber Veraenderliche Sterne, 7, 29
- Iben, I. J. 1991, *ApJ*, 76, 55
- Iben, I. J. 1998, *Sky Telesc.*, 95, 42
- Iben, I. J. & Tutukov, A. V. 1997, *Sky Telesc.*, 94, 36
- Illarionov, A. F. & Sunyaev, R. A. 1975, *A&A*, 39, 185
- Inoue, H. 1975, *PASJ*, 27, 311
- Inoue, H., Kunieda, H., White, N., et al. 2005, *ATel*, 613
- Jahoda, K., Swank, J. H., Giles, A. B., et al. 1996, in *Proc. SPIE Vol. 2808, EUV, X-Ray, and Gamma-Ray Instrumentation for Astronomy VII*, ed. O. H. Siegmund & M. A. Gummin, 59–70
- Jansen, F., Lumb, D., Altieri, B., et al. 2001, *A&A*, 365, L1
- Jensen, P. L., Clausen, K., Cassi, C., et al. 2003, *A&A*, 411, L7
- Kendziorra, E., Kretschmar, P., Pan, H. C., et al. 1994, *A&A*, 291, L31
- Kendziorra, E., Mony, B., Kretschmar, P., et al. 1992, in *The Compton Observatory Science Workshop*, ed. C. R. Shrader, N. Gehrels, & B. Dennis, 217
- Kirsch, M. G., Briel, U. G., Burrows, D., et al. 2005, in *UV, X-Ray, and Gamma-Ray Space Instrumentation for Astronomy XIV. Proceedings of the SPIE, Volume 5898*, ed. O. H. W. Siegmund, 22–33
- Kiziloglu, U., Kiziloglu, N., Baykal, A., Yerli, S. K., & Ozbey, M. 2008, *Information Bulletin on Variable Stars*, 5865, 1
- Klochkov, D., Horns, D., Santangelo, A., et al. 2007, *A&A*, 464, L45
- Klochkov, D., Santangelo, A., Staubert, R., & Ferrigno, C. 2008a, *A&A*, 491, 833
- Klochkov, D., Staubert, R., Postnov, K., et al. 2008b, *A&A*, 482, 907
- Knoll, G. F. 2000, *Radiation detection and measurement 3rd ed.* (New York, NY: Wiley, 802 p. ISBN 0471073385)
- Kraus, U. 1998, in *Relativistic Astrophysics*, 66–81
- Kraus, U. 2001, *ApJ*, 563, 289
- Kraus, U., Blum, S., Schulte, J., Ruder, H., & Meszaros, P. 1996, *ApJ*, 467, 794
- Kraus, U., Nollert, H.-P., Ruder, H., & Riffert, H. 1995, *ApJ*, 450, 763
- Kraus, U., Zahn, C., Weth, C., & Ruder, H. 2003, *ApJ*, 590, 424
- Kretschmar, P. 1996, PhD thesis, Universität Tübingen
- Kretschmar, P., Kreykenbohm, I., Pottschmidt, K., et al. 2005, *ATel*, 601
- Kreykenbohm, I. 2004, PhD thesis, Universität Tübingen
- Kreykenbohm, I., Coburn, W., Wilms, J., et al. 2002, *A&A*, 395, 129
- Kreykenbohm, I., Wilms, J., Coburn, W., et al. 2004, *A&A*, 427, 975
- Kreykenbohm, I., Wilms, J., Kretschmar, P., et al. 2008, *A&A*, 492, 511
- Kruskal, M., Schwarzschild, M., & Haerm, R. 1977, *ApJ*, 214, 498
- Kulkarni, A. K. & Romanova, M. M. 2008, *MNRAS*, 386, 673
- Kuster, M. 2004, PhD thesis, Universität Tübingen
- La Barbera, A., Burderi, L., Di Salvo, T., Iaria, R., & Robba, N. R. 2001, *ApJ*, 553, 375
- La Barbera, A., Santangelo, A., Orlandini, M., & Segreto, A. 2003, *A&A*, 400, 993
- La Barbera, A., Segreto, A., Santangelo, A., Kreykenbohm, I., & Orlandini, M. 2005, *A&A*, 438, 617
- Landau, L. & Lifshitz, E. 1977, *Quantum Mechanics* (Pergamon Press: New York)
- Lattimer, J. M. & Prakash, M. 2001, *ApJ*, 550, 426

- Lattimer, J. M. & Prakash, M. 2007, *Physics Report*, 442, 109
- Leahy, D. A. 1991, *MNRAS*, 251, 203
- Leahy, D. A., Darbro, W., Elsner, R. F., et al. 1983, *ApJ*, 266, 160
- Lebrun, F., Leray, J. P., Lavocat, P., et al. 2003, *A&A*, 411, L141
- Levine, A. M., Bradt, H., Cui, W., et al. 1996, *ApJ*, 469, L33
- Lewin, W. H. G. & van der Klis, M. 2006, *Compact stellar X-ray sources* (Cambridge University Press)
- Lewin, W. H. G., van Paradijs, J., & van den Heuvel, E. P. J. 1995, *Cambridge Astrophysics Series*, 26
- Lipunov, V. M. 1978, *Soviet Astronomy*, 22, 702
- Lipunov, V. M., Börner, G., & Wadhwa, R. S. 1992, *Astrophysics of Neutron Stars* (Astronomische Nachrichten Supplement)
- Liu, Q. Z., van Paradijs, J., & van den Heuvel, E. P. J. 2005, *A&A*, 442, 1135
- Liu, Q. Z., van Paradijs, J., & van den Heuvel, E. P. J. 2006, *A&A*, 455, 1165
- Liu, Q. Z., van Paradijs, J., & van den Heuvel, E. P. J. 2007, *A&A*, 469, 807
- Long, M., Romanova, M. M., & Lovelace, R. V. E. 2007, *MNRAS*, 374, 436
- Long, M., Romanova, M. M., & Lovelace, R. V. E. 2008, *MNRAS*, 386, 1274
- Longair, M. S. 1992, *High energy astrophysics. Vol.1: Particles, photons and their detection* (ISBN 0521387736. Cambridge, UK: Cambridge University Press)
- Longair, M. S. 1994, *High energy astrophysics. Vol.2: Stars, the galaxy and the interstellar medium* (Cambridge: Cambridge University Press, 2nd ed.)
- Lovelace, R. V. E., Romanova, M. M., & Bisnovatyi-Kogan, G. S. 1995, *MNRAS*, 275, 244
- Lund, N., Budtz-Jørgensen, C., Westergaard, N. J., et al. 2003, *A&A*, 411, L231
- Lutovinov, A. & Tsygankov, S. 2008, in *American Institute of Physics Conference Series*, Vol. 1054, 191–202
- Lyne, A. G. & Graham-Smith, F. 1990, *Pulsar astronomy* (Cambridge Astrophysics Series, No. 16)
- Lyuty, V. M. & Zaitseva, G. V. 2000, *Astronomy Letters*, 26, 9
- Lyutyi, V. M., Zaitseva, G. V., & Latysheva, I. D. 1989, *Soviet Astronomy Letters*, 15, 182
- Makino, F., Cook, W., Grunsfeld, J., et al. 1989, *IAU Circ.*, 4769
- Makishima, K. & Mihara, T. 1992, in *Frontiers Science Series*, ed. Y. Tanaka & K. Koyama, 23
- Makishima, K., Mihara, T., Ishida, M., et al. 1990, *ApJ*, 365, L59
- Makishima, K., Mihara, T., Nagase, F., & Tanaka, Y. 1999, *ApJ*, 525, 978
- Mas-Hesse, J. M., Giménez, A., Culhane, J. L., et al. 2003, *A&A*, 411, L261
- Mayer, W. F. 1975, *Johns Hopkins APL Technical Digest*, 14, 14
- Meszáros, P., Harding, A. K., Kirk, J. G., & Galloway, D. J. 1983, *ApJ*, 266, L33
- Meszáros, P. & Nagel, W. 1985, *ApJ*, 299, 138
- Mihara, T. 1995, PhD thesis, Dept. of Physics, Univ. of Tokyo
- Mihara, T., Makishima, K., Kamijo, S., et al. 1991, *ApJ*, 379, L61
- Mihara, T., Makishima, K., & Nagase, F. 2004, *ApJ*, 610, 390
- Miller, K. A. & Stone, J. M. 1997, *ApJ*, 489, 890
- Mineo, T., Ferrigno, C., Foschini, L., et al. 2006, *A&A*, 450, 617
- Misner, C. W., Thorne, K. S., & Wheeler, J. A. 1973, *Gravitation* (San Francisco: W.H. Freeman and Co., 1973)
- Mitsuda, K., Kunieda, H., Inoue, H., & Kelley, R. 2004, in *Society of Photo-Optical Instrumentation Engineers (SPIE) Confer-*

- ence Series, ed. G. Hasinger & M. J. L. Turner, Vol. 5488, 177–186
- Motch, C., Stella, L., Janot-Pacheco, E., & Mouchet, M. 1991, *ApJ*, 369, 490
- Mukherjee, U. & Paul, B. 2005, *A&A*, 431, 667
- Nagase, F., Hayakawa, S., Kunieda, H., et al. 1982, *ApJ*, 263, 814
- Nagel, W. 1981a, *ApJ*, 251, 288
- Nagel, W. 1981b, *ApJ*, 251, 278
- Nakajima, M., Mihara, T., Makishima, K., & Niko, H. 2006, *ApJ*, 646, 1125
- Negueruela, I. 2004a, *ArXiv Astrophysics e-prints*:0411758
- Negueruela, I. 2004b, *ArXiv Astrophysics e-prints*:0411759
- Negueruela, I., Reig, P., Finger, M. H., & Roche, P. 2000, *A&A*, 356, 1003
- Nelson, R. W., Salpeter, E. E., & Wasserman, I. 1993, *ApJ*, 418, 874
- Nishimura, O. 2005, *PASP*, 57, 769
- Nollert, H.-P., Ruder, H., Herold, H., & Kraus, U. 1989, *A&A*, 208, 153
- Oed, A. 1988, *Nuclear Instruments and Methods in Physics Research A*, 263, 351
- Orlandini, M., Bartolini, C., Campana, S., et al. 2004, *Nuclear Physics B Proceedings Supplements*, 132, 476
- Orlandini, M., dal Fiume, D., del Sordo, S., et al. 1999, *A&A*, 349, L9
- Orlandini, M., dal Fiume, D., Frontera, F., et al. 1998, in *The Active X-ray Sky: Results from BeppoSAX and RXTE*, ed. L. Scarsi, H. Bradt, P. Giommi, & F. Fiore, 158
- Ostriker, J. P. & Gunn, J. E. 1969, *ApJ*, 157, 1395
- Özel, F. 2006, *Nat*, 441, 1115
- Panchenko, I. E. & Postnov, K. A. 1994, *A&A*, 286, 497
- Perryman, M. A. C., Lindegren, L., Kovalevsky, J., et al. 1997, *A&A*, 323, L49
- Peterson, L. E. 1975, *ARA&A*, 13, 423
- Piraino, S., Santangelo, A., & Kaaret, P. 2000, *A&A*, 360, L35
- Popov, S. B. 2000, *Astronomical and Astrophysical Transactions*, 19, 191
- Porter, J. M. & Rivinius, T. 2003, *PASP*, 115, 1153
- Postnov, K., Staubert, R., Santangelo, A., et al. 2008, *A&A*, 480, L21
- Pottschmidt, K., Kreykenbohm, I., Wilms, J., et al. 2005, *ApJ*, 634, L97
- Press, W. H., Flannery, B. P., Teukolsky, S., & T., V. W. 1992, *Numerical Recipes in FORTRAN 77: The Art of Scientific Computing* (ISBN 0 521 43064 X, Cambridge University Press)
- Pringle, J. E. 1981, *ARA&A*, 19, 137
- Proctor, R. J., Skinner, G. K., & Willmore, A. P. 1979, *MNRAS*, 187, 633
- Rauch, T., Suleimanov, V., & Werner, K. 2008, *A&A*, 490, 1127
- Riffert, H. & Meszaros, P. 1988, *ApJ*, 325, 207
- Ritz, S. M., Michelson, P. F., Meegan, C., Grindlay, J., & GLAST Mission Team. 2007, in *Bulletin of the American Astronomical Society*, Vol. 38, 909
- Ritz, S. M., Michelson, P. F., Meegan, C., Grindlay, J. E., & GLAST Mission Team. 2006, in *Bulletin of the American Astronomical Society*, Vol. 38, 1105
- Roche, E. A. 1873, *Essai sur la constitution et l'origine du système solaire (Mémoires de l'Académie des Sciences et Lettres de Montpellier, Section des Sciences, Vol. VIII)*
- Romanova, M. M., Kulkarni, A. K., & Lovelace, R. V. E. 2008, *ApJ*, 673, L171
- Romanova, M. M., Ustyugova, G. V., Koldoba, A. V., & Lovelace, R. V. E. 2002, *ApJ*, 578, 420
- Romanova, M. M., Ustyugova, G. V., Koldoba, A. V., & Lovelace, R. V. E. 2004, *ApJ*, 610, 920

- Romanova, M. M., Ustyugova, G. V., Koldoba, A. V., Wick, J. V., & Lovelace, R. V. E. 2003, *ApJ*, 595, 1009
- Rosenberg, F. D., Eyles, C. J., Skinner, G. K., & Willmore, A. P. 1975, *Nat*, 256, 628
- Rothschild, R. E., Blanco, P. R., Gruber, D. E., et al. 1998, *ApJ*, 496, 538
- Rothschild, R. E., Wilms, J., Tomsick, J., et al. 2006, *ApJ*, 641, 801
- Santangelo, A., Del Sordo, S., Piraino, S., et al. 1999a, *Nuclear Physics B Proceedings Supplements*, 69, 151
- Santangelo, A., del Sordo, S., Segreto, A., et al. 1998, *A&A*, 340, L55
- Santangelo, A., Segreto, A., Giarrusso, S., et al. 1999b, *ApJ*, 523, L85
- Saz Parkinson, P. M. et al. 2009, *ArXiv e-prints:0901:3405*
- Scharlemann, E. T. 1978, *ApJ*, 219, 617
- Schönherr, G., Wilms, J., Kretschmar, P., et al. 2007, *A&A*, 472, 353
- Sembay, S., Schwartz, R. A., Orwig, L. E., Dennis, B. R., & Davies, S. R. 1990, *ApJ*, 351, 675
- Seward, F. D. & Charles, P. A. 1995, *Exploring the X-Ray Universe* (ISBN 0521437121. Cambridge, UK: Cambridge University Press)
- Shakura, N. I., Postnov, K. A., & Prokhorov, M. E. 1991, *Soviet Astronomy Letters*, 17, 339
- Shakura, N. I. & Syunyaev, R. A. 1973, *A&A*, 24, 337
- Shaposhnikov, N., Titarchuk, L., & Haberl, F. 2003, *ApJ*, 593, L35
- Skinner, G. K. 2004, *New Astronomy Review*, 48, 205
- Skinner, G. K. & Ponman, T. J. 1994, *MNRAS*, 267, 518
- Smith, D. M., Hazelton, B., Coburn, W., et al. 2005, *ATel*, 557
- Smith, J. F. & Courtier, G. M. 1976, *Royal Society of London Proceedings Series A*, 350, 421
- Staelin, D. H. & Reifenstein, E. C. 1968, *Science*, 162, 1481
- Staubert, R., Kendziorra, E., Pietsch, W., et al. 1980, *ApJ*, 239, 1010
- Staubert, R., Shakura, N. I., Postnov, K., et al. 2007, *A&A*, 465, L25
- Steele, I. A., Negueruela, I., Coe, M. J., & Roche, P. 1998, *MNRAS*, 297, L5
- Stella, L., White, N. E., & Rosner, R. 1986, *ApJ*, 308, 669
- Strohmayer, T. & Bildsten, L. 2003, *ArXiv Astrophysics e-prints:0301544*
- Suchy, S., Pottschmidt, K., Wilms, J., et al. 2008, *ApJ*, 675, 1487
- Takahashi, T., Kelley, R., Mitsuda, K., et al. 2008, in *Society of Photo-Optical Instrumentation Engineers (SPIE) Conference Series*, Vol. 7011, *Society of Photo-Optical Instrumentation Engineers (SPIE) Conference Series*
- Tanaka, Y. 1986, in *Lecture Notes in Physics*, Berlin Springer Verlag, Vol. 255, *IAU Colloq. 89: Radiation Hydrodynamics in Stars and Compact Objects*, ed. D. Mihalas & K.-H. A. Winkler, 198
- Tavani, M., Barbiellini, G., Argan, A., et al. 2008, *Nuclear Instruments and Methods in Physics Research A*, 588, 52
- Tenzer, C. 2008, *PhD thesis*, Universität Tübingen
- Terada, Y., Mihara, T., Nakajima, M., et al. 2006, *ApJ*, 648, L139
- Thorsett, S. E. & Chakrabarty, D. 1999, *ApJ*, 512, 288
- Toor, A. & Seward, F. D. 1974, *AJ*, 79, 995
- Truemper, J., Pietsch, W., Reppin, C., et al. 1978, *ApJ*, 219, L105
- Trümper, J. 1984, *Advances in Space Research*, 3, 483
- Trümper, J., Pietsch, W., Reppin, C., & Sacco, B. 1977, in *New York Academy Sciences Annals*, Vol. 302, *Eighth Texas Symposium*

- on Relativistic Astrophysics, ed. M. D. Paggiannis, 538
- Trunkovsky, E. M. 1995, *Space Science Reviews*, 74, 485
- Tsygankov, S. S., Lutovinov, A. A., Churazov, E. M., & Sunyaev, R. A. 2006, *MNRAS*, 371, 19
- Tsygankov, S. S., Lutovinov, A. A., Churazov, E. M., & Sunyaev, R. A. 2007, *Astronomy Letters*, 33, 368
- Tueller, J., Ajello, M., Barthelmy, S., et al. 2005, *ATel*, 504
- Turner, M. J. L., Thomas, H. D., Patchett, B. E., et al. 1989, *PASJ*, 41, 345
- Ubertini, P., Lebrun, F., Di Cocco, G., et al. 2003, *A&A*, 411, L131
- van der Meer, A., Kaper, L., van Kerkwijk, M. H., Heemskerk, M. H. M., & van den Heuvel, E. P. J. 2007, *A&A*, 473, 523
- Vedrenne, G., Roques, J.-P., Schönfelder, V., et al. 2003, *A&A*, 411, L63
- von Rekowski, B. & Brandenburg, A. 2004, *A&A*, 420, 17
- Wang, Y.-M. 1996, *ApJ*, 465, L111
- Wang, Y.-M. 1997, *ApJ*, 475, L135
- Wang, Y.-M. & Welter, G. L. 1981, *A&A*, 102, 97
- Weisskopf, M. C., Brinkman, B., Canizares, C., et al. 2002, *PASP*, 114, 1
- Wheaton, W. A., Doty, J. P., Primini, F. A., et al. 1979, *Nat*, 282, 240
- White, N. E. & Hornschemeier, A. E. 2009, in *American Astronomical Society Meeting Abstracts*, Vol. 213, 217.02
- White, N. E., Swank, J. H., & Holt, S. S. 1983, *ApJ*, 270, 711
- Wickramasinghe, D. T. & Ferrario, L. 2000, *PASP*, 112, 873
- Wijnands, R. 2006, in *Bulletin of the American Astronomical Society*, Vol. 38, *Bulletin of the American Astronomical Society*, 1183
- Wijnands, R. & van der Klis, M. 1998, *Nat*, 394, 344
- Wilms, J., Nowak, M. A., Dove, J. B., Fender, R. P., & di Matteo, T. 1999, *ApJ*, 522, 460
- Wilson, C. A. & Finger, M. H. 2005, *ATel*, 605
- Wilson, C. A., Finger, M. H., & Camero-Arranz, A. 2008, *ApJ*, 678, 1263
- Wilson, C. A., Finger, M. H., Coe, M. J., Laycock, S., & Fabregat, J. 2002, *ApJ*, 570, 287
- Wilson, R. B., Harmon, B. A., & Finger, M. H. 1994, *IAU Circ.*, 5933, 2
- Winkler, C., Courvoisier, T. J.-L., Di Cocco, G., et al. 2003, *A&A*, 411, L1
- Woods, P. M. & Thompson, C. 2006, *Soft gamma repeaters and anomalous X-ray pulsars: magnetar candidates (Compact stellar X-ray sources)*, 547–586
- Ziolkowski, J. 2002, *Memorie della Societa Astronomica Italiana*, 73, 1038
- Zombeck, M. 2007, *Handbook of Space Astronomy and Astrophysics: Third Edition (ISBN-13 781-0-521-78242-5 (HB). Published by Cambridge University Press, Cambridge, UK.)*

APPENDIX A

Log of *RXTE* observations

Table A.1: Log of *RXTE* observations used in this work. The individual pointings correspond to observations P91085 and P91086, and are sorted chronologically.

	Observation	MJD start	PCA exp.(ks)
1	91086-02-01-00	53608.7	1.73
2	91086-01-03-00	53610.1	3.38
3	91086-01-03-01	53610.6	1.15
4	91086-01-03-02	53610.7	2.22
5	91086-01-03-03	53610.7	2.56
6	91086-02-02-00	53611.6	1.94
7	91086-02-02-01	53612.7	1.82
8	91086-01-03-04	53613.0	3.42
9	91086-01-03-05	53613.1	1.57
10	91085-01-01-01	53613.5	1.20
11	91086-02-03-00	53613.6	1.90
12	91085-01-01-04	53613.7	2.30
13	91085-01-01-00	53613.8	6.83
14	91085-01-01-02	53614.0	3.39
15	91086-02-03-01	53614.1	1.44
16	91085-01-01-03	53614.7	12.35
17	91085-01-01-05	53615.0	0.80
18	91085-01-02-00	53615.0	2.46
19	91085-01-02-01	53615.1	1.55
20	91085-01-02-02	53615.1	1.26
21	91085-01-02-03	53615.6	2.03
22	91085-01-02-04	53615.7	9.55
23	91086-02-04-00	53616.1	1.55
24	91086-01-04-00	53617.7	9.58

Table A.1: continued from previous page

	Observation	MJD start	PCA exp.(ks)
25	91086-01-04-01	53617.9	2.93
26	91086-02-05-00	53619.0	1.47
27	91086-02-06-00	53620.0	1.49
28	91086-02-06-01	53621.0	1.52
29	91086-03-01-00	53622.0	1.54
30	91086-03-01-01	53623.1	1.44
31	91086-01-05-00	53624.6	10.59
32	91086-03-02-00	53626.0	1.34
33	91086-03-02-01	53626.8	1.04
34	91086-03-03-00	53628.0	1.46
35	91086-03-03-01	53628.8	0.77
36	91085-01-03-00	53629.8	7.10
37	91085-01-03-01	53630.7	10.48
38	91085-01-03-02	53631.7	4.72
39	91085-01-03-03	53632.7	2.54
40	91085-01-03-04	53633.9	2.64
41	91085-01-03-05	53634.9	2.43
42	91085-01-04-02	53637.8	2.98
43	91085-01-04-00	53638.8	1.09
44	91085-01-04-01	53638.8	2.75

APPENDIX B

Pulse period with *RXTE*

Table B.1: Best values for the pulse period of A 0535+26 obtained with *RXTE*. The estimated uncertainty for the period is 0.5 ms.

MJD	Period (s)
53608.703184	103.3960
53610.071014	103.3960
53610.596363	103.3960
53610.660992	103.3960
53610.726814	103.3960
53611.647099	103.3960
53612.694213	103.3960
53613.022118	103.3960
53613.104697	103.3958
53613.480443	103.3952
53613.612084	103.3951
53613.677905	103.3950
53613.808360	103.3948
53614.005812	103.3945
53614.095744	103.3943
53614.661587	103.3936
53614.989486	103.3932
53615.001809	103.3930
53615.075640	103.3928
53615.145061	103.3926
53615.645258	103.3921
53615.711075	103.3920
53616.058114	103.3916
53617.678346	103.3890
53617.945194	103.3887

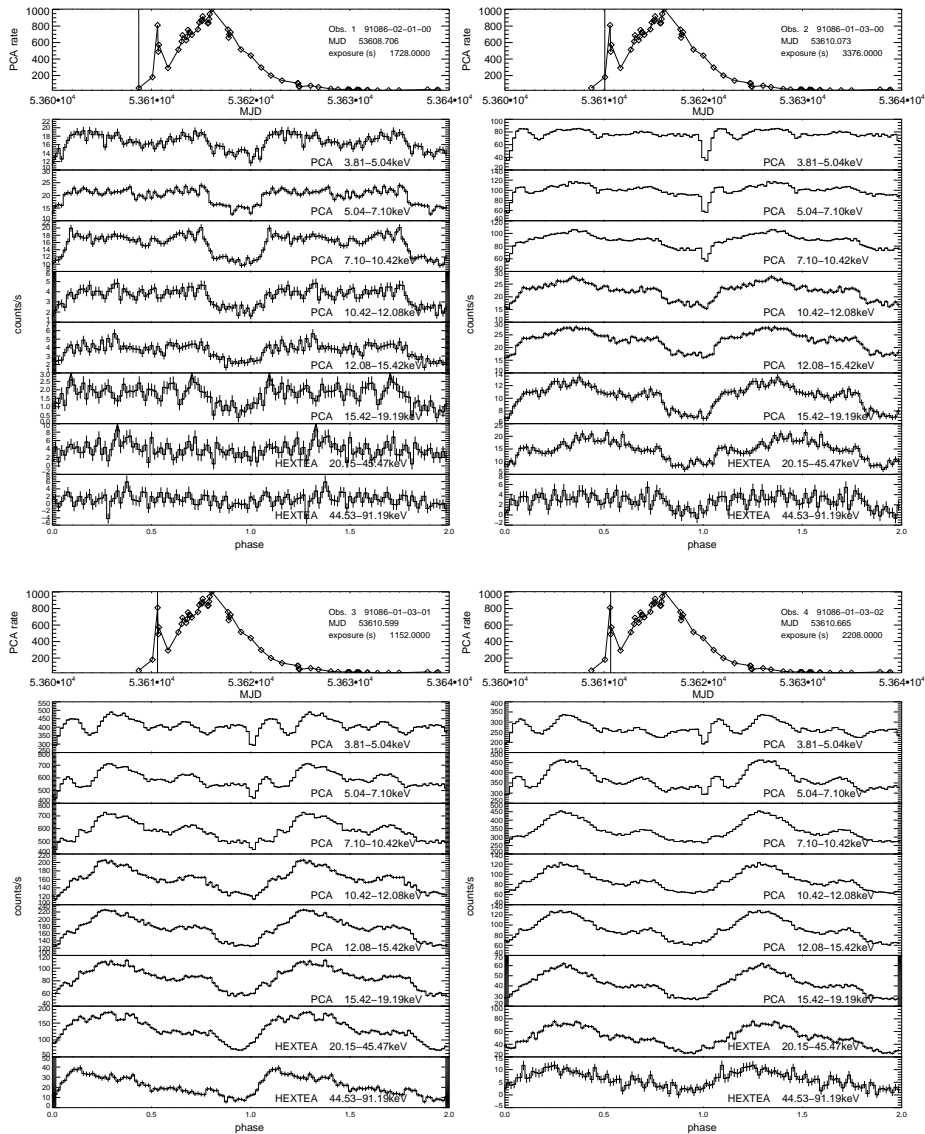
Table B.1: continued from previous page

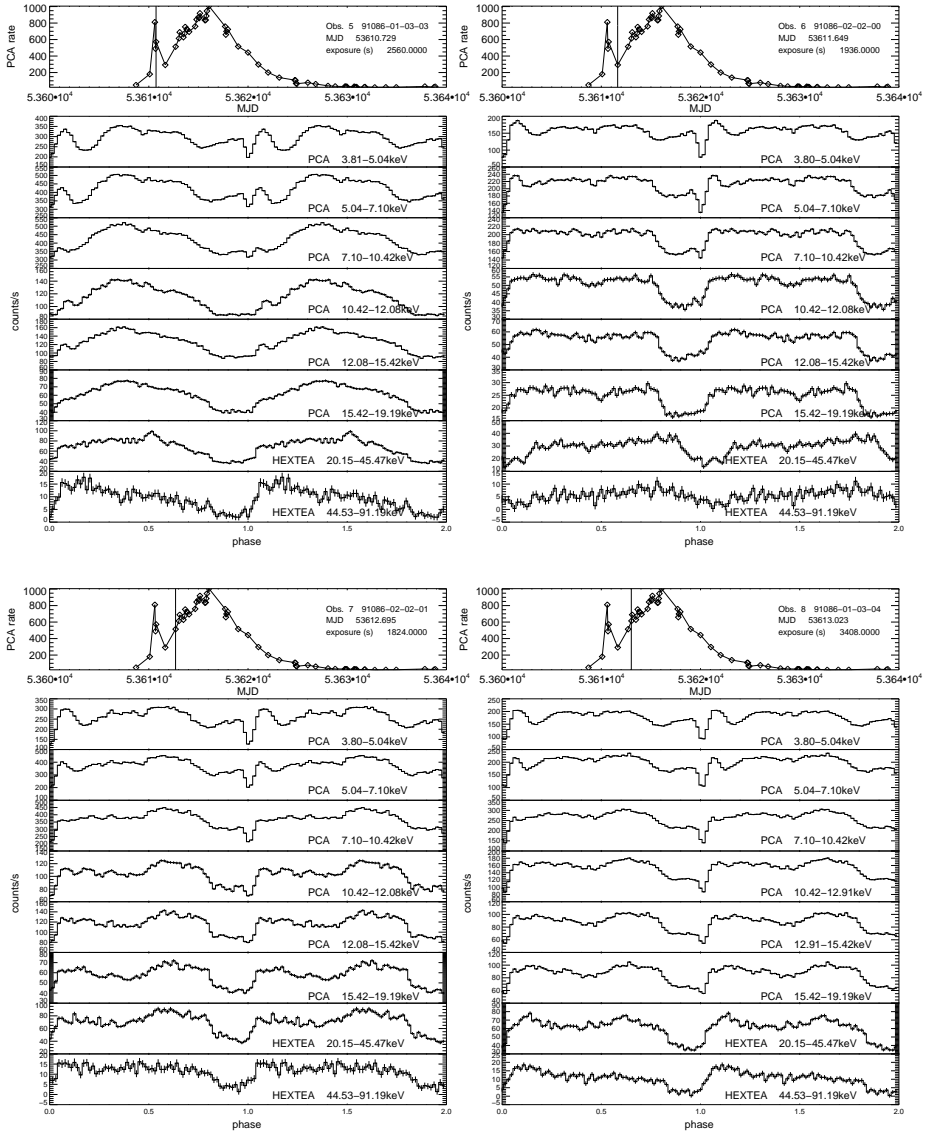
MJD	Period (s)
53619.005376	103.3865
53619.987786	103.3851
53621.038352	103.3838
53622.020739	103.3828
53623.141888	103.3820
53624.653113	103.3811
53626.019557	103.3807
53626.080000	103.3805
53628.780000	103.3801
53629.760000	103.3800
53630.680000	103.3800

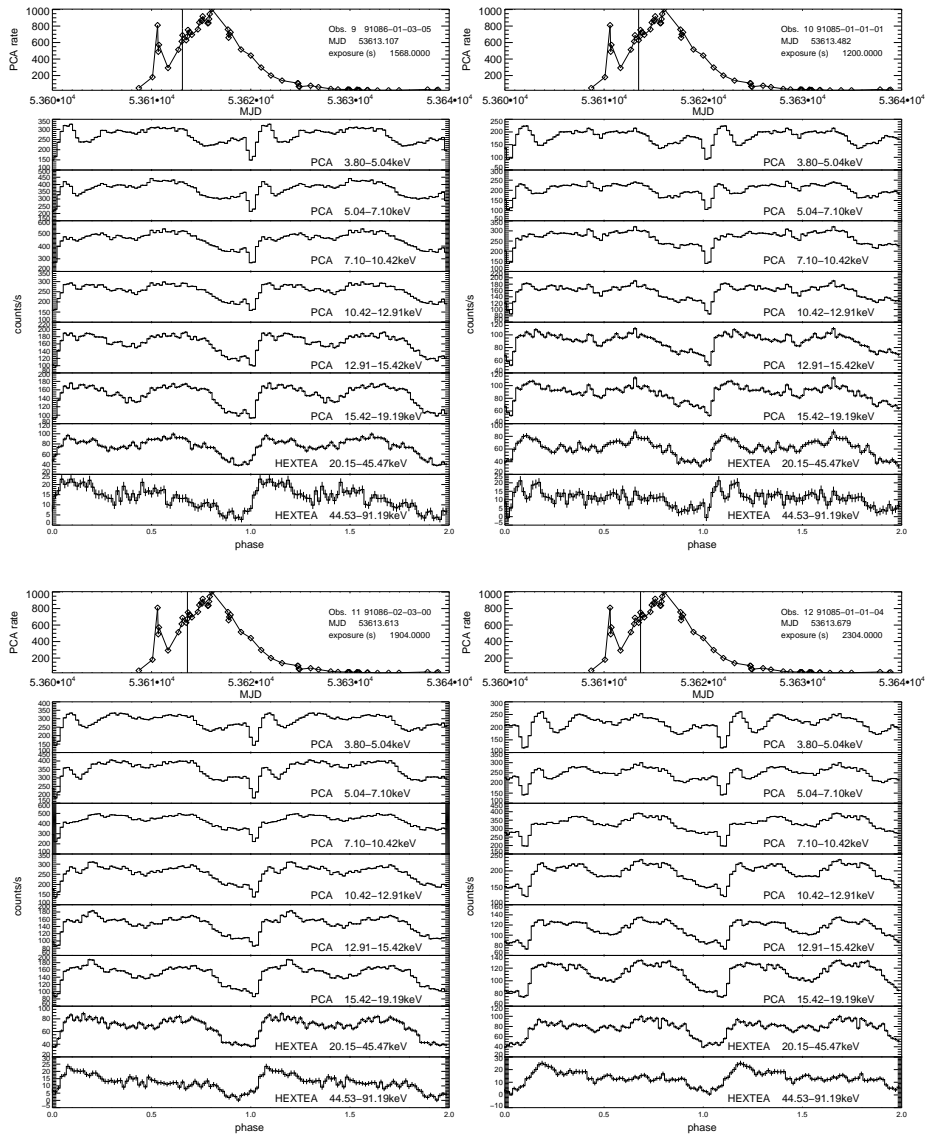
APPENDIX C

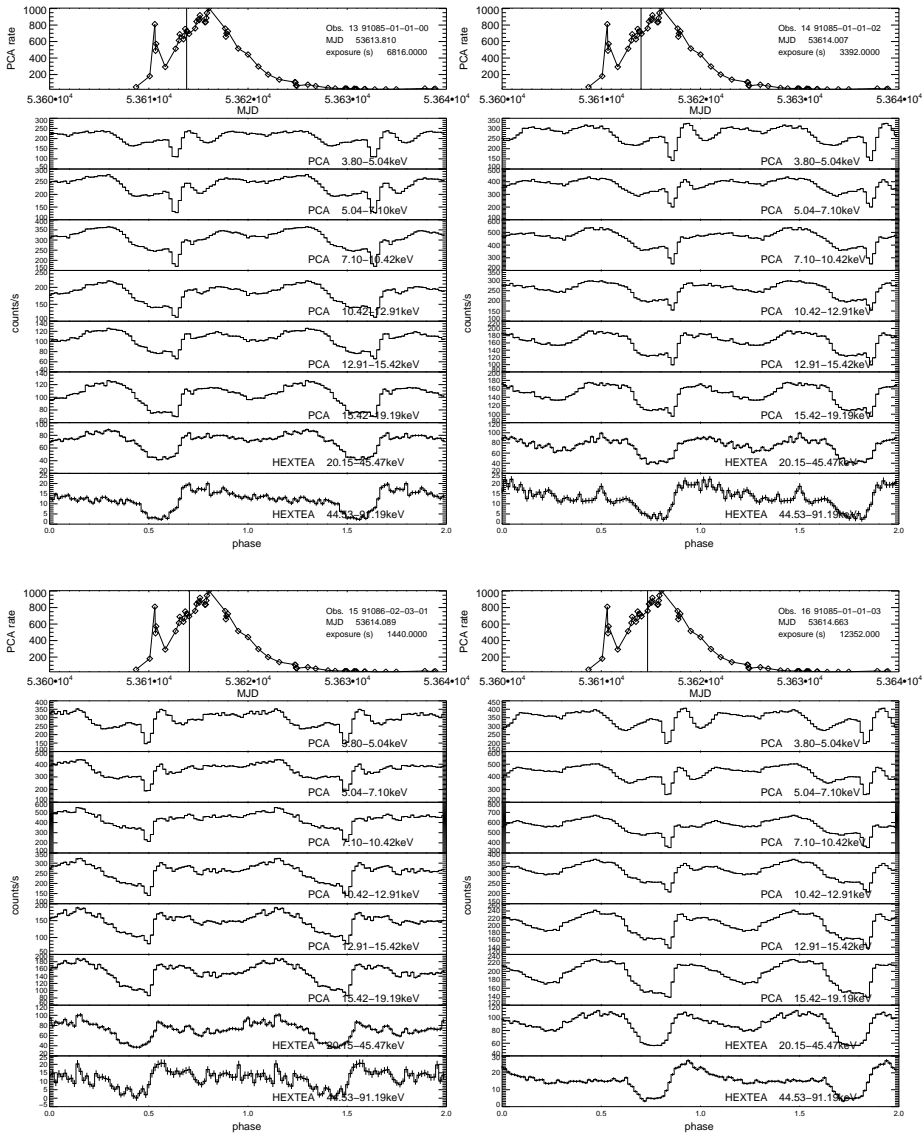
***RXTE* pulse profiles**

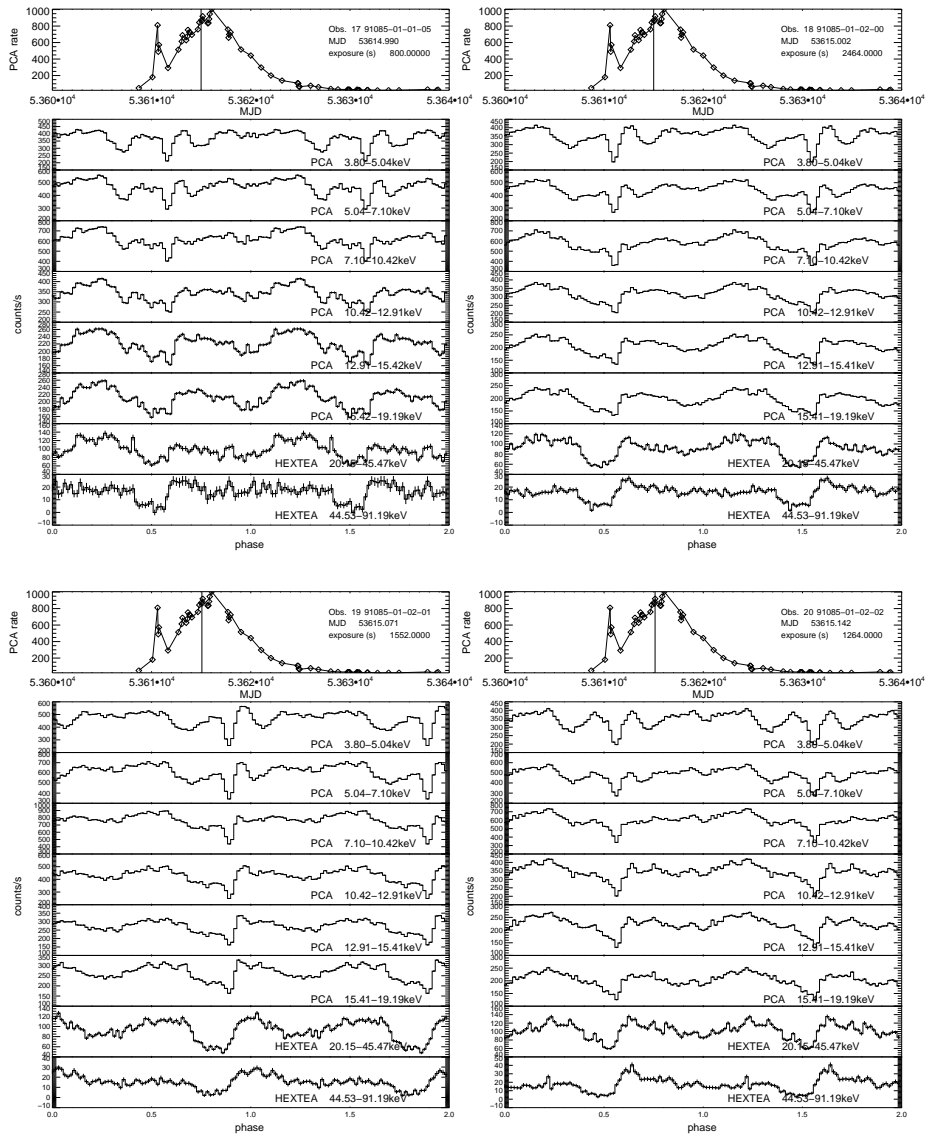
The energy dependent pulse profiles of all the *RXTE* observations of A 0535+26 are plotted. In each figure the upper panel contains the *PCA* light curve, with a vertical line indicating the time of the observation. The *PCA* count rate is given in counts $\text{s}^{-1} \text{PCU}^{-1}$. The energy ranges of the *PCA* and *HEXTE* pulse profiles are indicated in the figures. Two pulse cycles are shown for clarity.

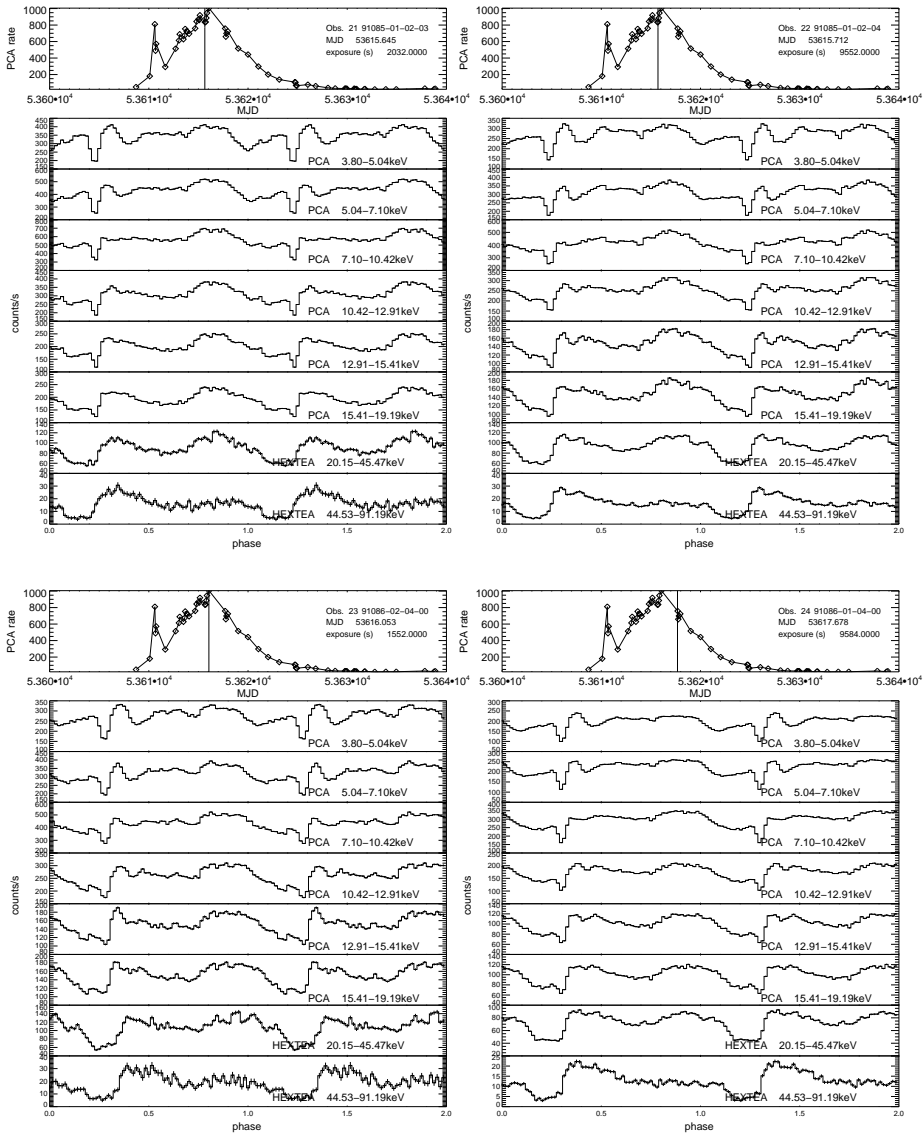


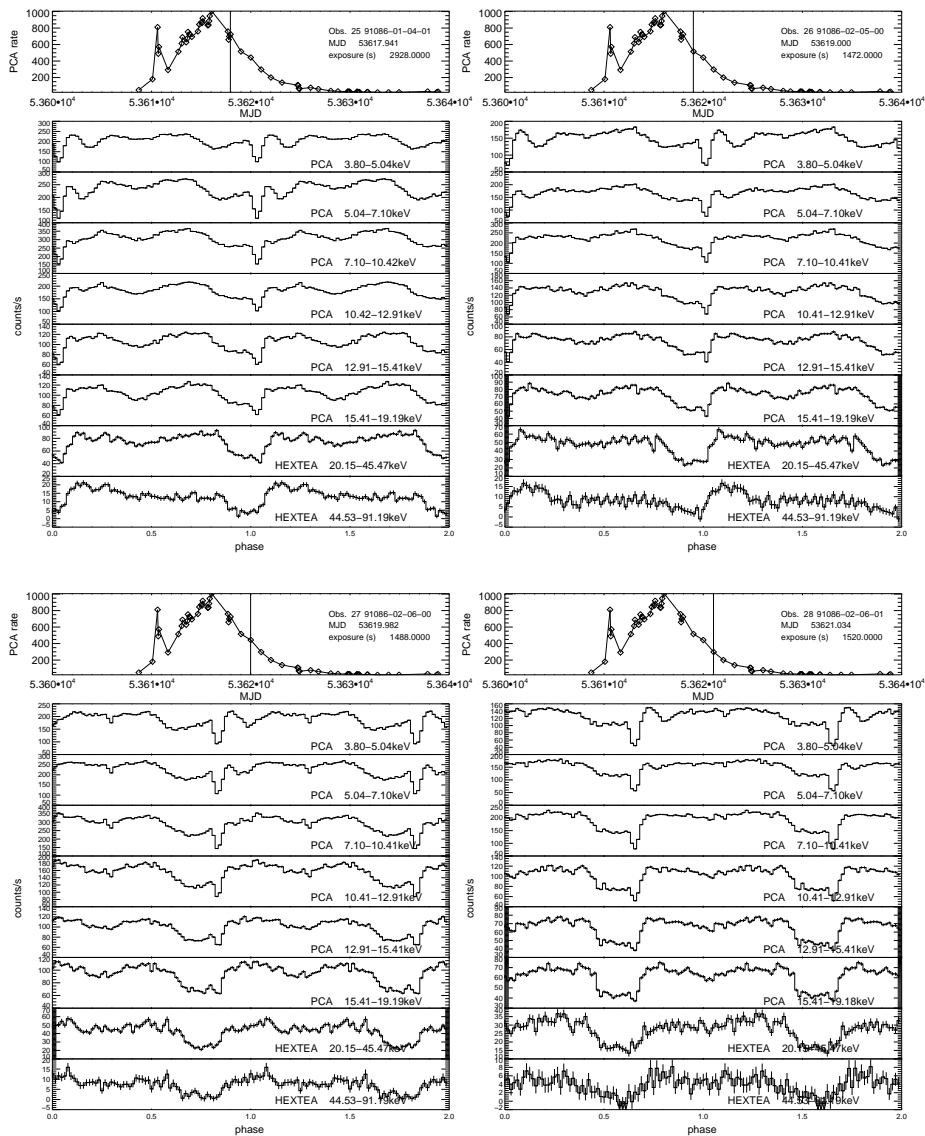


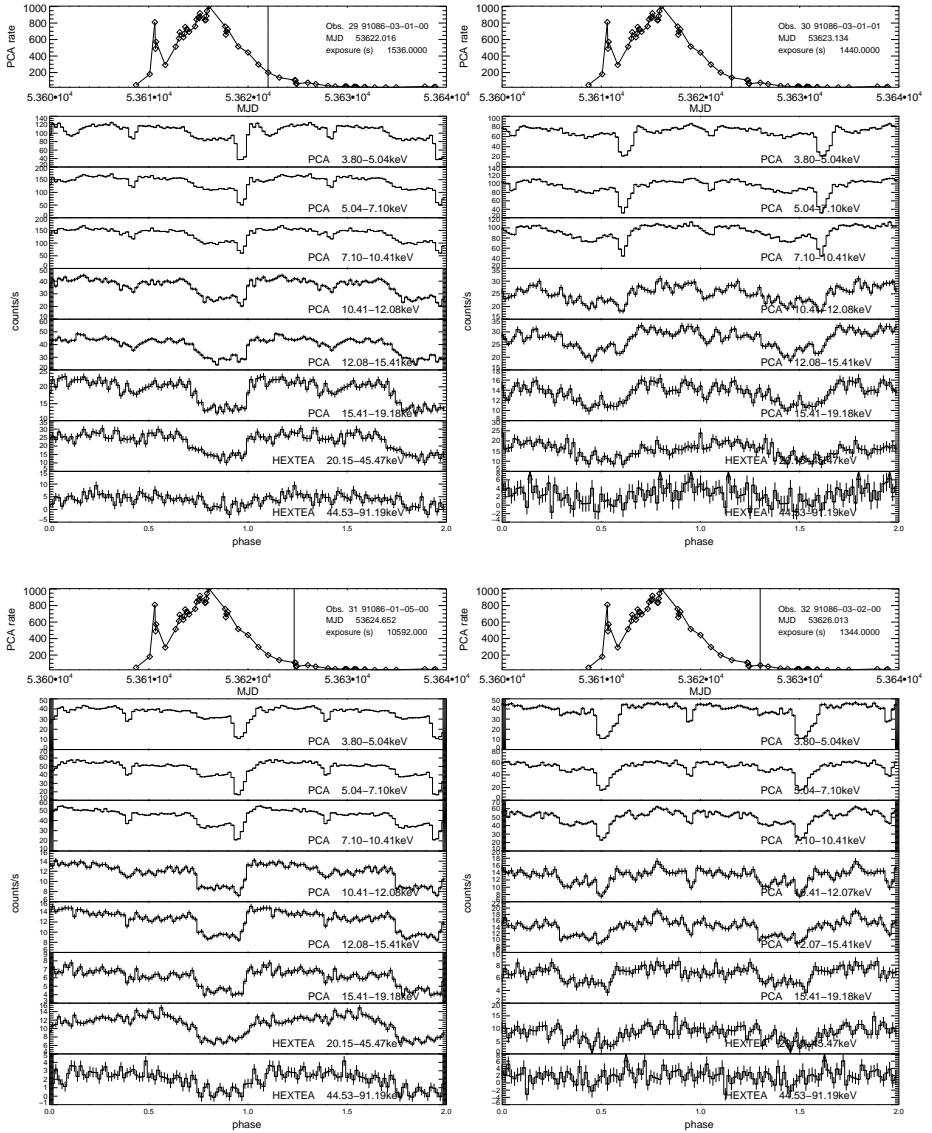


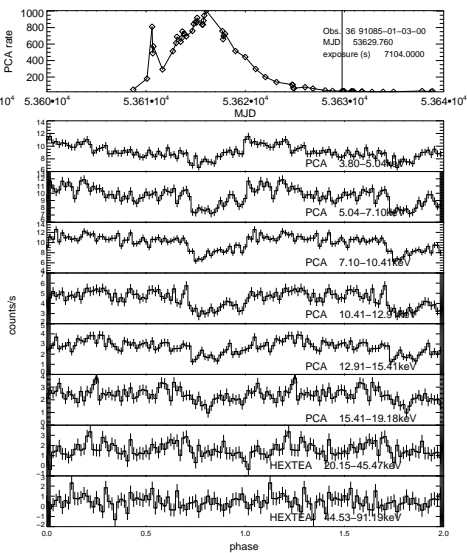
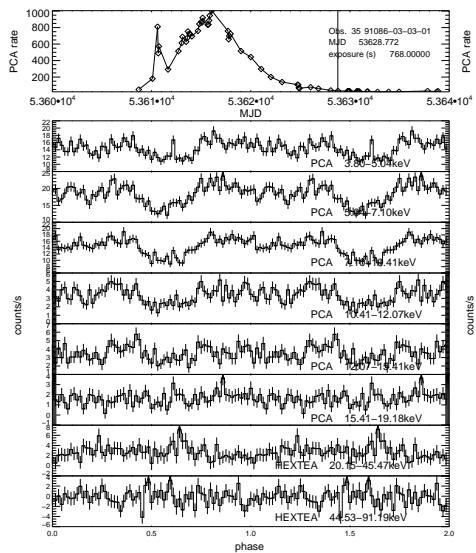
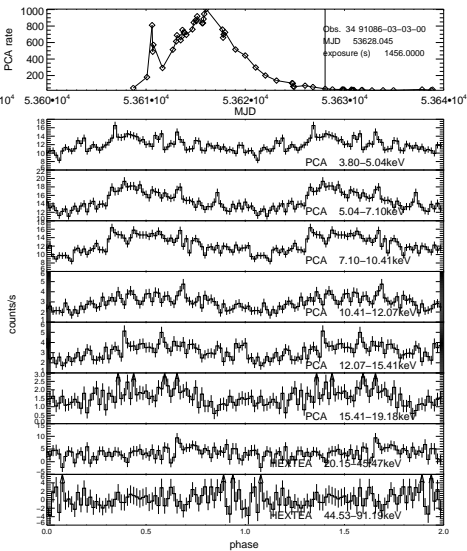
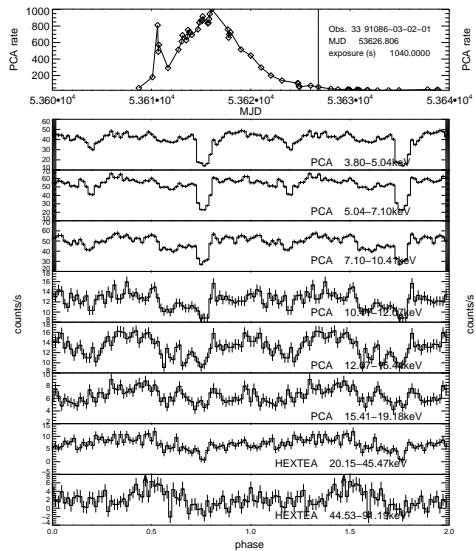


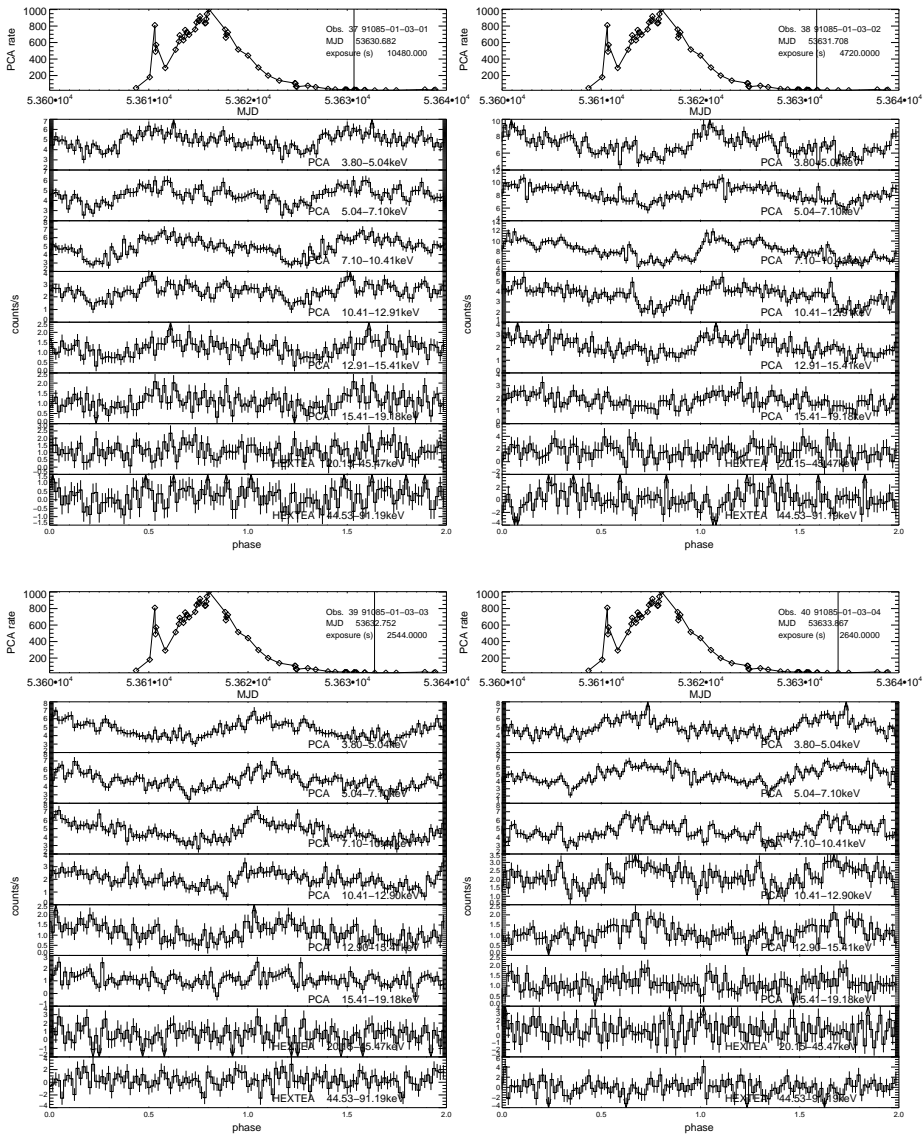


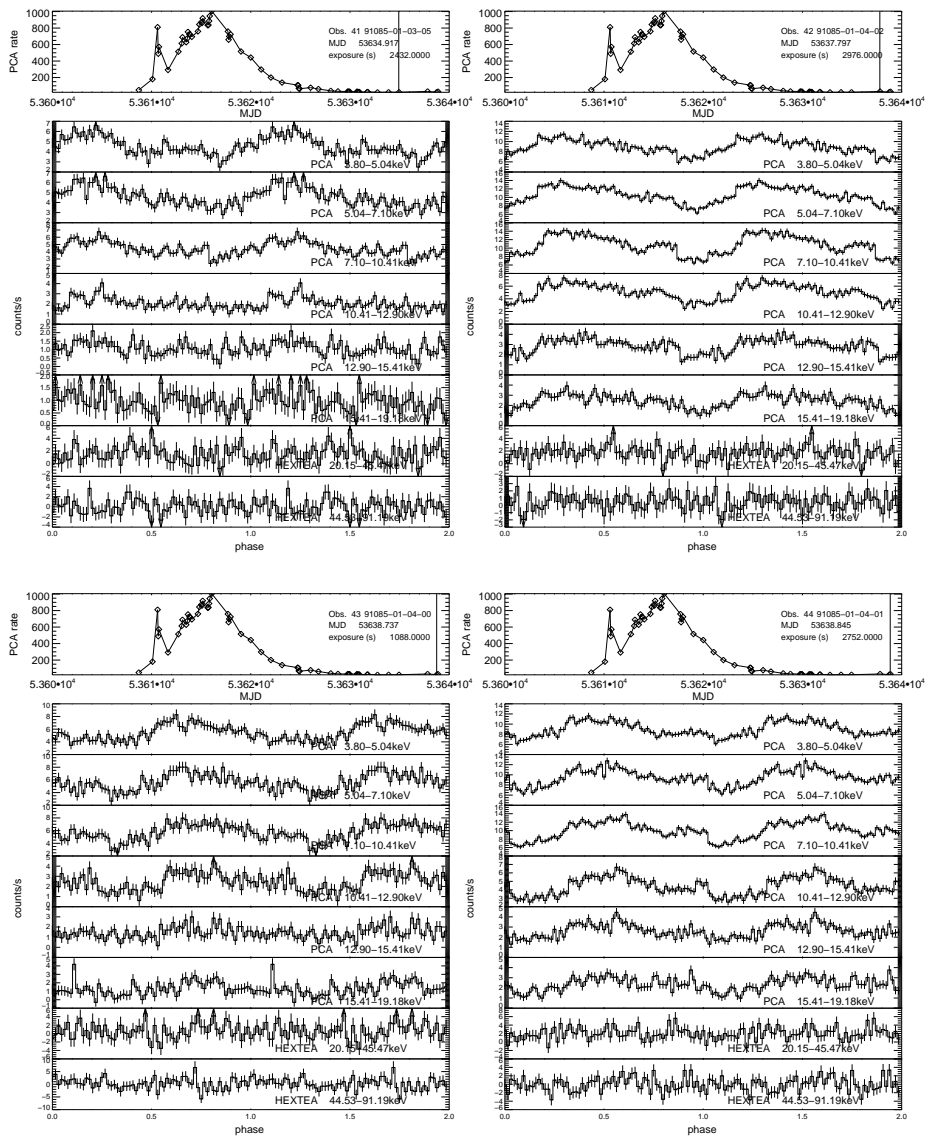












APPENDIX D

Results of *RXTE* spectral analysis

Table D.1 and Table D.2 contain the best fit parameters of the *RXTE* observations of A 0535+26 for which a cyclotron line was significantly detected. When required by the fit, two cyclotron lines were included in the model. For some observations the width of the first harmonic was fixed at 10 keV. The uncertainties are 90 % confidence for one parameter of interest.

Table D.1: Best fit parameters from RXTE observations - Part I. The flux is given in units of $10^{-8} \text{ erg cm}^{-2} \text{ s}^{-1}$.

Obs	α	E_{fold} (keV)	E_{cyc} (keV)	σ_{cyc} (keV)	τ_{cyc}	Flux _{(3–50) keV}	$\chi^2_{\text{red}}/\text{dof}$
02	$1.17^{+0.04}_{-0.05}$	$23.4^{+2.1}_{-1.8}$	$45.9^{+2.0}_{-1.7}$	$4.3^{+2.1}_{-2.3}$	$0.46^{+0.40}_{-0.14}$	$0.381^{+0.004}_{-0.006}$	0.88/170
03	$0.73^{+0.02}_{-0.02}$	$18.2^{+0.4}_{-0.4}$	$48.3^{+1.1}_{-1.0}$	$6.4^{+1.0}_{-1.0}$	$0.27^{+0.03}_{-0.03}$	$1.894^{+0.006}_{-0.011}$	1.19/170
04	$0.91^{+0.04}_{-0.04}$	$18.8^{+1.1}_{-1.0}$	$50.2^{+1.8}_{-1.6}$	$8.7^{+1.4}_{-1.3}$	$0.57^{+0.08}_{-0.08}$	$1.030^{+0.005}_{-0.010}$	0.90/170
05	$0.83^{+0.03}_{-0.03}$	$19.2^{+0.8}_{-0.7}$	$52.0^{+1.6}_{-1.4}$	$10.8^{+1.3}_{-1.1}$	$0.53^{+0.06}_{-0.06}$	$1.288^{+0.007}_{-0.010}$	0.90/170
06	$0.97^{+0.04}_{-0.04}$	$21.7^{+1.6}_{-1.5}$	$45.7^{+1.9}_{-1.7}$	$7.6^{+1.7}_{-1.6}$	$0.47^{+0.09}_{-0.09}$	$0.608^{+0.004}_{-0.009}$	1.06/170
07	$0.61^{+0.03}_{-0.03}$	$17.6^{+0.6}_{-0.6}$	$45.7^{+1.0}_{-1.0}$	$8.3^{+0.9}_{-0.8}$	$0.51^{+0.05}_{-0.05}$	$1.222^{+0.008}_{-0.010}$	1.29/170
08	$0.66^{+0.02}_{-0.02}$	$18.2^{+0.5}_{-0.5}$	$45.1^{+0.7}_{-0.7}$	$8.2^{+0.7}_{-0.7}$	$0.49^{+0.03}_{-0.03}$	$1.128^{+0.006}_{-0.007}$	1.17/170
09	$0.65^{+0.02}_{-0.02}$	$19.1^{+0.6}_{-0.5}$	$45.7^{+0.9}_{-0.8}$	$8.5^{+0.8}_{-0.8}$	$0.52^{+0.04}_{-0.04}$	$1.364^{+0.007}_{-0.010}$	1.02/200
10	$0.67^{+0.03}_{-0.03}$	$18.4^{+0.9}_{-0.8}$	$45.0^{+1.5}_{-1.4}$	$9.9^{+1.3}_{-1.2}$	$0.51^{+0.06}_{-0.06}$	$1.142^{+0.009}_{-0.010}$	1.04/186
11	$0.65^{+0.02}_{-0.02}$	$18.5^{+0.6}_{-0.6}$	$45.0^{+1.1}_{-1.0}$	$8.9^{+0.9}_{-0.9}$	$0.44^{+0.04}_{-0.04}$	$1.281^{+0.009}_{-0.011}$	1.01/186
12	$0.59^{+0.02}_{-0.02}$	$17.8^{+0.4}_{-0.4}$	$44.8^{+0.8}_{-0.8}$	$8.8^{+0.8}_{-0.7}$	$0.44^{+0.03}_{-0.03}$	$1.455^{+0.009}_{-0.011}$	1.18/200
13	$0.62^{+0.02}_{-0.02}$	$17.9^{+0.3}_{-0.3}$	$45.9^{+0.5}_{-0.5}$	$9.2^{+0.5}_{-0.5}$	$0.48^{+0.02}_{-0.02}$	$1.348^{+0.006}_{-0.007}$	1.29/216
14	$0.61^{+0.02}_{-0.02}$	$17.7^{+0.4}_{-0.4}$	$44.7^{+0.7}_{-0.7}$	$8.1^{+0.7}_{-0.6}$	$0.47^{+0.03}_{-0.03}$	$1.345^{+0.007}_{-0.008}$	1.17/200
15	$0.65^{+0.02}_{-0.02}$	$18.2^{+0.6}_{-0.6}$	$45.3^{+0.9}_{-0.9}$	$7.6^{+0.9}_{-0.8}$	$0.52^{+0.05}_{-0.05}$	$1.303^{+0.008}_{-0.010}$	1.10/228
16	$0.55^{+0.02}_{-0.02}$	$17.7^{+0.3}_{-0.3}$	$46.1^{+0.4}_{-0.5}$	$10.3^{+0.5}_{-0.5}$	$0.48^{+0.02}_{-0.02}$	$1.681^{+0.004}_{-0.012}$	1.10/211
			102^{+4}_{-3}	8^{+3}_{-3}	$1.0^{+0.4}_{-0.3}$		

Table D.2: Best fit parameters from RXTE observations - Part II. The flux given in units of $10^{-8} \text{ erg cm}^{-2} \text{ s}^{-1}$.

Obs	α	E_{fold} (keV)	E_{cyc} (keV)	σ_{cyc} (keV)	τ_{cyc}	Flux _{(3–50) keV}	$\chi_{\text{red}}^2/\text{dof}$
17	$0.58^{+0.03}_{-0.03}$	$17.6^{+0.6}_{-0.6}$	$46.8^{+1.5}_{-1.4}$	$9.5^{+1.4}_{-1.3}$	$0.45^{+0.06}_{-0.05}$	$1.840^{+0.015}_{-0.019}$	0.96/200
18	$0.58^{+0.02}_{-0.02}$	$17.5^{+0.4}_{-0.4}$	$45.1^{+0.8}_{-0.7}$	$9.0^{+0.8}_{-0.7}$	$0.43^{+0.03}_{-0.03}$	$1.707^{+0.010}_{-0.012}$	1.17/200
19	$0.56^{+0.02}_{-0.02}$	$17.1^{+0.4}_{-0.4}$	$44.2^{+0.9}_{-0.9}$	$8.5^{+0.9}_{-0.9}$	$0.39^{+0.03}_{-0.03}$	$1.727^{+0.011}_{-0.015}$	1.27/200
20	$0.51^{+0.02}_{-0.02}$	$17.0^{+0.4}_{-0.4}$	$45.4^{+1.0}_{-1.0}$	$9.6^{+0.9}_{-0.9}$	$0.43^{+0.04}_{-0.04}$	$1.850^{+0.012}_{-0.016}$	1.16/200
21	$0.59^{+0.02}_{-0.02}$	$17.6^{+0.4}_{-0.4}$	$44.3^{+0.8}_{-0.8}$	$8.1^{+0.9}_{-0.8}$	$0.45^{+0.03}_{-0.03}$	$1.656^{+0.008}_{-0.010}$	1.02/216
22	$0.59^{+0.02}_{-0.02}$	$18.0^{+0.3}_{-0.3}$	$45.8^{+0.5}_{-0.5}$	$9.4^{+0.5}_{-0.5}$	$0.48^{+0.02}_{-0.02}$	$1.711^{+0.006}_{-0.006}$	1.15/214
			105^{+4}_{-4}	10-	$0.77^{+0.31}_{-0.26}$		
23	$0.52^{+0.02}_{-0.02}$	$16.7^{+0.4}_{-0.4}$	$45.4^{+0.9}_{-0.9}$	$9.0^{+0.9}_{-0.8}$	$0.42^{+0.03}_{-0.03}$	$1.950^{+0.009}_{-0.014}$	1.07/186
24	$0.61^{+0.02}_{-0.02}$	$18.2^{+0.4}_{-0.3}$	$45.9^{+0.5}_{-0.5}$	$9.8^{+0.6}_{-0.5}$	$0.49^{+0.03}_{-0.03}$	$1.320^{+0.004}_{-0.006}$	1.17/214
			105^{+5}_{-4}	10-	$0.76^{+0.4}_{-0.3}$		
25	$0.61^{+0.02}_{-0.02}$	$17.8^{+0.4}_{-0.4}$	$45.1^{+0.7}_{-0.6}$	$9.2^{+0.7}_{-0.6}$	$0.51^{+0.03}_{-0.03}$	$1.337^{+0.006}_{-0.009}$	1.04/216
26	$0.67^{+0.03}_{-0.03}$	$18.2^{+0.7}_{-0.7}$	$44.7^{+1.1}_{-1.0}$	$8.0^{+1.0}_{-1.0}$	$0.52^{+0.06}_{-0.06}$	$0.934^{+0.006}_{-0.010}$	0.96/192
27	$0.70^{+0.03}_{-0.03}$	$18.9^{+0.9}_{-0.9}$	$44.5^{+1.3}_{-1.2}$	$7.8^{+1.1}_{-1.0}$	$0.61^{+0.07}_{-0.07}$	$0.820^{+0.007}_{-0.009}$	0.95/162
28	$0.77^{+0.04}_{-0.04}$	$19.7^{+1.2}_{-1.1}$	$45.6^{+1.7}_{-1.6}$	$7.8^{+1.3}_{-1.3}$	$0.62^{+0.10}_{-0.05}$	$0.543^{+0.005}_{-0.008}$	1.01/162
29	$0.82^{+0.05}_{-0.05}$	$21.2^{+1.8}_{-1.6}$	$47.3^{+2.6}_{-2.2}$	$8.8^{+2.0}_{-1.8}$	$0.61^{+0.11}_{-0.11}$	$0.445^{+0.005}_{-0.009}$	0.96/150
30	$0.98^{+0.06}_{-0.06}$	$25.1^{+3.4}_{-2.8}$	$47.8^{+3.6}_{-2.7}$	$7.5^{+2.4}_{-2.0}$	$0.80^{+0.20}_{-0.20}$	$0.296^{+0.004}_{-0.008}$	0.87/130
31	$1.00^{+0.03}_{-0.03}$	$24.5^{+1.4}_{-1.4}$	$46.7^{+1.3}_{-1.2}$	$6.8^{+1.0}_{-0.9}$	$0.63^{+0.08}_{-0.08}$	$0.197^{+0.001}_{-0.002}$	1.25/150

APPENDIX E

Fundamental and astronomical physical constants

In Table E.1 the fundamental physical constants and astronomical constants used in this work are listed. The values are given in the International System of Units (SI) and in cgs (system of units commonly used in astronomy). The source for the fundamental physical constants is the NIST reference on Constants, Units and uncertainty, recommended by CODATA (Committee on Data for Science and Technology). The astronomical constants are from Zombeck (2007).

Table E.1: Fundamental and astronomical physical constants used in this work.

Quantity		Value (SI)	Value (cgs)
Newtonian constant of gravitation	G	$6.67428(67) \times 10^{-11} \text{ J m kg}^{-2}$	$6.67428(67) \times 10^{-8} \text{ erg cm g}^{-2}$
Speed of light in vacuum	c	$2.99792458 \times 10^8 \text{ m s}^{-1}$	$2.99792458 \times 10^{10} \text{ cm s}^{-1}$
Elementary charge	e	$1.602176487(40) \times 10^{-19} \text{ C}$	$4.8032(12) \times 10^{-10} \text{ esu}$
Electron mass	m_e	$9.10938215(45) \times 10^{-31} \text{ kg}$	$9.10938215(45) \times 10^{-28} \text{ g}$
Proton mass	m_p	$1.672621637(83) \times 10^{-27} \text{ kg}$	$1.672621637(83) \times 10^{-24} \text{ g}$
Planck constant	h	$6.62606896(33) \times 10^{-34} \text{ J s}$	$6.62606896(33) \times 10^{-27} \text{ erg s}$
h/π	\hbar	$1.054571628(53) \times 10^{-34} \text{ J s}$	$1.054571628(53) \times 10^{-27} \text{ erg s}$
Boltzmann constant	k	$1.3806504(24) \times 10^{-23} \text{ J K}^{-1}$	$1.3806504(24) \times 10^{-16} \text{ erg K}^{-1}$
Solar mass	M_\odot	$1.98844(30) \times 10^{30} \text{ kg}$	$1.98844(30) \times 10^{33} \text{ g}$
Solar radius	R_\odot	$6.961 \times 10^8 \text{ m}$	$6.961 \times 10^{10} \text{ cm}$
Solar Luminosity	L_\odot	$3.846(8) \times 10^{26} \text{ J s}^{-1}$	$3.846(8) \times 10^{33} \text{ erg s}^{-1}$

Acknowledgments

First of all I would like to thank Andrea Santangelo for giving me the opportunity to join his group, for his support all these years, and for being always willing to listen. And for being patient until I understood the “subtle” sign that a closed door means “do not disturb”!

A very big thanks goes to Peter Kretschmar. He is the person who “introduced” me to A 0535+26, and has been an unconditional support during this years, always available for help and discussions. Thanks for welcoming me in your office during my visits to ESAC. I am willing to wait eleven years for the next outburst of A 0535+26 and never lose the enthusiasm like you did!

I am grateful to Prof. Staubert for his very good advices, for teaching me the secrets of timing analysis, and for being always available for discussion.

A big thanks goes to Konstantin Postnov. This thesis would not have been the same without your contribution. I am in debt for all the very stimulating conversations and your help.

I would also like to thank Ute Kraus for her help while we worked together, and for the very interesting conversations about the mysteries of pulse profiles. It has been a pleasure to work with you.

A very special thanks goes to Marcus Kirsch, for the great work you did with the trainees in ESAC, and for introducing me into the world of “real” science, and talking to me in the first place about Tübingen.

I would also like to thanks Jörn Wilms, for being always available for advice and willing to help. And I also would like to thank all the “magneteters”, Rick Rothschild, Katja Pottschmidt, Slawo Suchy, Ingo Kreykenbohm . . . I have learned a lot this years during the telecons (at a not so friendly CET!) and during the meetings in ISSI.

I also want to thank Dmitry Klochkov for his help, specially while I was writing my first paper.

I am also grateful to Mark Finger, who shared with us part of the *RXTE* observations subject of this work.

I also want to thank Thorsten Nagel for being always willing to help, and for his patience helping me doing old-fashioned black and white photographs of the Moon with the 80 cm telescope. And I also want to thank all the other colleagues at the AIT,

with whom I have shared a large amount of espressos, stressy times but also sunny times in the terrace. And thanks also to Michael Martin for our “brain waves sharing” days the last summer.

I can't forget my office mates during this years, Gabrielle Schönherr, Rozaliya Doroshenko and Victor Doroshenko. Thanks for understanding that in the cold long German winters it is important to keep the office warm!

I also want to thank Alex and Antonio, for the good times we spent together in Tübingen and for being there in the not so good ones. A very big thanks goes also to Beppe.

Thanks also to Benjamín Montesinos for his advice while I was deciding what to do after my studies.

I also want to thank Juan, Julia and Guille for being good friends.

And last but not least I want to thank my mother, my sisters, Miguel, Carmen and Pepe for their unconditional support. ¡Con la que se nos viene encima!

Curriculum vitae

- 05.07.1980 Born in Madrid, Spain
- 1985-1989 Elementary School, Colegio Los Peñascales, Madrid, Spain
- 1989-1990 Elementary School, Colegio Español Federico García Lorca, Paris, France
- 1990-1993 Middle School, Lycée International de Saint-Germain-en-Laye, Paris, France
- 1994-1995 High School, Colegio Los Peñascales, Madrid, Spain
- 1995-1996 High School, International School of Beijing, Beijing, People's Republic of China
- 1996-1998 High School, Colegio Los Peñascales, Madrid, Spain
- 10.1998–02.2005 Study of Physics, branch of Astrophysics, at the Universidad Complutense, Madrid, Spain
- 09.2001–06.2002 ERASMUS scholarship at the Universidade de Coimbra, Portugal
- 04.2005–07.2005 Traineeship at the European Space Astronomy Centre (ESAC) of the European Space Agency (ESA), Villafranca, Spain
- 08.2005–12.2008 Scientific employee at Eberhard-Karls-Universität Tübingen, Institute of Astronomy and Astrophysics
Preparation of the thesis entitled: "X-ray observations of the accreting Be/X-ray binary pulsar A 0535+26 in outburst". Advisor: Prof. A. Santangelo

Apart from the professors of the Universidad Complutense of Madrid and Universidade de Coimbra, my academic teachers of the University of Tübingen have been the professors: A. Santangelo and J. Jochum